MICROFLUIDIC TECHNOLOGICAL ADVANCEMENTS FOR *IN SITU* NUTRIENT ANALYSIS

by

Sean Morgan

Submitted in partial fulfilment of the requirements
for the degree of Doctor of Philosophy

at

Dalhousie University
Halifax, Nova Scotia
April 2023

TABLE OF CONTENTS

LIST OF TABLES

LIST OF FIGURES

ABSTRACT

Comprehensive ocean variable mapping is an inter-disciplinary field that requires data and measurement capabilities for several areas of study, including nutrient flux dynamics in aquatic and marine environments. To this end, microfluidic technologies are uniquely suited to developing *in situ* sensors for remote or long-term deployment. Microfluidic devices require enabling technologies such as valves for effective fluid handling and absorbance measurement cells to spectrophotometrically determine nutrient concentrations in water samples. This thesis presents a fully automated *in situ* phosphate analyzer based on an inlaid microfluidic absorbance cell technology. Furthermore, embedded microvalves for integral fluid control are developed and explored for use in microfluidic devices.

This thesis first presents the fabrication and characterization of a tunable microfluidic check valve for use in marine nutrient sensing. The ball-style valve makes use of a rare-earth permanent magnet, which exerts a pulling force to ensure it remains passively sealed until the prescribed cracking pressure is met. By adjusting the position of the magnet, the cracking pressure is shown to be customizable to meet design requirements. It is low cost, requires no power, and is easily implemented on microfluidic platforms. However, the microvalve displayed poor chemical resistance towards several colourimetric reagents. Alternative valve designs using elastomer membranes and compressible O-rings are explored with the intention of creating a chemically robust valve. Design parametrization and simulations using COMSOL are used to determine the viability of these valves.

The microfluidic sensor developed over the course of this work employs colorimetric absorbance spectrophotometry to measure nutrient concentrations in seawater. The primary enabling technology of the device is an integrated inlaid optical absorbance cell that takes advantage of total internal reflection (TIR) to optically interrogate water samples. The sensor is field tested through its application to phosphate measurement in the Bedford Basin after undergoing in-lab validation and bench-top calibration. Finally, alternative flow configurations and optical enhancement methods are explored to improve the sampling rate and sensitivity of the *in situ* unit.

LIST OF ABBREVIATIONS USED

AUV	Autonomous Underwater Vehicle
CAD	Computer Aided Design
CEAS	Cavity Enhanced Absorption Spectroscopy
CFA	Continuous Flow Analysis
CO_2	Carbon Dioxide
COC	Cyclic Olefin Polymers
CRDS	Cavity Ring Down Spectroscopy
CTD	Conductivity, Temperature, Depth
DIC	Dissolved Inorganic Carbon
eDNA	Environmental DNA
FIA	Flow Injection Analysis
FEMM	Finite Element Method Magnetics
GOOS	Global Ocean Observing System
ISFET	Ion-Sensitive Field-Effect Transistors
ISUS	*In Situ* Ultraviolet Spectroscopy
LOAD	Lab-On-a-Disk
LOC	Lab-On-Chip
LOD	Limit of Detection
NDIR	Nondispersive Infrared
NH_4^+	Ammonium
NO_2^-	Nitrite
NO_3^-	Nitrate
NOC	National Oceanography Center
PC	Polycarbonate
PCB	Printed Circuit Board
PCR	Polymerase Chain Reaction
PDMS	Polydimethylsiloxane
PMB	Phosphomolybdenum Blue
PMMA	Poly(methyl methacrylate)
PO_4^{3-}	Phosphate
POC	Point of Care
PVP	Polyvinylpyrrolidone
SAMI-Alk	Submersible Autonomous Moored Instrument for Alkalinity
SUNA	Submersible Ultraviolet Nitrate Analyzer
TLAS	Tunable Laser Absorption Spectroscopy
TMT	Tracer-Monitored Titration
TRL	Technology Readiness Level
UV-Vis	Ultraviolet-Visible
µTAS	Micro Total Analysis Systems

ACKNOWLEDGEMENTS

First, I want to express gratitude to my supervisor Professor Vincent Sieben. This work would not be possible without your advice and feedback. Over the course of my degree, you have shown me the importance of reaching beyond what I think is feasible, and acknowledging the value of building with my own hands, and I am a better researcher because of it.

I also want to thank my examining committee: Professors Mae Seto, Ghada Koleilat, and Chris Algar for volunteering your time to review this work and attend our meetings and exams throughout the years. Your insights have been extremely helpful and appreciated for project development and broadening my understanding in this multi-disciplinary field.

I am also very lucky to have had the help and support of my fellow lab members. Andre Hendricks and Joshua Creelman patiently worked with me to program microcontrollers and fill me in on the aspects of electrical engineering in which I was lacking. But mostly I would like to acknowledge the help and capabilities of Edward Luy; without him, this would probably not have been possible.

I am also very grateful for everything the people at Dartmouth Ocean Technologies have accomplished. They transformed the sensor from a faulty prototype to a fully functioning unit. In particular I would like to acknowledge Lee Miller, Merle Pittman, Mark Wright and Arnold Furlong as the driving forces behind the success of the instrument. However I would also like to acknowledge the contributions of Iain Grundke, James Smith and Connor Mackie for their help with sensor development and data acquisition.

Finally, I need to express my gratitude for the unconditional support of my family. Thank you to my parents and brothers for always encouraging me to do what I can and never back away. Lastly, thank you Sarah for being my partner and best friend as I fumbled my way through this.

CHAPTER 1 INTRODUCTION

1.1. Motivation

Advancing our knowledge of the anthropogenic impact on the changing state of our oceans requires wide-scale, comprehensive, multi-parameter studies of ocean variables. The Global Ocean Observing System (GOOS) has stated that the main elements for coastal ocean observations are measurements, data management, and data analysis, but the first and primary element is measurement and sensing ability [1]. Global oceanic primary production is affected by biogeochemical cycles, genetic diversity and other physical parameters such as temperature, pH and salinity. Furthermore, it is largely driven by the transport dynamics of marine macronutrients such as nitrate, nitrite, and phosphate, which also tie in to the larger overarching elemental cycles for nitrogen and phosphorus [2], [3]. Industrial nutrient runoff can alter these cycles, leading to eutrophication-induced hypoxia, which has resulted in an extreme increase in coastal dead zones [4] and a widespread declining oxygen on a global scale [5]. Similarly, trace metals like iron, manganese, and boron have nutrient-like characteristics and directly impact primary production and oceanic carbon dioxide (CO_2) uptake [6]. Furthermore, although the carbon cycle is a complex and multi-faceted system, it has become evident that it is inherently entwined with the state of global waterbodies, both freshwater and marine [7]. Widespread acidification is a clear product of oceanic CO_2 sequestration and has the potential to irreparably impact the diversity of calcifying organisms [8]. Other threats such as declining biodiversity [9], oil spills and their associated consequences [10], and plastic marine debris [11] are factors that again require effective monitoring and measurement methods if they are to be realistically addressed or mitigated. For these reasons, the Global Ocean Observing System has listed the following biogeochemical elements as Essential Ocean Variables (EOVs): oxygen, nutrients, inorganic carbon, transient tracers, particulate matter, nitrous oxide, stable carbon isotopes and dissolved organic carbon. Not all of these variables will be discussed here, but most of what is discussed in further sections is drawn from this list.

Most ocean variable measurements are traditionally performed *ex situ* on benchtop instruments in a laboratory. Water samples for the measurements are collected in the field using containers such as Niskin bottles that have been cast down to a known depth, either from a ship or from a mooring [12]. After the bottles are retrieved, the seawater samples are manually filtered through a membrane and then either chemically or thermally preserved depending on the intended application, although sample degradation still occurs. The samples are then transported to the laboratory to undergo processing and analysis, days or even weeks later. The large financial overhead and time cost involved with this form of sample acquisition and analysis severely limits the frequency and scale of what is feasible in terms of comprehensive ocean monitoring. In the past few decades, the restrictions of this reality have motivated a shift towards developing *in situ* instruments for ocean variable measurements. The processes and risks associated with *ex situ* sampling become largely irrelevant when using *in situ* devices. Furthermore, they typically allow much higher sampling frequencies, on the order of hours or minutes instead of days or weeks. Also, when integrated with autonomous underwater vehicles (AUVs) or other mobile platforms, the high sampling frequency of *in situ* instruments enables much higher spatial resolutions to be captured. The Argo program is an excellent example of this. It is a component of GOOS and consists of over 30 countries deploying over 4000 profiling floats, each equipped with a suite of *in situ* sensors. Although there are very specific requirements for the sensors on the Argo floats, the basic requirements for any *in situ* sensor are a low power consumption, low reagent usage, and a fast sampling rate. Through miniaturization of established benchtop analytical techniques, microfluidic technologies form the functional component of many of these *in situ* instruments. Colorimetric absorbance spectrophotometry [13], fluorescence spectroscopy [14], luminescence measurements, and electrochemical techniques [15] are now all performed *in situ* by miniaturized sensors, largely built on microfluidic devices.

Microfluidics is the field of study surrounding the control and analysis of fluid volumes on the order of tens of micrometers [16]. Although the first microfluidic devices were miniature gas phase chromatographers, they have since been applied extensively in medicine [17], [18], biology [19]–[21], biochemistry [22], genetics [23], [24], pharmaceuticals [25], and even oil and gas [26], [27]. Figure 1.1A is an example of an early microfluidic chemostat used for monitoring cell cultures with singe cell resolution [28]. A coin is shown next to the device to indicate scale, highlighting the level size reduction that is possible when employing microfluidic devices. Figure 1.1B is an example of a microfluidic concentration separator fabricated using laser ablation techniques [29]. Figure 1.1C is a concept image for a microfluidic droplet generator [30]. Alternating droplets are generated for analysis in the microchannel by taking advantage of the geometry of tapered channels. This application demonstrates how these microfluidic devices can be used for extremely high throughput and sampling rate. A droplet based system such as the one displayed here is capable of generating and analyzing several thousand samples per hour. In recent years, marine and environmental monitoring technologies have also taken

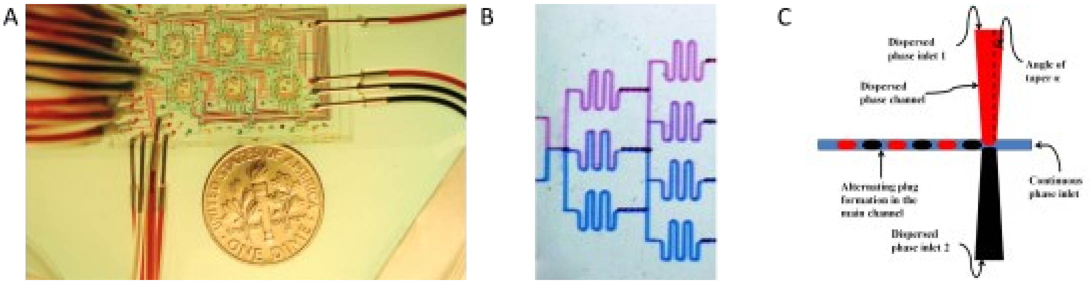

Figure 1.1: Microfluidic example applications. A. Bioreactor for cell cultures. Reprinted with permission from reference [28]. B. On-chip fluid mixer. Reprinted with permission from reference [29]. C. Multi-phase droplet generator. Reprinted with permission from reference [30] .

advantage of the low reagent requirement and small size of microfluidic devices [13], [31]–[36]. These microfluidic sensors are designed to be deployed *in situ* in remote environments or mounted to profiling platforms to determine nutrient concentrations in marine environments.

Microfluidic technologies focus mainly on the analysis and handling of fluids on the sub-milliliter scale. Well established techniques for benchtop fluid analysis are miniaturized and performed on these devices to reduce energy consumption, shorten sampling time and lower reagent usage from several milliliters or even liters to the order of microliters and potentially down to picolitres. Each of these characteristics overlap with the essential requirements for any *in situ* measurement device, highlighting the compatibility of microfluidic technologies with *in situ* instrumentation. As a result, *in situ* microfluidic devices are becoming common place for use in marine environments [31]. However, some *in situ* sensors for ocean parameters such as pH, dissolved oxygen and salinity do not always require fluid handling, and consequently are not based on microfluidic technologies. When reagents are required, the sophisticated fluid control gained by use of microfluidic systems is having a transformative impact on observation capacity.

1.2. Thesis Objectives

Microfluidic technologies are uniquely suited to the development of *in situ* sensors for marine and freshwater environments. Nutrients such as phosphate, nitrite and nitrate are excellent candidates for *in situ* sensing on a microfluidic system because they can be quantified using reagent based colourimetric measurement techniques. However, a fully functioning sensor is comprised of several different technologies integrated in a single unit. Absorbance cells, pumps, valves, mixers, optical components, and electronics are required to develop an *in situ* nutrient sensor.

The main objective of this thesis is to detail and outline the development and deployment of a fully functional *in situ* microfluidic nutrient sensor. Although the Argo program is directed more towards open ocean monitoring rather than coastal, the requirements for a sensor to be deployed on an Argo profiling float can be treated as ideal, considering their need for multi-year and remote sensing capability. To that end the ideal requirements for the sensor are set both by the requirements of a typical profiling float in the Argo program, and the *in situ* sensors it currently supports. They are as follows:

Energy consumption (joules/sample)	< 45 J
Reagent consumption (volume/sample)	< 30 μL
Sensor size (volume)	< 2000 cm^3
Deployment period (time)	> 24 months

These requirements are strictly ideals, that represent a target to work towards in the long term. A shorter term set of requirements would be those that make the device commercially competitive with existing options. With that as the framework, an intermediate set of requirements are as follows:

Energy consumption (joules/sample)	< 500 J
Reagent consumption (volume/sample)	< 1 mL
Sensor size (volume)	< 7000 cm^3
Deployment period (time)	>3 months

I will also discuss some designs for integrated valves for fluid control, highlighting both the successful designs as well as the unsuccessful designs. Furthermore, I will briefly describe the manufacturing process for a novel inlaid microfluidic absorbance cell and lastly, we will examine some alternative optical and fluid handling techniques for improved sensitivity and sampling rate.

1.3. Outline of the Thesis

The structure of the thesis is framed so that each chapter describes the work done to build up to the development of a fully functional sensor. Chapter 2 is a literature review of the existing technology and analytical techniques relevant to *in situ* ocean sensing. It also describes the theory behind some of the more applicable techniques such as colourimetric absorbance spectrophotometry or fluorescence spectroscopy. The intention of this chapter is to build a knowledge base to contextualize the work described in Chapters 3 – 7.

Chapters 3 and 4 focus on designing and manufacturing integrated microfluidic check valves. Chapter 3 outlines the creation and characterization of a magnetically tunable check valve. The valve was integrated into an early version of the nutrient sensor for a proof-of-concept deployment in the Dalhousie Aquatron. Chapter 4 highlights further efforts to create chemically robust check valves. Both elastomer style check valves and ball-style valves are explored using simulations and parametrization in the manufacturing process. The limited success of these endeavours is discussed and expanded upon.

Chapter 5 describes the novel inlaid absorbance cell used as the basis for the microfluidic component of the sensor. It is only presented as an overview because the fully detailed manufacturing process and characterization of the absorbance cells is covered in Edward Luy's 2021 Master's thesis, but was a collaborative work between Edward and myself

Chapter 6 presents the entire sensor as a functional unit. The conceptual design and practical implementation is discussed, and each integrated component is described. The sensor is calibrated on the bench and then further calibrated to determine the temperature dependence of the results between 5 and 20° C. It is then deployed in the Bedford Basin to demonstrate its real-world applicability and the results are compared against a standard benchtop measurement as validation.

Chapter 7 outlines some alternative measurement techniques that can be performed on the sensor. Continuous Flow Analysis with reagent injection is performed on a benchtop testing apparatus with the intention of improving the sampling rate and reagent consumption rate of the sensor. Furthermore, Cavity Enhanced Absorption Spectrophotometry is explored in simulation as an option to lower the detection limit of the sensor.

General observations from Chapters 2 – 7 and considerations for future study are presented in Chapter 8 as a concluding chapter.

1.4. Publications and Conferences

The contents of this dissertation represent my intellectual work during the time I spent working in the Sieben Lab at Dalhousie University between 2018 and 2023. The work presented here has been supported and/or funded by the Ocean Frontier Institute (OFI), the Innovacorp Early Stage Commercialization Fund (ESCF), RBR Ltd., the Centre for Ocean Ventures & Entrepreneurship (COVE), the Marine Environmental Observation, Prediction and Response Network (MEOPAR), the Natural Sciences and Engineering Research Council (NSERC), and most importantly Dartmouth Ocean Technologies Inc. (DOT).

Any portion of the work contained in this thesis that was performed in part by or in collaboration with another is explicitly stated as such. Furthermore, the contents of some chapters of this work are based largely on peer-reviewed publications, listed below.

1.4.1 Peer-Reviewed Publications

The following list represents the peer-reviewed journal articles I have worked on during the period of this dissertation. First authorships as well as secondary and other authorships are included.

1. **S. C. Morgan**, A. D. Hendricks, M. L. Seto, and V. J. Sieben, "A Magnetically Tunable Check Valve Applied to a Lab-on-Chip Nitrite Sensor," *Sensors*, vol. 19, no. 21, Jan. 2019 [37]

2. **S. Morgan**, E. Luy, A. Furlong, and V. Sieben, "A submersible phosphate analyzer for marine environments based on inlaid microfluidics," *Anal. Methods*, vol. 14, no. 1, 2022 [38]

3. E. A. Luy, **S. C. Morgan**, J. J. Creelman, B. J. Murphy, and V. J. Sieben, "Inlaid microfluidic optics: absorbance cells in clear devices applied to nitrite and phosphate detection," *J. Micromechanics Microengineering*, vol. 30, no. 9 Jun. 2020 [39]

4. C. Sonnichsen, D. Atamanchuk,, A. Hendricks, **S. Morgan**, J. Smith. *et al.* "An Automated Microfluidic Analyzer for *In situ* Monitoring of Total Alkalinity," *ACS Sens.*, Jan. 2023 [40]

1.4.2 Conference Proceedings

The following list represents all conference proceedings, including abstracts, papers, presentations and posters that I have been involved with during the period of this work.

1. **S. Morgan,** E. Luy, and V. Sieben, "Inlaid microfluidics for nutrient monitoring," in *The 23rd International Conference on Miniaturized Systems for Chemistry and Life Sciences*, µTAS, Basel, Switzerland, Oct. 2019. [41]

2. B. Murphy, **S. Morgan**, E. Luy, J. Creelman, and V. Sieben, "Lab-on-a-chip Sensor for *In situ* Nutrient Monitoring," in *OCEANS 2019 MTS/IEEE SEATTLE*, Oct. 2019, pp. 1–7. [42]

3. **S. Morgan** *et al.*, “An *In situ* Phosphate Analyzer for Marine Environments Using Inlaid Microfluidics,” in *OCEANS 2021: San Diego – Porto*, Sep. 2021, pp. 1–9. [43]

4. **S. Morgan**, “Inlaid Microfluidics for *In situ* Phosphate Sensing,” in *Emerging Investigators in Microfluidics*, Online, 2021. [44]

5. E. Luy, J. Smith, I. Grundke, C. Sonnichsen, **S. Morgan**, A. Furlong, V. Sieben, “Simultaneous *in situ* Nitrate and Orthophosphate Measurement Using a Dual Chemistry Microfluidic Sensor,” in *OCEANS 2022, Hampton Roads*, Oct. 2022, pp. 1–8. [45]

6. **S. Morgan**, E. Luy, and V. Sieben, “Low-cost Microfluidic Nutrient Sensors,” presented at the Marine Environmental Observation, Prediction and Response Network Annual General Meeting, Victoria, B.C. Canada, 2019. [46]

7. **S. Morgan** *et al.*, “*In situ* Phosphate Analysis Using Inlaid Microfluidics,” in *The 25th International Conference on Miniaturized Systems for Chemistry and Life Sciences*, µTAS, Palm Springs, California, 2021. [47]

8. **S. Morgan**, A. Hendricks, and V. Sieben, “Improvements to colourimetric absorbance measurement techniques for nutrient analysis on microfluidic devices,” in *Ocean Frontier Institute*, 2022. [48]

1.4.3 Patents

During the course of my work on the microfluidic sensor projects, I was involved in the patent application for four technologies in which I was involved. To date, one has been fully granted, two are still in the provisional phase. We decided not to pursue a full application for the fourth technology after the provisional period had ended, so it is not included in the list below.

1. E. A. Luy, **S. C. Morgan**, and V. J. Sieben, “Optical cell and methods of manufacturing an optical cell,” US 11,231,356 B2, Mar. 17, 2022 [49]
2. Provisional Patent – Microfluidic Chip, Systems, and Methods for Capturing of Environmental DNA: Joshua J. Creelman, Edward A. Luy, Gabryelle Beland, **Sean C. Morgan**, Julie LaRoche, Mahtab Tavasoli, Robert Beiko, Roger Race, Arnold Furlong, Vincent Sieben; US App 17/468,986
3. Provisional Patent – Magnetically Tunable Microfluidic Check Valve, Microfluidic Pumps, Syringe Pump, and Methods of Manufacturing Thereof: **Sean C. Morgan**, Vincent J. Sieben, Edward A. Luy; US App 17/603,356

CHAPTER 2 LITERATURE REVIEW

This will be a review of recent *in situ* instruments developed for ocean monitoring and observation. The focus will be primarily on devices built around microfluidic technology, however other relevant solid-state devices will be included to build a more complete survey of the state-of-the-art. I will first outline the main relevant analysis techniques involved in ocean monitoring, with brief explanations of the theory underlying them. I will also point out some key microfluidic technologies that are essential for marine applications. I will then highlight and review some recent instruments based on their intended application and performance metrics and examine some of their end uses.

2.1. Relevant Analytical Techniques for Ocean Monitoring

Here I will discuss some of the more common analytical methods that have been adapted for *in situ* devices. The most common fluid analysis methods involved in ocean monitoring are based on quantifying optical responses, with the majority being either optical absorbance or fluorescence measurements. However, some *in situ* sensors use electrochemical measurements, and other applications require more advanced techniques such as flow cytometry.

2.1.1 Colorimetric Absorbance

Optical absorption spectrophotometry is a well-established technique for biological and chemical analysis. It is a simple and robust method of detecting the presence of a variety of species or chemicals within a fluid sample. In ocean monitoring applications, a seawater sample is mixed with a reagent that reacts with a specific analyte within the sample to form a coloured dye and the attenuation of light through the dye provides an absorbance value. The emission spectrum of the light source typically overlaps significantly with the absorption spectrum of the product dye. Next, the concentration of the analyte is determined directly from wavelength dependent absorbance using the Beer-Lambert law.

$$A(\lambda) = \log_{10}\left(\frac{I_o}{I}\right) = \epsilon(\lambda)lc$$

Absorbance, A is measured as the logarithm of the ratio of incident to transmitted light intensities, and used to find the concentration, c, as a function of l and ϵ, the optical path length and the attenuation coefficient of the analyte. The molecular attenuation coefficient is an experimentally determined value that indicates how strongly a species attenuates light at a given wavelength, combining the attenuation due to both absorption and scattering. The absorbance is a linear function of not only the concentration, but also the optical path length. In standard benchtop absorption measurements, the path length dependence is hardly a limitation. In microfluidic setups, however, this can become an obstacle as they are often geometrically constrained. Optical absorption spectrophotometry is traditionally one of the main techniques for benchtop analysis of nutrients and trace metals such as nitrite [39], [50], nitrate [50], [51], phosphate [52], [53], silicate [36], [54], iron [55], [56], boron [57] and manganese [58], [59]. However, benchtop methods still require the use of large sample sizes and in-lab analysis. For this reason, optical absorption on microfluidic platforms has been the focus of much research in the past couple of decades [60].

UV/vis spectroscopy is well suited for microfluidic platforms, and microfluidic absorption cells have already been implemented and studied for sensing and monitoring in many fields. Biosensors are a perfect example of this: microfluidic absorption spectroscopy has been used for analyzing biofilms [61], studying single molecules in enzymatic reactions [62], detecting the presence of specific bacteria species [63], cellular phenotyping [64], detecting changes in cell morphology [65] and other applications [66]. The primary focus of this work, however, is to look at the use of microfluidic devices in marine environments. Specific applications of colourimetric absorbance measurements done on microfluidic systems in the UV-Vis (Ultraviolet-Visible) region (approx. 200 nm to 900 nm) will be discussed in later sections.

2.1.2 Fluorescence

One important application of fluorescence measurements is to quantify and identify species of cyanobacteria in a water sample. Pigments such as chlorophyll-*a*, which is a common proxy for phytoplankton biomass, and phycocyanin absorb incident light over a specific range of wavelengths, causing the electrons within the molecules to become excited to a higher state [67]. The electrons then return to a lower state, releasing energy in the form of emitted light known as fluorescence. Fluorometers provide an excitation light source targeted for a specific fluorescing species and measure the emission response, which is proportional and often linear to the concentration of the species [14]. Issues arise with selectivity and accuracy due to overlapping emission and excitation bands. For example, chlorophyll-*a* has an excitation band at 550 – 680 nm, which overlaps with the excitation band of phycocyanin at 590 – 610 nm. Furthermore, chlorophyll-*a* has an emission band at 680 – 685 nm, which also overlaps with the emission band of phycocyanin at 660 – 685 nm [14]. These limitations can be partially addressed and minimized by using narrower band pass filters, both on the emission side and excitation side and by employing other coincident measurements and statistical analysis techniques [68]. However, in optically complex waters with multiple fluorescing and luminescing species, fluorescence measurement can seldom be fully deconvolved to individual species leading to errors in reported values.

Although there are some exceptions such as the combined absorbance and fluorescence cell presented by Creelman et al. [69], *in situ* fluorometers typically do not use microfluidic technologies because they do not require fluid handling to function. All-optical sensors are very attractive options for *in situ* applications because they do not contain large power drawing elements, such as pumps and active valves, and can be deployed without the overhead of preparing and preserving reagents. However, depending on the concentration of the species in question and the interferences in the seawater matrix, the relative measurement error can exceed 200 % [14]. Although fluorescence has been used in microfluidic flow cytometers, the fluorescence-based instruments presented in the applications section will be primarily solid-state devices that do not require pumping and control of fluids and are therefore not considered to be microfluidic.

2.1.3 Optodes

Optical electrodes, or optodes, are purely optical sensors, requiring no reagents and producing no waste. They indirectly employ fluorescence to quantify analytes rather than directly measuring the fluorescence signal of the analyte. Typically, they consume much less power and can achieve much shorter response times than their benchtop counterparts. For these reasons, optodes have been gaining widespread recognition for *in situ* sensing, particularly for dissolved oxygen [70]. Optodes have also been created to measure other analytes, such as carbon dioxide and pH [71].

Optodes are based on four key components: a light source with a specific wavelength, a fluorescing indicator that is quenched in the presence of the analyte, a structural material to hold the chemical indicator, and a detector for the fluorescence emissions [72]. Directly measuring and comparing the magnitude of the fluoresced light is possible but the results can suffer greatly from noisy signals. This is often circumvented by measuring the lifetime of a signal using a technique called luminescence quenching. The magnitude of fluorescing light from the sensing foil will experience more quenching when faced with a higher concentration of the analyte in the environment. The luminophore (sensing foil) is typically made from a transition metal complex, often based on ruthenium for oxygen [73], [74]. However, ruthenium is sensitive to photobleaching [75], so other luminophores, such as platinum based ones [76] have been explored as possible alternatives.

The lifetime of a fluorescing molecule is the time it takes for the molecule to go from an excited state back to its original state [77] only a fraction of the energy in the excited state is emitted in the form of fluorescing light. The rest of the energy is used as thermal energy or in other chemical reactions, such as reactions with a quenching molecule. The higher the concentration of the quencher, the more likely the fluorescing molecule will react with it, and the quicker the molecule will lose energy and fluoresce. In the application of the oxygen optode, the higher the oxygen concentration is, the shorter the average lifetime of the fluorescing molecules will be.

To directly measure the lifetime of the emission is very difficult and would require very fast electronics, as the fluorescing lifetime can sometimes be just a few microseconds, or even nano seconds [78]. For this reason, the amplitude of the excitation light source is modulated with a known frequency. The lifetime of the fluorescence will cause emitted light signal to be shifted out of phase with the input signal, but at the same frequency. The resultant combined signal can then be deconvolved into the two distinct signals and the phase shift taken as the fluorescence lifetime. The measured lifetime is then used to determine the analyte concentration using the Stern-Volmer equation [79]:

$$[A] = \frac{1}{K_{SV}}\left(\frac{\tau_0}{\tau} - 1\right)$$

where K_{SV} is the experimentally determined Stern-Volmer quenching coefficient for the analyte, τ is the measured lifetime and τ_0 is the lifetime in the absence of the analyte as a quenching material.

There are alternative designs of optodes for other analytes such as carbon dioxide. The main difference is in the indicator layer and the two-step fluorescence quenching mechanism. Where oxygen directly quenches the fluorescence emissions in an oxygen optode, there is an intermediate excitation and re-emission happening in typical carbon dioxide optode [80]. The indicator layer houses two species of molecules: one fluorescing species that is insensitive to carbon dioxide, and one absorbing species that is sensitive to changes in pH, and therefore carbon dioxide. In the absence of carbon dioxide, there is a large degree of overlap between the emission spectrum of the fluorescing species and the absorption spectrum of the pH sensitive species. As the carbon dioxide concentration increases, the absorbing species becomes protonated (dropping the pH) and the overlap decreases. This manifests as an increase in lifetime for the fluorescing species [81]. The lifetime can then be used to determine the concentration of carbon dioxide in the environment.

A different set up uses an indicator layer with two separate carbon dioxide insensitive luminescing species, each with drastically different lifetimes [82]. One species is fluorescent with a near instantaneous lifetime, while the other is phosphorescent with a 150 μs lifetime. A third pH-sensitive species has an absorbance peak that shifts with a change in pH. This allows the resultant ratio between the two emitted peaks to be used as a measurement for carbon dioxide. The ratio is found by modulating the input signal at a known frequency. The phase shift is known as the difference in lifetimes, so the output signal can be deconvolved to find the relative amplitudes of the two emission signals.

Although optodes as instruments are not microfluidic devices, they are important sensors for *in situ* ocean variable monitoring. Furthermore, optode technologies and sensing films have been fused with microfluidic technologies to different ends. Grate et al. [83] were able to impregnate the channels of microfluidic devices with oxygen sensitive optode materials into to enable the sensing of the oxygen gradients and interior conditions of the device itself. Previous to this, Grate et al. used similar materials and microfluidic technology to analyze carbon sequestration in porous media [84]. Also, Ashagre et al. [85] embedded an ion-selective optode within a microfluidic device to sense cationic surfactants in dental rinses.

2.1.4 Electrochemical

For decades, electrochemical probes have been widely used for *in situ* monitoring. The conductivity, temperature, depth (CTD) probe commercialized in the 1980s by Neil Brown Instrument Systems [86] has established CTDs as essential ocean monitoring tools. CTDs are a good example of a commercialized product capable of full use by the end user; however, many other electrochemical devices require professional handling or further laboratory analysis to function [15].

Electrochemical sensors use the ionic properties of molecules combined with unique electrodes to measure concentrations in seawater. A common technique, most often applied to trace metal detection, is stripping voltammetry [87]–[89]. Stripping voltammetry uses three electrodes (working, reference and counter electrode) to measure the redox potential of the analytes in the sample. The first step to perform stripping voltammetry is deposition. A low potential is applied to the working electrode to reduce the analyte metal ions in the sample and cause the metal to deposit onto its surface. The next step, stripping, involves reversing the potential to re-oxidize and strip the analyte from the working electrode. The magnitude of this "stripping potential" can be used to quantify the analyte concentration, because it is related to the redox potential of the analyte. The reference electrode and counter electrode are used to control and balance the potential and current in the cell.

For substances that cannot undergo redox reactions, a second common type of electrochemical sensor based on potentiometry is used. Potentiometry, in general terms, is measuring the potential between two electrodes to determine the concentration of the analyte [90]. Ion selective electrodes, often incorporating liquid or polymer membranes are needed to functionalize the sensors and make them selective to the analyte in question. For *in situ* ocean applications, polymer membranes are more often used, partially because solid-state devices are more deployable than the liquid filled electrodes [15]. These solid-state potentiometric sensors do not require reagents, use very little energy and have fast sampling rates. However, they require frequent recalibration and suffer large drift issues because they are sensitive to salinity, temperature and external electromagnetic interference [91].

2.1.5 Flow Cytometry

Flow cytometers have a long history of cellular analysis in laboratory settings, and have been used by oceanographers for sorting and quantification since the 1980s [92]. They are not strictly a measurement technique and could be classified as an application but are included here because they are fundamental for enabling other applications. They are capable of high throughput and perform multi-parameter measurements using several optical analysis techniques. The basic setup of a flow cytometer involves a narrow flow cell, an interrogation laser, and a detector. The flow cell permits the molecules to pass through the optical path in single file and each cell that passes through will be interrogated using absorbance and/or fluorescence techniques. Filters and mirrors are employed to measure multiple species on the same device. The narrow channel and fluid flow requirement for flow cytometers make them ideal candidates for microfluidic technologies. For example, fluorescence *in situ* hybridization (FISH) techniques have been frequently performed on microfluidic devices over the past two decades [93], and have even been used for quantitative analysis of marine bacterial communities [94]. Flow cytometers are still being developed for *in situ* analysis [95] and continue to appear in the marine sector for studying microbial and algal properties [96], [97]. The complexity of the optical system and fluid handling, even microfluidic based versions, have slowed the ruggedization engineering of the technology for enabling in situ deployments.

2.2. Literature and Commercial Instrument Review

Here we will discuss some of the more crucial ocean applications for *in situ* and microfluidic sensors. *In situ* sensors are suited to measuring variables that fluctuate on small temporal and spatial scales, such as pH, salinity, nutrient concentrations, and dissolved gasses. We will consider sensors for each application in terms of basic requirements and minimum performance metrics. We will also frame each application with regard to how it fits into the overall technological landscape of ocean monitoring. Lastly, we will consider the maturity of the sensors according to their Technology Readiness Level

Table 1: Technology Readiness Level Descriptions

TRL 1	Basic principles observed
TRL 2	Technology concept formulated
TRL 3	Experimental proof of concept
TRL 4	Technology validated in lab
TRL 5	Technology validated in relevant environment
TRL 6	Technology demonstrated in relevant environment
TRL 7	System prototype demonstration in operational environment
TRL 8	System complete and qualified
TRL 9	Actual system proven in operational environment

(TRL). The details for each of the 9 levels of the European Union version of the TRL scale for the public sector [98] are briefly listed in Table 1. As previously mentioned, we will be primarily highlighting microfluidic devices, but will also include other relevant *in situ* instruments, so long as they are applied to the list of EOVs presented by GOOS.

2.2.1 Nutrient Analysis

Dissolved nutrients are one of the most important parameters in ocean monitoring. Limiting nutrients such as phosphorus, nitrogen and silicon are largely responsible for the primary production that drives all life in the ocean. Nitrogen in the ocean exists mostly in three forms: nitrate (NO_3^-), nitrite (NO_2^-) and ammonium (NH_4^+), and is required by many phytoplankton species for the development of proteins and nucleic acids, making it a limiting nutrient for phytoplankton growth [99]. Most nitrogen in the ocean is in the form of nitrate, and a large portion is in the form of ammonium, created in surface waters by the cyanobacteria *trichodesmium* through atmospheric nitrogen fixation [100]. Likewise, phosphorus is available in the ocean as orthophosphate (PO_4^{3-}) and is needed by phytoplankton to produce the molecules ATP and ADP to aid in energy storage. Most phosphate is introduced through the weathering of rocks, but a portion comes from dissolved organic molecules and anthropogenic runoff [101]. Silicate is the third major nutrient when considering effects on primary production and the carbon pump, due to its role in the growth of diatoms. Diatoms possess hard mineral shells made of opal, or hydrated silicic acid, which is a compound of silicate, and they are perhaps the most ecologically impactful phytoplankton species, as they are responsible for approximately 20% of global primary production [102]. On a global scale, the three primary macronutrients exist in a stoichiometric equilibrium with carbon (C) known as the Redfield ratio: 106 C : 16 N : 1 P : 15 Si. However, on smaller more localized scales the ratio can be skewed by natural phenomena or human involvement, the effects of which can only be understood through effective and consistent monitoring.

Most *ex situ* nutrient measurements are performed on large benchtop devices called AutoAnalyzers using air-segmented continuous flow absorption spectrophotometry. These devices are considered the “gold-standard” within the oceanographic community as they have nanomolar level limits of detection for the three main macronutrients and have good precision between measurements. A 2015 study by Dafner compared the analytical performance of two well-established AutoAnalyzers and determined that they were capable of measurements with limits of detection (LODs) of 18 nM, 9 nM and 12 nM for phosphate, nitrate and silicic acid respectively and were precise to within 2.8 % across two bottle samples [103]. These values will be used as a performance benchmark for comparing the *in situ* devices, but other metrics such as power consumption and size need consideration depending on the application.

As previously stated, most *ex situ* nutrient analysis is performed using absorbance spectrophotometry, the details of which have been described in a previous section. With a few exceptions, this trend holds true with *in situ* sensors because absorbance spectrophotometry, with its very few electronic requirements, is well adapted to microfluidic applications. Table 2 lists some recent developments at the research level for microfluidic nutrient sensors for marine monitoring, as well as some key metrics such as detection limit and sampling period. In 2010, Sieben et al. [104] at the National Oceanography Center (NOC) in Southampton, UK introduced the concept of using partially transparent acrylic to manufacture a microfluidic optical absorbance cell for colourimetric absorbance measurements. Using an LED as the incident source, the tinted acrylic attenuates all scattered and non-directional light while still allowing transmission through thin (<1mm) windows. The low material cost and reliable chemical bonding method using chloroform and heat [105] has enabled rapid prototyping capabilities for these microfluidic devices. NOC has since developed an entire suite of *in situ* microfluidic sensors, many based on the now-patented tinted absorbance cell technology [99]. The details of the absorbance cell will be discussed in more detail in Section 5.1.

Table 2: Recent Microfluidic Nutrient Sensors

Author	Year	Analyte	Analytical Technique	Method	LOD (3σ)	Error	Period	TRL
Beaton et al. [107]	2017	NO_3^-	CAS	*In situ*	25 nM	n/a	20 min	6-7
Nightingale et al. [108]	2019	NO_2^-/ NO_3^-	CAS, Droplet	*In situ*	1.7 µM	6 %	10 s	5-6
Clinton-Bailey et al. [52]	2017	PO_4^{3-}	CAS	*In situ*	40 nM	4 %	35 min	5-6
Cao et al. [36]	2017	SiO_4^{4-}	CAS	*In situ*	45.1 nM	<4 %	5 min	5
Duffy et al. [33]	2017	PO_4^{3-}	CAS, Centrifugal	POC	52.6 nM	<8 %	10 min	5-6
Grand et al. [109]	2017	PO_4^{3-}	CAS	*In situ*	40 nM	6 %	< 30 min	6-7
Donohoe et al. [110]	2018	PO_4^{3-}	CAS	POC	90 nM	<12 %	<24 min	4-5
Hull et al. [111]	2021	NO_3^-	CAS	*In situ*	25 nM	n/a	n/a	6-7
Lahari et al. [112]	2022	NH_3	EC	POC	8.69 µM	< 7%	n/a	3-4
Rajasulochana et al. [113]	2022	NO_2^-	Colorimetric	POC	2.6 µM	<17 %	NA	3-4
Morgan et al. [37]	2019	NO_2^-	CAS	POC	n/a	n/a	45 s	4-5
Morgan et al. [38]	2022	PO_4^{3-}	CAS	*In situ*	15.2 nM	<28 %	< 30 min	6-7
O'Grady et al. [114]	2021	PO_4^{3-}	CAS, centrifugal	POC	168 nM	n/a	<10 min	5-6
Chen et al. [115]	2018	PO_4^{3-}	CAS	POC	n/a	n/a	<6 min	3-4
Khongpet et al. [116]	2019	PO_4^{3-}/NH_4^+	CAS	POC	1.89 µM	<10 %	5 min	3-4
Barus et al. [117]	2018	SiO_4^{4-}	EC	*In situ*	0.3 µM	n/a	<30 min	4-5

The earlier microfluidic sensor development at NOC was centered on *in situ* nitrite and nitrate detection at a fixed mooring using the well established Griess assay for total nitrite determination [13], however the technology has since been applied to glacial runoff analysis in Greenland [107], seafloor nitrate detection in Mauritania [118] and spring bloom nitrate dynamics using AUV integration in the Celtic Sea [35]. These more recent iterations of the *in situ* nitrite/nitrate sensors have LODs of less than 25 nM and sampling periods less than 15 min [118], making them competitive with benchtop autoanalyzers. More recently, Clinton-Bailey at al. [52] and Grand et al. [109] have reported on the development and deployment of an *in situ* phosphate sensor that uses a modified version of the EPA standard phosphomolybdenum blue (PMB) reagent for phosphate detection in water. They added a low concentration (0.01% w/v) of polyvinylpyrrolidone (PVP) to the assay to prevent the PMB from aggregating and to improve performance at lower temperatures down to 5 °C allowing a limit of detection (LOD) of 40 nM for phosphate and deployment in colder climates. This particular sensor will be discussed more thoroughly in CHAPTER 6 Other groups outside of the UK have also explored the tinted absorbance cell technology for nutrient detection. Using a very similar sensor design, Cao et al. in China used tinted acrylic to create an *in situ* microfluidic silicate sensor for deployment in Jiaozhou Bay, Qingdao [36]. Likewise, we used the same cell technology to create a surface vehicle mounted nitrite detector from otherwise entirely off-the-shelf components [37].

The basic mechanical elements of the types of reagent-based stop flow nutrient sensors developed by NOC consist of the microfluidic chip, up to 15 micro-solenoid valves, a stepper motor, between 1 and 4 syringes, reagent containers, and a pressure tolerant housing. The tinted absorbance cell technology allows colourimetric measurements to be taken using simple off the shelf components such as LEDs and photodiodes rather than expensive detectors and sensitive laser systems. However, the LED and photodiode still require careful manual alignment and immobilization using specialized adhesive. Furthermore, the electrical connections need to cross the water-air pressure interface, requiring expensive ports or connectors.

In 2022, Morgan et al. [38] reported the development and deployment of an *in situ* phosphate analyzer based on the same modified PMB assay as previously mentioned. Similar to the already reported stop flow *in situ* sensors, the mechanical components consist of stepper motors, solenoid valves, and an acrylic microfluidic device while the optical components consist of LED's photodiodes and collimating lenses. The main design differences between the two types of sensors are the number of stepper motors and the absorbance cell integrated within the microfluidic chip. Morgan et al. use three separate stepper motors to drive four syringes, leaving potential for alternative flow configurations such as continuous flow analysis in future works. The most critical difference is the inlaid absorbance cell [39] that uses embedded microprisms to direct light through the top interface of the chip, allowing the optical components to be entirely decoupled from the microfluidic chip, enabling easier chip replacement and fewer connectors across the pressure barrier.

Some groups have been developing devices for point of care (POC) testing rather than fully *in situ* sensing. POC measurements are an intermediate between *in situ* and *ex situ* methods. Rather than the sample being preserved and transported to a lab for *ex situ* analysis, the sample is analyzed at the extraction site, but not while being fully submersed in the water body. POC devices for nutrient analysis do not need to be pressure tolerant or in some cases even waterproof and can be externally powered more easily than *in situ* instruments. Duffy et al. at Dublin City University in Ireland [33] reported on the PhosphaSense phosphate analyzer, which uses centrifugal microfluidics, or lab-on-a-disc (LOAD) technologies for fluid pumping and handling, and the PMB assay for colourimetric analysis of soluble reactive phosphate. The device has three optical cells, allowing simultaneous measurements of three samples in 10 minutes, and requires only 96 μL of reagent per sample. This work was followed up in 2021 by O'Grady et al. [114], with added on board reagent storage. Also based out of Dublin, Donohoe et al. [110] developed a low cost on site phosphate analyzer that uses a custom 3D printed alignment jig that accepts a removable acrylic microfluidic cassette, allowing the optical components to be easily replaced and realigned as needed.

Table 3: Commercial *In Situ* Nutrient Sensors

Company	Product	Analyte	Analytical Technique	LOD (3σ)	Error	Sample Period
Sea-Bird Scientific [87]	HydroCycle-PO_4	Phosphate	CAS	24 nM	8 %	15 min
Sea-Bird Scientific [88]	SUNA V2	Nitrate	ISUS	0.3 μM	2 μM	Instant
Systea S.p.A [89]	WIZ probe	Phosphate, Nitrite, Nitrate, Ammonia	CAS, FLUO	8 μg P/L: [DRP], 1 μg N/L [$N\text{-}NH_4$]	<25%	38 min
ClearWater Sensors [90]	Phosphate Sensor	Phosphate	CAS	40 nM	NA	5 min
SouthWestSensor [91]	Nitrite and Nitrate sensor	Nitrite/Nitrate	CAS, droplet	0.3 μM	<10%	10 sec
Dartmouth Ocean Technologies [76]	Phosphate sensor	Phosphate	CAS	15.2 nM	<28 %	<30 min

Paper based microfluidics have frequently been used for POC measurements due to their low cost and ease of use. The most common example is the litmus test for pH analysis, but the techniques have also been applied to nutrient detection. Rajasulochana et al. [113] in India reported on the development of a smart-phone assisted nitrite sensor. Although the LOD of the technology is very high, at 2.6 μM for nitrite, it is still a cheap and fast method for applications such as drinking water analysis. One of the key draws of paper microfluidics is the ability to extend reagent shelf lives through lyophilization. Although reagents such as the Griess assay for nitrite can have a shelf life of 1 year [119] and the PMB assay for phosphate has a reasonably long shelf life of 2 – 6 months when kept in its two constituent components[120], the shelf life can be extended by up to 2 years using 'freeze drying' or lyophilization techniques [121]. The reagents can then be reactivated through the introduction of fluid when required. Regardless of the merits of the POC instruments in development, *in situ* sensors are more relevant to the overall goals of ocean monitoring at a range of depths, for uncrewed deployments (buoys/vehicles), and for multi-month -year durations.

Table 3 highlights some of the more prominent nutrient sensors available commercially, as well as some new to market instruments being released by start-up companies. Sea-Bird Scientific is well known for the SUNA V2 (Submersible Ultraviolet Nitrate Analyzer). It is an all-optical device based on *in situ* ultraviolet spectroscopy (ISUS) and requires no reagents and consumes 7.5 W to function. However, without external salinity and temperature correction, the detection limit of the SUNA V2 is 2.4 μM, which is considerably higher than other reagent-based devices and is indeed too high for many applications. With the external correction from coincident measurements from a separate CTD, the detection limit drops to 0.3 μM. Although currently discontinued by Sea-Bird Scientific, the HydroCycle-PO_4 is one of the only commercially available *in situ* phosphate analyzers. It uses continuous flow analysis with reagent injection to perform measurements down to a detection limit of 24 nM, however the large waste generation of 30 mL per sample and the external power dependence make it impractical for longer term or remote deployments. The WIZ probe by Systea Analytical Technologies in Italy is a four parameter *in situ* probe for ammonia, orthophosphate, combined nitrate and nitrite, and only nitrite. Using the patented micro loop flow analysis (μLFA), it employs both colourimetric absorbance spectrophotometry and fluorescence techniques for measurement results within 38 minutes. Although the probe performs within 25 % error at higher nutrient concentrations, it can be highly inaccurate at lower concentrations, with errors exceeding 100 %. Furthermore, the device has a maximum deployment depth of 8 m, which restricts the possible applications to those focused on surface water measurements [122].

2.2.2 Trace Metal Analysis

Although they have historically not received as much attention as macronutrients such as nitrate or phosphate, the importance of trace metals in the biogeochemical cycles of the oceans is now being more fully explored. In particular, iron plays a large role in regulating primary production and acts as a limiting nutrient in regions of the oceans that have high nutrient levels but low chlorophyll levels [123]. It is required by many phytoplankton species for electron transport in both respiration and photosynthesis. Unlike for nitrate and nitrite, there is not a significant biological source of iron in the ocean, and it is mostly introduced by wind-blown dust, making iron levels in rivers and along coastlines as high as 25 μM [124]. This is several orders of magnitude higher than in the open ocean, which can be below 0.2 nM [125]. Iron(II) and iron(III) coexist in natural waters, but iron(II) is the more soluble form and is more often the subject of analysis. Other trace metals such as manganese, zinc, copper, cobalt and molybdenum have similar 'nutrient-like' characteristics, in that they are required by some microbes for growth, but none as significant as iron.

The same principles for *in situ* nutrient measurements can be applied to *in situ* iron measurements. The most common technique is reagent-based colourimetric absorbance spectrophotometry, which dates back to before the 1940s for iron determination [126]. However, the assay currently in use is the ferrozine method developed by Lawrence Stookey in 1970 [56]. Starting in the 1990s, researchers have applied these colourimetric methods *in situ* at deep sea hydrothermal vents [127], and the technology has since expanded to enable further *in situ* applications through pre concentrating for low iron environments [128], and faster sampling using flow injection analysis, both *in situ* and *ex situ* [129], [130]. Advancements in absorbance cell technologies such as liquid core waveguides for gas segmented continuous flow analysis [131] and cavity ringdown spectroscopy [124] have also improved iron detection by lowering the possible detection limit in an effort to reach open ocean concentrations.

More recently groups such as those based at NOC have developed microfluidic sensors for trace metal analysis. Milani et al. expanded upon the earlier tinted microfluidic technology produced out of NOC to create an *in situ* sensor for both dissolved iron(II) and manganese [132]. The analyzer used the popular ferrozine assay for iron determination and the PAN ((1-(2-pyridylazo)-2-naphthol)) assay for manganese determination, and produced a reported LOD of 27 nM for iron(II) and 28 nM for manganese. This work was followed up by Geiβler et al. in 2017 by a full characterization and enhancement of the *in situ* iron(II) analyzer [133]. The improved analyzer used three concurrent flow cells with different path lengths to expand the functional concentration range up to more than 20 µM and lower the limit of detection to 1.9 nM. However, they reported large errors of up to 84 % when compared to the values determined via mass spectroscopy. The authors theorized that the poor recovery was due to the acidification step before the mass spectroscopy analysis and suggested that an acidification step implemented into the *in situ* protocol could improve the results. Although iron is the most commonly measured trace metal in the ocean, other analytes like zinc and mercury have also been the focus of some instrument development. In 2011, Grand et al. [134] reported a micro-sequential injection lab-on-valve instrument that used fluorescence to determine zinc concentrations in seawater. With optimal conditions, they were able to produce a limit of detection of 0.3 nM and a functional range up to 40 nM. However, a common issue with using fluorescence probes is poor selectivity, which they attempted to partially remedy by analysing the results from four different fluorescing indicators and choosing the most selective one. Furthermore, the detection limit of 0.3 nM for zinc is too high by a factor of 10 for many open ocean environments. Grand et al. followed this work up in 2016 [135], in which they addressed the shortcomings by preconcentrating the sample by running it through a solid phase extraction step in the analysis. They were able to lower the limit of detection to 0.02 nM, and drastically improve the selectivity by nature of the zinc extraction. However, the added complexity increased the total sampling cycle from roughly 1 minute to 13 minutes. Zhang et al. [136] likewise used a selective fluorescence probe in a digital microfluidics device to measure mercury in seawater.

Some groups have put more emphasis on creating low-cost point of care sensors for aquaculture, particularly using paper-based microfluidics. Deng et al. [137] created a paper-based microfluidic device for POC iron detection manufactured using aerosol spray cans and a simple hole puncher. The simple device used a cell phone for image capturing and produced linear colourimetric results up to 350 μM and displayed a detection limit of 16 μM, with errors less than 20 %. Ghosh et al. [138] sought to improve the detection limit of these paper-based iron detectors by analysing the peripheral "coffee ring" formation due to outward capillary flow.

2.2.3 Genetic Analysis

Measuring macronutrient and micronutrient concentrations gives insight into biogeochemical cycles and can give information about the overall health or state of a waterbody, however it does not provide specifics about how many or what species make up the biomass of an ecosystem. More importantly, it does not reveal quantitative or even qualitative information about the issue of rapidly declining biodiversity in marine environments. The Living Planet report released by World Wild Fund For Nature (WWF) in 2020 [139] states that global wildlife populations have declined by 68 % since 1970, and even more in marine and ocean environments. To work towards addressing the issue of declining species biodiversity, environmental DNA (eDNA) metabarcoding has surfaced as a method by which marine biodiversity can be quantified and analyzed [140].

Traditional DNA-based surveying techniques can be destructive to the samples and organisms, and are often restricted to detecting a single species [141], whereas metabarcoding can be used to detect a wide taxonomical range. To perform eDNA metabarcoding, DNA is extracted from a water sample using one of many different methods, and is then amplified using general polymerase chain reaction (PCR) primers and then sequenced and categorized [142]. From beginning to end, the process requires many steps (filtering, freezing, heating, preserving, lysing etc…) and specialized equipment, which makes it difficult to fully automate and ruggedize for *in situ* deployment. Nonetheless, the Monterey Bay Aquarium Research Institute (MBARI) in California has developed several generations of the Environmental Sample Processor (ESP), some of which perform real-time sample acquisition, quantitative PCR (qPCR) and processing in one mobile unit [143]. However, the added complexity and size of the components required for *in situ* organism quantification by qPCR or competitive ELISA assays in the second generation ESP (2G ESP) creates limited mobility and restricts it from vehicle integration [144]. This has prompted MBARI to build a third generation ESP (3G ESP) that performs only the sample acquisition and preservation *in situ*, leaving the amplification and sequencing for laboratory devices or externally mounted components [145]. In the 3G ESP the environmental DNA samples are collected on filters housed in reusable cartridges and preserved using RNAlater$^{©}$. The device holds up to 60 cartridges arranged around a toroid valve, allowing it to collect up to 60 samples at a time and has an overall volume of 40 L. Yamahara et al. [145] demonstrated the applicability of the device to real-time monitoring by integrated the 3G ESP with a long-range AUV (LRAUV) and collecting 11 samples over 12 hours outside Monterey Bay.

Groups outside of MBARI have also acknowledged the importance of developing eDNA samplers and processors for the ocean. Ribeiro et al. [146], based out of Portugal, reported on the development of what they coined an *in situ* autonomous biosampler (IS-

ABS). Built using off the shelf components, an STM microcontroller and Sterivex filters, the instrument can collect up to 16 samples at a time and can operate to a depth of 150 m. The sampler is cased in an aluminum housing with an overall volume of 8835 cm^3 (8.835 L), making it much more compact than the 3G ESP. Formel et al. [147] report a low-cost single point sampler as an alternative to the ESP devices. Using a peristaltic pump and a replaceable Sterivex filter, it can capture and preserve a single sample at a time, with a maximum operating depth of 55 m. By using off the shelf components and additive manufacturing, they report the production costs to be less than 300 USD, making it at least two orders of magnitude cheaper than other eDNA samplers. However, its applicability is restricted by its inability to make multiple measurements during a deployment.

In its current state, the general technological landscape for eDNA samplers does not usually include microfluidic devices. However, as the field progresses and the need to characterize ocean ecology increases, microfluidic devices are likely to play a central role. The reagent delivery mechanisms and low form factor introduced by microfluidic technology will advance the field of eDNA sampling in the coming decades.

2.2.4 Dissolved Oxygen

Hypoxia is an effect characterized by too little dissolved oxygen (DO) – less than 2 ppm [148] - in an aquatic environment. A normal oxygen concentration in which most fish can live is in the range of 9 to 13 ppm [149]. Although hypoxic regions can be caused by naturally occurring events, it is also a severe side effect of eutrophication caused by nutrient runoff from industrialization - oxygen becomes the limiting reagent for microbial growth instead of nutrients. Most life in a marine ecosystem relies in some way on dissolved oxygen, so chronic hypoxia can create massive areas known as “dead zones”, wherein very little can survive [150].

Ocean sensing to monitor the effects of hypoxia and acidification is only one of the many applications of *in situ* dissolved oxygen sensors. A tangential application to remote *in situ* monitoring is point-of-care testing in streams and other fresh water bodies [131]. Oxygen measurements are a good indicator of the overall health of a water body and can also be used to study the effects of algal blooms. Fresh water is typically warmer and more saturated with dissolved oxygen than seawater, with average concentrations reaching 20 ppm [149]. Despite this, an algal bloom can easily drive concentrations down to hypoxic or even anoxic levels.

Aquaculture is another industry that makes frequent use of dissolved oxygen sensors. Oxygen concentrations in a fish pen can vary between 3 and 16 ppm in a single day [152]. The extremes of this range are mostly driven by the availability of sunlight and the ability of marine plants to photosynthesize. During the day, plant life can balance the concentrations of carbon dioxide and oxygen by converting one into the other. However, at night - when photosynthesis stops - oxygen concentrations drop, and carbon dioxide concentrations rise. When oxygen concentrations drop too low, fish farms can introduce more oxygen to the pond with a bubbler, or by artificially mixing the surface and sub-surface water together.

Aquaponics takes advantage of the respiratory cycle of marine environments to farm both plants and fish together [153]. The same pond will house a variety of surface growing plants as well as several species of fish species below the surface. The oxygen concentration in the water needs to be kept above 5 ppm for optimal growth. The carbon dioxide concentration needs to be monitored to keep the alkalinity above 100 ppm of calcium carbonate and the pH level between 6 and 7.

Most *in situ* dissolved oxygen sensors and many carbon dioxide sensors are based on electrochemical technology. The Clark electrode [154], [155] is a standard example of an electrochemical sensor setup. It consists of an oxygen permeable membrane surrounding a catalytic metal (usually platinum) cathode. When oxygen diffuses across the membrane and into the electrolyte, an applied voltage will cause it to undergo electrolytic reduction at the cathode. The resulting change in current is then correlated to the dissolved oxygen concentration. The Clark electrode has also been modified for use in carbon dioxide sensing [156]. Two common shortcomings of electrochemical sensors are their long response times and propensity for measurement drift. The diffusion across the membrane can take from 1 - 5 minutes, and the electrolyte requires frequent replacement and calibration to reduce drift.

As previously mentioned, optodes are a common device for measuring oxygen concentrations *in situ*, and they are becoming increasingly available at the commercial level. Although they have widespread applications, the primary focus here will be on sensors designed specifically for ocean and marine monitoring applications. Table 4 shows several of the available optodes, with selected specifications shown for comparison.

The two key figures of merit for ocean monitoring applications specific to hypoxia are measurement range and response time. As previously stated, a marine environment is considered to be hypoxic if oxygen levels drop below 2 ppm and healthy if the levels are between 9 and 13 ppm. Therefore, to sufficiently monitor hypoxic regions, a measurement range that goes from < 2 ppm to > 13 ppm is ideal. However, to study mainly hypoxic regions, only the lower limit is required. The range of the RBRcodo T.ODO and SBE 63 does not reach this upper limit, however they are meant for deep open ocean measurements where the dissolved oxygen concentration is much lower (< 10 ppm) at the surface or along a coastline.

Table 4: Commercial Oxygen Sensors

Product	RBRcoda T.ODO [126]	OxyGuard [127]	Aanderaa 4330 [128]	SBE 63 [129]	AquapHOx [130]
Company	RBR	OxyGuard	Aanderaa	SeaBird Scientific	PyroScience GmbH
Accuracy (%)	5	1	1	2	2
Response Time (s)	1	10	8	6	0.8
Range (ppm)	11	23	23	11	30
Resolution (ppm)	0.02	NA	0.2	0.004	0.003
Price (USD)	NA	NA	5,951.00	NA	12,424.00
TRL	8-9	8-9	8-9	8-9	7-8

The response times are only a few seconds, which is very fast when compared to the previously discussed electrochemical sensors. This is ideal for integration into floats and other vehicles, where the spatial resolution will be dependent on the response time. For example, if an AUV is moving at 1 m/s, a response time of 5 minutes would be unacceptable, as it would represent the average reading over a 300 m range. However, if the response time is 1 s, like the RBRcodo T.ODO, then the AUV could make a measurement every meter, producing much more highly resolved data. This is particularly important when measuring the vertical water column because oxygen concentrations can change rapidly when moving from the photic zone to the aphotic zone; a 1 – 2 m resolution is required to capture this [157].

Oxygen optodes are shown to be well established at the commercial level, however electrochemical sensors are still widely used in *ex situ* applications. Wei et al. [158] claim that this will change as dissolved oxygen sensors in general move towards optodes. They mention that groups will likely be looking into new materials that reduce cross sensitivity to other analytes, such as chlorine. They also say that “intelligent sensing technology” will be a recurring theme in dissolved oxygen optode research. This is when multiple sensors are integrated onto a single platform and communicate with each other. It will enable the sensor to have real time compensation for depth, salinity, temperature, and other variables. It will have on board signal processing and will make the resultant data more reliable and easily managed by the end user.

2.2.5 Carbon Cycle

The topic of carbon cycling in the ocean is complex and multi-faceted, with several interconnected variables that can be difficult to isolate. However, because this work is concerned with sensor instrumentation more than the biogeochemical cycles themselves, I will focus on devices that are developed for the detection and measurement of four key variables: carbon dioxide (CO_2), pH, total alkalinity (A_T), and dissolved inorganic carbon (DIC).

The ocean is one of the largest carbon sinks on the planet. Of the 1 million tons per hour of carbon dioxide emissions, roughly 25% is sunk into the ocean. This is causing the average global pH level to fall by approximately 0.002 pH units per year (0.1 pH units since before industrialization) [159]. This effect, known as acidification, is governed by a set of reversible chemical reactions to form carbonate [160]:

$$CO_{2(aq)} + H_2O \rightleftarrows H_2CO_3 \rightleftarrows H^+ + HCO_3^- \rightleftarrows 2H^+ + CO_3^{2-}.$$

Dissolved carbon dioxide ($CO_{2(aq)}$) reacts with water (H_2O) to form carbonic acid (H_2CO_3). This weak acid will then lose hydrogen ions (H^+), dissociating to form both bicarbonate (HCO_3^-) and carbonate (CO_3^{2-}) ions. The excess hydrogen ions directly lower the pH of the seawater; pH is defined as the negative logarithm of the hydrogen ion concentration ($pH = -\log_{10}[H^+]$). The increased acidity and dissolved CO_2 concentration has endangered many calcifying organisms [161], reduced biodiversity [162] and disrupted natural carbon cycling [163]. Furthermore, many marine species will suffer irreversible damage If the concentration of CO_2 stays above 400 - 500 ppmv (parts per million by volume) for an extended period of time [164].

To combat or contain the effects of hypoxia and acidification, environmental ocean monitoring efforts need to turn towards widespread, comprehensive ocean variable mapping. *Ex situ* methods of sample analysis are far too time consuming, costly, and vulnerable to sample degradation for truly comprehensive analysis. For this reason, *in situ* sensors designed for floats, gliders, moorings and other platforms are required to meet this need.

The majority of *in situ* dissolved carbon dioxide sensors can be placed in one of four categories: electrochemical, gas based, wet chemical, or purely optical [81]. The gas based CO_2 sensors function by separating the CO_2 into the gas phase using a membrane and a nitrogen gas stream, or some other equilibrator mechanism [158]. The gaseous CO_2 can then be transferred to a detection cell for optical measurements, often using an nondispersive infrared (NDIR) laser [165]. Liu *et al* [166] recently used the gas separation technique to create a sensor based on tunable laser absorption spectroscopy (TLAS) with a cavity ring down absorbance cell. The primary drawback of these types of sensors is again the response time. It can take from 2 – 10 minutes to separate enough of the gas phase to take a measurement.

Typically, *in situ* wet chemical CO_2 sensors are designed as microfluidic systems over traditional fluidic systems to minimize reagent consumption and waste production. A CO_2 permeable membrane allows a colourimetric pH indicator to equilibrate with the CO_2 in the surrounding seawater. The reaction between the indicator reagent and the dissolved CO_2 causes a measurable shift in colour. The reacted solution is then pumped into an absorbance cell where the absorbance at three different wavelengths is measured [167]. The relative amplitudes of the three absorbance measurements are specific to the reagent and are used to calculate the change in pH of the sample. The change in pH is then correlated to the concentration of CO_2 in the outside environment. The response times of these systems are also governed by diffusion across gas permeable membranes and reaction kinetics, meaning it can take 1 – 5 minutes for a full measurement. Furthermore, wet chemical sensors rely on consumable reagents and produce waste that needs to be stored, which is not always ideal for remote *in situ* sensors.

Table 5 lists a few commercial carbon dioxide sensors. Note, however, that they are not optodes. This is because carbon dioxide optodes have not quite reached a technology readiness level where they can compete with traditional sensing equipment. These commercial sensors were chosen to compare against both the oxygen optode products as well as carbon dioxide optodes still being researched. This will be discussed in a later section.

Again, for the same reasons as the oxygen sensors, range and response time of carbon dioxide sensors are considered as the primary figures of merit. The range will need to extend to 500 ppmv because at this concentration the damage to marine organisms can be irreversible. Fortunately, most dissolved carbon dioxide sensors can easily measure well beyond 500 ppmv. The response time of these sensors, however, is too slow for many AUVs and profiling floats. The CO_2 Pro CV has the fastest response time of 50 s but would still be unable to achieve a 1 m spatial resolution on these platforms. Furthermore, the sensor with this “fast” response time costs more than 42,000 USD compared to the roughly 6,000 USD Aanderaa 4330 oxygen optode.

Table 5: Commercial Carbon Dioxide Sensors

Product	C-Sense [142]	CO_2 Pro CV [143]	CO_2 Probe [144]
Company	Turner Designs	Pro-Oceanus	Aquams
Accuracy (%)	3	0.5	3.5
Response time (s)	240	50	NA
Range (ppmv)	10000	2000	340
Resolution (ppmv)	NA	0.01	NA
Size (cm^3)	400	3000	190
Price (USD)	22,081.15	42,222.25	NA

It is evident that carbon dioxide optodes are not widely commercially available. However, they are still the topic of many recent research efforts. In 2014, Atamanchuk et al. [168] reported their findings on a prototype carbon dioxide optode developed by Aanderaa. They commented that the optode's 5 min response time and its sensitivity to salinity were two areas in which it needed improvement. Staudinger et al. [82] modified the AquapHOx optode to be able to measure dissolved carbon dioxide as well. Their sensor costs less than 1200 USD to develop, and can measure oxygen, pH, and carbon dioxide, although not simultaneously; a sensing cap needs to be switched out to enable each function. Despite this, they saw smoothing across measurements due to the 180 s response time. Thomas et al. [169] investigated a novel carbon dioxide optode for use in the live haul of fish. They reported a response time of 90 s and commented that it was a likely cause of error in their measurements. Clarke et al. [170] reported on an optode deployed in the North Atlantic Ocean with a response time of 50 s. This is comparable to the widely used

NDIR sensors and demonstrates that the gap between the two technologies is closing. To become competitive on a commercial scale, the response time of carbon dioxide optodes needs to be reduced. Despite this shortcoming, Clarke et al. predict that future research will be geared mainly towards remote sensing applications [81].

As previously mentioned, pH and alkalinity are intimately connected to CO_2 levels and therefore need to be discussed in the same context. In particular, pH measurements are often combined with other carbon parameters (A_T, pCO_2, DIC) for inorganic carbon calculations [171], [172], although any two of the four parameters can be used to fully constrain the chemistry. Most *in situ* pH sensors are either based on colourimetric spectrophotometry or electrochemical methods. Although electrochemical sensors such as ion-sensitive field-effect transistors (ISFET) can perform with high frequency over long terms and do not consume reagents, they require careful and frequent *in situ* calibration as they are very sensitive to drift [173]. Spectrophotometric pH sensors provide high-precision measurements with far less drift than the ISFET alternatives, but require longer sampling periods to allow colour development. Total alkalinity (A_T) can also be determined using ISFET sensors [174], or using a technique called tracer-monitored-titration (TMT) [175].

Recently, some groups have created further developments in both microfluidic and electrochemical technologies for pH and A_T determination. Briggs et al. [176] presented a combined solid-state ISFET sensor for both A_T and pH. They modified a Sea-Bird Scientific SeapHOx multiparameter sensor by replacing the oxygen sensor with a custom pH and A_T ISFET sensor. The combined sensor reported a precision of 2 – 10 μmol/kg for total alkalinity, which is comparable to the precision exhibited by some commercial sensors

[175] and a pH precision of 0.005 units. Yamamoto et al. [174] also reported an automated A_T sensor based on ISFET technology. By using three different reference materials they were able to obtain an uncertainty of 2.2 μmol/kg, which almost meets the requirements set by the Global Ocean Acidification Observing Network (GOA-ON) of a maximum of 2 μmol/kg uncertainty [177]. Fassbender et al. [178] attempted to develop a single carbon parameter measurement system by creating an empirical relationship between salinity and alkalinity in their local waters. They used historical pCO_2, pH and salinity measurements to create salinity-based estimates of A_T with a precision of 17 μmol/kg in waters within the salinity range of 20 and 35 ‰. Saba et al. [179] integrated a deep ISFET pH sensor system into a Slocum glider, and found that it likewise had a precision of 0.005 pH units and an accuracy of 0.011 units. They also used on board salinity measurements coupled with pH measurements to estimate the total alkalinity. Land et al. [180] present an alternative approach to measuring carbonate chemistry parameters by using empirical algorithms that use satellite observations to estimate A_T and DIC. The calculated errors between the satellite sensor estimates and validation measurements are 17 μmol/kg for A_T and 30 μmol/kg for DIC.

One of the prominent commercial sensors for total alkalinity is the Submersible Autonomous Moored Instrument for Alkalinity (SAMI-alk) by Sunburst Sensors [161]. It uses the TMT technique, which involves an acidified indicator titrated into a flow cell until colourimetric shifts are witnessed. The A_T is then determined from a nonlinear fit to a series of titration points. Shangguan et al. [182] performed a systematic study of SAMI sensors for pH, CO_2 and alkalinity, and found that after careful calibration and adjustment of coefficients three SAMI-alk sensors had only a 1.6 % inter-instrumental variation and were accurate to bottle samples to within 1 %. This highlights the extremely good performance possible with reagent-based methods when compared with ISFETs at present.

In most of the above sensors, from carbon to nutrients, microfluidics will play a pivotal role in making these measurements more efficiently, by decreasing power requirements and reagent consumption and lengthening deployment limits. This will require new ocean-worthy technological advancements, from micro-valves and fluid control mechanisms to micro-optics and sensitivity improvements. As microfluidic technology matures in the ocean monitoring sector, it will become integral to the development and commercialization of new sensing instruments.

2.3. Materials and Fabrication Techniques for Microfluidic Devices

Microfluidic technologies have existed for decades and have employed several methods of fabrication and substrate materials depending on their application. Lithography techniques [183], borrowed from the semiconductor and PCB manufacturing industry, are historically the most documented method of creating microfluidic devices, but less specialized methods such as embossing [23], milling [184] and even 3D printing [185] have gained popularity due to their propensity for rapid prototyping. In laboratory environments, devices created with silica glass substrates [186] are commonplace due to their chemical resistance, but fragile materials do not perform well in *in situ*, high pressure environments. Likewise, deformable polymers such as polydimethylsiloxane (PDMS) are prevalent in benchtop microfluidic devices, as they have good chemical resistance and are easy to manufacture

[187]. However, they are not rigid enough to perform reliably under the hydrostatic pressure of the ocean.

Microfluidic sensors created from more rigid thermoplastics laminated together tend to perform better under higher pressures than the traditional substrates and techniques. Devices made from cyclic olefin polymers (COC) have been considered for high pressure environments. Layers of COC that have been chemically bonded together via cyclohexane vapor exposure and pressure have been shown to withstand up to 23 MPa backpressure [188]. Similarly, polycarbonate (PC) is a rigid thermoplastic that has been used to manufacture microfluidic devices [189] and it has a wider range of chemical resistance and higher optical clarity than some other transparent thermoplastics, but it has yet to become a common material for *in situ* marine instruments due to difficulties in bonding.

The most common material for creating ocean deployable microfluidic devices is poly(methyl methacrylate) (PMMA) because it is inexpensive and uncomplicated to mill, bonds without a cleanroom, and has been shown to withstand up to 6000 m depth [190]. Most of the microfluidic sensors developed by NOC use tinted PMMA as the main substrate [106] to facilitate their patented absorbance cell technology. Microfluidic channels and features can be easily engraved into PMMA sheets using micromills, or even laser engravers [191], and can then be thermally or chemically bonded using a chloroform vapor exposure; a technique that has been shown to withstand deep ocean pressures. Because of the relative ease of manufacturing for PMMA devices, ocean sensor groups outside of NOC have also begun to fashion microfluidic chips from PMMA [33], [36], [37]. Our group has used PMMA to create inlaid absorbance cells, in which opaque black PMMA is inlaid and chemically bonded into milled cavities in transparent PMMA [38],

[39], [69]. Song et al. [192] have also reported a method by which a PMMA based adhesive can be used to bond polycarbonate and PMMA sheets together, enabling the creation of hybrid PMMA-PC devices.

Developing or identifying substrate materials and fabrication methods that are sufficient for *in situ* deployment is only the first step for making a robust microfluidic device. Consistent and reliable fluid handling using ports, pumps and valves is of equal importance and is an ongoing topic of research for many groups.

2.4. Relevant Fluid Dynamics and Dimensionless Numbers

The scale of the fluidic systems discussed in this thesis are typically on the order of tens or hundreds of microns, which adds complexity when applying traditional fluid dynamics equations and understanding. Fluid flow can either be entirely laminar, entirely turbulent, or part way between. The Reynolds number is a dimensionless number that relates the viscosity of a fluid to its inertia, and is used to dictate which regime the flow will fall into. However, the criteria for what is considered turbulent or laminar is different when applied to microfluidic systems. For example, the Reynolds number for water going through a 0.7 mm via at flow rate of 10 mL/min is only 343. In traditional mechanical fluid applications, a Reynolds number below 2000 is considered to be in the laminar regime, however in microfluidic applications only Reynolds numbers below 100 are considered laminar [217].

However, most microfluidic systems will be handling fluids of almost negligible mass so the Reynolds numbers may not be the most useful metric to consider. What could be a more relevant and meaningful calculation is what is known as the capillary number, which relates the viscosity to the interfacial tension between fluid interfaces. Water makes a contact angle of 67° [218] with PMMA, meaning that it is hydrophilic and would result in a higher capillary pressures. When water is flowing at 10 mL/min through a 400 micron square channel it will have a capillary number of 1.29×10^{-2}, which implies that the capillary forces are negligible compared to the viscous forces. Furthermore, water flowing at the same rate through a 0.1 mm circular via, which is applicable to some of the valve designs presented in CHAPTER 4, will have a capillary number of 0.26, which means that the capillary forces are even less significant when compared to the viscous forces acting in the system.

2.5. Conclusions

Microfluidics and ocean monitoring are becoming more entwined as ocean technology and our understanding and knowledge of ocean dynamics grow. In applications such as nutrient and trace metal analysis, where the analysis techniques are based on colourimetric reagents and optical interrogation, microfluidics are becoming standard as sensing instruments although there are some underrepresented variables such as silicate and trace metals other than iron. In other applications such as optode technology, where solid-state devices are more common, microfluidics are less effective. However, in newer fields and applications such as eDNA sampling, where complex fluid handling and reagent delivery are required, microfluidic technologies could be very impactful.

To make microfluidic systems more widely applicable and efficient, a few key technological components require improvement. Among them are absorbance cells for optical interrogation, passive check valves for low power fluid control and complete instrumentation packages for *in situ* deployment and data acquisition. These aspects are the focus of the contributions to the field presented in this thesis.

CHAPTER 3 EMBEDDED MAGNETIC CHECK VALVES

This chapter describes the design and manufacturing process for a magnetically tunable check valve. The valve is integrated into an early version of the nutrient sensor and then deployed in the Dalhousie Aquatron as a demonstrative application. The contents of this chapter are largely based on the publication "A Magnetically Tunable Check Valve Applied to a Lab-on-Chip Nitrite Sensor" by Morgan *et al.* in Sensors, 2019 [37].

3.1. Introduction

Microfluidic devices have obtained global relevance since their initial application in miniaturized separation and chromatographic instrumentation [16]. More recently, micro-total-analysis systems (μTAS), have been applied to chemical analysis [193] and environmental monitoring [31], [194]. The small, low-cost, power efficient nature of microfluidic analysis platforms have even been used for *in situ* ocean nutrient sensors in recent years [108], [195]. Their potential to do automated and low-volume measurements at high pressures [196] makes them amenable for sensor deployment in deep ocean environments [197]. However, reliable fluid handling remains a core-development area in establishing higher levels of integration on microfluidic devices. This is typically accomplished with specialized micro-valves and micro-pumps [198], [199].

Microfabricated valves fall into one of two categories: active or passive. Active valves require external actuation and often rely on off-chip support systems. A typical active membrane valve uses induced fluid pressure to actuate a movable diaphragm to seal a channel [200]. Generating and controlling pressure for these on-chip active valves require a substantial amount of energy and external equipment that limit the ability to miniaturize. Complex *in situ* lab-on-chip systems employ multiple pneumatic or hydraulic actuators driven by off-chip solenoids. In the works by Ogilvie et al. [201] and Beaton et al. [13], completely automated lab-on-chip nutrient sensors contained 10-15 actuators. The solenoids contributed to a significant power draw during operation for fluid routing and handling, over 10 Watts, equating to 100's if not 1000's of Joules of energy per sample measurement. Using this much energy per sample limits the number of measurements possible per deployment with current battery capacities on small autonomous underwater vehicles and drifting floats. Incorporating rugged passive valves can reduce the energy demand for fluid handling on microfluidic devices.

Passive valves require no external power or interface and most often use simple mechanical biases, like an elastomeric membrane [202], or some other physical property to restrict fluid flow in one direction. The Tesla valve, for example, uses an in-channel geometric pattern to increase fluidic resistance in one direction and not the other [203]. Passive valves can also be made by exploiting capillary pressure differences in microchannels [204], or by using an air bladder to create a capillary stop-valve [205]. Other types of valves include using comb-like structures [206] or centrifugal elastic valves [207]. Flap valves are perhaps the most common and use a thin membrane that seals against a rigid body in one direction, and have freedom to deflect in the other [208]. Although flap valves generally seal well against reverse flow, they are still subject to leakage at low flow rates and do not have a strong seal in an unbiased state. Furthermore, such membrane valves are usually made up of at least two distinct materials, requiring unique bonding procedures between layers. This introduces extra manufacturing equipment and methods, such as UV exposure/oxygen plasma/chemical surface modifications and are prone to sealing failures if stringent quality controls are not implemented. Alternatively, a few researchers have implemented ball and cage valves [209] based on the Starr-Edwards valve used in heart surgery [210]. When forward flow is applied, the ball is dislodged from a seat and retained by the cage. In reverse flow, the ball is pushed into the seat creating a seal. However, like flap valves, ball valves show appreciable leakage, on the order of 100 μL min^{-1} when a reverse pressure of 25 kPa is applied [211]. Backflow is unacceptable and must be minimized on any *in situ* marine sensor, as reagent cross-contamination reduces the integrity and accuracy of the measurements.

Here, we report the design of a tunable poly(methyl methacrylate) (PMMA) ball-type check valve. An embedded neodymium-iron-boron (NdFeB) permanent magnet was used to passively seal the valve with a tunable cracking pressure. Other groups have explored the use of permanent magnets embedded in microfluidic systems [211], [212], but here they were used to increase the strength of the valve seal while still allowing forward flow. The valves exhibited very low leakage rates at high back pressures (< 2 μL min^{-1} at ~350 kPa) and an average cracking pressure of 18 ± 2 kPa in their default state. To demonstrate the utility of this valve design, we integrated it into a complete lab-on-chip nitrite sensor. The lab-on-chip nutrient sensor was made as a portable alternative to traditional instruments such as Autoanalyzers, which are far too large and expensive for widespread *in situ* deployment. Nitrite was detected with the standard colourimetric Griess approach based on optical absorbance spectroscopy, along with accompanying electronics and software to enable complete automation. The final sensor was calibrated using solutions of known standard concentrations, integrated on an unmanned surface vehicle and shown to perform nitrite measurements when deployed in tank trials as described below.

3.2. Materials and Methods

3.2.1 Chemicals and Preparation

All chemicals and reagents were supplied by Fisher Chemical, US, unless otherwise stated. The nitrite standards for the sensor calibration were prepared via a serial dilution of a 1000 μM stock, made from 69 mg of sodium nitrite ($NaNO_2$, CAS 7632-00-0, EMD Millipore, Germany) diluted with 1 L of Milli-Q water. The Griess reagent for the colourimetric measurement was prepared in 500 mL portions by mixing 0.5 g of sulfanilamide ($C_6H_8N_2O_2S$, CAS 63-74-1), 5 mL of concentrated hydrochloric acid (HCl, A144-500) and

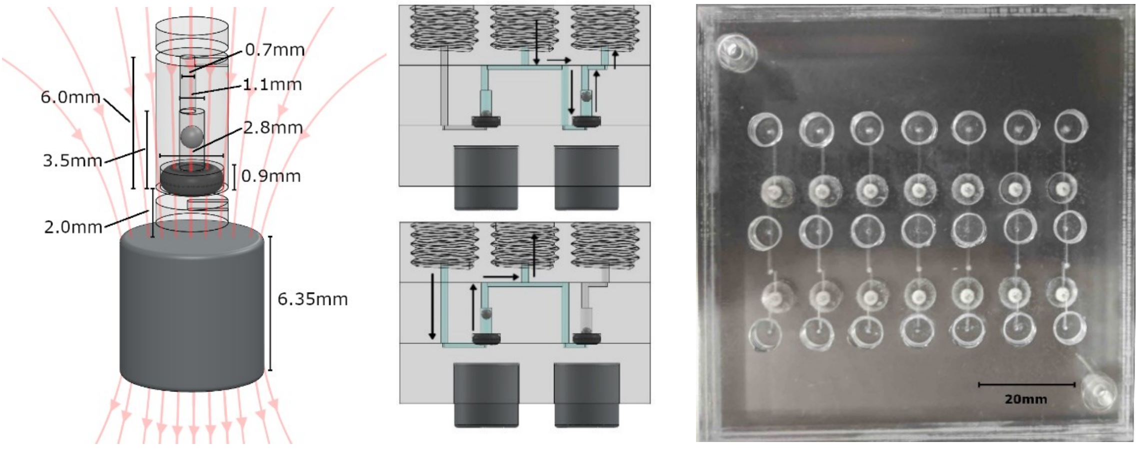

(a) (b) (c)

Figure 3.1: (a) CAD view of a single check valve, where the magnet position is adjusted/set to control the cracking pressure; (b) A valve system that is based on two check valves. The top image shows fluid dispensing, while the bottom image shows fluid withdrawal. A syringe screws into the center thread, while fluid lines connect to the inlet on the left and outlet on the right; (c) Photograph of a panel of valve systems used for testing and characterization.

0.05 g of NEDD (N-(1-Naphthyl)ethylenediamine dihydrochloride) ($C_{12}H_{14}N_22HCl$, 42399-0250) before dilution to volume with Milli-Q water. The chip bonding procedure required both chloroform ($CHCl_3$, C607-4) and isopropyl alcohol (C_3H_8O, A451-4).

3.2.2 Valve Design

Figure 3.1 (a) is a 3-D rendering of the valve design along with dimensions. The chip itself, as well as all the features (including the valves), was cut out of 12-inch x 12-inch PMMA sheets (8505K734, McMaster-Carr, US) using an LPKF S103 micromill (LPKF, Germany). PMMA was selected as our demonstration material because when bonded to itself, it is capable of withstanding high pressures without delaminating; please refer to previous work in ocean deployments [197], [213].

The valve was constructed with a 001 dash size soft Viton O-ring (1284N101, McMaster-Carr, US), a stainless-steel 440C ball bearing (1598K16, McMaster-Carr, US), an N-40 rare-earth (NdFeB) permanent magnet (NSN0617, MagCraft, US), and three PMMA discs with microfabricated features. The stainless-steel ball was 1 mm in diameter, while the cylindrical recess in which it was housed was milled to be 1.1 mm in diameter and 2.4 mm high, allowing liquid to flow around it when the valve was open. Above the ball recess was a 0.7 mm diameter via to the top of the centre layer where it met a fluid channel. The via was offset by 0.15 mm to the cylindrical axis of the valve to ensure that the ball did not act as a plug when brought to the top of the recess. The volume of the via and ball recess together, subtracting the volume of the ball itself, gave the valve an internal fluid volume of < 3 µL. Beneath the ball sat the 001 sized O-ring. The slot into which it was seated was 0.9 mm deep and 2.8 mm in diameter. It was pressed between the middle and bottom layers of PMMA to hold it in place. A fluid channel in the bottom PMMA layer passed beneath the O-ring to meet the valve chamber in the central layer and form a fluidic connection. When fluid is applied against the allowable flow direction of the valve, the steel ball will be pressed into the O-ring to create a seal.

Beneath the valve, embedded in the PMMA, was the N-40 grade cylindrical NdFeB permanent magnet (displayed in Figure 3.1 (b)). It was 6.35 mm in diameter and 6.35 mm in height, exerting a calculated force of 0.0152 N on the ball, resulting in a theoretical cracking pressure of 19.41 kPa. This served to keep the valve closed until the cracking pressure was overcome, which prevented backflow during periods of inactivity. Both finite element method (FEM) simulations and analytical calculations were used to determine the force on the steel ball. Approximating the ball to be a single magnetic dipole in comparison to the permanent magnet resulted in a force calculation of [214], [215]:

$$F(z) \simeq -m(z)\frac{B_r R^2}{2}\left(\frac{\left((z+D)^2+R^2\right)^{3/2}-\left(z^2+R^2\right)^{3/2}}{\left(z^2+R^2\right)^{3/2}\left((z+D)^2+R^2\right)^{3/2}}\right) \tag{3-1}$$

where *R* and *D* were the radius and height of the cylindrical magnet, B_r was the remanence field of the permanent magnet, and *m(z)* was the magnetic moment of the ball at height *z* above the surface of the magnet. The derivation of the above force equation is detailed in the following section.

Figure 3.1 (b) is a computer rendering of a simple two-valve system for withdrawing fluid from one source (inlet) and dispensing to another (outlet). A syringe is screwed into the center ¼-28 threaded port while fluid lines are screwed into the outer two threaded ports. The top image is the valve system state while the syringe is dispensing, and the bottom image is the valve system state during withdrawal. Figure 3.1 (c) is a testing panel for seven of these valve systems. This basic set up was used for characterization of our magnetically tunable valves. Two separate cylindrical magnets were used in the testing system to ensure an axially symmetric magnetic field through the steel ball. However, in the future, a thinner flat bar magnet could be used to seal dozens of valves at a time in a single chip.

3.2.3 Magnetic Force Calculation

A Neodymium Iron Boron (NdFeB) permanent magnet is used to exert pull on a 1mm diameter stainless steel ball bearing for use inside the microfluidic check valve. The geometry of a permanent magnet determines the strength and shape of its magnetic field.

When a ferromagnetic object, such as a steel ball, is introduced to the non-uniform magnetic field produced by the permanent magnet, an induced magnetic dipole is created within the ferromagnetic object. In the case of the axis-symmetric cylinder and sphere, the resulting force between the two objects can be analytically calculated.

To find magnetic force, the magnetic flux density at a given point must first be found. The total flux density at a point will be the vector sum of all the components at that point. This means that the flux density from the permanent magnet must be added to that of the induced magnet to calculate the force between them at a given distance.

The magnetic flux density directly above a cylindrical permanent magnet is given by the following:

$$B(z) = \frac{B_r}{2}\left(\frac{D+z}{\sqrt{R^2+(D+z)^2}} - \frac{z}{\sqrt{R^2+z^2}}\right) \tag{3-2}$$

where B_r is the geometry independent remanence flux density of the magnet. D is the height of the cylinder, R is the radius, and z is the measurement height of the magnetic field. In this case, the magnet classification is N40 and therefore has a remanence field averaging 1.275 Tesla. The permanent magnet is 6.35 mm in height and has a 3.175 mm radius. Using the above equation to calculate the flux density at 3.25 mm above the center of the magnet gives a value of 0.149 Tesla.

The field produced by the magnetized ball bearing is more difficult to calculate. Ferromagnetic substances are subject to a phenomenon called hysteresis when exposed to a magnetic field. This is essentially the property that allows them to stay magnetized after being removed from the field. The strength of this magnetization for a sphere is given by:

$$M_{sphere} = \frac{3}{\mu_o}\left(\frac{\mu - \mu_o}{\mu + 2\mu_o}\right) B_o \qquad 3\text{-}3$$

where μ is the permeability of the sphere, μ_o is the permeability of free space, and B_o is the flux density of the surrounding magnetic field. This can then be used to find the strength of the internal field H and from there, the internal flux density B:

$$H = \frac{1}{\mu_o} B_o - \frac{1}{3} M \qquad 3\text{-}4$$

$$B = -2\mu_o H + 3B_o \qquad 3\text{-}5$$

Which gives:

$$B = 2\left(\frac{\mu - \mu_o}{\mu + 2\mu_o}\right) B_o + B_o \qquad 3\text{-}6$$

Stainless-steel 440 has an average relative permeability of 62, which gives a total permeability of 7.79×10^{-5} N/A^2, while freespace has a permeability of $4\pi\times10^{-7}$ N/A^2. Using the result of equation 3-2 as the external field, the calculated internal flux density of the sphere is then 0.434 Tesla.

Approximating the small ball bearing as a single magnetic dipole of moment *m* means that the force can be calculated as the gradient of the field in the direction of the dipole.

$$F = \nabla(m \cdot B) \qquad 3\text{-}7$$

where $m = MV$, the total magnetization over the sphere of volume V. The magnetization of the sphere in the external field with a density of 0.149 Tesla calculates to be 339000 A/m, which gives the magnetic moment of the dipole to be 1.77×10^{-4} A m^2 at a height of 3.25 mm when using a sphere with a radius of 0.5 mm. Because the movement of the ball is restricted to the *z* dimension, the force calculation becomes:

$$F(z) = m(z)\frac{\partial}{\partial z}B(z) \tag{3-8}$$

which, when used in conjunction with equation 3-2 becomes:

$$F(z) = -m(z)\frac{B_r R^2}{2}\left(\frac{((z+D)^2+R^2)^{3/2}-(z^2+R^2)^{3/2}}{(z^2+R^2)^{3/2}((z+D)^2+R^2)^{3/2}}\right) \tag{3-9}$$

Equation 3-9 gives a magnetic force of -1.105×10^{-2} N on the ball bearing when evaluated at a height of 3.25 mm directly above the center of the magnet.

3.2.4 FEMM Simulations

Finite Element Method Magnetics software (FEMM) was used to simulate the force that the magnet exerts on the steel ball. FEM analysis is a numerical method of studying materials and structures. It works by dividing the whole item or object into smaller pieces and each local property and boundary. In this way, magnetic flux density can be modeled for a variety of scenarios. The system was modeled in only 2 dimensions, but due to the axial symmetry of both objects, 3-dimensional simulations are not required.

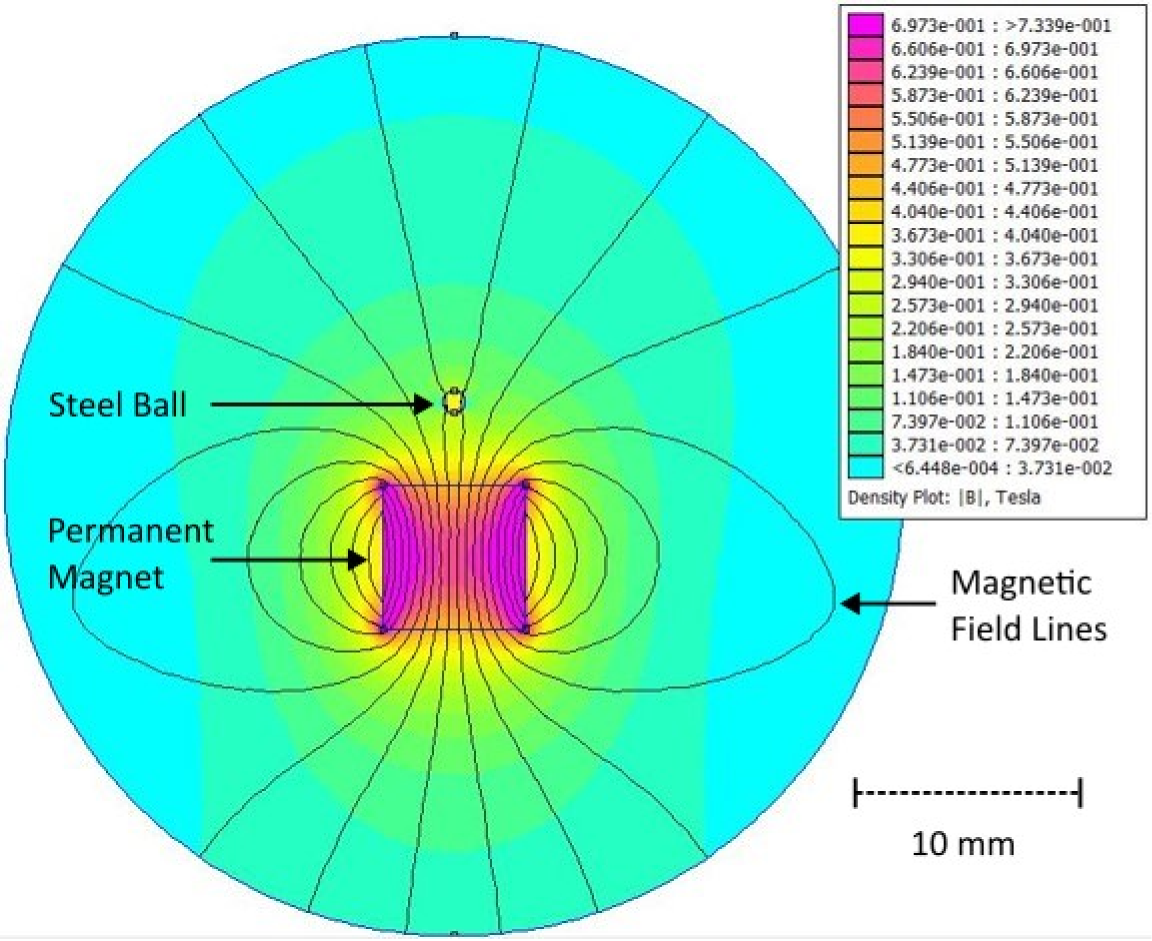

Figure 3.2: Flux density of the magnetic check valve system, in Tesla. The ball bearing is modeled as a steel circle above the center of the rectangular cross section of the permanent magnet.

Figure 3.2 shows a plot of the flux density as it gets further from the poles of the permanent magnet. The software auto-calculates the mesh size based on the size and radius of the individual features and corners. The smallest allowable side length for an individual mesh element was 1×10^{-8} m, and the programs ended up creating a mesh with 7216 nodes for the auto-calculation. To verify that it was sufficient, I reprogrammed it to have a finer mesh (maximum 0.01 mm) around the magnet and steel ball, resulting in over 29000 total nodes, and it produced the same result. Note how the magnetic field lines close to the ball bend towards the ball due to the induced magnetization of the steel ball. From here the program can now use a weighted stress tensor integration to find the force acting on the ball.

The result comes out to be -1.45×10^{-2} N, which is a similar force magnitude to the theoretical calculation, although it is approximately 30 % higher. This is likely due to the single dipole approximation, which can affect the effective position of the steel ball. If the ball is shifted down by its own radius (0.5 mm), the calculated force becomes $-1.75\ 10^{-2}$ N, which is now higher than the model. If the ball is only shifted by 0.255 mm, the calculation matches the model. This indicates that the model is accurate to the calculation to within less than a half of a millimeter.

3.2.5 Valve Characterization Method

The valves were characterized when flow with Milli-Q water was applied in forward and reverse directions. A Honeywell in-line differential pressure gauge (26PCFFA6G, Digi-Key, Canada) was used for all pressure measurements, and a National Instruments USB-6009 DAQ (National Instruments, US) and Lab-View were used for data acquisition. The reported range and accuracy of the pressure sensor was ± 100 mV, which corresponded to ± 100 psi with an accuracy of ± 5 %. The resolution and offset of the gauge were measured by taking the root mean square (RMS) of a blank reading at 1000 Hz. All subsequent measurements were taken at a sampling rate of 1000 Hz, with the measured pressure offset considered. Furthermore, the range on the DAQ, which had a 14 bit input resolution, was set to ± 500mV, which meant the bit resolution of the analog to digital conversion was well within the error of the pressure sensor noise. A 14 bit resolution corresponds to 16384 input levels, which means that the resolution over a 1000 mV range is 0.061 mV, which is much smaller than the ± 5 mV accuracy of the pressure sensor. The pressure sensor was fluidically connected to the chip through a T-junction (IDEX, USA) at either the inlet or outlet of the valve system. The pressure drop through the tubing was measured separately and subtracted from all measurements reported.

Backflow leakage rates were calculated using outlet pressure measurements. A benchtop KD Scientific syringe pump (788101, Legato 101, KD Scientific, US) was used to inject discrete volumes of water backwards into the valve in a step-like fashion (see Figure 3.5(a) in Results). The subsequent increases in pressure were recorded and used to determine a pressure to volume ratio, which was then used to calculate the back-leakage rate over a 20-minute window. The data was collected as 1 second averages of the signal sampled at 1000 Hz. This process was repeated for 5 different set points, where volumes from 10 μL to 80 μL were pumped into the valve outlet to achieve a dead-end pressure test. This equated to back pressures of approximately 40 kPa to 380 kPa, respectively.

Forward flow characterization was done by using the syringe pumps to inject Milli-Q water into the valve inlet at set rates. The syringe pump was programmed to inject for 10 seconds at each flow rate. The measured pressure at these set flowrates was averaged

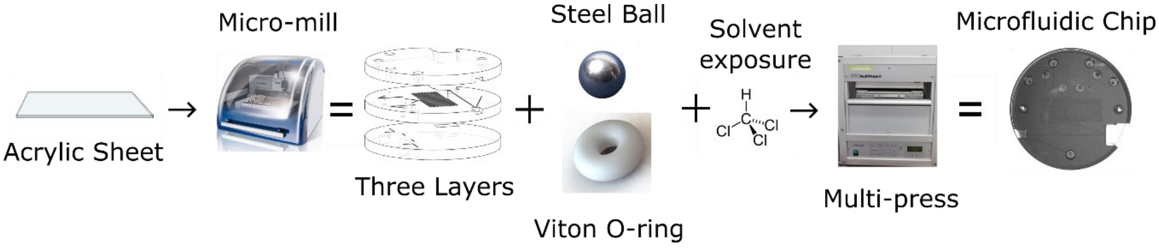

Figure 3.3: Process steps for manufacturing microfluidic chips with integral check valves.

and the standard deviation was recorded. Raw measurements were taken at a 1000 Hz sampling rate and the data reported is from a 0.1 second moving average window.

To determine the cracking pressure of the valves experimentally, the syringe pump was set to inject fluid into the valve inlet at a rate of 0.05 mL min^{-1}. The measured pressure peaked at the cracking point and then dropped off once the valve was opened and fluid was moving through. The process was repeated with five different magnetic field strengths to show the tunability of the cracking pressure. This was accomplished by using a permanent magnet positioned at increasing distances from the ball seat in the check valve.

3.2.6 Microfluidic Chip Fabrication

In addition to the microvalve test chip shown in Figure 3.1, a complete nitrite microfluidic chip with 4-check valves was created shown in Figure 3.4. The valves were integrated into a three-layer, tinted-PMMA microfluidic chip made for use in the nitrite sensor. Figure 3.3 shows the flow of events involved in the fabrication of both microfluidic chips. The features of each chip layer were first milled into a 6.35 mm thick sheet of tinted PMMA using the micromill. Both the channels and the absorbance cell were cut to have a square cross section with a height and width of 400 µm, and all vias were drilled to have a 0.7 mm

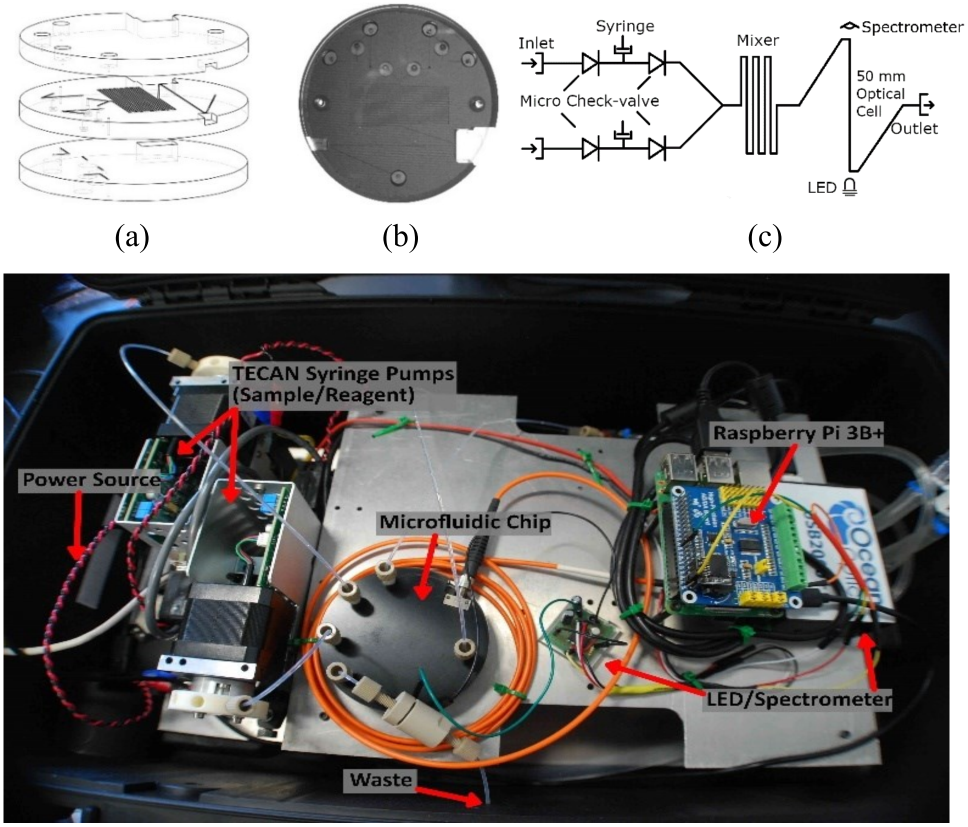

(a) (b) (c)

(d)

Figure 3.4: (a) Microfluidic chip design; (b) Photograph of the microfluidic chip with integrated valves; (c) Flow schematic; (d) Lab-on-chip sensor housed in a water-tight case with labeled components.

diameter. Figure 3.4(a) shows the three individual layers of the chip before they are bonded. The bottom layer of the chip mainly served to seal the base of the valves and provide a housing for the permanent magnets, ensuring they were axially aligned to the valves. The central layer contained most of the features and channels. The recesses for the valve parts (O-rings and ball bearings) were milled into the bottom side of the central layer. The optical cell and mixing channels were milled into the top side of the central layer. The top layer provided external fluidic connections via threaded ports to external tubing and also provided a cap to seal the channels of the central layer. Receptacles for the LED and optical fiber were milled between the top and central layers; their dimensions and positions were designed to ensure optical alignment.

After the three discs were cut out, they were cleaned and their surfaces prepared for bonding. Following the steps provided by Ogilvie et al. for PMMA bonding [216], the discs were scrubbed under hot water with a brush and dish soap, rinsed with both tap water and Milli-Q, dried with pressurized air, rinsed with isopropyl alcohol, and then dried again. The O-rings and ball bearings were then set into their respective grooves in the central layer. Next, petri dish bases were placed on a hot plate set to 30 °C and filled with chloroform up to a pre-marked point. The marked point ensured the liquid level was ~2 mm from the surface of each disc. Permanent magnets were then used to suspend each PMMA disc from the lids of the petri dishes, with the bonding side facing down. The central layer had to bond on both sides, but it was decided that only the top side would face down, to prevent the O-rings and ball bearings from falling out. The petri dish lids with the attached PMMA discs were then set onto the petri dish bases filled with chloroform. Substrates were exposed for 5 minutes and then removed from the vapour. The discs were manually aligned and pushed together to form a preliminary bond. The three-layer puck was then inserted into an LPKF PCB Multipress II (LPKF, Germany) and pressed together with 6.25 MPa of pressure at 85 °C for 2 hours to ensure a solid bond. Figure 3.4(b) shows a photograph of a microfluidic chip with 4 integral check valves and absorbance cell, bonded in this manner.

Figure 3.4(c) is a fluid schematic of the nitrite chip design. Two Tecan syringe pumps (733085-B: Cavro XCalibur, Tecan Trading AG, Switzerland) were used to withdraw and inject fluid. The pumps were controlled by a Raspberry Pi 3B+ via a USB-serial connection. The fluids were mixed in a 0.75 m long serpentine microchannel, and then analyzed in the on-chip optical absorbance cell before reaching the outlet. The integral absorbance cell was manufactured in tinted PMMA to prevent light scattering within the chip and to reduce the influence of background light [195]. The light source was a 525 nm LED (C503B-GAN, Cree Inc., US) that was optically coupled to the absorbance cell through a 1 mm thick window of tinted plastic. The light output from the absorbance cell was coupled into an SMA fiber optic patch cable (M92L02, Thor Labs Inc., US) to the detector, which was an Ocean Optics spectrometer (USB 2000+, Ocean Optics, US). A custom scripting language was created to control and coordinate the pumps, the spectrometer, and the LED driver. The components were mounted to a custom aluminum frame and enclosed in a water-tight Pelican case as shown in Figure 3.4(d) for deployment on an uncrewed surface vehicle.

3.3. Results and Discussion

Figure 3.5(a) shows the results of the dead-end pressure test described above. Here, 5 µL increments of Milli-Q water were delivered to the valve outlet until a volume setpoint was reached, ranging from 10 µL to 80 µL. This can be observed by the staircase climb to the peak pressure value for each run. At pressures below ~150 kPa, the backflow was insignificant, less than < 0.4 µL min^{-1}. The stable pressure plateau observed from these dead-end pressure tests indicates excellent valve sealing—red, blue and green data sets. At higher back pressures the valves did exhibit small leakage rates, less than < 2 µL min^{-1}. The leakage behaviour at pressures above ~150 kPa showed a greater degree of variation with a standard deviation of 1.3 µL min^{-1}, indicating that some valves leaked more than

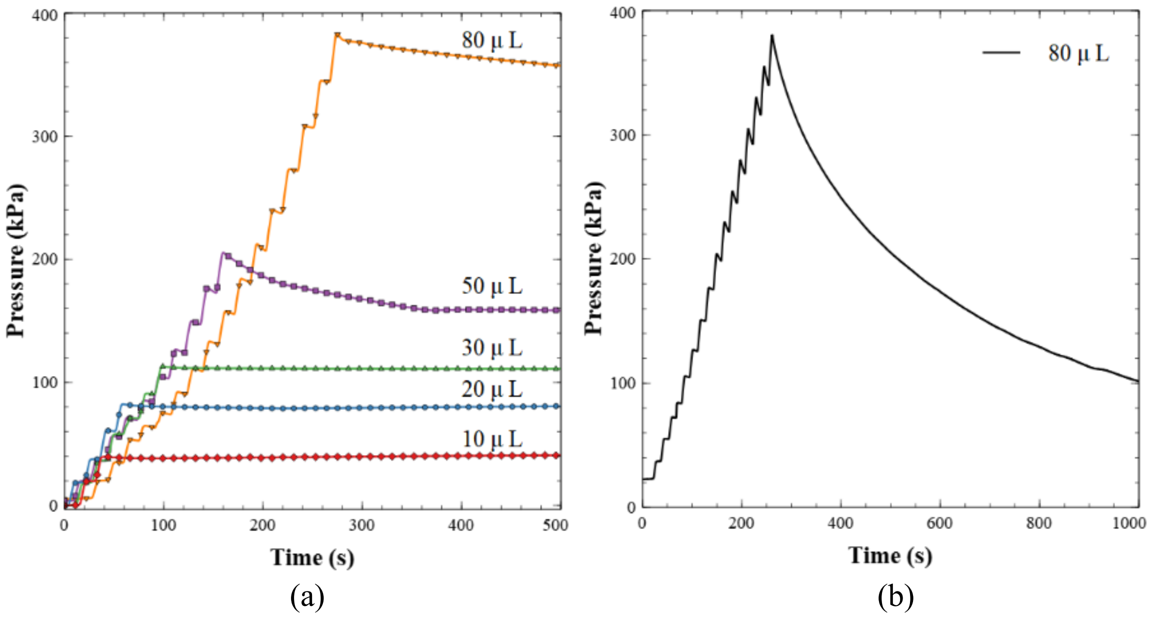

Figure 3.5: (a) Dead-end pressure test for leakage characterization. Fluid is injected backwards into the valve in 5 µL increments and then held after a total volume has been reached as shown. (b) Example of a failed valve. The pressure did not hold or stabilize over the 20-minute window when fluid was injected backwards into the valve.

others. The maximum pressure expected from the final nitrite sensor in this and future work is 100 kPa, based on flow rates and channel geometries. Therefore, these valves are more than adequate and will not have leakage issues.

During the manufacturing process, we observed a final yield of 75%. When the valves would not function correctly, the most frequent issue was an ineffective sealing against backpressure. Figure 3.5(b) is the back pressure drop of a valve with a non-functional seal; the majority of the fluid leaked across the valve over the 20-minute window. This was most likely due to imperfect alignment during the bonding of the PMMA sheets, as visually observed. Misalignment would lead to O-ring deformation or improper seating in the PMMA groove during bonding. We noticed that the misalignment occurred primarily when the substrates/PMMA sheets were pressed together in the hydraulic press.

This could have happened as the pressure distribution of the Multipress II is not guaranteed to be uniform, particularly if the chip was not centred perfectly. The alignment issue was partially mitigated by embedding at least three steel dowels in the chip before it was pressed. Alternatively, fit-for-purpose jigs to constrain the chips to proper alignment in the hydraulic press can be created to improve bonding yields. Figure 3.6(a) displays the pressure versus time when the valve is operated in the forward flow mode. This demonstrates that the pressure in the valve increased to the cracking point, before it dropped to a steady state pressure of ~17 kPa for a flow rate of 0.05 mL min^{-1}. Figure 3.6(b) shows the cracking pressure versus the separation distance between the permanent magnet and the valve seat. The graph shows two data sets, one for the calculated/expected cracking

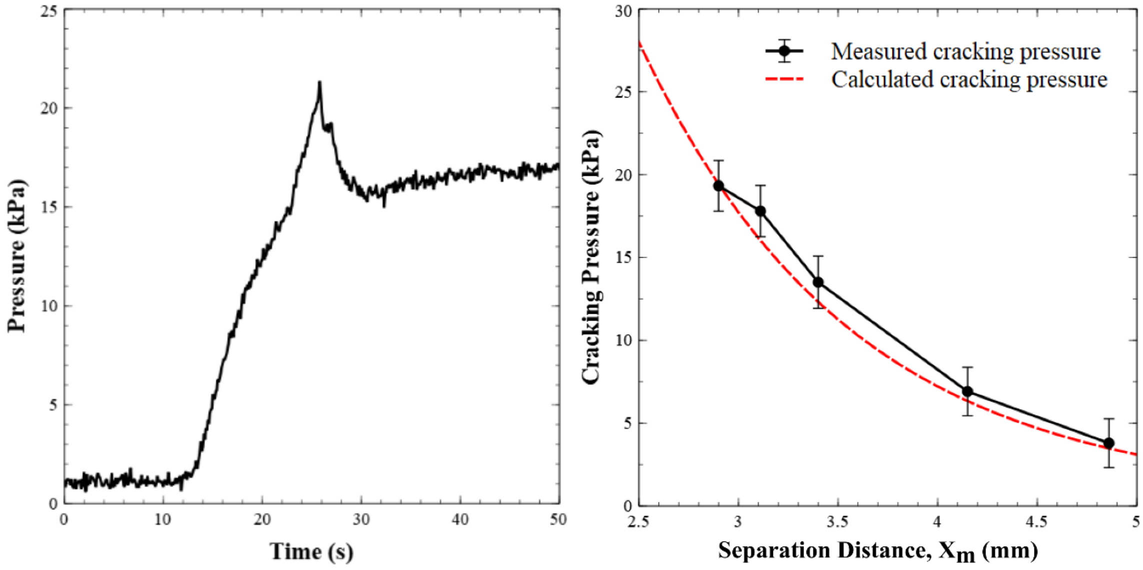

(a) (b)

Figure 3.6: (a) Pressure profile of a valve as it opens under forward flow conditions. Milli-Q water is injected into the valve inlet at 0.05 mL min-1. Pressure increases until the point where it overcomes the magnetic pulling force on the steel ball. After the valve opens, flow occurs and pressure drops. (b) Experimental and calculated cracking pressures of the valve versus separation distance between the permanent magnet and the valve seat.

pressure (given the separation distance) and one for the experimentally observed cracking pressure (n=6 for each data point). Equation 3.9 was used to generate the theoretical curve of the cracking pressure as the separation distance was increased. Analytically, the cracking pressure at the default magnet position (2.9 mm separation distance) was calculated to be 19.41 kPa and it was experimentally found to be 18 ± 2 kPa. The minor difference between the two values was likely due to uncertainty in the exact position of the ball as there will be slight deformation of the O-ring as the ball compresses the rubber/Viton. Within the ranges tested, our experimental cracking pressures agreed with the calculated or predicted values.

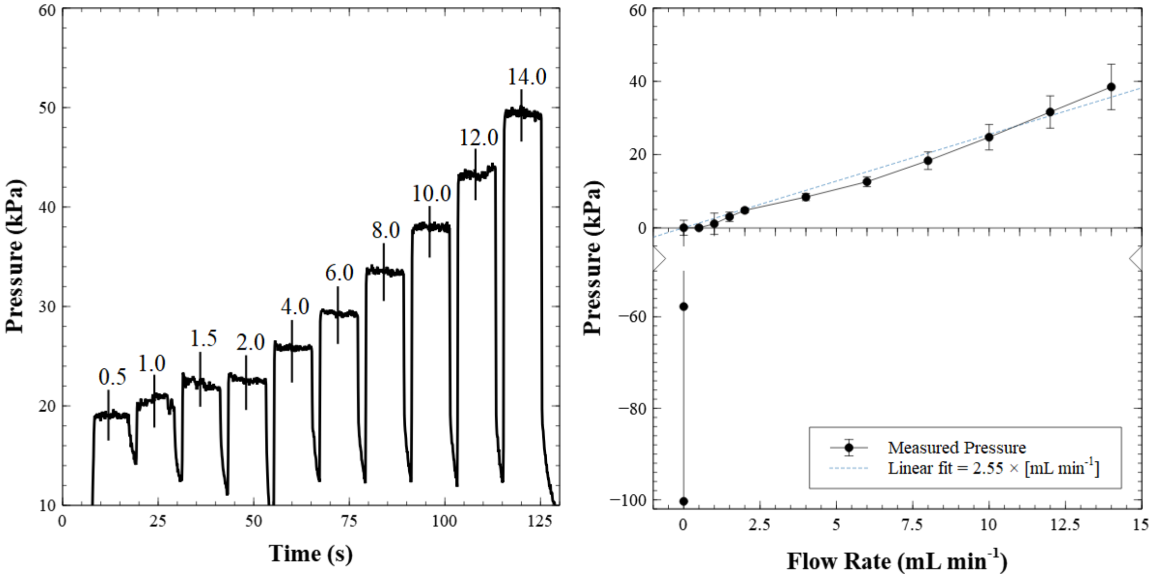

(a) (b)

Figure 3.7: (a) Forward flow characterization. Fluid is injected into the valve inlet at set flow rates as labelled (mL min^{-1}) in 10 second intervals. The pressures corresponding to each flow rate are measured as the average of each plateau, with the standard deviation about the average used as the experimental error; (b) Characterization curve of the valve. The cracking pressure of the valve is subtracted from each measurement. The displayed error is the standard deviation from the results of 6 different test valves.

Figure 3.7(a) shows pressure versus time for a series of flow rates applied to the valve inlet ranging from 0.5 to 14 mL min^{-1}. Figure 3.7(b) is a characterization curve constructed from both the forward pressure and back pressure measurements, where the cracking pressure of the valve is subtracted from each measurement. At flow rates greater than 1 mL min^{-1}, the pressure increase was proportional to the increase in volumetric flow rate, as expected. However, we noticed that the pressure measured at flow rates less than 1 mL min^{-1} did not fit the linear trend. We attribute this behavior to the force experienced by the steel ball in the recess after the valve cracks open. At low flow rates, post-cracking, the magnetic force on the ball is at its relative maximum. As the ball moved further into the recess, the pull from the magnet decreases quadratically with distance, reducing the required pressure to keep the ball off the valve seat. This opposition of forces between fluid pressure and magnetic pull continued until the ball reached the top of the recess where it could move no further. After this point, the change in flow rate was the only factor affecting the pressure measurements, causing the pressure to increase linearly with flow rate. The error in this chart was calculated as the standard deviation of the averaged results of six different test valves.

The tunable nature of these check valves enables them to be integrated with a variety of micro-pumps. For example, piezoelectric actuators are often used in conjunction with two valves [217], much like our valve system in Figure 3.4. Using our valves would allow slight adjustments to the cracking pressures post-manufacture by altering the magnet separation/placement, thereby enabling the valves to function optimally during pumping.

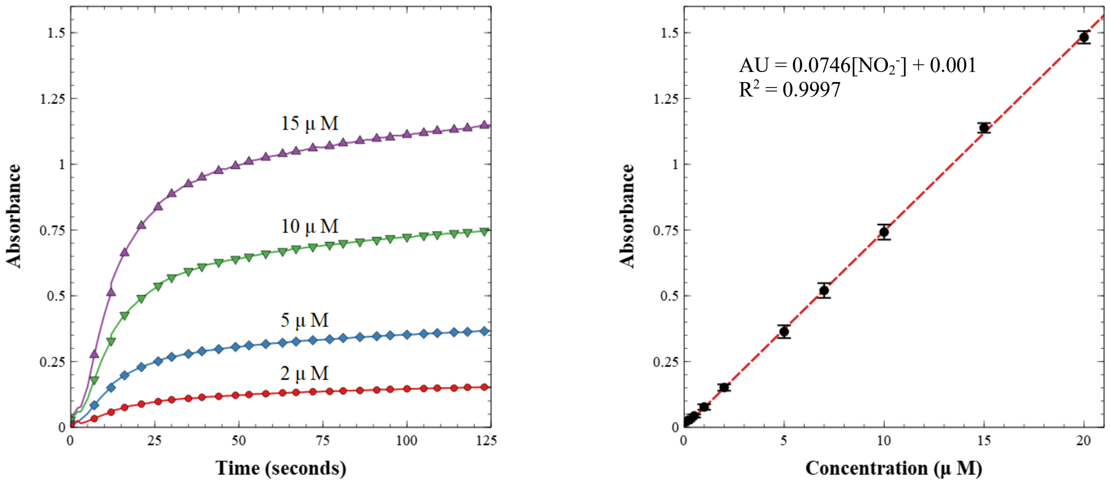

(a) (b)

Figure 3.8: (a) Absorbance over time of premade standard nitrite concentrations; (b) Calibration curve of nitrite lab-on-chip sensor showing absorbance versus concentration.

3.3.1 Application: Nitrite Sensor

The working valves were then integrated into a complete nitrite sensor. The sensor was calibrated with known nitrite concentrations between 0.1 µM and 20.0 µM. First, a light reference measurement was acquired with the LED on and a blank water sample in the cell. Second, a dark reference measurement was acquired with the LED off. The light and dark spectra were stored and used to calculate absorbance from the intensity measured during subsequent sample readings. The prepared nitrite solutions were then injected one at a time and mixed with the reagent at a 1:1 volumetric ratio. Each fluid was injected at a rate of 250 µL min^{-1} for a total of 500 µL min^{-1}. Flow was then stopped, and the solution was held in the optical cell for 125 seconds to allow for colour development. The last 5 seconds of each data set were averaged and used as the absorbance measurement for each concentration. A linear calibration curve was then built from these measurements as per the Beer-Lambert law, shown in Figure 3.8. Figure 3.8(a) displays the absorbance over time as the azo dye developed from the reagent and nitrite standard sample. Figure 3.8 (b) is the resultant calibration curve, relating absorbance to concentration.

Next, the sensor was mounted to an unmanned surface vehicle as shown in Figure 3.9(a). The combined platform and sensor were tested in a large tank of seawater at the Dalhousie University Aquatron facility. The Aquatron main tank is 15.24 m in diameter and holds 684,050 L of water pumped directly from the Bedford Basin, Nova Scotia, Canada. The Basin had a nitrite concentration ranging from 0.1-0.6 μM at the time of study. The initial concentration of the tank was adjusted to 1 μM to ensure a uniform starting point.

The sensor and platform were then deployed three times to gather spatial concentration data, while we simultaneously delivered nitrite into the tank at a known point. For each of the three consecutive runs, we gradually added 1 L of 100 mM nitrite solution into the tank at sampling point three, shown in Figure 3.9(b). Next, the vehicle with our sensor was driven around the tank, stopping at each of the waypoints shown in Figure 3.9(b). At each waypoint, the concentration was measured as the average of five readings taken over a 5-minute window. For the vehicle tests, we shortened the sensor colour development time from 2-minutes as per the calibration above, down to 45-seconds, in an effort to speed up the sampling rate. The final 75 measurements, 25 from each run, are displayed in Figure 3.9(c) as an intensity map of concentration over the surface of the Aquatron. The Aquatron was equipped with recirculation pumps that effectively moved the high concentration of nitrite from the delivery point (6 o'clock) to the drainage point in the center of the tank. Furthermore, the background nitrite concentration gradually

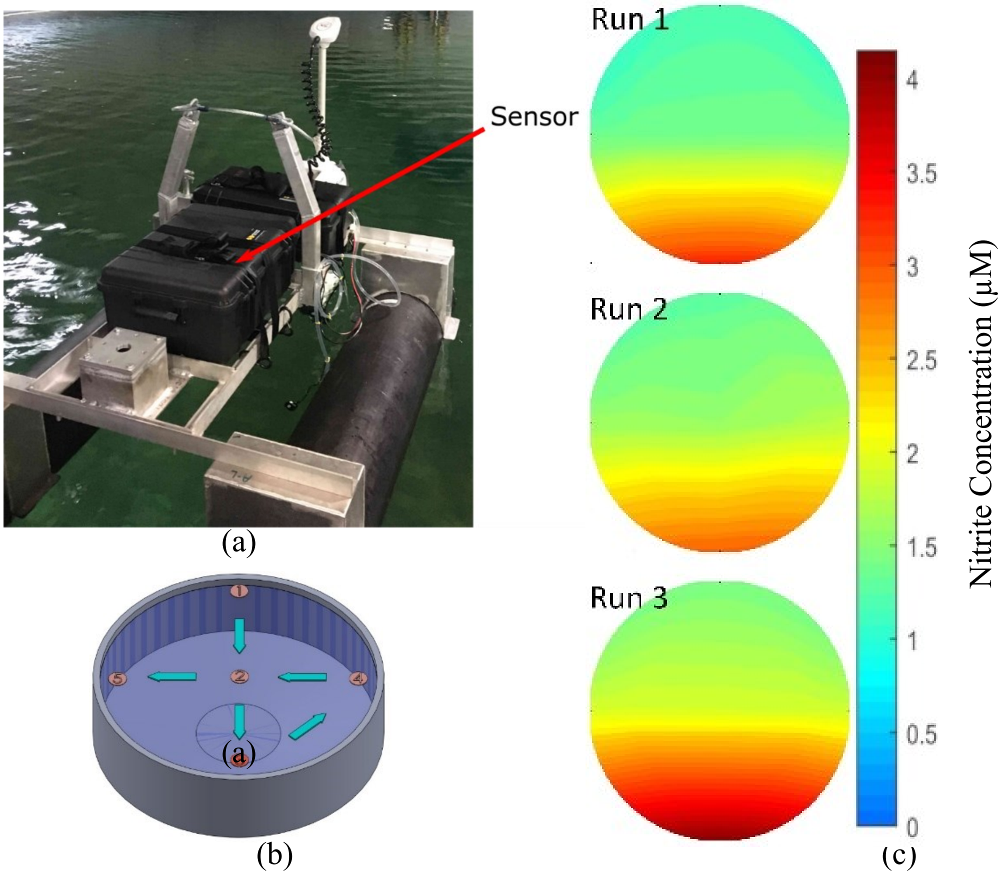

Figure 3.9: (a) Sensor in a water-tight case mounted to an unmanned surface vehicle in the Aquatron; (b) Aquatron CAD model with sampling points labeled. Nitrite dosing was done at point 3; (c) Concentration mapping of three consecutive runs in μM, showing increase concentration between runs, demonstrating that the system was effectively deployed on a vehicle and was capable of tracking nitrite concentrations.

increased between runs as expected, given the amount of added nitrite. The background nitrite concentration increased from 1.0 μM to 1.2 μM between the initial level and run 1, from 1.2 μM to 1.3 μM between runs 1 and 2, and from 1.3 μM to 1.5 μM between runs 2 and 3. The magnitude of concentration increase was confirmed through analytical calculations. If a 1 L bottle of 100 mM nitrite stock is diluted into 684,050 L of water, the resultant nitrite concentration increase is 0.146 μM. This is in alignment with the 0.1 μM to 0.2 μM concentration increases that we observed. The advancing nitrite front and the overall increase in the background concentration was observed in all three runs, thereby successfully demonstrating our tunable check valves integrated with a fully automated lab-on-chip nitrite sensor.

3.4. Conclusions

The valve presented here was made for the purpose of marine sensing but has widespread applicability. Most microfluidic devices require fluid control mechanisms, and a passive, simple, tunable check valve enables lab-on-chip designs flexibility in adjusting cracking pressure post-creation. Our novel valve was integrated into a microfluidic chip and used in a working nitrite sensor both in the lab and in a seawater filled tank environment. Despite the success of these valves when applied to nitrite detection, they did not perform as well when used with more aggressive chemical reagents. This is the topic of the next section and will be discussed in more detail there.

CHAPTER 4 FLAP AND BALL-STYLE CHECK VALVES

The previous chapter detailed the development and characterization of a magnetically tunable check valve with ferromagnetic steel ball bearings as the movable locking component. The valves described there were applied to a nitrite sensor that used the Griess assay as the chemical reagent. The Griess assay has a pH that is close to neutral and therefore does not corrode the steel bearings inside the valves. However, when the valves are used with a more acidic reagent such as the yellow phosphate method, which has concentrated sulfuric acid as one of the components, they were observed to degrade quickly. When the bearings were submerged separately in the reagent, they fully dissolved in a manner of days. Alternative, more chemically robust valves are required if other reagents are to be used with these devices. The following sections outline valve designs that I explored in an effort to address the chemical robustness issue.

4.1. Elastomer Flap-Style Valves

The first styles of valve we designed use an FKM elastomer as a deformable membrane in different arrangements. One arrangement uses an oval-shaped membrane with a through port offset to the center, another uses a circular membrane with a through port in the center, and another uses a circular membrane without a through port. The following sections will describe each design and the attained results.

4.1.1 Oval-Shaped Elastomer Valve Design

The oval-shaped valve design uses an offset through hole to only allow flow in one direction. The valve is made from an FKM elastomer membrane and three layers of 6 mm

PMMA. The membrane is clamped around its perimeter between the top two layers of PMMA, which are bonded using the same methods described in previous sections. There are two vias under the membrane, which act as the input and output of the valve and are either sealed or opened depending on how the membrane is deformed. There is a cavity milled into the bottom of the top layer of PMMA above each valve seat, which provides room for the membrane to deflect. Figure 4.1 shows two of these valves arranged in a pumping configuration that is actuated by a syringe attached to the center port, and Figure 4.2 is a depiction of the membrane itself, with the offset through port. The side of the valve that has the through hole is the output side, and the side with no through hole is the input side. When positive fluid pressure is applied to the input side, or negative fluid pressure applied to the output side, the membrane is pushed up into the cavity in the top layer of the

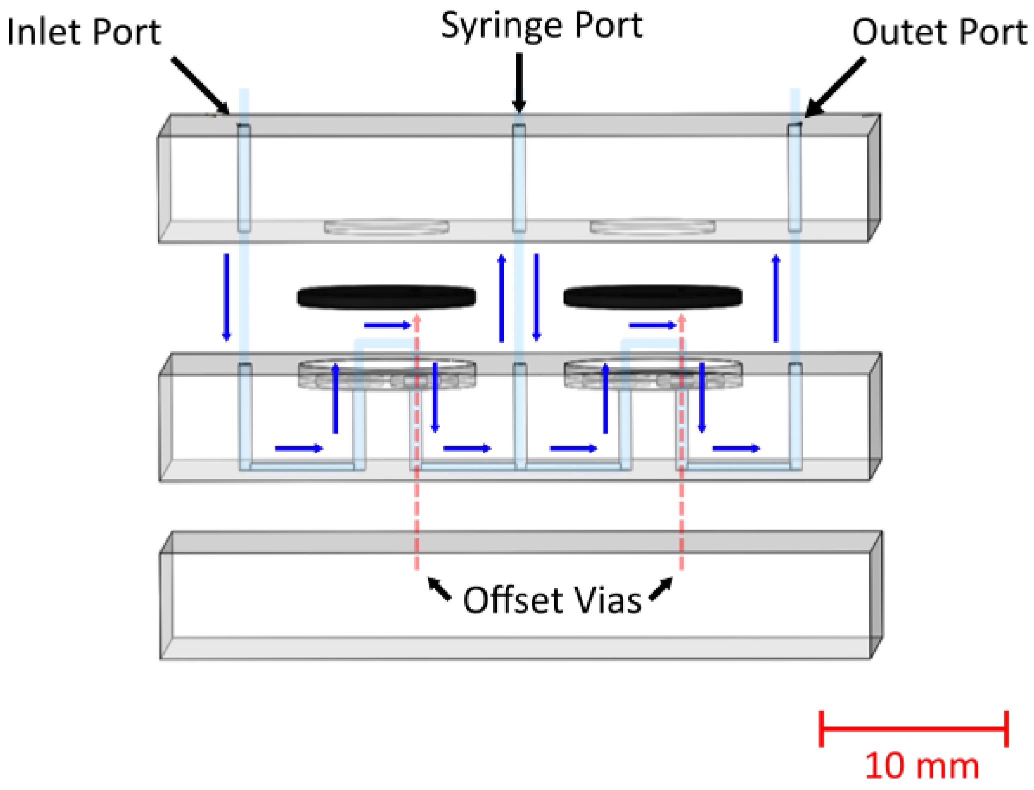

Figure 4.1: Oval-shaped valve design in pumping configuration.

Figure 4.2: Oval valve membrane with offset through hole.

chip, which allows a fluid connection between the two bottom vias to form. If fluid is pushed into the output side, it flows into the top cavity and forces the elastomer membrane down into the valve seat, which seals it. Figure 4.3 shows the valve seat more clearly. There are areas milled out around the vias to form a thin wall that circles the via, which allows the membrane to deform more easily and seal the valve. APPENDIX B contains the dimensions and further design details of the valve, including a discussion on the thickness and expected deflection.

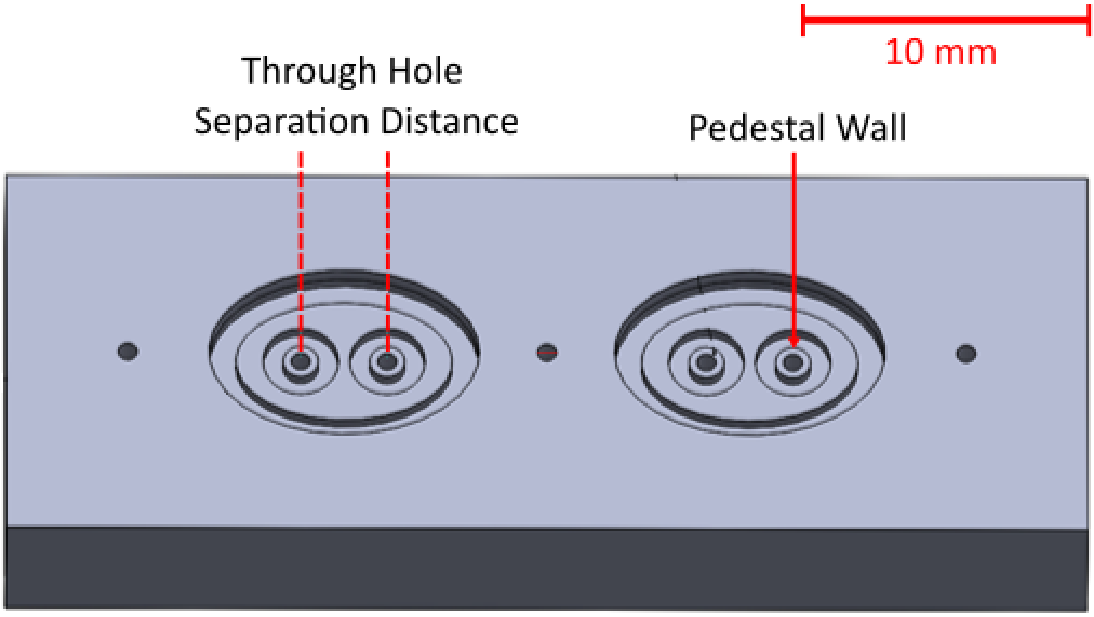

Figure 4.3: Oval-shaped valve seat with pedestals.

4.1.2 Circular Elastomer Valve Design

The circular valve designs were implemented to reduce manufacturing errors by making each individual valve serviceable. The functional concept is similar to the oval-shaped valves, with the main difference being that the through hole in the membrane is not offset, but in the center. The circular membrane is not orientation dependant, which means that the input and output are entirely determined by the positions of the vias drilled into the PMMA layers. The valve will open when fluid is pushed into the offset inlet via which deflects the membrane up into the upper cavity, forming a fluid connection between the input and output vias. Likewise it will seal if fluid is pushed into the output, which will fill the upper cavity and force the membrane to deform against the raised concentric ridge circling the central pedestal. Figure 4.4 is a side profile of a two-valve system to demonstrate the concept. A syringe will be attached to the center port, which when actuated will push and pull on the two valves. When the syringe is pulling, the left valve will open and the right valve will close. When pushing, it will be in reverse. This is the same mechanism that the oval valve uses, but the biggest difference between the circular and oval valves is the accessibility of the membranes through a removable insert into which the upper cavity is milled. Figure 4.5 is an exploded view of the valve system and shows the inserts in green.

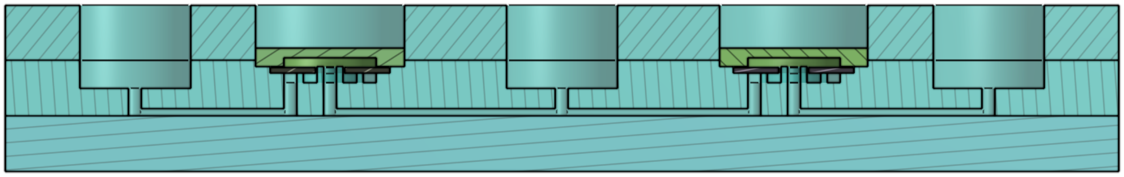

Figure 4.4: Circular valve design - side profile.

For this design, the chip is milled and bonded before the valve components are inserted. After bonding, the circular membrane with the central hole is dropped in through the access hole in the top layer and onto the valve seat in the top of the middle layer. The individually milled cavity inserts are then dropped on top of the membrane and clamped down using a hollow locking nut (not shown in the diagram) until the base of the insert comes into contact with the top of the seat. This causes compression of the elastomer circle around the perimeter, which seals it against the external environment. The amount of compression is determined by the difference between the membrane thickness and the seat depth. The removable locking nut allows access to the membrane and cavity insert so they

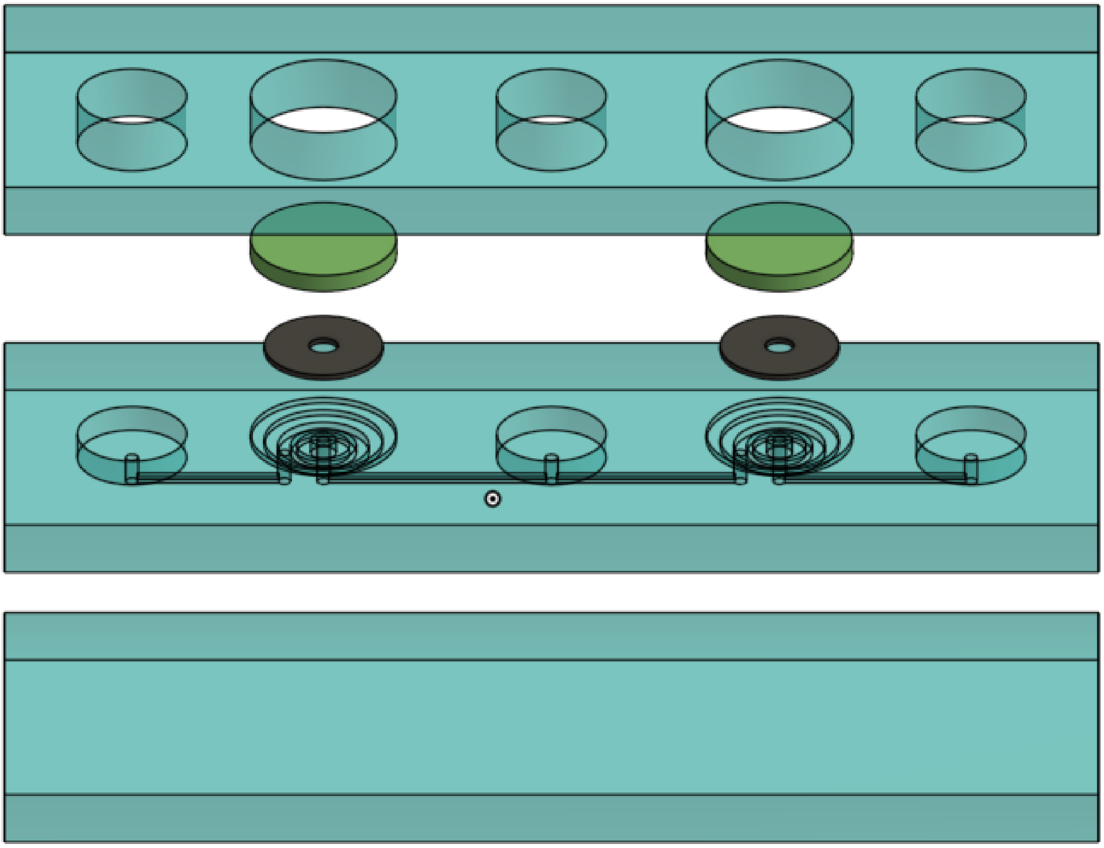

Figure 4.5: Circular valve design - exploded view.

can be replaced if they are faulty or damaged. It also allows rapid iteration of cavity insert designs.

4.1.3 Circular Elastomer Valve Testing Methodology

The circular valves were tested and characterized to assess their performance and reproducibility. They were tested both in isolation as single valves and in the two-valve pumping systems discussed in the previous section.

The first test was monitoring the back pressure of a single valve when performing at increasing flow rates. This was done to obtain a rough estimate of how much back pressure is can be expected in the system when fluid is steadily pushed forward through a single open valve at any given rate. The same Honeywell differential pressure gauge from Chapter 3 was attached in line, between a syringe pump and the valve. PTFE tubing with a 0.030" inner diameter was used to connect the components together. The syringe pump was programmed to inject fluid at a pre-set flow rate for 10 seconds. The measured pressure over the 10 seconds was then averaged, and the next programmed flow rate was set up. The test covered flow rates between 0.1 and 10.0 mL/min. To remove the effects of the added fluidic resistance of the tubing, the test was repeated without the valve set up in line with the system. This baseline pressure curve was subtracted from the total pressure curve to produce a resultant curve that was representative of only the valve resistance.

The next set of studies was to look at the cracking pressure of the valve. That is the pressure at which the passively sealed valve will begin to permit fluid to flow forward through it. Fluid was very slowly (0.05 mL/min) injected forward into the valve, and the pressure was recorded so that the point where the pressure stops building can be noted and taken as the cracking pressure.

The last test conducted on the circular flap valve design was a fluid leakage rate test. Similar to the leakage tests described in section 3.2.5, the leakage rates were determined by pumping fluid backwards into a valve in discrete 10 μL volumes and monitoring the rate at which the pressure dropped after a target volume had been met. The fluid leakage rate could then be interpreted from the pressure decrease rate.

4.1.4 Circular Elastomer Valve Results and Discussion

Figure 4.6 shows the raw data from the back pressure tests plotted against time, with the corresponding flow rates indicated on the plot. At the start of each injection rate there is a visible upward spike in the pressure. This is possibly a result of increased resistance from the valve as it is adjusting to the increased flow rate before it stabilizes. Another important observation from the data displayed in Figure 4.6 is the variation of the results across the five trials. The standard deviation of the averaged results for the 10 mL/min injection rate is 8.3 kPa, which is almost 10% of the measured pressure, which is far too large because it will affect the mixing ratios of reagents if used in a microfluidic device. The relative deviation at lower flow rates is even higher, which is more concerning because the lower flow rates are more representative of the end use rates. The standard deviation of the 0.1 mL/min injection rate is 4.8 kPa, which is approximately 25 % of the measured pressure. For the valves to work for their intended application, the relative deviation at the lower flow rates must be closer to the values observed in Chapter 3, approx. 10%.

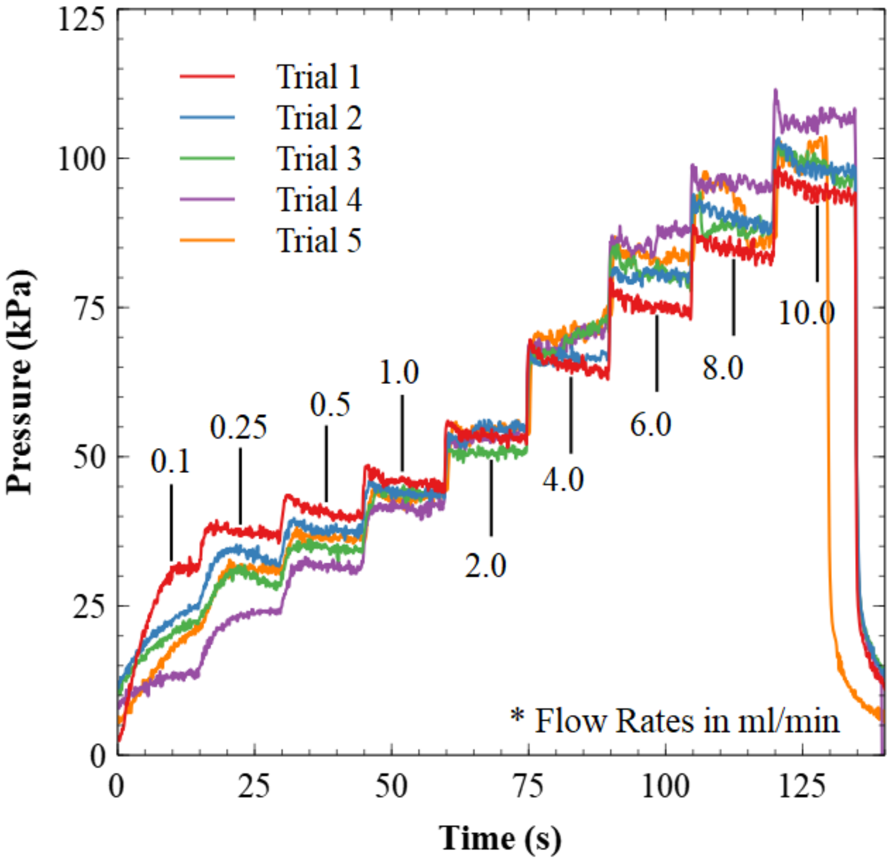

Figure 4.6: Back pressure of elastomer valve as fluid flow rates are increased. Plotted against time to show transient response.

Figure 4.7 shows the averaged back pressure tests, with the measured pressures plotted against their corresponding injection flow rates. The curve starts very steep, as the pressure increases at a quick rate with increasing flow rate. It then starts to flatten out into a roughly logarithmic curve. This indicates that the flow through the valve at the higher flow rates is likely at least somewhat turbulent, despite the fact that calculated Reynolds number for water going through a 0.7 mm via at flow rate of 10 mL/min is only 343. In traditional mechanical fluid applications, a Reynolds number below 2000 is considered to be in the laminar regime, however in microfluidic applications only Reynolds numbers below 100 are considered laminar [218]. There is likely additional turbulence because the

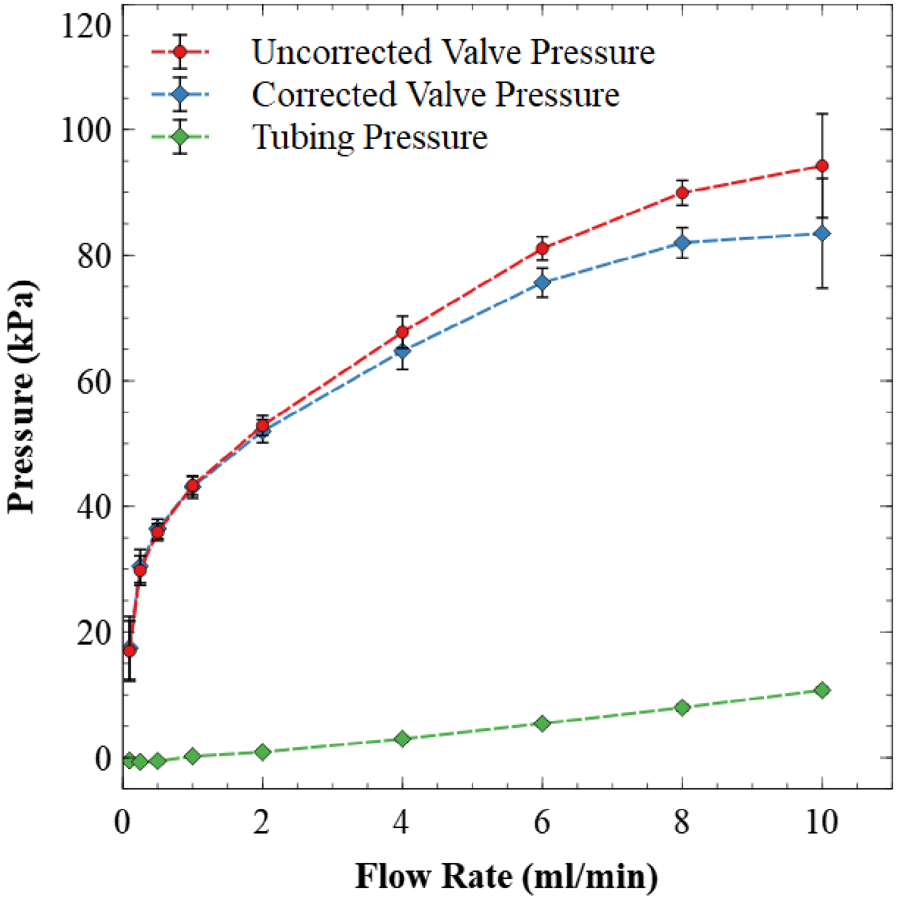

Figure 4.7: Averaged back pressures for the elastomer valve plotted against flow rate. The tubing pressure is subtracted for the corrected pressure curve.

geometry of the valve causes it to have regions with fluid paths as small as 0.1 mm across. Although these regions are nor circular or tubular, it is worth noting that the calculated Reynolds number for such a gap if it were tubular is over 16000, which is very much in the turbulent region, even in larger applications. This is further supported by the fact that the pressure curve for the tubing alone, where there are no sharp angles or added resistance, is seemingly linear with flow rate in the region shown here. Furthermore, the magnitude of the back pressure caused by the tubing has minimal effect on the overall magnitude of the system back pressure.

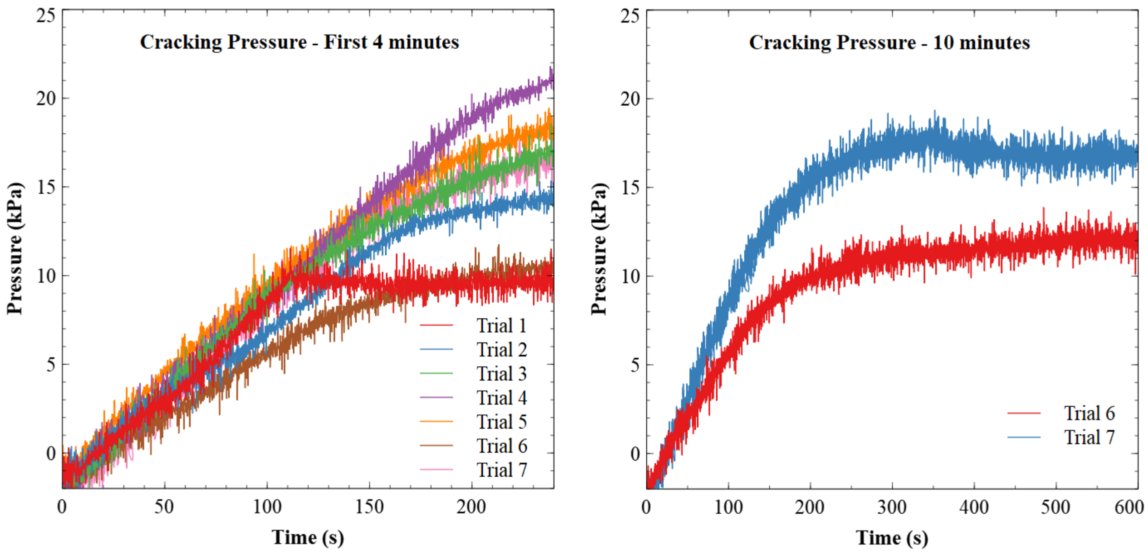

Figure 4.8: Elastomer valve cracking pressure curves. Results from seven trials are shown. The left panel shows the first 4 minutes for all seven trials. The right panel shows the first 10 minutes for trials 6 and 7.

The issue of variable results is even more apparent and relevant in the cracking pressure tests. Figure 4.8 shows the results of the cracking pressure test for seven trials. Trials 6 and 7 were conducted for a longer period to fully show the pressure plateaus. The results show that for all seven trials, the pressure increases linearly at the start, presumably as more fluid is injected into the valve and pressure builds before there is enough pressure to open, or ‘crack’ the valve. The point where the pressure curve starts to plateau is assumed to be the cracking point, because at that point the pressure is enough to open the valve, creating an open system. It is clear from the data that after about 50 seconds of pressure building the results begin to diverge. Each valve had a different plateau point, ranging between 9 and 21 kPa. It should also be noted that the results shown in Figure 4.8 are seven trials of the same valve, indicating that there is very large variation between results of identical tests.

The primary issue with having variations in the cracking pressure is that it would result in unequal and unpredictable flow rates when two or more valves are used in a pulling configuration. If the valves are used in a pushing configuration (syringes are pushing fluid through the valve), the flow rates, and therefore mixing ratios, are entirely driven by the syringes and are therefore as accurate as the syringes pumps are. However, if the valves are used in a pulling configuration (syringes are pulling fluid through from the other side), the flow rate is affected by the valve. In a device that has two parallel two-valve systems, each with its own syringe, one syringe could fill by a different amount than the other if the variations in cracking pressures cause them to cavitate the fluid at different points. However, that issue is more relevant to bench top applications as cavitation does not happen as easily under higher hydrostatic pressure. A bigger issue with the variable cracking pressures in a two-syringe system is that they can cause oscillating flow. If one valve cracks first, the fluid can apply a back pressure on the other valve, momentarily increasing its cracking pressure. The second valve will then require more pressure to open, which means that when it does open it could apply a back pressure to the first valve, starting the cycle over. This oscillating fluid behaviour makes mixing unpredictable, and can affect mixing ratios, especially in the scenario where the syringe is not meant to expel its entire contents in one stroke.

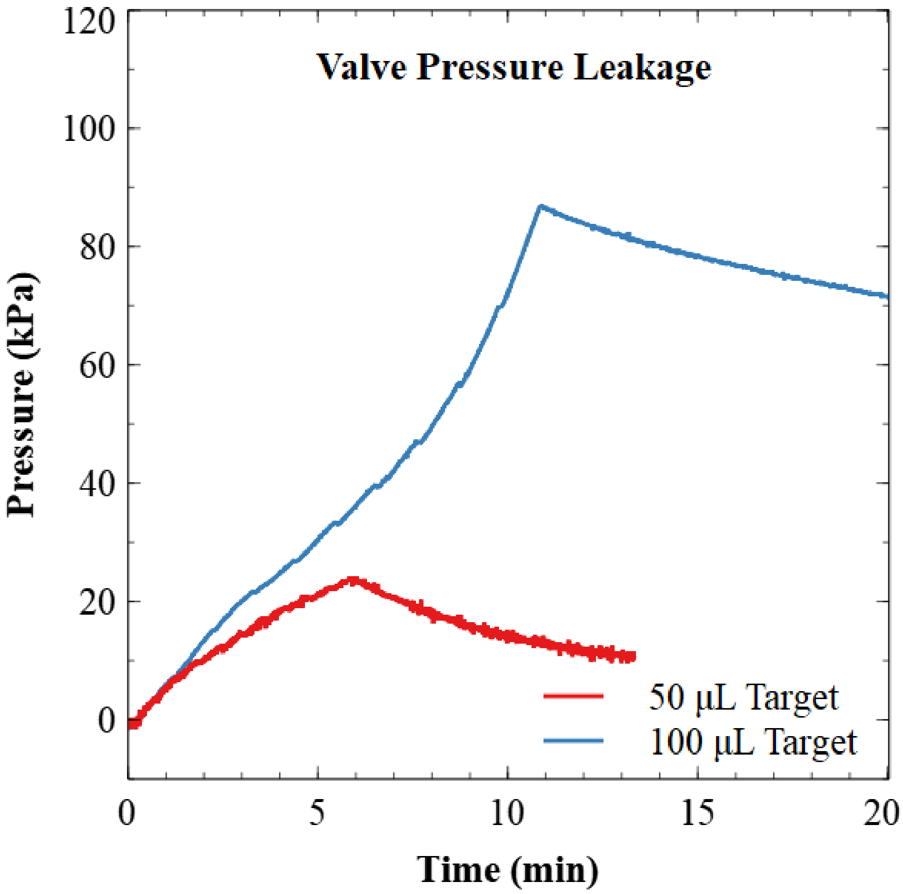

Figure 4.9: Valve pressure leakage curves. Two target volumes are shown, resulting in maximum pressures of 20 and 90 kPa respectively.

The last tests performed on these valves were the pressure leakage tests, with the results displayed in Figure 4.9. The results show that even at very high back pressures of almost 90 kPa, the valves do not remain completely sealed, and fluid is able to pass through them, albeit very slowly. The valve lost approximately 9 µL over 10 minutes, giving it a leakage rate of 0.9 µL/min when the back pressure is at 90 kPa. This leakage rate is minimal and likely would have been acceptable if the other cracking/ opening issues were not so impactful.

As a point of comparison and as a possible off-the-shelf alternative, I also briefly tested the Lee Company Zero-Leak Micro Check Valves (CSRA5006008A, Lee Co., United States) in a similar manner. However, we observed similar issues as with the custom valves. Furthermore, at the flow rate we require, the Zero-Leak valves leaked even more than the custom valves.

4.1.5 Circular Elastomer Valve Conclusions

As discussed already, the reproducibility and sealing ability of the membrane valves are the biggest issues that we faced. Moving forward, we considered using thinner material as the deflecting membrane, with the assumption that thinner membranes will be able to deflect and conform to rigid bodies more easily, thereby increasing the sealing ability. However, we were unable to find off-the-shelf options that were thinner than the membranes we had already been using. Furthermore, the design and fabrication took for each new valve took over a week and was not producing the results to justify it. For these reasons, we decided to perform further tests using simulations rather than creating physical devices. The details and results these simulations can be found in APPENDIX A. Furthermore, because we had found some success with the ball style valves described in CHAPTER 3 we decided to pursue similar designs, as described in the next section.

4.2. Ball-Style Valves

The manufacturing process for the magnetic ball valves was much more reliable, and the results were more consistent and quantifiable than for any of the elastomer membrane designs. However, the ferromagnetic stainless steel ball bearings are not resistant to the chemicals used in other reagents such as the PMB assay for phosphate. To this end, we attempted to design a passively sealed, chemically robust, microfluidic ball check valve.

4.2.1 Valve Design Choices

To create a fluidic seal without extreme machining tolerance and hard materials (such as sapphire), there typically needs to be deformation of one surface against another. In the case of the magnetic valve, the O-ring deforms against the ball bearing, while in the case of the flap valves the FKM membrane deforms against the PMMA.

The first design explored here is modeled very closely off the magnetic valves previously described and is shown in the left panel of Figure 4.10. An O-ring is used as the deformable surface and acts as a seat for a hard ball bearing. However, the bearing is made

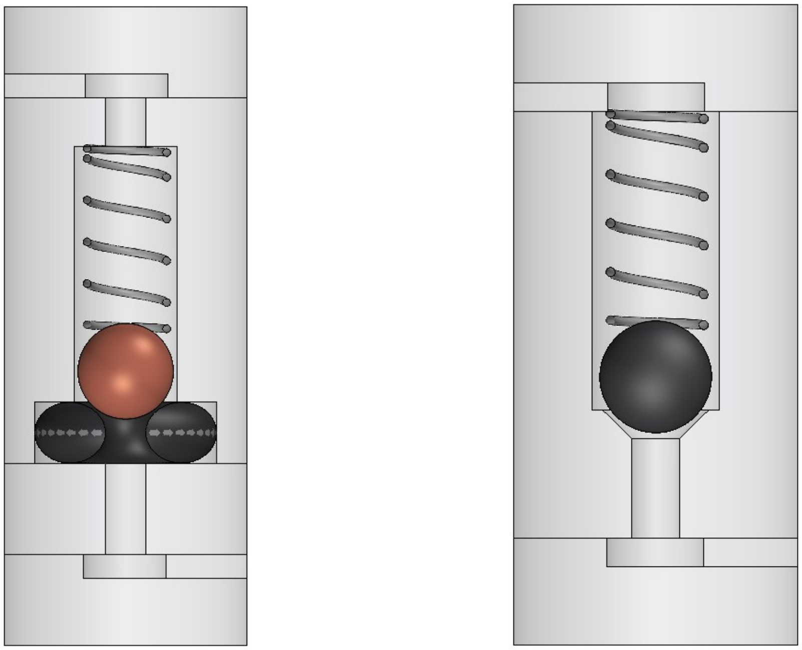

Figure 4.10: Left: Spring actuated ball vale with an O-ring seat and ceramic bearing. Right: Spring actuated ball-valve with an FKM ball and PMMA seat.

from chemically resistant ceramic rather than a ferromagnetic material like steel. Instead of using a magnet for passive sealing, a spring is used to push the ceramic ball into the O-ring to seal it when there is no external pressure applied. The springs are made from a chemically resistant nickel alloy called Hastelloy, and the force applied by the spring can be set by changing the depth of the recess in which it is set.

The second design explored here, shown in the right panel of Figure 4.10 uses FKM balls that deform against the PMMA seat, which creates a fluidic seal, and the same springs are used to provide passive sealing. This reduces the manufacturing complexity because there is one less step during the bonding process, and one less point of possible alignment error.

4.2.2 Testing Setup and Methods

Similar to the previous valve designs, there are three steps in testing the valve designs. The first step is simply an observation to identify if the valve works at all. This is done by using a syringe to slowly inject fluid from the input to the output, and then doing the same from the output to the input. If either there is no flow in the correct direction or there is clear and noticeable back flow in the wrong direction, the valve does not work.

The second step in testing is observing the behaviour of the valve in the four states that it can exist in, depending on how fluid pressure is applied:

A. Applying positive fluid pressure to the input. i.e. pushing fluid through
B. Applying negative fluid pressure to the output. i.e. pulling fluid through.
C. Applying positive fluid pressure to the output. i.e. pushing it closed.
D. Applying negative pressure to the input. i.e. pulling it closed.

The ideal valve would easily allow flow if it is in either state A or B, but would not allow flow in state C or D.

The third step is measuring the fluidic pressure of the system to monitor how well the valves hold back pressures and see how the pressure presents in a two-valve system. Figure 4.11 is a diagram of the two configurations for each testing setup. Panel A is the setup for testing back pressure leakage rates. A set amount of fluid is injected into the outlet of the valve, and the pressure is monitored over 1000 s to see how much pressure is lost. Because water is considered incompressible at this scale, this test is a good indicator for fluid leakage rates. Panel B shows the testing setup for a two-valve system. In an ideal system, one pressure gauge will read zero, and the other will read non-zero in one state. When they switch states, the pressure gauge readings should also switch: the opposite gauges should read zero and non-zero.

The O-ring style ball valves were fabricated to have a target cracking pressure. This was accomplished by varying the depth of the spring cavity, and therefore the amount of compression in the spring. Referring back to Figure 4.10, the depth of the spring cavity is predetermined, and can be milled to a specific measurement. Using the manufacturer's value for the spring constant (k), the force output of the compressed spring can be calculated using Hooke’s Law: $F = k\Delta x$, where Δx is the amount that the spring has been compressed by. The cracking pressure is calculated from the force using the area cross section of the via that meets with the bottom of the O-ring. In this way, I created valves with calculated cracking pressures ranging from 0.5 psi to 20 psi.

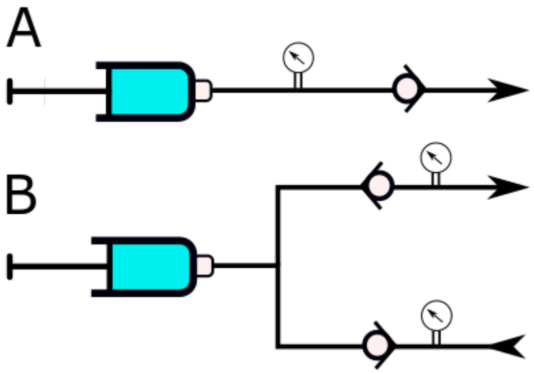

Figure 4.11: A: Back pressure monitoring setup. B: Two valve system monitoring setup.

4.2.3 Testing Results

Each valve was first tested to check general functionality. Fluid was injected the correct way into the valve, and if there was no flow at all it was considered permanently sealed and therefore broken. If the first test succeeded, fluid was then injected backwards into the

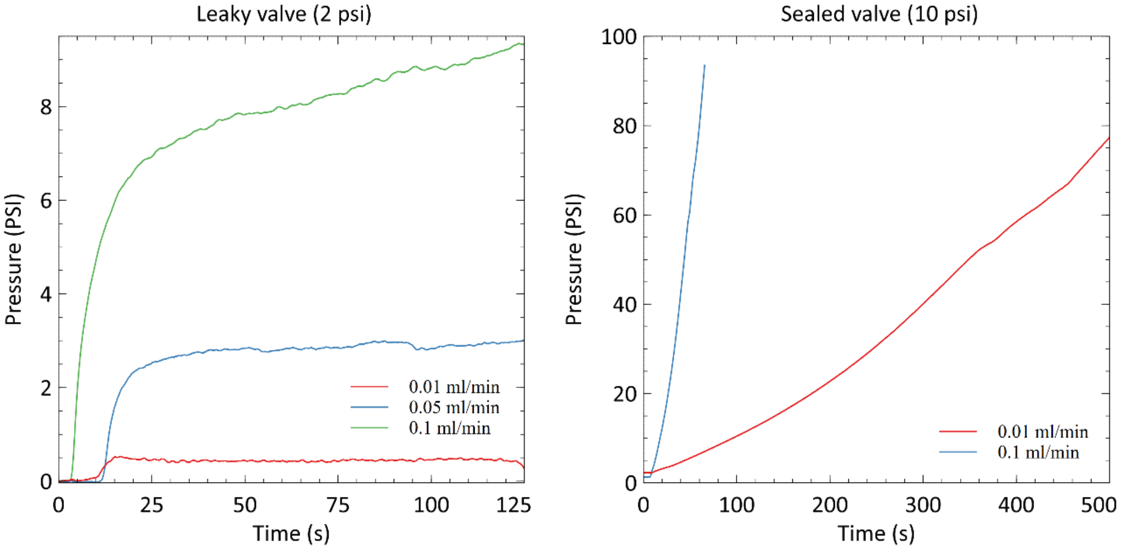

Figure 4.12: Left: Example of pressure data from a valve that does not seal properly when fluid is injected into the output of the valve. Right: Example of pressure data from a valve that does not open properly when fluid is injected into the input of the valve.

valve, and if there was noticeably backflow and/or no ability to maintain pressure, it was considered permanently open and therefore broken. Figure 4.12 displays some pressure data from failed valves. The left panel shows data from a valve that was designed to have a 2 psi cracking pressure. Fluid was injected backwards into it at set flow rates between 0.01 mL/min and 0.1 mL/min. If it sealed properly, the pressure would have continued to build until the test stopped or until a fluid element burst (e.g. tubing). However, from the data it is clear the pressure plateaus at the two slower rates, indicating that fluid was able to flow through the valve and the plateau is caused by the fluidic resistance of the system at that flow rate. The ideal valve would seal entirely with minimal back flow, which is not the case in this leaky valve. The right panel displays data from a valve that is permanently sealed. It was designed to open at a pressure of 10 psi, but it is clear from the data that the pressure is building well beyond that, indicating that the valve is completely sealed.

If the valve passed the first set of tests it was further tested for functionality by testing it in its four working states. Table 6 is a truth table for the tested valves and the four states they can work in. A correctly working valve would have the following set of state values:

Push on input	Pull on input	Push on output	Pull on output
Yes	No	No	Yes

However, not a single valve that was tested had state values that matched the ideals. The valves with lower cracking pressures tended to show back leakage when pulling on the input, because the restoring force of the spring was not enough to seal the fluid path. The valves with higher cracking pressures did not leak when pulling on the input, but they also

Table 6: Table of Results for O-ring Style Ball Valve Designs.

Pressure	Push on input	Pull on input	Push on output	Pull on output
0.5 PSI	Yes	Slow	No	Yes
1 PSI	Yes	No	No	Slow
1.5 PSI	Yes	No	No	Slow
2 PSI	Yes	Slow	No	Yes
2 PSI	Yes	Slow	No	Yes
3 PSI	Yes	No	No	Slow
3 PSI	Yes	No	No	Slow
4 PSI	Yes	No	No	Slow
4 PSI	Yes	No	No	No
5 PSI	Yes	No	No	No
5 PSI	Yes	No	No	No
7 PSI	Yes	No	No	No
7 PSI	Yes	No	No	No
10 PSI	Yes	No	No	No
10 PSI	Yes	No	No	No
20 PSI	Yes	No	No	No
20 PSI	Yes	No	No	No

did not open when pulling on the output. When the syringes pulled on the valve, the fluid either cavitated, forming gas pockets, or a pocket of vacuum formed within the channel. The pressure differential required to open the valve was higher than the negative pressure required to cavitate the fluid. For some ranges of cracking pressures around 4 psi, there was very slow positive flow when pulling on the output. This means that when the syringe pulled, it originally created a vacuum and then it slowly filled in with fluid as time went on. However, in these situations the syringes were never able to completely fill because as the vacuum cavity filled in, the pressure differential decreased until it was no longer enough to pull fluid through the valve.

Figure 4.13 shows some results from a back pressure leakage test. As previously described, the leakage rates were determined by injecting known volumes of fluid backwards into a valve until a target volume was met. In general, the valves designed with higher cracking pressures performed better for this test than the valves with lower pressures. It is shown in the bottom left corner of Figure 4.13 that the lower cracking pressure valves were unable to hold/maintain the fluid at all, and the pressure dropped back to zero as soon as each injection was finished. However, most of the higher cracking pressure valves were able to plateau and hold their pressure after an initial slight decrease.

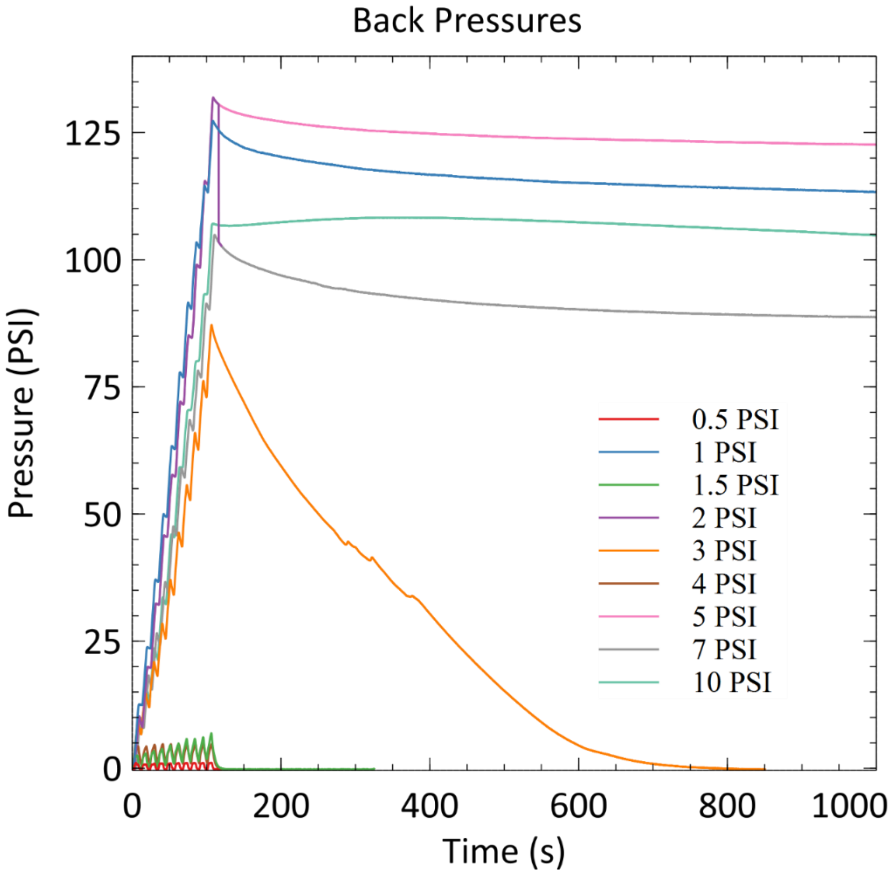

Figure 4.13: Back pressure curves for fluid injected into the output of the O-ring style ball valves. This demonstrates the potential for these valve designs to seal effectively at high back pressures, in laboratory conditions.

This was thought to be the pressure reduction from the system stabilizing as the fluid slowed. There is a decrease in pressure as the hydraulic resistance due to fluid motion decreases. Furthermore, it is possible that the elastomer O-rings relax slightly when there is no fluid actively moving.

The final test for the valves was to see how well they performed when working in a system containing multiple valves. The final chip design would require at least eight valves to function together on a single device but testing two in isolation was the first step. Figure 4.11(B) shows how the pressure gauges were set up for this test. Figure 4.14 shows the results of such a test. Fluid is injected in parallel at increasing flow rates into two valves: one facing forward and one facing backwards. In an ideal system, the pressure gauge on the backwards valve would always read zero, while the pressure gauge on the forwards valve would change in response to the injected flow rate. This is seen in the data, especially at flow rates beyond 2 mL/min. However, at flow rates below that point, the difference in pressures are minimal, and obscured by the noise of the system. There is also evidence that in some regions there is more flow out the backwards valve than the forward valve, which is counter to how it is meant to function. Although the results shown in Figure 4.14 are more promising than the previous tests indicate they should have been, they are still too variable and unreliable to consider using in a final product. This is particularly poignant when considering that a final design would require eight valves, and any issues seen in a two-valve system would be amplified when moving to an eight-valve system.

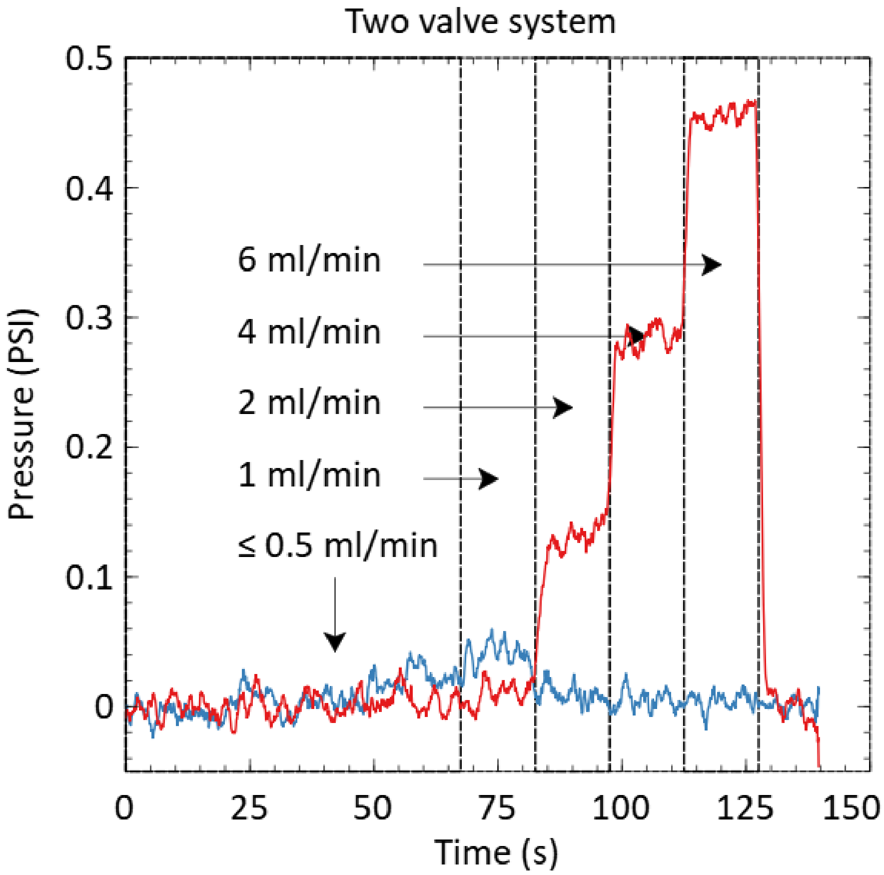

Figure 4.14: Output pressures for a two valve system.

4.3. Conclusions

The issue of valves in microfluidic devices is multifaceted and ongoing, due to the general size restraints, integration complexity and micro-fabrication. The work presented here provides a foundation and knowledge base for further work, as we were never able to design a valve that met all the design requirements for the *in situ* microfluidic sensor in development.

Because of the lack of chemical robustness displayed by the valves described in CHAPTER 3 we turned to designs based on chemically resistant elastomer membranes.

After several design iterations and testing, we were unable to produce valves with consistent cracking pressure and sealing ability. However, in the physical designs the performance of the valves was unreliable. Furthermore, the valves' sealing ability was greatly impacted if any air bubbles were introduced to the system. Air could get caught in the valve, causing it to fail entirely even if it had been functioning up to that point. Efforts to dislodge the air bubble were often ineffective and resulted in entire chips being rendered useless. Although air bubble introduction and cavitation is not typically an issue if the sensor were deployed below 10 – 20 m, it still greatly impacts bench top testing and surface water measurements. More work must be done in simulation and design to handle air bubbles if this style of valve is to ever be used for this application.

After attempting to use deformable membranes to create valves, we decided then to create a modified tunable ball valve that was functionalized by a micro-spring and an elastomer O-ring and made from chemically resistant materials. Despite the ability to tune the cracking pressure based on spring compression depth, the overly sensitive and complex fabrication process meant that we were still unable to create valves that yielded reproduceable results. Preliminary simulations show that there is potential to the valve designs if the design parameters can be optimized and if the fabrication procedures can be controlled and automated more carefully. However, more in-depth simulation work is needed before re-attempting a physical system.

The integrated check valves, although crucial for realizing an ultra low-power sensor, are not required to create the *in situ* sensor. After two years of design and testing efforts, we made the decision that the valves were halting sensor development and that we would use off-the-shelf active valves to create a functioning unit. This allowed us to continue development of a fully integrated system, with the option of removing the external active valves if the problem of the integrated passive valves was ever solved.

CHAPTER 5 INLAID OPTICAL CELLS

In this chapter we will continue the theme of developing supporting technologies for microfluidic devices by discussing the design, fabrication, and characterization process for a novel inlaid absorbance cell. We will first provide a literature review of existing absorbance cells, and the techniques and applications relevant to each style. It is important to note that much of the results presented in this chapter were done in collaboration with Edward Luy. Further details can be found both in his Master's thesis titled: *Inlaid Microfluidics: A Novel Approach to Optical Measurements on Lab-on-Chip Devices* [219] and in our co-authored 2020 article titled: *Inlaid Microfluidic Optics: Absorbance Cells in Clear Devices Applied to Nitrite and Phosphate Detection* [39].

5.1. Introduction and Literature Review

The degree to which light is absorbed in the flow cell is linearly related to the path length of the light, which creates difficulty in designing an effective microfluidic absorption cell. A single-pass system is one in which the path length is limited to one pass through the optical flow cell, while multi-pass systems use various techniques to virtually increase the optical path length. In the 2012 review by Rushworth *et al* [60], the various forms of single-pass and multi-pass systems are thoroughly explored. Here we will focus the discussion on more recent adaptations and specifically their use in marine sensing.

5.1.1 Single Pass Abnsorbance Cells

In a single-pass system, short path lengths are often insufficient unless the analyte exists in very high concentrations. However, increasing the path length to improve measurement sensitivity often creates difficulty with light scattering and coupling in and out of the channel. For the purpose of comparison, I will consider any path length less than 10 mm to be `short', and anything else to be `long'.

Short path lengths are most often on the scale of µm and are usually designed such that the light is directed perpendicular to the fluid flow. This limits the path length to the cross-sectional width (or depth) of the channel. For example, Onoshima *et al* [220] built an absorption cell with a 500 µm path length, resulting in an LOD of 15.9 µM for the yellow dye used in their experiment. They used dry film resist lithography techniques to build a mold for a polydimethylsiloxane (PDMS) microfluidic chip. This method allows the PDMS chip to be easily and quickly reproduced. Their design was such that the light source was above the channel, while the detector was below. It is common, however, for the light and detector to be to either side of the channel.

Starecki et al [221] used optical absorbance techniques to make a high pressure microfluidic CO_2 detector for use in deep aquifers. Using Dy^{3+} doped sulfide glass fibres in a microfluidic chip made from silicon bonded to Pyrex, they were able to detect the presence of CO_2 at a pressure of 5 MPa. This has potential to prove useful for CO_2 measurements in the aphotic zone of the ocean [222], however the complexity of production and use of rare-earth materials makes it difficult to reproduce. Gupta et al [223] took an interesting approach to dealing with a short path length by incorporating a metal-clad leaky waveguide (MCLW) [224] on a microfluidic chip to perform broad-band absorption spectroscopy. They designed a microfluidic pH sensor with an incorporated MCLW. The MCLW allowed them to obtain absorption measurements over the entire visible spectrum, which gave them an LOD of 15.49 µM for bromothymol blue (BTB) concentrations. In their previous work [224], they were able to obtain an LOD of 2.3 μM with methylene blue at 650 nm. However, the mechanical setup limited the range of wavelengths they could effectively couple in and out of the MCLW. The use of an MCLW allows them to do highly sensitive pH measurements without relying on excessive use of dyes. The current setup, however, is not designed for *in situ* measurements and would have limited use in a marine setting.

Liu et al [225] developed a microfluidic phosphate sensor with a vertical absorbance cell, as opposed to the typical in plane cells. They used an organic photodiode (OPD) at one end of a channel and an organic LED (OLED) at the other. The 5mm channel ran vertically through a PDMS chip bonded to glass. Their longer path length gave them a more sensitive measurement (0.21 μM LOD) than the previous groups, and their custom flat OPD fit nicely in the microfluidic chip. The OLED used a rare-earth complex, which resulted in a very narrow emission spectrum (10 nm FWHM). This worked out well for phosphate determination but would likely not be transferable to other nutrient sensors. Furthermore, their cylindrical absorbance cell had a diameter of 2.0 mm, giving the optical cell a dead volume of 157 μL, which is too high for the requirement of most microfluidic devices.

The most obvious way of increasing measurement sensitivity, according to the Beer-Lambert law, is to increase the path length. In microfluidic systems, this can be done by aligning the optical path length along the direction of flow [104]. However, when the cross-sectional width of the channel is on the order of 100 μm, and the path length is on the order of 10 mm, the aspect ratio is 100:1 at the very least. Coupling light in and out of the channel at this aspect ratio ends up being a tricky problem, and Rushworth *et al* discuss how it has been tackled in the past. For example, the idea of using prisms made from the interface between PDMS and air to steer light down the channel has been explored [226]. However, here we will look at some recent adaptations of the more promising techniques for nutrient sensing in aquatic environments.

In 2010, Sieben *et al* [104] introduced the idea of using carbon doped (tinted) PMMA as the material in which to manufacture the microfluidic flow cell. The LED emits light in a 15° cone at the start of the channel. Only the light running directly through the channel makes it into the detector, as the rest of the cone is absorbed in the tinted material. The partial transparency of the PMMA allowed them to leave a thin (1 mm) window in the plastic through which the light could be coupled in and out of the channel. Using a 25 mm long, 300 μm deep square channel, and an LED centered at 525 nm, Sieben *et al* were able to achieve an LOD of 14 nM when detecting nitrite in fluid samples. Nitrite was detected by mixing Griess reagent in with the fluid sample to produce an Azo dye that absorbs at 543 nm (82 nm FWHM).

This same method, with the same parameters, was followed up in 2012 by Beaton et al [13]. They developed a functional nitrite and nitrate sensor from the tinted PMMA technique. It used several standards for calibration, and was actually field tested in the waters of Southampton, UK. They achieved an LOD of 20 nM for nitrite detection and 25 nM for nitrate, while maintaining a low dead volume (2.25 μL) in the optical cell. A 2.5 mm long absorption cell was also added to the chip to increase the overall dynamic range (linear up to 350 μM) of the sensor by enabling it to measure high concentrations as well as low. To incorporate both nitrite and nitrate measurements in the sensor, two flow cells with a cadmium reduction column between them were used. The first cell would provide a

Table 7: Applications of Optical Absorbance Cells in Ocean Nutrient Sensing.

Author(s)	Year	Cell Material	Path Length	LOD	Volume	Wavelength	Application
Sieben *et al.* [195]	2010	Tinted PMMA	25 mm	14 nM	2.25 µL	525 nm	Nitrite
Beaton *et al.* [13]	2012	Tinted PMMA	25 mm	20/25 nM	2.25 µL	525 nm	Nitrite/Nitrate
Onoshima *et al.* [220]	2012	PDMS	500 µm	15.9 µM	2.50 µL	482 nm	Yellow Dye
Liu *et al.*[225]	2015	PDMS	5 mm	0.21 µM	157 µL	612 nm	Phosphate
Ahn *et al.* [32]	2015	Black PDMS	80 mm	8.6 nM	3.93 µL	526 nm	Nitrite
Cao *et al.* [36]	2017	Tinted PMMA	25 mm	45.1 nM	4.00 µL	810 nm	Silicate
Duffy *et al.* [33]	2017	PMMA, PSA	75 mm	51 nM	n/a	880 nm	Phosphate
Duffy *et al.* [227]	2018	PMMA, PSA	50 mm	28.8 nM	n/a	535 nm	Chromium
Rushworth *et al.* [124]	2012	Commercial	1.0 mm (1 m CRDS)	1.9/3.8 nM	196 nL	532 nm	Nitrite/Iron(II)
Rushworth *et al.* [228]	2015	PDMS	50 µm (1.4 mm CEAS)	7 µM	1 µL	Visible Light	Thymol Blue

reference nitrite measurement before the cadmium tube would reduce any present nitrate to nitrite. The sample would then flow into the second cell where the second nitrite measurement would be taken so the difference could be used to determine the nitrate concentration.

Cao *et al* [36] used a very similar design to Beaton's to create a functional microfluidic silicate sensor. Again, they used tinted PMMA to create a 25 mm long optical cell, with a shorter secondary cell (5 mm long) for high concentration measurements. They used an ammonium molybdate complex as the reagent to react with silicate to form a yellow silicomolybdate, which could be further reduced to silicomolybdenum blue using ascorbic acid. An 810 nm LED was used for the concentration measurement, resulting in an LOD of 45.1 nM and a dynamic range up to 400 μM.

Following in the theme of using darkened materials to absorb stray light, Ahn et al [32] used black PDMS to create a microfluidic nitrite sensing system. To extend the optical path length, they used a liquid core waveguide (LCW) that coupled in and out of the PDMS chip. The chip was made from black material to ensure that only a pinpoint of collimated light from the LED would be coupled into the LCW. The LCW uses the principle of total internal reflection (TIR) to manipulate light through a long, non-linear path. Successful TIR depends only on the refractive indices of the interfacing materials (RI_{teflon}= 1.29, RI_{water} = 1.33) and the angle of incidence of the light. Because the refractive index of the Teflon capillary tubing is smaller than that of the aqueous solution inside, it will undergo TIR so long as the tubing is not crimped or bent at an angle greater than the critical angle of the material interface. Using this method and an 80 mm long path length, Ahn et al were able to obtain an LOD of 8.6 nM. One drawback of an LCW setup is that it is difficult to know exactly what the path length is, as it depends on the incident angle of the light and the curvature of the tubing. However, so long as the initial incident angle is close to 0° and the tube is sufficiently long, the total path length can be approximated to be the length of the tube.

Centrifugal microfluidics also tends to use optical techniques, as coupling physical wires to a spinning disk is very difficult. Duffy *et al* developed two portable all-in-one centrifugal microfluidic sensors for detecting phosphate (PhosphaSense [33]) and chromium (ChromiSense [227]) in river water. Both designs use a reusable PMMA microfluidic disk with optical absorbance cells positioned towards the edges. The centrifugal force from the rotation pumps the sample and reagent into a micro channel where they are mixed before settling in the optical cell. The PhosphaSense device uses a 75 mm path length and achieves an LOD of 51 nM. The ChromiSense has a path length of 50 mm and achieves an LOD of 28.8 nm. The path lengths were experimentally optimized and chosen as a compromise between a low LOD and a large dynamic range. The absorbance cell in the ChromiSense has circular cutouts running along its length to act as bubble traps. When the disk spins, the low density bubbles are forced to the very outer edge, leaving only the uniform solution in the path of the optical measurement. To tackle the light coupling issues, the ChromiSense uses a 5 mm wide absorbance cell, which reduces the aspect ratio to 10:1 in the plane. Black acrylic paint is also applied to the PMMA on either side of the detection windows to further limit stray light. On top of this, the entire device is enclosed in a sealed box to eliminate any influence from external light.

5.1.2 Multi-Pass Absorbance Cells

Multiple passes through the analyte is the second way of increasing the effective path length. This is generally accomplished through the use of mirrors (or TIR), and sometimes lenses. Liquid core waveguides are an example of such a method. Technically, with an LCW, the light passes through the solution multiple times as it undergoes TIR. However, it is grouped in with single path methods because the total path length can be approximated to be the length of the tube itself. Rushworth *et al* cover the various techniques of creating multi-pass absorbance cells. The most basic method is to position two mirrors on either side of the channel with the light source at a steep angle and the detector some way down the channel [229], [230]. However, it is difficult to determine the exact path length of the light using this method. When an un-collimated light source is used, there is a large range of path lengths, making the absorption measurement a statistical estimation at best. Other methods use PDMS-air lenses and mirrors to steer light through the micro-channel. Llobera *et al* [231] do exactly this. Having first verified the concept using ray tracing simulations, they made a PDMS chip with molded air cavities around the fluid channel. The cavities used TIR to lens and reflect the light back through the channel in a zig-zag manner. With this method, they produced an LOD of 41 nM from an effective path length of 8.336 mm. Their use of simulations allowed them to shape and position the mirrors exactly as they needed. Despite this, the issue arises again with uncollimated light. They used an optical fibre to couple in and out of the setup, but a naked LED would scatter light throughout the chip. The difficulty in coupling raw light to these types of multi-pass systems is one of the reasons why, in recent years, there has been more focus on cavity enhanced absorption cells as an alternative.

Techniques that use an optical cavity to enhance sensitivity falls under the category of Cavity Enhanced Absorption Spectroscopy (CEAS). Cavity ring down spectroscopy (CRDS) is a type of CEAS and uses partially transparent mirrors on either side of a cavity to increase the effective path length of a light pulse. At each mirror, a portion of the light will transmit through, while a portion will be reflected back into the cavity. The number of pulses recorded by the detector can be used to determine the total path length of the light. The resulting ring down trace is an exponential decay that indicates the light loss in the cavity.

This method was used by Rushworth et al [124] to detect nitrite and iron(II) in water samples. Using a commercial flow cell with a path length of 1.0 mm, and a 532 nm laser they obtained a very impressive LOD of 1.9 nM for nitrite and 3.8 nM for iron(II). The mirrors were 99.8 % reflective and set up on either side of a 58.5 cm cavity. The commercial flow cell was positioned in the center where it is hit by a 0.9 ns laser pulse. The recorded ring down time is 458 ns, which gave an effective path length of 1 m for the 1.0 mm flow cell.

Rushworth *et al* followed this up by applying a CEAS technique on a fully microfluidic platform [232]. They encapsulated 98 % reflective polymer mirrors between the layers of PDMS to enhance the measurement sensitivity of a 50 μm wide channel at the center. They used commercial ESRII film as the mirror, which is a broadband reflector across the entire visible spectrum. The light source used here was not a pulsed laser, but rather a constant white light LED with a tunable intensity. Using a benchtop spectrometer and an optical fiber coupled to the PDMS chip, they were able to achieve an LOD (for thymol blue) of 7 μM at an absorption peak of 595 nm (basic peak), and 10.6 μM at 435

Table 8: Commercially Available Absorbance Cells.

Company	Cell	Path Length	Internal Volume	Price
FIA Labs	Ultra-Short	0.1 - 2.0 mm	30 – 560 µL	1,478 USD
FIA Labs	SMA Z-series	2.5 – 100	n/a	n/a
FIA Labs	Long Path	50 cm	220 µL	n/a
WPI	3100 Series	100 cm	250 µL	2,157 USD
WPI	3050 Series	50 cm	150 µL	2,037 USD

nm (acidic peak). This corresponds to a 4.5 to 5 fold increase in sensitivity from a single pass cell of the same dimensions. The actual effective path length of the setup depends on the wavelength of the light, but they found the maximum effective path length to be roughly 28 times the 50 µm channel (approximately 1.4 mm) at a wavelength of 544 nm.

When developing microfluidic nutrient sensors, it is more often easier to design a custom chip with an incorporated flow cell. As such, most commercially available flow cells are designed for benchtop tests and use in research. Companies such as Starna Scientific Ltd. [233] and FIA Labs [234] develop cells for these purposes. FIA Labs has short path length options that range from 0.1 to 2.0 mm. They have an internal volume of 30 to 560 µL and cost more than 1000 USD each. They also have a longer Z-series which come in a variety of materials (Steel, Teflon. Plexiglass etc...) with easy optical connectors and path lengths ranging between 2.5 and 100.0 mm. If a longer path length is needed, they also sell 50 cm options.

World Precision Instruments (WPI) has a series of Liquid Waveguide Capillary Cells (LWCCs), which are merely a commercialization of the LCW technique previously mentioned. Table 8 contains some specifications of the 3100 and 3050 series. They have long path lengths of 50 and 100 cm, with corresponding large cell volumes of 150 and 250 µL. The long path length of the cells gives them good measurement sensitivity, with a noise level < 0.2 mAU and a dynamic range between 0.01 and 2.00 AU. However, they are designed to be strictly benchtop devices and are rated only up to a pressure of 100 psi. These cells are not typical microfluidic cells but do provide a good example of what types of benchtop flow cells are available.

Single-pass flow cells have the benefit of being easy to construct and integrate into microfluidic chips. However, short path lengths lack the sensitivity required for effective nutrient concentration measurements in the ocean. They are only useful for high concentration analytes which are typically not found in ocean water. Long path lengths on the other hand do meet the sensitivity requirement for nutrient monitoring. So long as light is effectively coupled into the channel, they are a valid option for absorbance cells in microfluidics. The use of tinted cell material seems to be an effective way of tackling the light coupling issue. For multi-pass flow cells, CRDS is a promising technique. The impressively low LOD displayed by this method, and the potential for it to be integrated entirely into a microfluidic chip make it an exciting idea for *in situ* nutrient sensing. However, the manufacturing process for a fully integrated CRDS setup is potentially time consuming and difficult. Overall, single-pass flow cells with long path lengths have the best results and are more robust for most uses.

The absorbance cell we are presenting addresses several of the issues presented in the review of existing flow cells. It is a single pass flow cell with a long path length, which gives it greater ease of manufacturing while obtaining a low LOD. Furthermore, the optical components are entirely decoupled from the controlling electronics. This makes optical alignment much simpler when compared to flow cells such as the tinted PMMA cells previously discussed, because no epoxy or optical adhesive is required to secure the LED or photodiode. The configuration of the cell also allows easy replacement and servicing of the microfluidic chip because there are no physical wires attached to it and crossing the pressure barrier from the internals of the sensor. This will be further discussed in CHAPTER 6 , when the entire instrument is presented.

5.2. Inlaid Absorbance Cell Design and Theory

The two primary physical phenomena relevant to the absorbance cell presented here are Optical Absorption Spectrophotometry (OAS) and Total Internal Reflection (TIR). The theory and concept behind OAS has already been discussed in Section 2.1.1, and does not need to be reintroduced here. It is the fundamental theory behind absorbance cells and is not unique to the cell presented here.

The novel aspect of this cell is that it uses TIR to redirect light. TIR is a phenomenon that occurs as light passes through an interface from one material to another. Light refracts away from the normal when light is moving from a material of high refractive index to a material of low refractive index. If the incident angle of the light is steep enough, the light will reflect off the interface and back into source material. The angle at which this occurs is dependent on the ratio of the refractive indices of the two materials at the wavelength of the incident light. This angle is known as the critical angle and is calculated using Snell's Law:

$$\Theta_c = sin^{-1}\left(\frac{n_2(\lambda)}{n_1(\lambda)}\right) \qquad 5\text{-}1$$

If the incident angle exceeds the critical angle, the incident light will undergo total internal reflection. Grumann et al. [226] used this property to create micro-prisms from engraved V-grooves inside a microfluidic chip that direct perpendicular light through a 1 mm absorbance cell. In their setup, incident light enters through the top of the transparent COC chip, undergoes TIR on the air-COC interface and then travels in the plane of the chip and across a fluid channel, perpendicular to flow before it contacts the second V-groove prism and is directed back out of the chip into a detector.

Our design uses a similar setup, although the light travels through the absorbance cell in the same direction as fluid flow, through a much longer absorbance cell. Furthermore, the absorbance cell is milled into opaque black PMMA to absorb any stray light and eliminate most of the background noise due to scattering. Figure 5.1 is a CAD

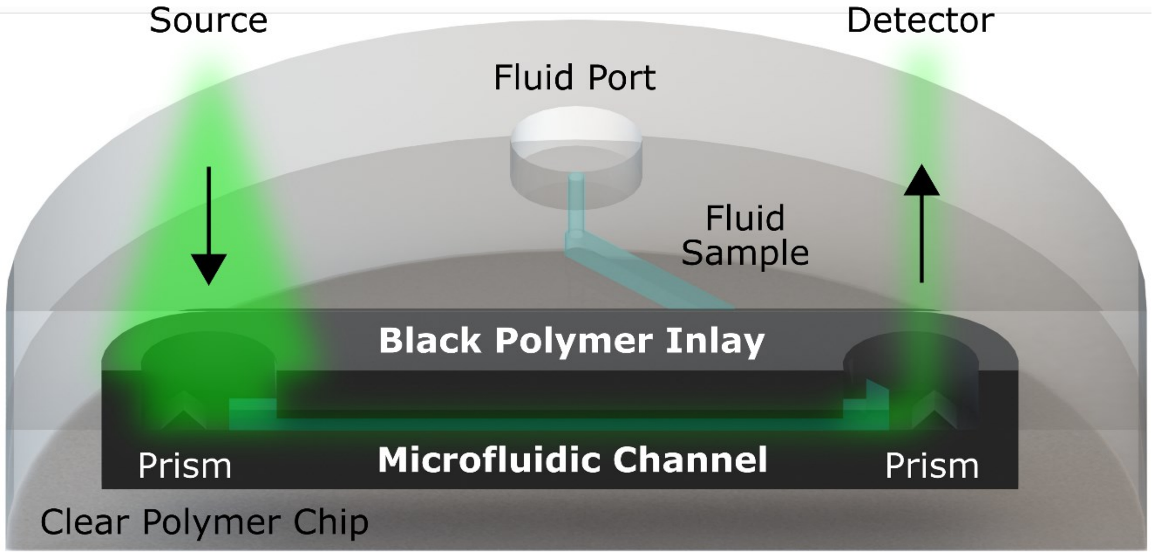

Figure 5.1: CAD cross section of inlaid absorbance cell design. Light is directed by engraved prisms from the source, through the fluid channel and then up to the detector.

rendering to convey the concept. An opaque black absorbance cell is inlaid into the clear microfluidic device, leaving windows of clear plastic where the micro-prisms are milled. This allows light to enter and exit the cell only through the two windows, and not from any other source.

The average refractive index of PMMA over the visible range is 1.4906. The widely accepted value for the refractive index of air is 1.0003, which means that Equation 5-1 results in a critical angle of 0.735 radians, or 42.15°. The engraved V-grooves have a side angle of 45°, which is larger than the critical angle, allowing the light to undergo TIR. It also makes optical alignment much simpler than larger angles because the incident light can be perpendicular to the chip face. The fabrication details and chip creation specifics will be further discussed in the upcoming section.

5.3. Inlaid Absorbance Cell Fabrication Method

The substrate material for both the microfluidic chip and the integrated absorbance cell is PMMA. The procedures used to bond PMMA in this work are based on the solvent bonding methods described by Ogilvie [105] in 2010. However, we have adapted the methods to bond the softer, more porous extruded PMMA rather than the cast PMMA used by Ogilvie. The novel aspect of this work is the inlaid absorbance cell, made from bonding opaque black extruded acrylic inserts (9M001, Acrylite, USA) into transparent acrylic cavities (0A000, Acrylite, USA).

The black inserts were cut out from a 3 mm thick sheet of 9 inch by 12 inch black acrylic on a 50 W Epilog Mini Laser Cutter. The focus head of the laser was adjusted so the tip was aligned to halfway through the thickness of the material. The cutter was set to

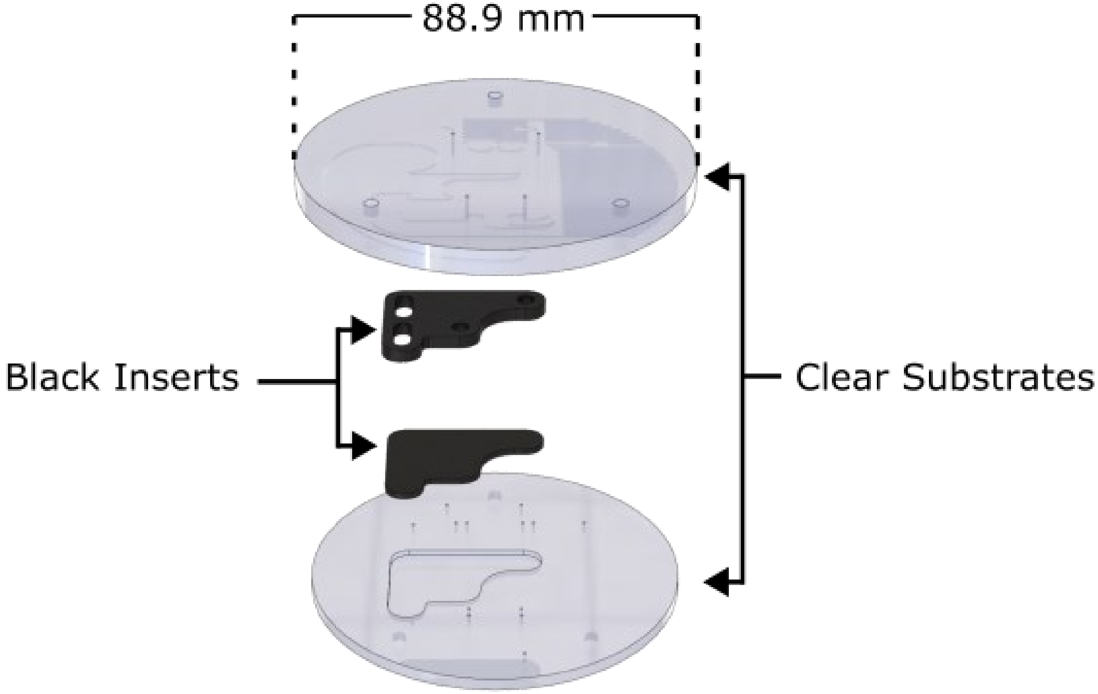

Figure 5.2: Assembly of microfluidic chip with black acrylic inlays.

have a speed parameter of 20 and a power parameter of 100 to fully cut through the Acrylic without heating the aluminum grid below to the point that it begins to melt the acrylic. Even with the laser focus point set to halfway through the material, the top edge becomes rounded due to the Gaussian profile of the laser. For that reason, the inserts are always positioned so that the top face (with the rounded edges) faces down in the microfluidic device because the rounded edge allows the insert to be more easily pressed into the cavity. The inserts were cut to have a window in the top piece to allow light coupling to the prisms. This can be seen in the top insert shown in Figure 5.2.

The cavities in the clear acrylic substrates (also shown in Figure 5.2) were milled into blank 9 inch by 12 inch sheets of 6 mm thick PMMA on either an S104 or an S103

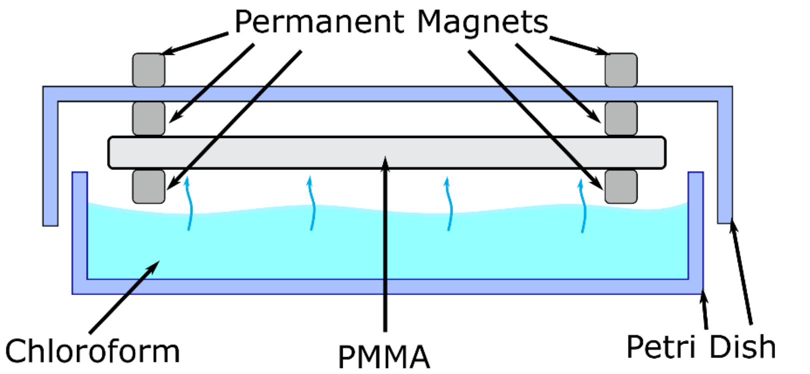

Figure 5.3: Setup for chloroform vapor exposure using permanent magnets for suspension.

LPKF Micromill. They were milled to be 25 µm wider than the inserts on all sides to give tolerance for the inserts to be pressed in by hand. Furthermore, they were milled to be 150 µM shallower than the inserts were thick. This served two-fold reasons, both to accommodate for variability in the insert thickness and to provide excess material for the insert to expand to fill any gaps between the inserts and the milled cavities in the substrates.

After the inserts and clear substrates with cavities had been created on the mill and laser, they were cleaned and prepared for bonding. First, any excess debris from the milling process was removed using a vacuum and then blasts of compressed air. Next, they were thoroughly scrubbed using standard dish soap with hot tap water and the rough side of a sponge. A toothbrush was used to access any parts that were too small or difficult to reach with the sponge. They were then rinsed and scrubbed again using only water to remove the dish soap. Following this they were rinsed carefully with Milli-Q, while wearing gloves to prevent any residue from fingers contacting the surface. Next, they were dried thoroughly using compressed air, and then rinsed using isopropyl alcohol to remove any water that had absorbed into the surface of the PMMA. After being dried once again with filtered compressed air, they were ready for bonding and inlaying.

The inlaying process is very similar to the bonding process for PMMA sheets discussed in section 3.2.6. Chloroform was poured into a petri dish to a marked point and then covered and heated to 30° C on a hot plate. The opaque inserts were attached to the underside of the petri dish lid using permanent magnets so that they were suspended 3 mm above the surface of the chloroform. Figure 5.3 shows how the acrylic is suspended above the chloroform in the petri dish. The inserts were oriented so that the rounded edge created by the laser faced down. After 45 seconds of exposure, the inserts were removed from the vapor chamber and then pressed by hand into their respective cavities in the clear acrylic substrate. The entire sheet was then pressed in an LPKF Multipress II for 2.5 hours using 30 kN of force at 116° C, which is just above the glass transition point of PMMA. After 2.5 hours at 116 °C, the sheet was pressed for a further 2.5 hours while the press was allowed to cool down to room temperature. This was done so the acrylic sheet could not warp as it cooled. The inlaid sheet was then removed from the press and prepared for milling.

The inlaying process often caused non-uniformity in the thickness of the resultant sheet. This was most likely caused by the platens in the press not being perfectly aligned with each other. As a result, the inlaid sheets needed to be back-planed to ensure the two faces were parallel. This was done by milling down 0.3 mm on the inlaid side of the sheet using a 2 mm endmill on the S103 Micromill. After this, if there were still visible areas where the mill had not reached, the back plane was repeated until all areas had been planed. At this point, the sheet was ready for the features to be milled.

The sheet was then moved to the S104 Micromill for the prisms, vias and channels to be milled. All channels were milled using a 500 or 400 µm flat endmill to create square channels. A 700 µm spiral drill was used for the vias, and a 90 ° V-groove endmill was used to engrave the prisms. Fiducial holes milled prior to inlaying were used for alignment during the entire process. The feature milling process was also dependent on the application and design of the chip that was being manufactured and could vary between projects. However, the overall workflow is what is being described here.

The next phase of the manufacturing process is cutting out the individual discs from the inlaid sheet and bonding the halves together. A 50 W Epilog Mini Laser cutter was used to cut the chip halves out of the larger inlaid sheet. Again, the focus point of the laser was set to come to halfway up the material thickness to create a more even edge profile The laser was set to have a power level of 100 and a speed of 10 to cut through the 6 mm thick acrylic. Each half was then gently sanded using 320 grit sandpaper to help reduce the ridges that were created when the sheet was back planed. The cleaning, preparation and solvent vapor exposure process for the chip halves was identical to the process already described for the inlay inserts. After the chloroform exposure, the two halves were aligned either using a custom alignment jig or steel dowels embedded in the chip. They were then pressed in an LPKF Multipress S at 85° C at a pressure of 625 N/cm^2 for 2.5 hours to ensure a solid bond. Again, the chip was allowed to cool under pressure to reduce warping in the product. This process is described in less detail in Luy et al. 2020 [219], and was not fully detailed.

5.4. Inlaid Absorbance Cell Calibration Methods

The emphasis of the results shown in the 2020 article is on demonstrating the effectiveness of the inlaid absorbance cell through generating calibration curves. A microfluidic chip with three separate absorbance cells with pathlengths of 10 mm, 25 mm and 50 mm was used for all of the calibration tests. Stable red and yellow food dyes were first used as proxies for nitrite and yellow phosphate reagents respectively. Next, the nutrient solutions and reagents themselves were used to generate the calibration curves. A green LED centered at 527 nm (Cree C503B-GANCB0F0791-ND, FWHM = 15 nm) was used as the light source for the nitrite reagent and red food dye, while a UV LED centered at 380 nm (Superbrightleds RL5-UV0315-380, FWHM = 12 nm) was used as the light source for the yellow phosphate reagent and yellow food dye. A TSL257 light to voltage converter was used as the detector for all calibrations, and a B&K Precision 5491B bench multimeter with 10^{-7} V precision was used to measure and log the voltage measurements every second. The chip, LEDs and photodiodes were all sealed into an optically isolating box for testing to reduce the influence of varying background light.

The first calibration data set was obtained from using serial dilution to create a series of red food dye concentrations ranging from 0.0016 % to 0.05 % v/v. Each sequential concentration was injected into each absorbance cell with a Milli-Q blank injection separating them, and the voltage for each sample was measured and converted to absorbance by comparing it against the voltage measured through the blank. The same procedure was followed for the other solutions, however the yellow food dye ranged in concentration between 0.0063 % and 0.1 %, the nitrite solutions ranged between 0.1 µM and 100 μM, and the phosphate concentrations were between 0.1 μM and 50 μM. For the two nutrient calibrations, each nutrient solution sample was pumped through a serpentine mixer at 1:1 ratio with its respective reagent. Once pumping was complete, the mixed solution was given 5 minutes to stabilize and react, and the voltage readings from the last minute were averaged and then used to determine absorbance. Further details on the reagent and standard preparation can be found in the 2020 article [39].

5.5. Inlaid Absorbance Cell Calibration Results and Discussion

Here I will present only some of the results from the several calibration studies performed on the inlaid absorbance cell. This will not be an exhaustive compendium of the acquired data, as that can be found in the Masters thesis by Edward Luy [219], but only an overview containing some calibration curves and representative data produced from the nitrite tests described in the previous section.

Figure 5.4 shows the raw voltage data measured by the multimeter as the mixed nitrite and reagent solutions are sequentially injected into the 10 mm absorbance cell. Each concentration is separated by a Milli-Q injection to both rinse the previous sample from the cell and to provide a blank measurement. It is visible in the data, especially in the higher concentrations, that colour development is happening within the absorbance cell. The voltage profile for each concentration has a similar shape, resembling a backwards J. Nearing the end of the allotted five minute reaction time the profiles begin to plateau, indicating that the reaction is almost complete. More in-depth analysis on the reaction kinetics of the Griess Assay and be found in Edward Luy's Masters thesis.

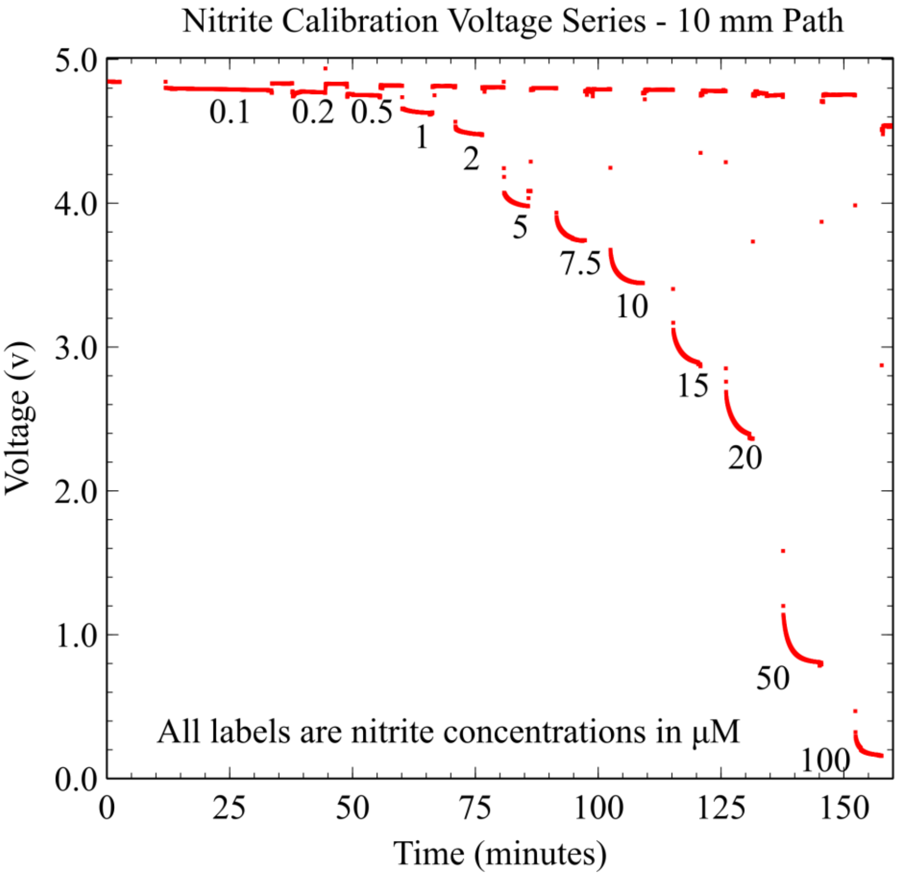

Figure 5.4: Example voltage data from a nitrite calibration on a 10 mm inlaid absorbance cell. All concentrations are marked in the figure.

Figure 5.5 is the resultant calibration curve based on data sets such as the one displayed in Figure 5.4. As well as the curve for the 10 mm pathlength, it also contains the calibration curves for the 25 mm and 50 mm pathlengths. The longer pathlengths produce a higher sensitivity, in accordance with the Beer-Lambert law. Furthermore, also in accordance to the Beer-Lambert law, the pathlength ratios matches very closely to the sensitivity ratios:

	50:25	50:10	25:10
Path:Path	1.98	4.85	2.44
Slope:Slope	2.01	4.73	2.35

In this set of calibration curves, the sensitivity (slope) ratio between the 50 mm and 25 mm absorbance cells is almost exact to the pathlength ratio. However, both of the sensitivity ratios that contain the slope from the 10 mm absorbance cell fall slightly short

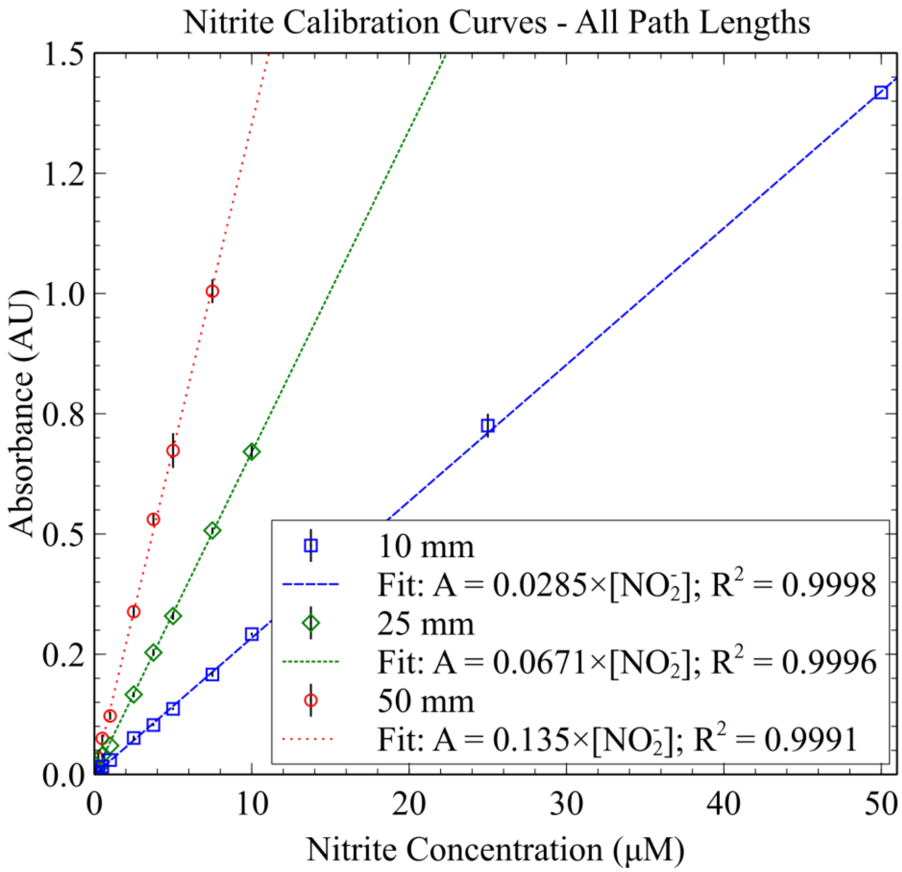

Figure 5.5: Examples of calibration curves generated from the nitrite measurements obtained from the inlaid absorbance cells. All three path lengths (10 mm, 25 mm and 50 mm) are shown. Each calibration shows excellent linearity, demonstrating a comparable measurement sensitivity to autoanalyzers.

of the path length ratios, although are still very close. The reason the path length ratios are not exactly 2, 5, and 2.5 respectively as would be expected is that the absorbance cells are actually 50.4 mm, 25.4 mm and 10.4 mm in length. This is a result of an oversight in the fabrication, because when the cells were designed the width of the milling bit was not considered, which adds a total of 0.4 mm to each path.

After a full set of calibrations for nitrite and phosphate using the yellow phosphate method, the system was found to have limits of detection (LODs) as low as 6 ± 8 nM for nitrite and 40 ± 30 nM for phosphate using the 50 mm pathlength. This is comparable to the detection limit of AutoAnalyzers and many of the sensors presented in the introductory section of this chapter.

5.6. Conclusions

Following the characterization and optimization of the fabrication method for the inlaid optical cells, they were integrated into deployable microfluidic devices. The second iteration of the sensor (the first was presented in CHAPTER 3 is described in the Murphy *et al* conference proceeding titled *Lab-on-a-chip Sensor for In situ Nutrient Monitoring* [42]. The third iteration is presented in the 2020 article *Inlaid Microfluidic Optics: Absorbance Cells in Clear Devices Applied to Nitrite and Phosphate Detection* [39]. The fourth iteration, functionalized by the inlaid absorbance cell, will be the focus of the upcoming CHAPTER 6

CHAPTER 6 PHOSPHATE SYSTEM DEVELOPMENT

This chapter describes the development and deployment of the microfluidic nutrient sensor as a final product. All of the work described in this chapter was done in cooperation with Dartmouth Ocean Technologies (DOT), and the sensor described here was built using the resources and personnel provided by DOT. Furthermore, most of the following chapter is based on the publication "A submersible phosphate analyzer for marine environments based on inlaid microfluidics" by Morgan et al., published by Analytical Methods in 2022.

6.1. Introduction

Orthophosphate, as well as other forms of phosphorus, is an integral component of the energy storage mechanisms of phytoplankton [235] and is therefore considered a key limiting nutrient for phytoplankton growth in many ecosystems [236]. Additionally, there are species that have adapted to utilize phosphate to bloom under low nitrate conditions in marine environments [237]. Furthermore, nutrient pollution from increased levels of anthropogenic phosphate flux in freshwater or coastal regions can lead to blooms of toxic phytoplankton species such as Karenia brevis [238]. To address this, governing bodies have implemented restrictions on allowable levels of phosphate loading from industrial effluent. For example, the Environmental Protection Agency (EPA) and the Department of Natural Resources in the United States have set a limit of phosphate concentration in effluent to 1 mg/L (10.5 µM as PO_4^{3-}) as a monthly average from public and private wastewater sites [239]. Furthermore, the Canadian Water Network reports that Canada has implemented provincial restrictions ranging from 0.1 to 1 mg/L (1.05 to 10.5 µM) of phosphate in effluent [240]. Accurate and automatic *in situ* phosphate analyzers are required to ensure that these policies are effectively realized, and to quantify the effects of anthropogenic phosphate loading on marine environments.

There are several well-documented approaches to measuring environmental phosphate in water, including electrochemical techniques [241], biomimetic receptor technologies [242], and fluorescence probes [243]. Of the available analytical techniques, the most widely used method for determining orthophosphate concentrations in seawater is flow analysis using reagent-based colourimetry [244], [245]. The two common reagents used to accomplish this are the yellow vanadomolybdate method and the phosphomolybdenum blue method. There are commercial instruments, such as the Alyza IQ PO4 (YSI Inc., Ohio, United States) that use the yellow vanadomolybdate reagent for phosphate detection. It has the advantage of having a long shelf life, and requires only a single reagent [246]. However, it lacks sensitivity compared to the blue method and is considered highly toxic due to the vanadate in the reagent. The more sensitive and less dangerous molybdenum blue phosphate reagent, first introduced by Murphy and Riley in 1962 [247], is the more often used alternative. Since 1971, it has been recognized as the EPA standard (EPA-NERL 365.2) for phosphate determination in water [248]. There have been many different variations of the method since its creation, but the basic mechanism occurs in two stages [249]. The first stage involves the reaction of the phosphate ion with molybdate under acidic conditions to form a Keggin ion (polyoxometalate species). This molecule is then reduced using an application specific agent in the second stage to form the phosphomolybdenum blue (PMB) assay. Phosphate concentrations are then determined by employing absorbance spectrophotometry on the final PMB complex. When the PMB assay is kept separated and in cool conditions (approx. 4 °C), the components have been shown to be stable for 2 – 6 months [120], which highlights its potential application for remote sensing. Furthermore, groups have shown that the reagent can be lyophilized and embedded in paper substances to further prolong its shelf life to up to 2 years while maintaining sensitivity [121].

In the laboratory, the spectrophotometric analytical technique for the PMB assay is accomplished using benchtop systems, like auto-analyzers, due to their high precision (<1 % relative standard deviation), high accuracy (<2 % relative error) and low limits of detection (< 20 nM for phosphate) [103]. However, this is an *ex situ* approach that requires the sample to be collected and removed from the environment. For open ocean sampling, this requires large financial overhead of approximately 10 – 15K CAD per day for the ship and crew, and several hours between sample collection and analysis. Furthermore, the samples require on site manual filtering and near immediate freezing to be properly preserved. These considerations severely limit the maximum possible spatial and temporal resolution of the technique, making it difficult to capture short term events such as tidal cycles. *In situ* sensors provide an effective alternative as they can make more frequent measurements (several samples per hour) directly in the environment.

The HydroCycle PO_4 (Sea-Bird Scientific, Washington, United States) is an example of a widely used *in situ* commercial phosphate analyzer that uses the molybdenum blue method. It is capable of making up to 4 measurements per hour with a detection limit of 24 nM, however it generates 30 mL of waste and consumes from 1.6 – 2.5 kJ of energy per sample [250]. Microfluidic devices on the other hand can perform laboratory analytical techniques such as spectrophotometric analysis on a miniature scale, making them ideal for *in situ* instruments in environments where power, weight and reagents need to be conserved. Several groups around the world have developed these instruments, with wide reaching applications including nutrient detection. Duffy et al., based out of Dublin, have combined centrifugal microfluidics with absorption spectrophotometry to create an on site phosphate analyzer [33]. Donohue et al. have utilized 3D printing technology to build a phosphate sensing platform based on the yellow vanadomolybdate method [110], and Zhu et al. are looking at using cavity enhancement techniques to perform absorption measurements with limits of detection (LODs) comparable to those of the auto-analyzers [251]. In 2010, Sieben et al. explored the use of tinted absorbance cells [104], [252], [253] to perform *in situ* absorption measurements applied to nutrient sensing. Since then, the Mowlem group at the National Oceanography Center (NOC) UK, has built on the tinted absorbance cell technology to deploy a nitrite sensor on the seafloor at a depth of 170 m in 2015 [118], they have measured nitrate from glacial runoff in Greenland over 14 days in 2017 [107], and have incorporated a nitrate sensor onto an autonomous glider to obtain high resolution measurements in the Celtic Sea in 2018 [35]. Recently, the NOC team have used a phosphate analyzer to identify relationships between nutrients and flow rate in a riverine environment over the course of 9 weeks in 2017 [52], and have also deployed a phosphate sensor for 44 days on an autonomous glider to measure the variability of the nutricline in the North Sea in 2021 [254]. Although the tinted absorbance cell has made it possible to obtain data across a range of deployment environments, it requires the optical electronics of the sensor to be carefully aligned and physically secured to the microfluidic chip via an adhesive, thereby restricting serviceability, easy replacement, and limits reconfigurability. Furthermore, the tinted material inhibits visual inspection for flaws or delamination created during or after the chip manufacturing process. Lastly, the microfluidic devices made from the semi-transparent acrylic cannot be readily adapted to perform other analytical techniques such as fluorescence measurements or cavity ring down spectroscopy (CRDS) that rely on transparent window/optical interfaces.

Here we present a fully automated *in situ* phosphate analyzer that incorporates our previously reported inlaid microfluidic absorbance cell [39], allowing the electronics to be entirely decoupled from the microfluidic chip through use of embedded beam-steering optical components. We interface our novel chip approach to a custom-made and ruggedized sensor instrument with 3-syringe pumps, 10-valves, and 4-optical measurement channels for enabling a wide range of chemical assays. Additionally, the 3 separate syringe pumps and 10 valves provide increased reconfigurability that can allow techniques such as continuous flow analysis (CFA) and flow injection analysis (FIA) [255] to be performed by only replacing the microfluidic chip and modifying the protocol. Furthermore, the transparent windows in the chip enable the ability to perform improved absorption measurements through cavity enhanced absorption spectroscopy (CEAS) and multi-bounce configurations [60]. In this Chapter, the sensor uses the well documented PMB assay, but with the addition of polyvinylpyrrolidone (PVP) to inhibit aggregation, decrease temperature sensitivity, and lower the limit of detection [52], [109], [256]. The temperature sensitivity of the absorbance measurements is determined through 4 sequential calibrations done at even temperature intervals between 5° C and 20° C. A first standalone deployment from a near-shore pier shows data captured over a period of 36 hours, with bottle samples taken for verification. A second deployment on the Stella Maris multi-sensor seabed platform (MSSP), 100 m offshore in the Bedford Basin, Nova Scotia, Canada (44.66° N, -

63.56° W) demonstrates the analyzer's ability to integrate with platforms or vehicles. We anticipate the successful deployment of the fully automated phosphate sensor presented here will permit a readily expandable platform to perform a range of colourimetric chemistries for widespread *in situ* observations by changing the microfluidic chip, reagents, and automation protocol.

6.2. Materials and Methods

6.2.1 Chemical Preparation

All chemicals and reagents were supplied by Fisher Chemical (New Jersey, United States), unless otherwise stated. The PMB assay was prepared as two reagents: an ammonium molybdate solution and an ascorbic acid solution. To prepare the first reagent, 0.3005 g of potassium antimonyl tartrate ($C_8H_{10}K_2O_{15}Sb_2 \cdot 3H_2O$, CAS-No 28300-74-5, Sigma-Aldrich, Missouri, United States) was first dissolved in 100 mL of Milli-Q and set aside. Next, 0.56 g of ammonium molybdate(VI) tetrahydrate ($H_{24}Mo_7N_6O_{24} \cdot 4H_2O$, CAS-No 12054-85-2) was dissolved in 200 mL Milli-Q in a 1 L volumetric flask. After that, 6.73 mL of concentrated sulfuric acid (H_2SO_4, CAS-No 7664-93-9, EMD Millipore, Darmstadt, Germany) was added to the volumetric flask, which was then allowed to cool to room temperature. Lastly, 12.5 mL of the antimonyl potassium tartrate solution was added to the flask, which was then filled to volume with Milli-Q.

The second reagent was prepared by dissolving 10 g of L-ascorbic acid ($C_6H_8O_6$, CAS-No 50-81-7, Sigma Aldrich, Missouri, United States) in roughly 600 mL of Milli-Q in a 1 L volumetric flask. Next, 0.10 g of polyvinylpyrrolidone (PVP) ($(C_6H_9NO)_n$, CAS-No 9003-39-8, 10000 g/mol, Sigma Aldrich, Missouri, United States) was added to the volumetric flask and mixed in by shaking. Finally, the solution was diluted to the 1 L mark with Milli-Q and shaken again to mix.

The 1000 µM phosphate standard stock solution was prepared by dissolving 0.1361 g of potassium phosphate monobasic (KH_2PO_4, CAS-No 7778-77-0) in 1 L of Milli-Q. The remaining standards were prepared by performing a serial dilution of the appropriate portion of the stock solution with Milli-Q. Both reagents for the PMB assay and the phosphate standard were used for 2-3 months with no observable difference in the colour development profiles. The 50 µM copper(II) sulfate dye stock solution was prepared by dissolving 1.2484 g of copper(II) sulfate pentahydrate ($CuSO_4 \cdot 5H_2O$, CAS-No 7758-99-8, Sigma Aldrich, Missouri, United States) in 100 mL of Milli-Q and then shaking to mix. The remaining standards were then prepared by again performing a serial dilution of the appropriate portion of stock solution with Milli-Q.

6.2.2 Microfluidic Chip Fabrication

The substrate for the microfluidic chip (88.9 mm in diameter and 12 mm thick) was made from extruded opaque black poly(methyl methacrylate) (PMMA) (9M001, Acrylite, Maine, United States) inlaid into extruded clear PMMA (0A000, Acrylite, Maine, United States), according to the method documented by Luy et al [18]. A micromill (S103, LPKF Laser and Electronics, Garbsen, Germany) was used to mill the 400 µm deep square channels and other features, and a 50 W laser cutter (Mini Helix, Epilog Laser, Ontario, Canada) was used to cut the chips and inlaid pieces from the larger acrylic sheets. To bond the two halves of the microfluidic chip after the inlaying and milling process was complete, each side was first exposed to chloroform vapour for 45 seconds. They were then slotted into a custom fitting jig before being pressed in a PCB press (Multipress S, LPKF Laser and Electronics, Garbsen, Germany) at a pressure of 625 N/cm^2 and a temperature of 85 °C for 2.25 hours.

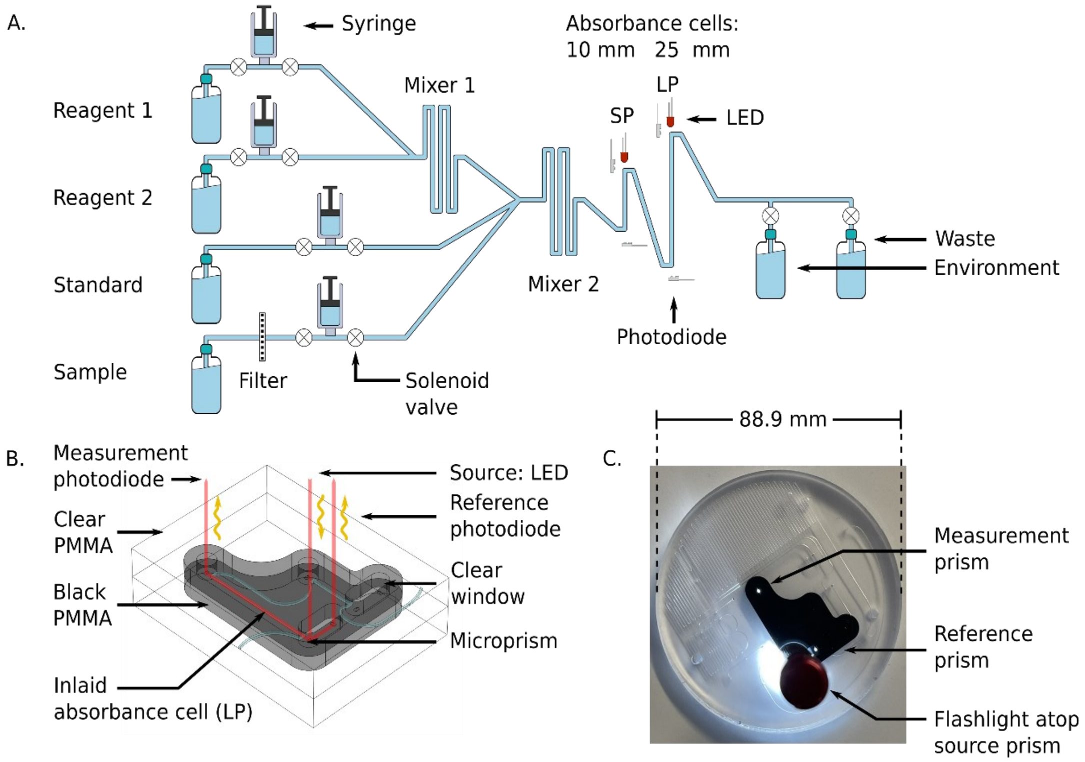

Figure 6.1: A) Fluid flow diagram for the microfluidic chip. Fluid from either the standard or sample is mixed with the two reagents, and the resultant product is analyzed in the two absorbance cells. B) CAD rendering of an inlaid absorbance cell. Microprisms are machined into the clear plastic to direct light from an LED, through the cell, and to a photodiode. Reference photodiodes monitor fluctuations in the light source. C) Photograph of the bonded microfluidic chip. The mixing chamber and fluid ports are milled into the clear plastic, and the absorbance cell is within the inlaid black plastic. Integral optical windows are realized by routing the microfluidic channel across the clear-black PMMA interface. A flashlight is placed atop the source prism to launch incident light down the optical-fluidic absorbance channel, which then shows light reflecting off the reference and measurement prisms associated with the long absorbance cell. Reprinted with permission from *Analytical Methods* [18].

6.2.3 Sensor Description

The underlying analytical technique for phosphate detection is carried out using the microfluidic chip and its integral absorbance cells. Figure 6.1A is a fluid flow diagram highlighting the internal and external processes of the chip. Depending on the stage in the protocol, either the sample or standard syringe is actuated, synchronized with the 2 reagent syringes. The sample is pulled from the environment (seawater) through a 0.45 µm hydrophilic filter membrane to remove larger particulate material and sediment. Filter blockage and clogging is one of the limiting factors for extended deployments, which is dependent on the particulate loading of the environment. However, 1–2-month deployments in marine environments with comparably sized filters has been demonstrated [27, 28]. The syringes for the sample and standard move fluid at a rate of 2 mL/minute, and the two reagent syringes move fluid at a rate of 1 mL/minute but are always actuated together, resulting in a combined reagent flow of 2 mL/minute. The intake valves (to the left side of the syringes) open as the syringes withdraw, and then close before the output valves (to the right side of the syringes) open for the syringes to dispense. The two reagents mix through diffusion in the first serpentine mixer before mixing with the third fluid in the second serpentine channel to realize 4 mL/minute total flow. The mixed fluid is pumped into the two absorbance cells (short path = SP, long path = LP) and flow is then stopped to allow a colourimetric reaction to take place. Afterwards the fluid is displaced by the next stage and dispensed through one of the two waste ports. One port is connected to the waste bag and is intended to capture the used reagents and chemicals during deployments; however, the other port is meant as an outlet when flushing the system either with seawater or during in-lab testing.

Figure 6.1B shows the working principle of the inlaid optical absorbance cell. Incident light from an LED centered at 880 nm and a 60 nm FWHM (MTE8800NK2, Marktech Optoelectronics, New York, United States) is directed by embedded microprisms using total internal reflection (TIR) into the absorbance cell of length, *l*, and again up into a photodiode (TSL257, AMS, Premstaetten, Austria) for detection. The black PMMA attenuates all non-directional light, allowing the photodiode to measure only light that has passed through the absorbance cell. The blank voltage, v_o, is defined as the photodiode output when only reagents or water have been pumped into the cell. The sample voltage, *v*, is the photodiode output when a dye has formed in the cell, either from a standard or a sample reacting with the two reagents. As previously detailed in CHAPTER 2 , the negative logarithm of the ratio of these two voltages determines how much of the initial light has been absorbed. For clarity, the theory and concept of absorbance will be briefly reintroduced here. The absorbance, A, is calculated using the Beer-Lambert law:

$$A = \epsilon l c = -log_{10} \frac{V}{V_o} \tag{6-1}$$

where absorbance is linearly related to concentration, *c*, by the path length, *l*, and the attenuation coefficient, ϵ. In addition to the main detection photodiode, another reference photodiode was used to measure the light intensity reflecting off a second prism directly adjacent to the light source. It is used to monitor and account for fluctuations in the LED intensity due to internal temperature changes and self heating effects in the optical system. The absorbance with the applied reference photodiode correction is:

$$A = -log_{10} \left(\frac{V}{V_o} \frac{r_o}{r} \right) \tag{6-2}$$

where r_o is the voltage measured by the reference photodiode during the blank measurements and r is the voltage measured by the reference photodiode during the sample or standard measurements. There are two absorbance cells in the chip, each with a different length (25.4 mm and 10.4 mm). This helps to expand the dynamic range of the sensor and increase its resilience to bubbles; if one cell is blocked by a bubble, the other will still function.

One concern for absorbance measurements performed in a real environment could be that the light transmission is affected by fouling of the windows or particulate matter in the sample. However, the instrument shown here has a 0.45 μm filter on the intake, which is small enough to prevent most microbes from entering the fluid channel and forming biofilms on the optical interfaces. In the case where finer particulate matter is able to pass through the filter, it could cause light scattering in the absorbance cell, but any scattering will be limited to Mie scattering or Rayleigh scattering. However, the Beer-Lambert law compares samples to blank measurements from the sample environment. In this way, the added scattering from particulate matter is accounted for in the end calculation, which is one of the reasons why absorbance measurements are so robust and are favored for ocean variable monitoring.

Figure 6.1C is a photograph of the completed microfluidic chip, with the inlaid absorbance cells and mixing channels fully integrated. The fluid ports and mixing serpentines are milled into the clear plastic to make it easier to visually inspect the device for collapsed channels or flaws resulting from the manufacturing process. The transparent material also makes it possible to see when and where bubbles have entered the system during laboratory testing. The channels and absorbance cells have square profiles, with 400 μm depth and width. The total fluid volume on the chip, including the 13 μL dead volume in each of the 10 valves, is approximately 450 μL. Of the total volume, roughly 34 μL of sample is required to reach the mixer 2 Y-junction in Figure 6.1A. However, since the standard and reagent fluids are not changing between measurements, the only relevant dead-volume on-chip is the sample-to-waste fluid path, which is 253 μL. This value is doubled in the automation protocol to provide a minimum flushing volume whilst avoiding crosstalk between samples.

Figure 6.2A shows the Stella Maris multi-sensor seabed platform (MSSP) with the phosphate analyzer integrated as one of the sensors. The MSSP is a submersible tripod testbed that supports over 20 different marine sensing instruments, with a subsea cable that provides power and a communications link with the shore station. The reagents and waste are contained in four separate fluid bags, three 100 mL bags for reagents 1 and 2 and the 2 μM on-board standard, while the waste was a 1 L bag. All reagent bags were housed in a perforated aluminum cannister. Both the sensor and reagent cannister are physically mounted to the frame of the Stella Maris, and communications and power are handled via the platform itself. The data is stored locally on an SD card in the sensor in memory mode, and, also transmitted in real-time to the shore via ethernet. To accomplish this, an RS232-to-ethernet hub is integrated within the tripod MSSP and is accessible through a subsea ethernet connection. This provides constant access to the sensor and data via the MSSP cabin onshore. Figure 6.2B is a rendering of the internal components of the phosphate sensor. There are three independently actuatable syringe pumps in total: one for reagent syringes, one for a standard and one for the sample intake. The pumps are comprised of four syringes actuated by three stepper motors threaded into moving plates on guide rails;

the two reagent syringes are coupled to the same stepper motor. Limit switches are used to indicate when a syringe is at the end of its stroke. Three pumps provide extensibility and flexibility for a variety of chemical protocols and microfluidic devices compared to prior work with a single actuation mechanism [107]. Fluid routing is accomplished with the 10 solenoid valves (LFN series, Lee Company, Connecticut, United States), along with their associated printed circuit board (PCB), housed in a separate compartment at the base of the sensor that can be oil filled for higher pressure deployments. A custom penetrator SubConn cable (MacArtney Canada Ltd.) establishes communication and power between the upper valve compartment and the lower main compartment. The microfluidic chip is sandwiched between the two compartments and fluidically interfaces with each cannister via O-ring face seals. The entire sensor is housed in an anodized aluminum pressure casing, and communications and power are handled using a second SubConn cable. An external cannister houses the reagents, standards, and waste bags. Fluid connections are accomplished using 1/16 in. inner diameter poly-tetrafluoroethylene (PTFE) tubing and ¼-28 polyether ether ketone (PEEK) connectors (P-359X, IDEX Health and Science, Washington, United States). Power is supplied by either an optional third cannister containing 12 D-cell batteries, not shown, or from an external platform such as the Stella Maris.

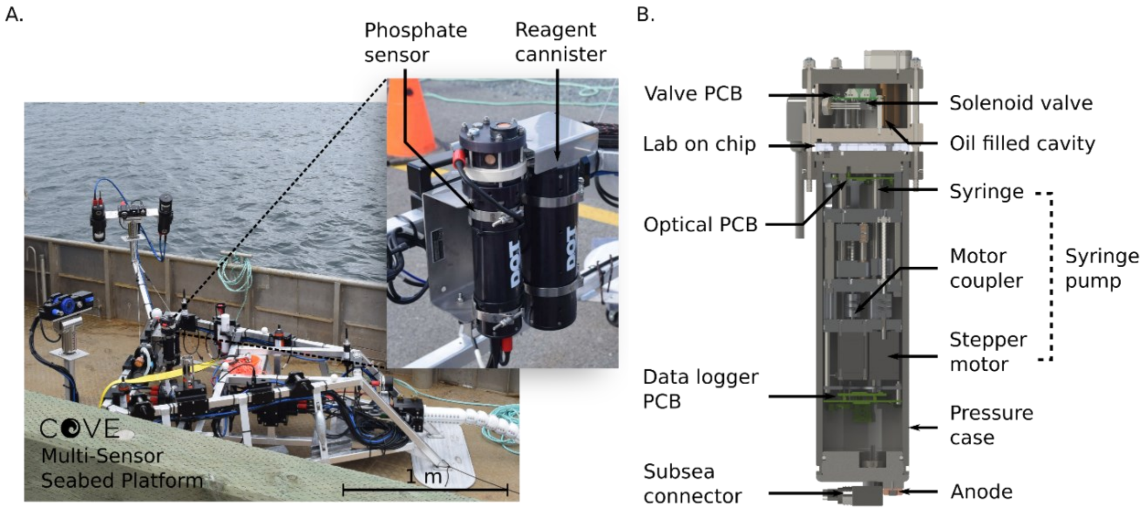

Figure 6.2: A) Stella Maris sensor platform on-board the ship prior to deployment in the Bedford Basin. Inset photograph: phosphate analyzer and reagent cannister mounted to the frame of the Stella Maris. B) Cross section view of the interior of the phosphate sensor. Fluid is pulled and directed into the lab-on-chip by stepper motor-actuated syringes and active solenoid valves. Valve control, data logging and optical control are handled using three separate electronics boards. Reprinted with permission from *Analytical Methods* [18].

The sensor electronics were controlled by three custom made PCBs with custom firmware and software. The automation, data collection and logging was accomplished with firmware written in C++, run on the data logger PCB. The optical PCB handled the stepper motors and optical elements; the LED voltages were controlled using a constant current driver on the optical board, and the measured photodiode voltages were streamed to the data logger PCB and stored on a memory card. The valve PCB was controlled by the data logger board through an RS-232 interface. The data logger also communicated to the outside world via RS-232 and ethernet. The sensor was designed to accept voltages from 7-24 VDC, and nominally consumed 0.1 A during the optical measurements and 1.2 A during pumping. The entire sensor was designed for operation to depths up to 450 m.

6.2.4 Sensor Calibration Procedures

The optical system of the sensor, consisting of the LEDs, absorbance cells and photodiodes, was first tested on its own by creating a calibration curve using copper (II) sulfate dye. This first step was necessary to verify that the system works reliably without the added uncertainty of reaction kinetics and mixing ratios that are introduced when using the phosphate assay. Copper(II) sulfate was chosen as a dye because it absorbs in the infrared region and has an absorption peak that overlaps with the emission peak of the 880 nm LED. The absorbance and transmission spectra for the dye and LED can be found in APPENDIX C.

To create the dye calibration curve, five standards were made ranging in concentrations from 31.25 μM to 500 μM using a serial dilution. Each standard was pumped into the cell for measurement three times, each time followed by a flush cycle. For each concentration, a blank measurement of only Milli-Q water was taken before the triplicate readings. The average voltage from the dye measurements and each preceding blank measurement was used to calculate the absorbance of each concentration. Starting with three blanks of pure water, the order in which the fluids were injected through the standard port was:

Step	Sample	Repetitions
1.	Blank	1
2.	500 μM	3
3.	Blank	1
4.	250 μM	3
5.	Blank	1
6.	125 μM	3
7.	Blank	1
8.	62.5 μM	3
9.	Blank	1
10.	31.25 μM	3

Voltage data from both the short path length (SP) and long path length (LP) were collected, and the last 5 seconds of each blank and sample was averaged to produce the calibration curve.

After the stable dye tests, the phosphate assay was performed using premade standards for calibration. Six phosphate standards ranging from 0.2 µM to 10 µM were prepared by serial dilution, and the two reagents for the PMB assay were prepared in the method previously described. To generate the calibration curve, each standard was pumped through the standard port into the cell for measurement three times, each time followed by a flush cycle. Three blank measurements were taken before each set of triplicate standard readings. In this case, the blanks were entirely Milli-Q water, with no reagent. The standards were pumped into the absorbance cell at a 1:1 ratio with the two-part reagent solution (1:1:2, R1:R2:S) and allowed to diffusively mix and undergo colour development for 10 minutes before being flushed out. The absorbance of each standard measurement was calculated using the averaged voltage from the last 5 seconds of the colour development and the averaged voltage from the last of the three blank measurements. The measured absorbances of each standard were plotted against their concentrations to determine the attenuation coefficient of the system. Starting with three blanks of pure water, the order in which the fluids were injected through the standard port was:

Step	Sample	Repetitions
1.	Blank	3
2.	10 µM	3
3.	Blank	3
4.	5 µM	3
5.	Blank	3
6.	2 µM	3
7.	Blank	3
8.	1 µM	3

9.	Blank	3
10.	0.5 µM	3
11.	Blank	3
12.	0.2 µM	3

Voltage data from both the short path length (SP) and long path length (LP) were collected, and the last 5 seconds of each blank and colour development phase were averaged and plotted.

The above sample handling for calibration was fully automated using the syringe pumps and solenoid valves in the sensor itself for fluid control, as well as an external 10-port selector valve (Cheminert C65 series, VICI, Texas, United States) for switching between standards and flushing. The selector valve linked the eight standards via PTFE tubing to the standard port on the sensor. The two reagent reservoirs were directly connected to the reagent ports on the sensor using PTFE tubing.

6.2.5 Temperature Sensitivity Analysis

To characterize the effects of temperature on the sensor performance, the entire unit, along with the reagents and standards, were submerged in a temperature-controlled water bath. A recirculating cooling unit (NESLAB RTE-7, Thermo Scientific, Massachusetts, United States) was used to fix the bath temperature at 5, 10, 15 and 20° C. At each of the four temperatures, a three-standard calibration was performed using the same triplicate method as the room temperature calibration. However, for this test, the selected standards were 10 µM, 2 µM, and 0.5 µM PO_4^{3-}, to cover a wide range. The bath temperatures were measured using both a standard laboratory glass thermometer with 0.5° C precision and the built-in

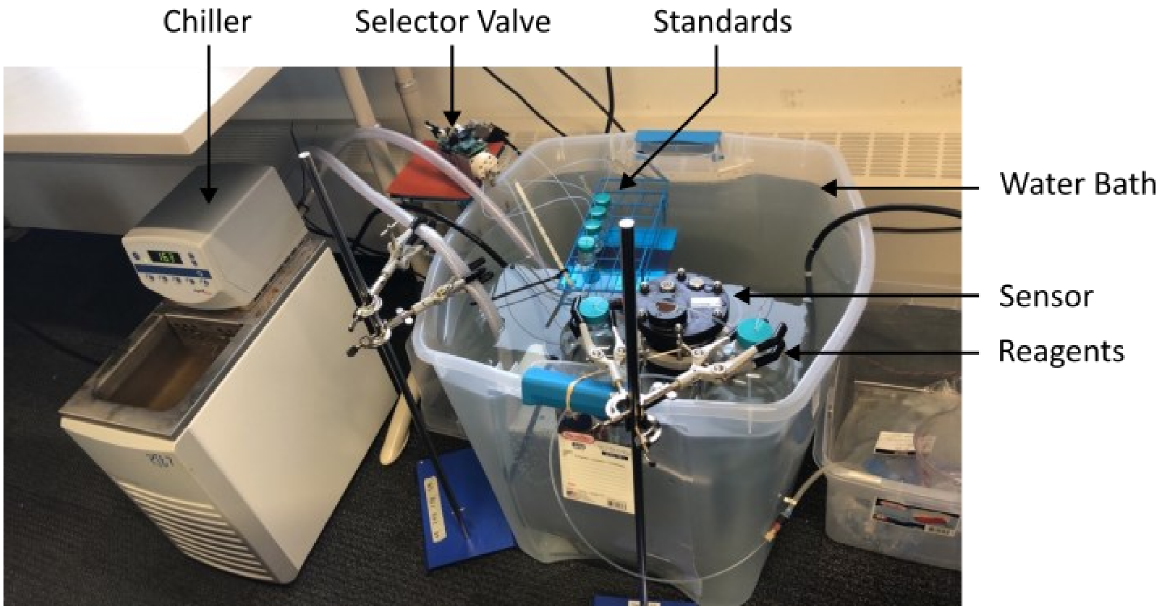

Figure 6.3: Setup for temperature sensitivity calibrations. The sensor, reagents and standards are all mostly submerged in a temperature-controlled water bath.

temperature sensor on the chilling unit itself. The setup for this set of calibrations is shown in Figure 6.3.

6.2.6 *In situ* Verification and Deployments

To test the repeatability and precision of the measurements in an unchanging *in situ* environment, the unit was fully submersed in a tank of water that had an unknown baseline phosphate concentration (tap water). First a blank measurement, and then three consecutive sample measurements, each preceded by a flushing cycle were taken and analyzed.

The sensor was then deployed at a depth of 6 m off a pier in the inlet to the Bedford Basin in Nova Scotia, Canada for 36 hours. Concurrent bottle samples were taken from the water next to the instrument at five different times using a Niskin bottle and were then processed and analyzed in duplicate in a benchtop auto-analyzer (Skalar San++). The sensor was then deployed for a second time on the Stella Maris, 100 m offshore and 9 m deep, again in the inlet to the Bedford Basin.

The sampling protocol and fluid usage volumes for the pier deployment was as follows. First, the system was flushed with 0.5 mL of the standard (2 µM PO_4^{3-}). Next, 0.25 mL of each reagent was injected into the system. After a 10-minute wait, the last 5 seconds from the measurement photodiode voltage was recorded to use as the blank voltage of the standard. After that, 0.5 mL of the standard, along with 0.25 mL of each reagent was injected and allowed to mix and react for 10 minutes to allow dye formation to occur. The voltage from the last 5 seconds was recorded and used as the sample voltage of the standard. This step was then repeated once to ensure there was no drift or carry over in the standards. The system was then thoroughly flushed with 0.5 mL of seawater, and monitored for 10 minutes, providing a blank measurement for the seawater sample. This step was then repeated to ensure there was no crosstalk between samples. Next, 0.5 mL of seawater and 0.25 mL of each reagent (1 mL total fluid) was injected into the cell and given a 10-minute reaction time. The last 5 seconds of the measurement photodiode voltage was recorded to use as the sample voltage. This step was repeated 10 times, generating 10 sample measurements and then the entire cycle was restarted. The calibration curve generated in the lab was used to convert the measured absorbances of the samples and standards into phosphate concentrations from the field deployments.

The sampling protocol for the MSSP deployment was the same as for the pier deployment, but with the fluid volumes increased. The seawater flushes were 3 mL instead of 1 mL to be certain of no crosstalk or sampling smearing, which proved to be unnecessary as shown in the results section. Likewise, the blank for the standard measurements also used 3 mL of fluid. The fluid volumes for both the sample measurements and the standard measurements used 3 mL of sample/standard and 3 mL of mixed reagent (1.5 mL of each reagent). Other than the differences in volumes, the automated protocol remained identical to the pier deployment.

6.3. Results and Discussion

The optical subsystem was verified using a series of stable copper (II) sulfate mixtures with varying concentrations to evaluate the measured absorbances of the complete system. The raw voltage measurements for each standard and blank are displayed in the top panel of Figure 6.4. The plot shows one blank measurement, indicated by the grey shaded regions, for every three copper sulfate measurements. The noisy periods preceding each voltage plateau (more clearly displayed in the long path cell) for the blank and sample measurements are the result of the fluid being displaced during pumping. The processed and averaged voltage data used to generate the calibration curve can be found in Figure 6.5. The bottom left panel of Figure 6.4 shows the calibration curve generated from the voltage data. Both the long path and short path length absorbance cells produced the expected Beer-Lambert linear result, each with an R^2 value over 0.99 and root-mean-square-error (RMSE) values of 0.23 and 0.20 mAU for the short and long paths respectively. The bottom right panel is a residual plot for the linear regression of both path lengths, short and long. At the lower concentrations (125 μM and lower), the spread on the residuals begins to increase presumably due to the weighting of the linear fit. However, the distribution of residuals is random and thus indicates no detectable systematic errors.

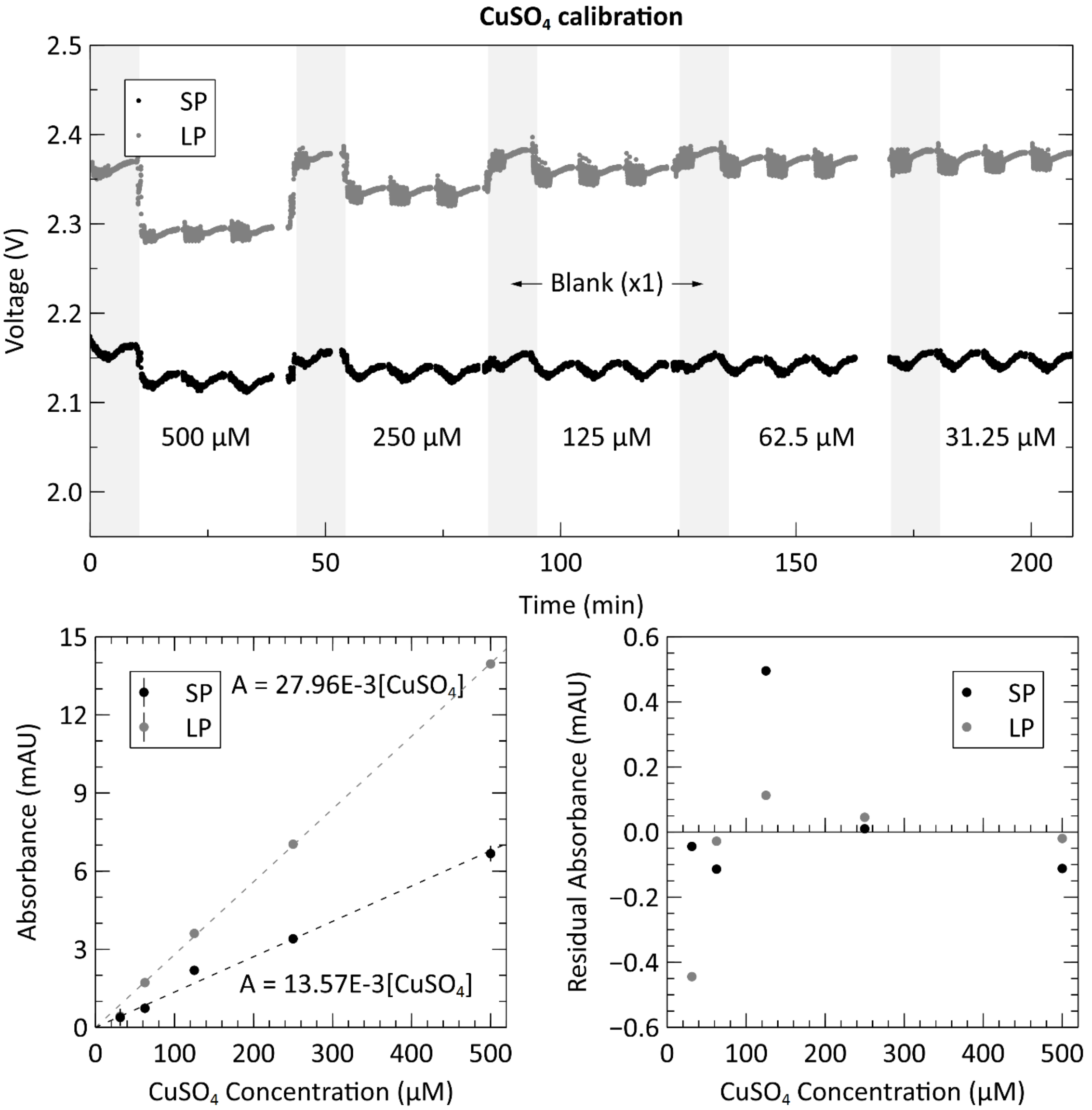

Figure 6.4: Top: Raw voltage from analyzing three repetitions of each of the five copper (II) sulfate (CuSO4) dye concentrations (ranging from 31.25 – 500 µM), with a blank measurement (shaded grey regions) between each new concentration. Data from both the short path length (SP = 10.4 mm) and long path length (LP = 25.4 mm) absorbance cells are displayed. Bottom Left: Calibration curve from the triplicate measurements of the $CuSO_4$ calibration. The absorbance values are determined from the voltage measurements shown in the top panel. Bottom Right: Residual plot of the linear regressions for the long and short path lengths. Reprinted with permission from [18].

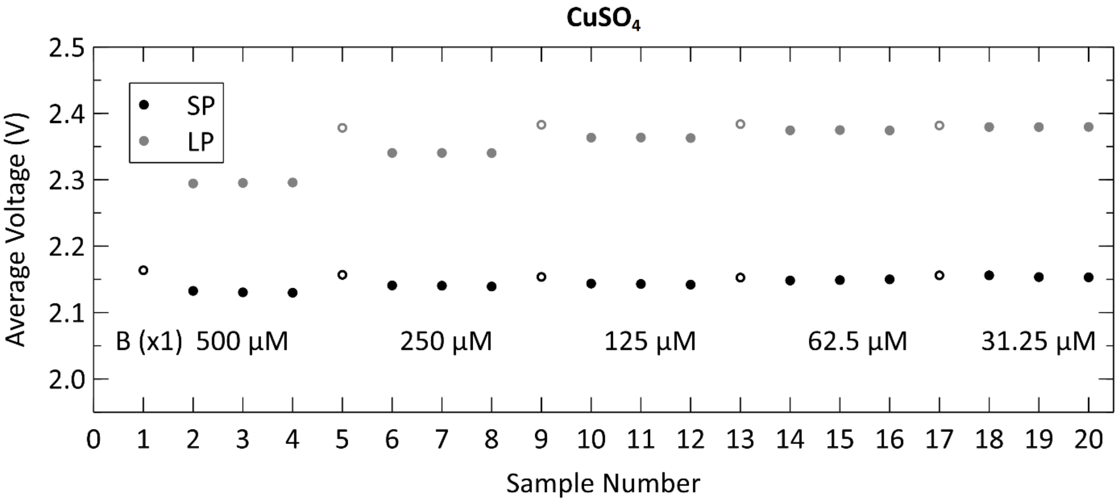

Figure 6.5: Averaged voltage data from the CuSO4 calibration curve for both the long path (LP) and the short path (SP). Each concentration is measured three times, preceded by three blank measurements (represented by unfilled data points) to displace the previous concentration of dye. Reprinted with permission from [18].

Next, we proceeded to evaluate the sensor by performing the phosphate assay on-chip with known premade standards. Figure 6.6 shows the calibration data acquired from the automated system when supplying the sensor with six phosphate standards ranging from 0.2 µM to 10 µM. The top panel shows the measured raw voltages for the three blank measurements, indicated by the grey shaded regions, and the three standard measurements for each concentration of PO_4^{3-} from both measurement cells. See Figure 6.7 for the processed and averaged voltage data. The concentrations displayed in the top panel are the actual concentrations of the prepared standards, before mixing, and fed directly into the sample intake port. The concentrations shown on the horizontal axes of the two bottom panels are the PO_4^{3-} concentrations in the absorbance cell, after being mixed at a 1:1 ratio with the reagents. The calibration curves were created by calculating the absorbance of each concentration using the triplicate standard measurements and the last of each blank

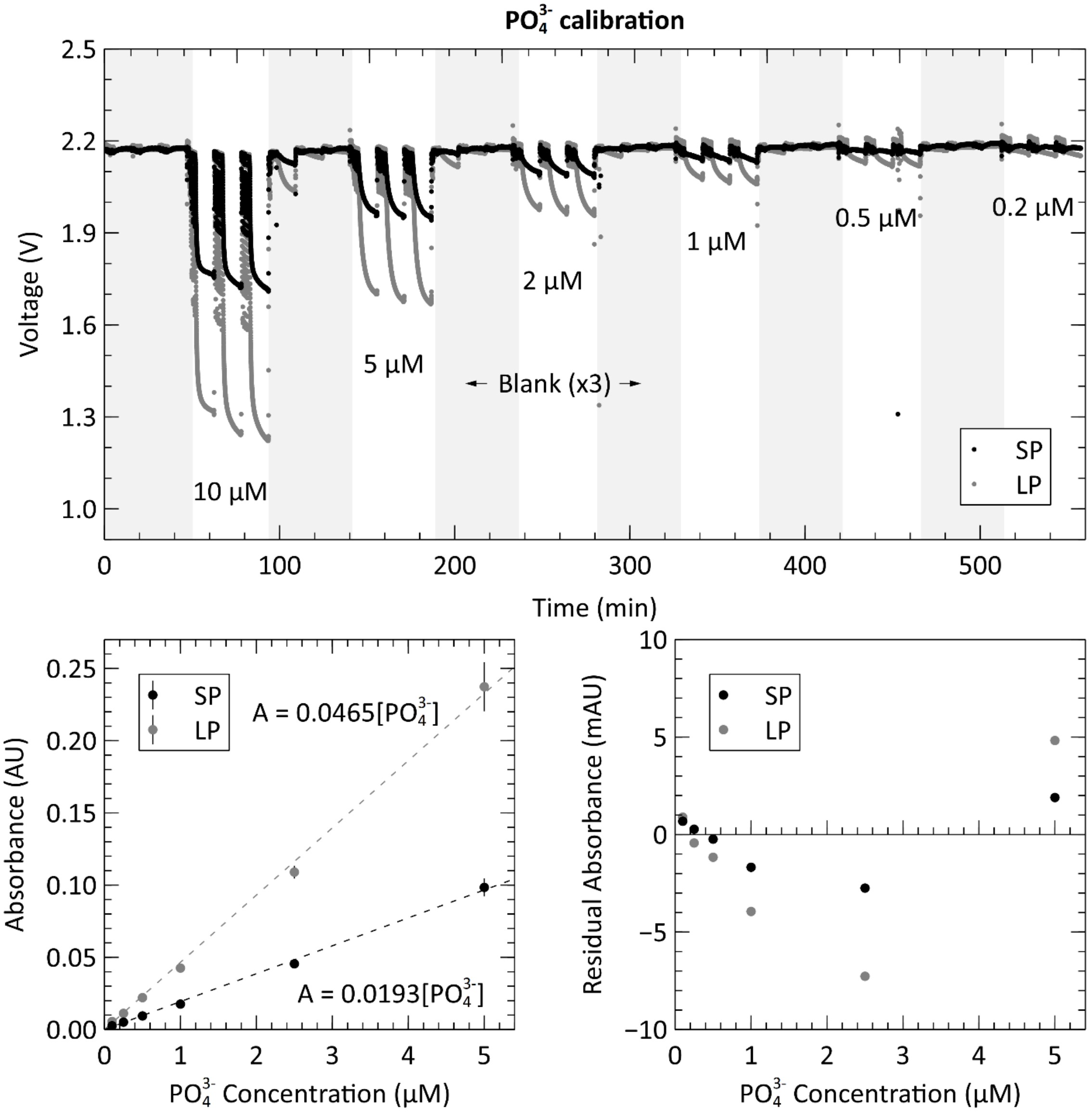

Figure 6.6: Top: Raw voltage from analyzing three repetitions of each of the five phosphate (PO_4^{3-}) standard concentrations (ranging from 0.2 – 10 µM), with three blank measurements (shaded grey regions) between each new concentration. Data from both the short path length (SP = 10.4 mm) and long path length (LP = 25.4 mm) absorbance cells are displayed. Bottom Left: Calibration curve from the triplicate measurements of the PO_4^{3-} calibration. Bottom Right: Residual plot of the linear regressions for the long and short path lengths. Measurements conducted at room temperature or 21-23°C. Reprinted with permission from [18].

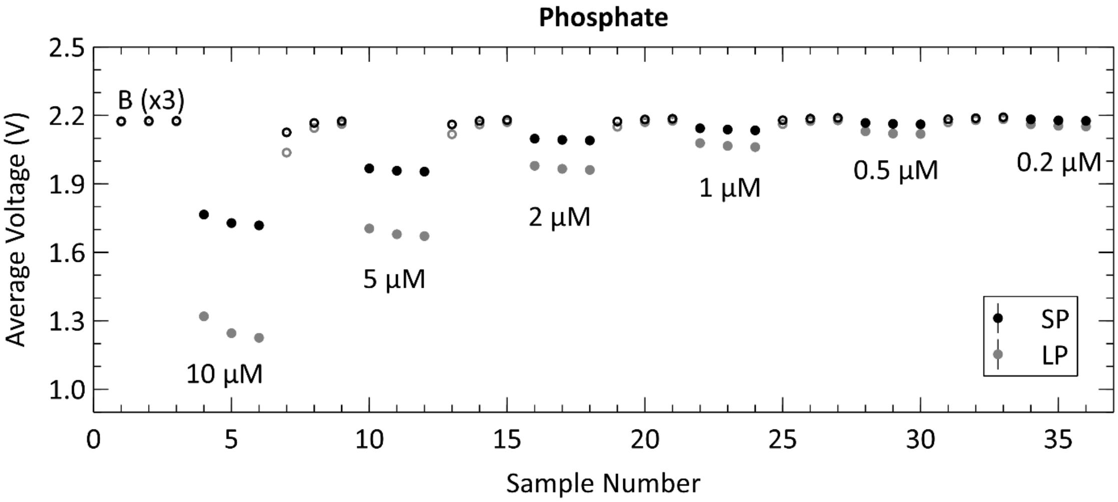

Figure 6.7: Averaged voltage data from the PO_4^{3-} calibration curve for both the long path (LP) and the short path (SP). Each standard is measured three times, preceded by three blank measurements (represented by unfilled data points) to displace the previous standard. Reprinted with permission from [18].

measurement. The slopes of the curves are 0.0465 AU μM^{-1} and 0.0193 AU μM^{-1} for the long and short path lengths, respectively. By dividing out the lengths of each absorbance cell, the attenuation coefficients of the long and short paths are calculated as 0.0183 cm^{-1} and 0.0186 cm^{-1}. This is higher than the coefficients reported by Clinton-Bailey et al., who reported 0.00584 – 0.00612 cm^{-1} [19] for the PMB assay modified with 0.01% PVP. This large difference is mostly due to the difference in how the concentrations are reported. Clinton-Bailey et al. reports the concentration of the standard before mixing at 1:1:1 ratio with the two reagents, whereas we report it after mixing. Therefore, their slope needs to be multiplied by three yielding 0.01752 cm^{-1} – 0.01836 cm^{-1}, showing that the coefficients are very similar. However, there are also other considerations, such as the difference in the selected reaction times. We use a 10-minute hold time to allow for more colour development and increased sensitivity, whereas Clinton-Bailey et al. use a 5-minute reaction time for increased sampling frequency. The 10-minute reaction time in the short

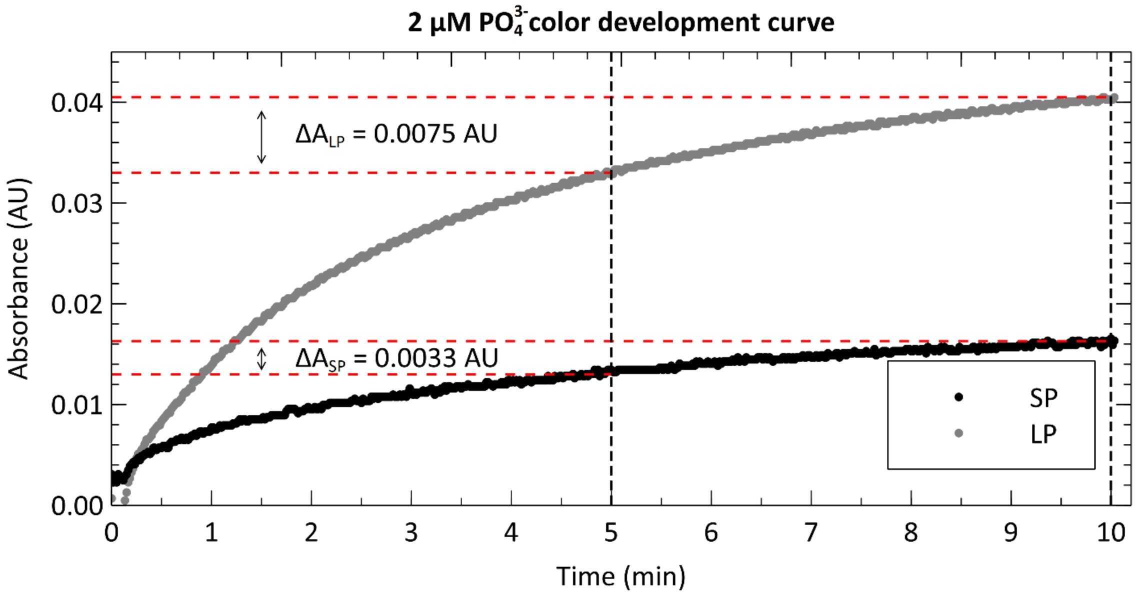

Figure 6.8: Absorbance measurements from the colour development of a 2 µM standard as it reacts with the two reagents. The absorbances at 5 minutes and 10 minutes respectively are indicated by the dashed red lines for both the short and long path length. The increase in absorbance between the 5 minute and 10 minute point is noted. Reprinted with permission from [18].

path accounts for a 25 % increase in the measured absorbance of a 2 µM standard when compared to a 5-minute reaction time. Please see Figure 6.8 for a plot of the colour development curve. A second important difference is that we use an LED centered at 880 nm, versus 700 nm in the work by Clinton-Bailey. A spectral analysis of a 2 µM standard revealed that the measured absorbance (averaged over a 5 nm window) at 880 nm was 133 % of the measured absorbance at 700 nm. Furthermore, the emission peak of our 880 nm LED has a 60 nm FWHM that is wider than the 700 nm LED with a FWHM of 21 nm. These details indicate that our measured coefficients should be higher than those reported by Clinton-Bailey et al. by 166 %; however, the photodiode used by both authors is roughly 50 % as sensitive at 880 nm as it is at 700 nm, which may explain why the final coefficients are comparable. Despite the discrepancy between our attenuation coefficients and the reported literature values, the calibration curves were linear, with R^2 values of 0.99 for both path lengths and RMSE values of 1.56 and 3.95 mAU for the short and long paths respectively. The bottom right panel of Figure 6.6 shows the residual plot of the linear regression for the measurements made in the two absorbance channels. The pattern shows that the residual error is very low at the lower concentrations, which is likely due to the addition of the 0.01% PVP to the reagents. In our previous trials that did not include PVP (data not shown), the residuals observed below 1 µM showed that the results were not linear, nor repeatable between successive tests. The residual analysis also indicates that the 10 µM (5 µM in the cell) measurement might be skewing the regression upwards, because most of the middle-concentration measurements (0.25 – 2.5 µM) are below the linear fit. The 10 µM data set in the long path length also has the largest error of the concentrations. Nevertheless, the calibration produced the expected linear relationship and showed a dynamic range between 0.2 to 10 µM with relative standard deviations (RSDs) ranging

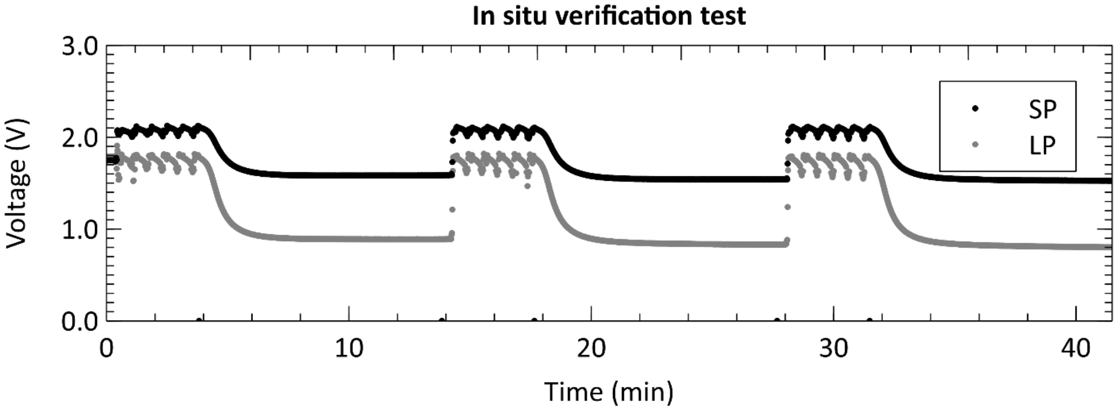

Figure 6.9: Raw voltage data from the *in situ* verification test. Voltage from both the short path (SP) and long path (LP) is displayed for the 3 consecutive sample measurements. Reprinted with permission from [18].

from 12.1 % to 3.45 %, respectively. To further quantify the repeatability of the sensor, an *in situ* verification test was performed on tap water, the results of which are displayed in Figure 6.9. The RSDs of the unknown concentrations from these three measurements were 1.48 % in the long channel and 1.06 % in the short channel, demonstrating excellent precision on bench and underwater.

To fully characterize the sensor's performance, we calculated the limit of detection (LOD) and limit of quantification (LOQ) from the 18 blank measurements taken during the preceding calibration. For a linear regression, the three-sigma LOD is defined as three times the standard deviation value of the blank baseline noise [257]. The LODs for the short and long paths were therefore calculated to be 0.33 and 0.29 mAU, corresponding to 16.9 and 15.2 nM [PO_4^{3-}]. The LOD metric is useful as a quantification for the resolution of the sensor, while the slope of the calibration curve determines its sensitivity. The LOD is a measurement of the systematic noise in the unit, which determines the precision of any one given measurement, and the sensitivity will inform how that translates into real concentration resolution. A more practical metric for the minimum measurable value for the sensor is the limit of quantification, which is defined as ten times the standard deviation value of the blank baseline noise for a linear regression, and was calculated as 1.09 and 0.98 mAU, corresponding to 56.5 and 50.8 nM [PO_4^{3-}] for the short and long paths, respectively.

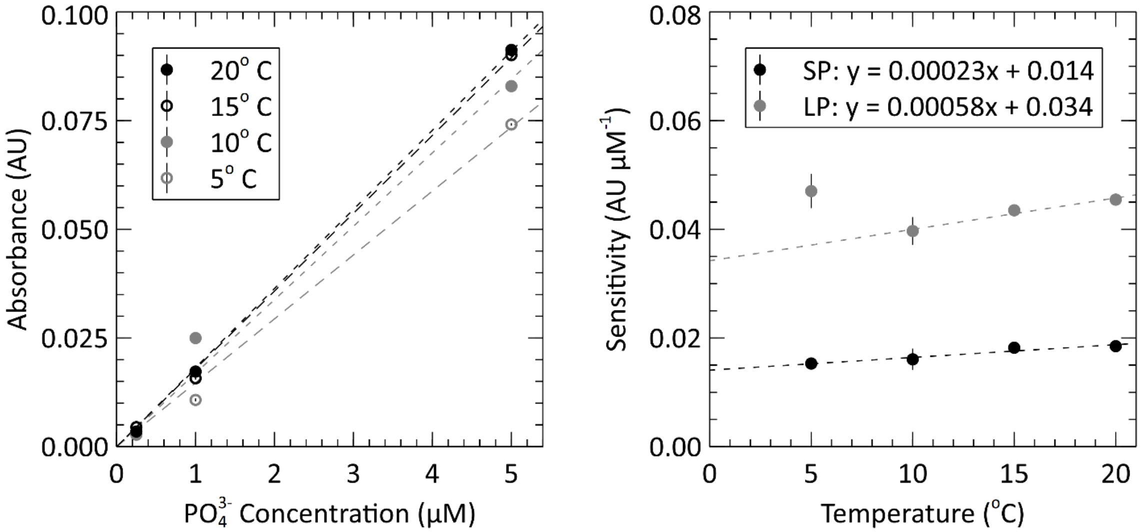

Figure 6.10: Left: *In situ* sensor calibration curves for the short path length at four temperatures between 5°C and 20°C. Each test was done using a 10 µM standard (5 µM in the cell), a 2 µM standard (1 µM in the cell) and a 0.5 µM standard (0.25 µM in the cell). Right: Temperature sensitivity analysis of the sensor; where, linear relationship describes the absorbance measurements of each flow cell changes with temperature. The 5°C point on the long path length data was omitted from the fit. Reprinted with permission from [18].

The submersible lab-on-chip phosphate sensor presented thus far shows that it performs well on the bench, but it is intended to be deployed in marine environments. As such, calibrations like that of Figure 6.6, were performed at the expected environmental water temperatures. The left panel of Figure 6.10 contains the short path calibration curves resulting from our temperature dependence study. Each of the four curves represent a calibration done at a different set temperature (5, 10, 15 and 20° C). The average value and standard error of each slope was calculated and plotted in the right panel of Figure 6.10 to show the sensitivity change with temperature. The slopes of each sensitivity curve are 2.3×10^{-4} and 5.8×10^{-4} AU×(µM °C)$^{-1}$ for the short and long absorbance cells, respectively. When the path lengths are divided out, the sensitivities for each cell become 2.21×10^{-4} and

2.28×10^{-4} AU×(µM °C cm)$^{-1}$. These sensitivities are slightly higher than the slopes reported by Grand et al., who measured 1.46×10^{-4} AU×(µM °C cm)$^{-1}$ when the path length is divided out [20]. The different reaction times and absorbance peaks are the likely source of the discrepancy. All three of the measurements done at 5° C in the long path were omitted from linear fit as outliers. It is suspected that a bubble was trapped in the long absorbance cell for the duration of the 5° C triplicate measurements, causing the absorbances to measure higher than they would have otherwise. The data from the short path does not show this outlying behavior, which further supports the idea that a bubble was impeding the light path in the longer cell. This also punctuates the value and robustness provided by having multiple absorbance cells. Nevertheless, the linear regressions from the sensitivity measurements of the two absorbance cells had R^2 values of 0.92 and 0.97 and RMSE values of 0.38 and 0.44 mAU µM^{-1} for the short and long cells, respectively.

Finally, we proceeded to deploy the fully lab-characterized phosphate sensor in marine environments. The three panels of Figure 6.11 show the phosphate concentration measurements made during the two *in situ* deployments, one at a local pier and one on the MSSP subsea platform, described in the methods, as well as standard measurements taken during the platform deployment. The concentrations were calculated from the measured absorbance by using the slope of the calibration curve generated in the laboratory as a conversion factor, i.e. the slopes in Figure 6.6 and Figure 6.10. The gaps in the data displayed on the two plots in Figure 6.11 are a result of the previously described sampling protocol. They represent the times when the sensor was making blank and standard measurements and therefore could not make sample measurements. The temperature logged on the sensor itself was used to determine the appropriate sensitivity according to the temperature dependence characterization from Figure 6.10. During the pier deployment in the top panel, manual bottle samples were taken and analyzed in an independent laboratory, shown with 'x' markers in Figure 6.11, to validate the sensor readings reported. Except for the first bottle sample, the phosphate concentrations measured by the auto-analyzer for the pier deployment are all within 100 nM of the closest sensor measurements, with the average discrepancy being 42 nM. Overall, the average percentage of difference between the two methods was 27.7%, comparing manual sample and autoanalyzer versus *in situ* lab-on-chip sensor, for this low concentration range. During the first bottle sample acquisition, the Niskin bottle hit the seabed, likely disturbing the sediment, and releasing phosphate into the surrounding water. This is the probable explanation for the large difference (177 nM) between the auto-analyzer measurement and the sensor measurement at the time of the first bottle sample. All other bottle samples were taken without contacting the ground. The bottom panel shows the measured concentration of a 1.97 µM standard fluid over a 36- hour period on the MSSP platform. There is a gradual increase in measurement value until the measurements plateau for around 20 hours. After the 20 hour point, the measurements begin to deviate from the plateau point, which is thought to be a result of depleting fluid in the standard reservoir. However, prior to that point, the measurements show self consistency although they are consistently reporting higher than the prepared concentration, as they had an average measured value of 2.09 µM with a standard deviation of 0.21 µM, which is a relative standard deviation of 10 %.

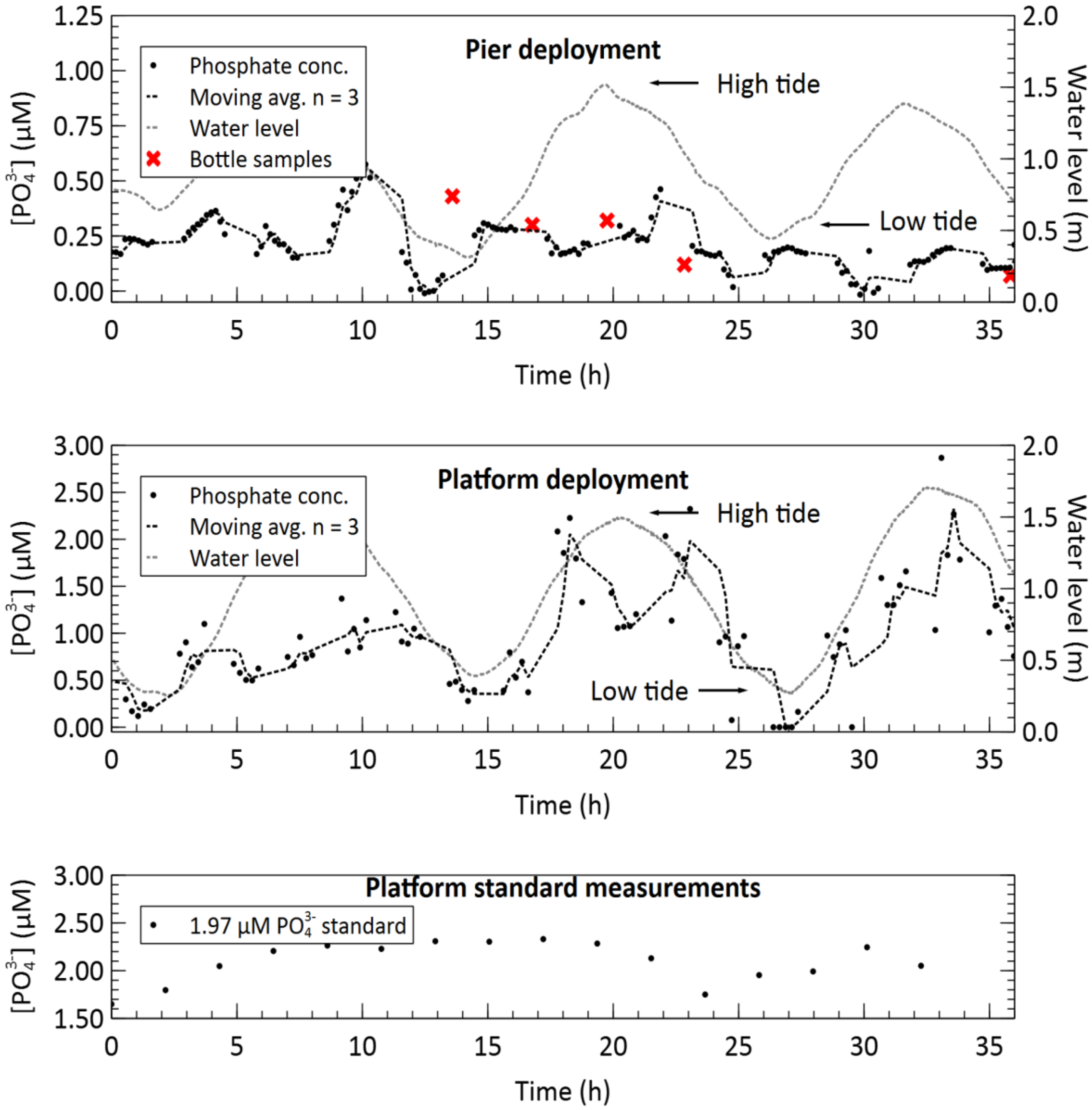

Figure 6.11: Top: *In situ* phosphate concentration measurements from a near-shore pier at a depth of 6 m. Concurrent bottle sample measurements are plotted alongside the sensor measurements at five different points in time. The tidal cycle is overlaid to show the mixing effect close to shore. Middle: *In situ* phosphate concentration measurements from a multi-sensor seabed platform (MSSP), 100 m offshore and 9 m deep in the inlet to the Bedford Basin. The tidal cycle is overlaid to show the mixing effect in the deployment region. Bottom: Standard measurements taken over a 36-hour period during deployment on the MSSP. The three plots displayed here show that the unit is field capable and can track the tidally influenced phosphate variations.

For both deployments, the water level, measured by the nearby Bedford Institute of Oceanography tide gauge at station BIO 00491, is overlaid on the deployment plots to highlight the correlation between the semi-diurnal tidal cycle and phosphate concentration. A correlation coefficient of 0.59 was found between the measured phosphate concentration and the water level for the platform deployment, indicating a moderate positive correlation. Figure 6.12 is a plot of the phosphate concentration versus water height, with the residuals to indicate no systematic measurement error. Furthermore, the magnitudes of the measured phosphate concentrations increase during a water level transition. The trend is observable in the pier deployment data in the top panel and in the MSSP deployment data in the bottom panel. The inlet to the Bedford Basin is a shallow, less than 20 m deep region, known as the "narrows" and is subject to strong currents during the ebb and flow phases of the tide [258]. This leads to turbulent vertical mixing, in which nutrient-rich water from the depths of the Scotian Shelf mixes with the surface waters during the incoming tide, and nutrient-rich runoff water from the Basin mixes during the outgoing tide [259]. This can explain the phosphate concentration profile observed during both deployments, in which the nutrient concentrations peak when the water current in either direction is strongest. However, further long-term deployments, potentially with multiple sensors positioned around the basin, are required to verify these findings. The Bedford Institute of Oceanography has done a thorough analysis of the seawater matrix in the Bedford Basin [260], including weekly phosphate measurements carried out using the blue method on the Skalar SAN ++ Autoanlayzer. In doing so, they have demonstrated that the phosphomolybdenum blue

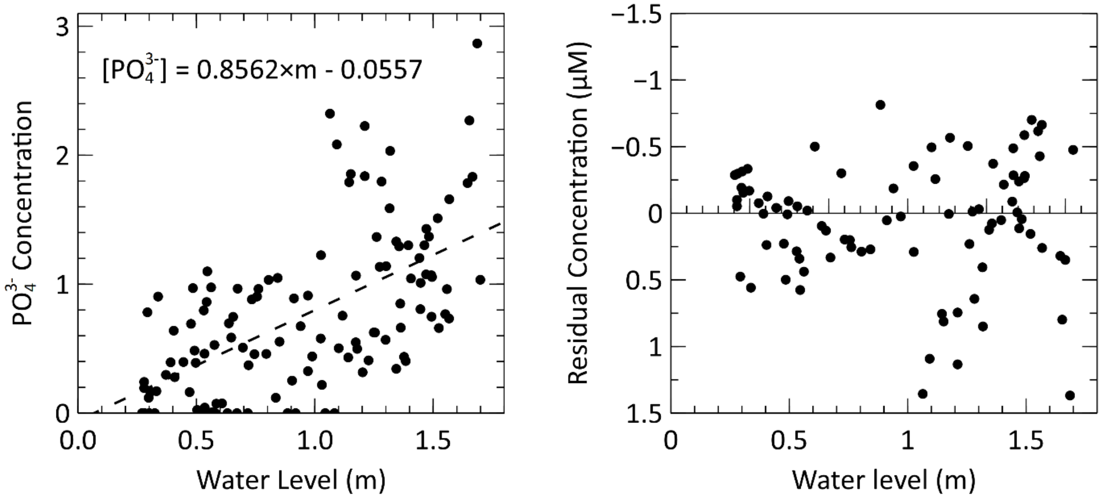

Figure 6.12: Measured concentration data from the MSSP deployment plotted against the water level measured by the Bedford Institute of Oceanography. A linear correlation coefficient of 0.59 was determined from the data. The right panel shows that the residual concentrations randomly distributed, indicating no systematic error in the measurements. Reprinted with permission from [18].

method is valid for the Bedford Basin, despite possible matrix effects or interferences in other bodies of water. Our future plans are to collect multi-parameter measurements to extract the necessary metadata for contextualizing nutrient concentrations with other biogeochemical measurements such as salinity, irradiance, nitrate, and chlorophyl-a, across a range of marine environments.

6.4. Conclusions

Robust, submersible, and fluid-efficient nutrient sensors are required if we are to improve our understanding of nutrient dynamics and fluxes in coastal regions. Here, we have presented a microfluidic phosphate analyzer capable of making precise *in situ* measurements, with less than 1.5 % RSD underwater, that cross-correlate within 42 nM [PO$_4^{3-}$] to the measurements performed by an auto-analyzer. It achieves a limit of detection of 15.2 nM and a quantification limit of 50.8 nM over a dynamic range of 0.2 to 10 μM. The sensor is based on inlaid microfluidic absorbance cells, that permit decoupling of the lab-on-chip (LOC) from the electronics package, allowing configurability for different LOC designs. Furthermore, the energy required to take one sample was within the requirements set in CHAPTER 1 at 378 joules for the MSSP deployment, calculated from the power draw and pumping time. The reagent consumption during the MSSP deployment was 1.5 mL per sample, which is higher than the set requirement of 1 mL per sample, but the pier deployment showed that 0.5 mL per sample was also sufficient.

The unit is readily serviceable in the event of clogging or chip failure, and has self-aligned optical components, requiring no physical adhesives to the LOC. We conducted two field deployments to monitor the change in phosphate concentrations during the semi-diurnal tidal cycle and highlight the sensor's ability to capture short term events in a way that discrete *ex situ* methods cannot. This provides further insight into phosphate dynamics in the Bedford Basin, and other bodies of water, where phosphate concentrations could be sampled at appropriate temporal and spatial resolutions that inform biogeochemical models and ensure local regulatory compliance. Long-term deployments with tens of sensors are the next phase in demonstrating suitable field endurance and will enable insight into biogeochemical observations with increased monitoring capacity. We believe that such field-portable and *in situ* lab-on-chip systems will be highly impactful in aquaculture, oceanographic science, waste-water treatment, and industrial runoff monitoring.

CHAPTER 7 OPTICAL AND FLUIDIC ENHANCEMENTS

This chapter will highlight some of the further work I have done on optimizing nutrient analysis in microfluidic systems. First, continuous flow analysis will be explored for use in the microfluidic system, with the aim of reducing reagent consumption and increasing the sampling rate. Secondly, cavity enhancement techniques will be looked at with the goal of improving the detection limit for microfluidic devices. While some of the work presented in this chapter is near complete, a portion of it is still ongoing at time of writing.

7.1. Continuous Flow Analysis in a Microfluidic System

7.1.1 Continuous Flow Analysis Overview

Continuous flow analysis provides a much higher throughput (30 – 60 samples per hour [255]) than stop flow methods (5 – 12 samples per hour). The approach is also capable of performing measurements using very little reagent. For example, the YSI orthophosphate analyzers use continuous flow analysis and require only 5 µL of reagent per sample. In comparison, the phosphate sensor in Chapter 6 currently required 500 µL of reagent per sample for stop flow analysis.

To perform this type of analysis, small plugs of reagent are injected into a carrier stream of sample. Colour will begin to develop as the plug flows through the absorbance cell. The time integrated signal will be analogous to an absorbance measurement provided the conditions are self-consistent, and even though the colour will not be fully developed it should still provide a linear relation to concentration if the velocity of the carrier stream does not change. The profile of the pressure driven flow will be parabolic, with the highest velocity at the center of the channel. This causes dispersion, known as Taylor-Aris dispersion [261], and the dispersion coefficient for square channels can be modeled as [262]:

$$K = D_m\left[1+\frac{1}{210}f\left(\frac{d}{W}\right)\left(\frac{Ud}{D_m}\right)^2\right].$$

In the above expression, D_m is the molecular diffusion constant, d and W are the depth and width of the channel, and U is the mean flow velocity. The function *f(d/W)* is a geometry dependent function used to determine the effect of the side walls of the channel on the overall dispersion. The dispersion coefficient will determine the rate at which the injection plug of reagent will disperse into the surrounding carrier stream. The system requires intentional design so that the reagent plugs can be injected with as high a frequency as possible without overlapping before they reach the absorbance cell.

7.1.2 Microfluidic Chip Design and Fabrication

Figure 7.1(a) is a fluid schematic for the microfluidic device and the required syringe pumps and solenoid valves. The chip was designed to function in a push-pull configuration, meaning that one syringe pulls the carrier stream through the chip while the other ejects its contents to waste, and then they switch roles at the end of their respective strokes. These two syringes are labelled W1 and W2 in the fluid schematic. To accomplish this push-pull behavior, active user-controlled valves, shown in the diagram as circles crossed through by an ‘x’, are required to open and close at prescribed times. The carrier stream composes most of the fluid within the microfluidic device, and can be either the environmental sample, or a calibration standard depending on which valve is opened and which is closed.

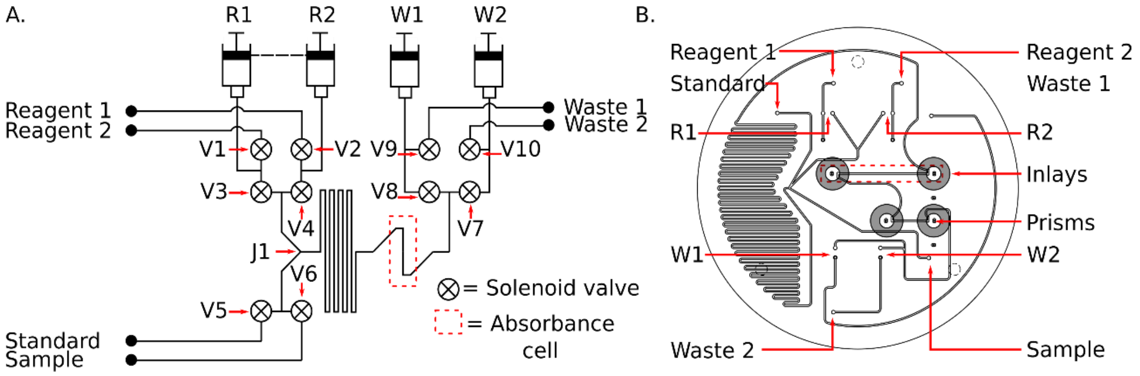

Figure 7.1: (a) Microfluidic chip flow diagram. (b) CAD image of microfluidic chip with components labelled.

Referring back to Figure 7.1(a), this is V5 for the environmental sample, and V6 for the calibration standard. The two reagent syringes, labelled R1 and R2, will be filled with either the same reagent in the case of a single reagent assay such as Griess reagent for nitrite, or the two parts of a two-reagent assay such as the phosphomolybdenum blue (PMB) assay for phosphate. Small volume plugs (50 µL or less) of reagent are periodically injected into the carrier stream at junction 1 (J1) to react as the plug travels through the serpentine mixer and into the absorbance cells. An example for the most basic protocol to perform flow injection analysis on the microfluidic system, drawing fluid in from the environment is shown in the following table of steps:

Table 9: Operational Sequence for CFA.

	Open	Close	Fill	Push	Pull
1. Open valve to draw from	V5	--	--	--	--
2. Set up to fill reagent syringes	V1,V2	V3,V4	--	--	--
3. Fill reagent syringes	--	--	R1,R2	--	--
4. Set up to begin flow injection	V3,V4	V1,V2	--	--	--
5. Set up push/pull configuration one	V8,V10	V9,V7	--	--	--
6. Push/pull configuration one	--	--	--	W1	W2
6.1 Delay during step 6	--	--	--	--	--
6.2 Reagent injection during step	--	--	--	R1,R2	--
7. Set up push/pull configuration two	V9,V7	V8,V10	--	--	--
8. Push/pull configuration two	--	--	--	W2	W1
8.1 Delay during step 8	--	--	--	--	--
8.2 Reagent injection during step	--	--	--	R1,R2	--

The microfluidic chip was manufactured from two discs of clear poly(methyl) methacrylate (PMMA) bonded together using a combination of chloroform vapor exposure, pressure, and heat. Furthermore, cylinders of opaque black PMMA were inlaid into each disc prior to bonding to create an aperture to reduce the effect of background light and scattering within the microfluidic chip. Full details concerning the inlay and bonding process were described in Chapter 5 and briefly reported by Luy et. al [39]. The features and substrate preparations were created using an LPKF S104 Micromill for milling and drilling, an LPKF Multipress S for pressing and heating, and an Epilog Mini laser cutter for separating the discs from the larger acrylic sheets.

The channels and absorbance cells have square cross sections, with 500 μm depth and width. The serpentine mixing chamber is 0.99 m long, resulting in a total volume of 247 μL. This volume was specifically chosen so that one stroke of a 500 μL syringe would be more than enough to carry the reagent plug all the way through the serpentine mixer and

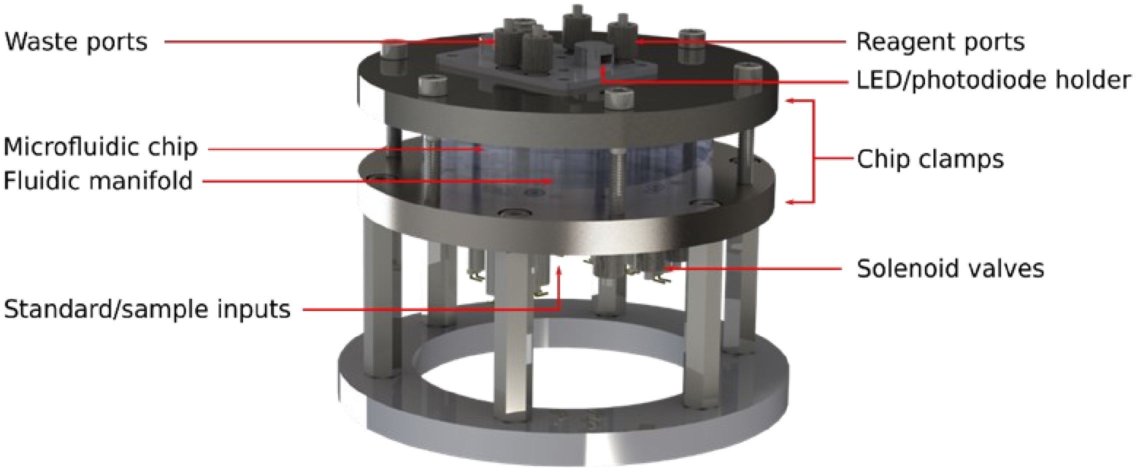

Figure 7.2: CAD Rendering of the benchtop testing apparatus.

absorbance cells. Figure 7.1(b) is a diagram of the microfluidic chip, with the reagents, sample, standard and waste ports all labelled. The syringes are labelled R1 and R2 for the two reagent syringes, and W1 and W2 for the two waste syringes. The inlaid apertures and engraved microprisms are also shown in the center of the chip. The inlaid apertures displayed in Figure 7.1(b) are individual circular inserts around each prism, rather than the single asymmetric shape from CHAPTER 6 that surrounds all the prisms. The circular inserts are much easier to press into the respective cavities and are more reliable in terms of fabrication. Furthermore, tests showed that there was no lost performance when using the circular inlays when compared to the asymmetric inlays.

7.1.3 Testing Apparatus and System Design

A custom benchtop testing jig was designed and manufactured to enable in-lab testing and characterization of the microfluidic chips. Figure 7.2 is a CAD rendering of the mechanical clamp and fluidic manifold for the system. An acrylic (PMMA) manifold acts as an interface between the chip and the 10 solenoid valves and fluid ports. O-rings (dash size

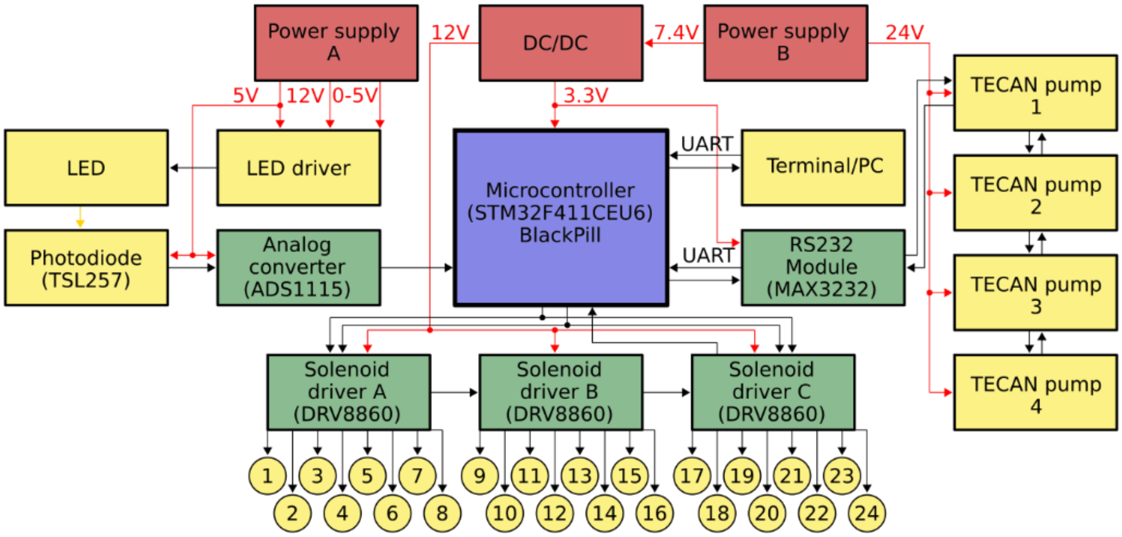

Figure 7.3: Electrical system block diagram.

006) and Viton gaskets are used to create seals between the manifold and the microfluidic chip. Both the manifold and chip are pressed between two aluminum clamp faces that are tightened using 6 M5 bolts threaded around the perimeter. A 3D-printed custom holder for the LEDs and photodiodes is bolted to the top plate using stainless steel M3 bolts.

A BlackPill microcontroller (STM32F411CEU6) and a custom PCB are used to control the solenoid valves, communicate with the TECAN pumps, log the photodiode readings, and establish terminal control from an external PC. Figure 7.3 is a block diagram overview of the electrical components of the entire system. The green and blue blocks in the diagram are integrated into the custom PCB, the red blocks represent power sources and the yellow blocks represent the external hardware components. The TECAN pumps require an RS232 protocol for communication, and the terminal communicates to the microcontroller via a UART protocol. Each solenoid driver is capable of controlling 8 solenoid valves, meaning 3 drivers in total are required. The LED driver is a separate custom made PCB and allows the intensity of the LED to be controlled by a variable voltage source. An analog to digital converter is used to read and log the output voltage of the photodiode. The microcontroller firmware and testing scripts are written in C using the STM32cubeIDE.

7.1.4 Flow Injection Interval Testing

Before calibrations and characterizations could be started, a suitable reagent injection frequency and volume had to be determined as well as a reasonable flow rate for flow injection analysis. Based on the results by Ogilvie et al [255] for phosphate determination using a continuous flow system, 50 μL was chosen as the maximum total reagent injection volume (25 μL from each syringe), but characterizations at lower volumes will also be carried out. Ogilvie et al used a flow rate of approx. 50 μL min^{-1}, however, due to the restraints of the TECAN pumps and the chosen syringes, the minimum possible flow rate was 100 μL min^{-1}, which was used going forward. To determine a suitable injection frequency for the 50 μL injection volume, a diluted concentration of red food dye was injected at specified intervals, and the output photodiode signal was monitored. It was assumed that the dispersion coefficient of the red food dye was similar enough to that of the reagent fluids to provide an accurate representation.

Figure 7.4 displays the results of the injection interval testing. The dark blue line is the photodiode output from a test with 4 injections spaced 30 seconds apart. It is clear that the tail ends of the dye plugs are smeared together (i.e. Taylor-Aris dispersion), and the voltage signal does not return to the original baseline value of approx. 2.8 V. The green line shows the results of 2 injections spaced 60 seconds apart. The individual peaks are clearer, but the voltage signal still does not rise to the baseline blank. The orange line shows

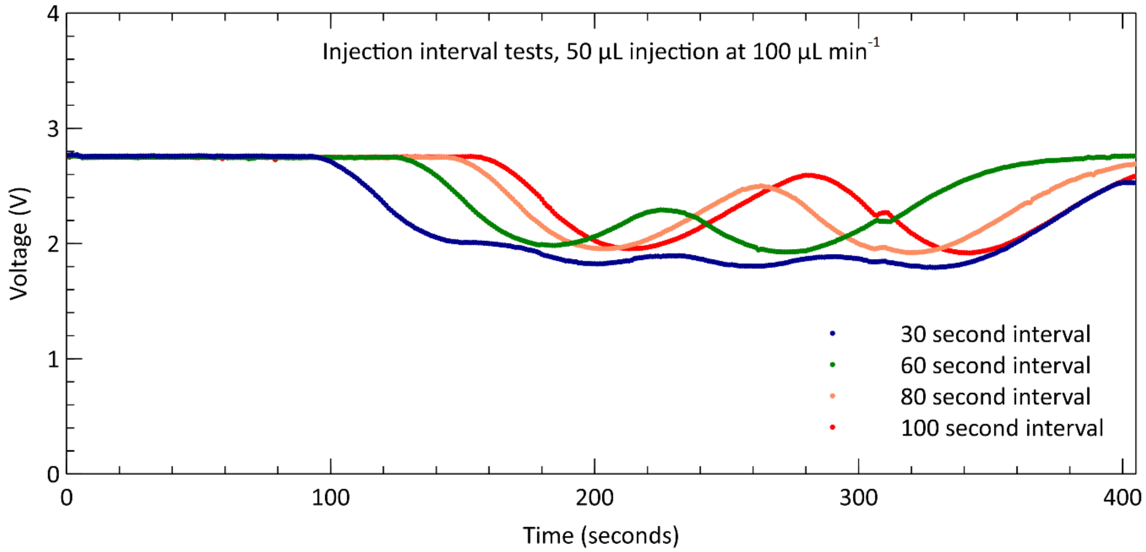

Figure 7.4: Injection interval test results for 30, 60, 80, and 100 second injection intervals.

the results from injections spaced 80 seconds apart, and the results are similar to the 60 second interval test. The red data is from a test with injections spaced 100 seconds apart. The voltage signal from this test almost returns to the blank baseline voltage, but still does not completely revert. However, it does show that the entire curve from the 50 μL injection is visible for approx. 150 seconds at the detector. The 150 second detection window means that a maximum of one dye injection (50 μL or 30 seconds) per syringe stroke (500 μL or 300 seconds) is possible, because it takes 148 seconds for the injection plug to reach the absorbance cell, which when combined with the detection window time is over half of the total syringe volume.

Due to the solenoid valves opening and closing, the switching of the syringes causes disturbances in the steady state flow that lead to measurement errors. This is visible in all of the voltage signals just after 300 seconds in Figure 7.4. A 100 second delay was used for the dye injection going forward, with the intention that the dyes would be injected into a carrier stream with a steady state flow. The stroke would then finish just after the plug volume has fully passed through the absorbance cell. At this point the syringes would switch and the process would repeat.

7.1.5 Nitrite Calibration Method

The next stage of testing involved injection of real functional reagents into a carrier stream comprised of standards with prescribed nutrient concentrations. The well documented Griess reagent for nitrite was chosen as the first assay to test due to its stability, fast reaction time at room temperature and narrow absorption peak. Because the Griess reagent is a single component assay, both of the reagent syringes were filled with the same fluid.

A simple script is used to run the calibration tests. Seven different standard concentrations ranging from 0.125 – 10 μM nitrite are used as the carrier stream. For each standard, the pre-set reagent volume is injected four times. The voltage signal is monitored as the reagent plugs react with the carrier stream and flow through the absorbance cell and is then used to determine the absorbance. The absorbance peaks are integrated to increase the sensitivity by monitoring the full colour development as the plug flows through the cell. Each set of four measurements are averaged and then the results are used to plot a calibration curve. The chip is flushed with 2 mL of Milli-Q water between each standard fluid, or every four measurements. This entire process is repeated three times, using three different injection volumes: 50 μL, 20 μL and 4 μL.

7.1.6 Nitrite Calibration Results

Figure 7.5 shows the voltage signal over time as the calibration script is run for each injection volume. The top panel displays the results from the 50 μL injection in blue, the

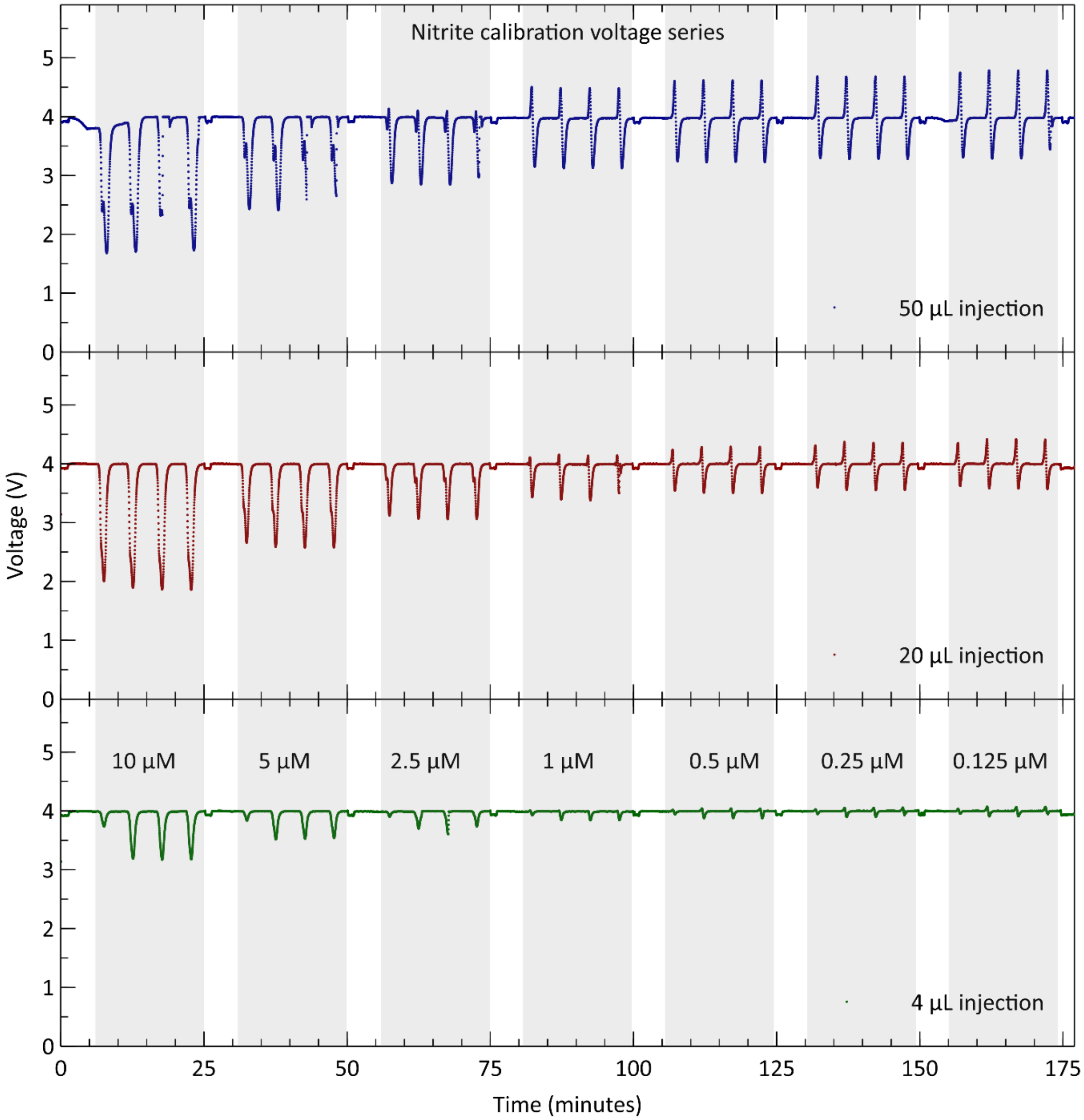

Figure 7.5: Nitrite calibration voltage series.

middle panel displays the results from the 20 µL injection in red and the bottom panel displays the results from the 4 µL injection in green. In the 50 µL injection it is visible, particularly in the 10 µM and 5 µM tests, that the voltage signal dips as the dye reaches the measurement cell as expected. However, it then increases slightly before dipping again to its full amplitude. This occurs because the regent plug is too long to fully react with the surrounding analyte before it reaches the absorbance cell. The tail ends of the plug react with the surrounding fluid to form the coloured dye, which appears as a dip in voltage due to light absorbance. However, the center of the plug has not yet fully reacted by the time the plug reaches the cell. Because the reagent is inherently colourless, it does not absorb as much light as the reacted portion, and therefore results in a higher voltage than the surrounding areas.

In the 4 μL injection results in the bottom panel, the first measurement of each set of four is consistently lower in amplitude than the following three. It is suspected that there is a very small amount of dead volume that needs to be filled after the reagent syringes are filled between each standard, leading to a smaller total volume in the first injection. This behaviour likely occurs in all three injection volumes, but the effect is too small to be noticeable in the larger two tests.

One important result highlighted by this test is the apparent increase in voltage in the lower concentrations in all three injection tests. It is significant, and in the lowest concentration, the voltage increase is even larger than the voltage decrease due to colour formation. This is a result of what is known as the Schlieren effect. It is the lensing and focusing of light due to the interface between two fluids and the parabolic flow profile in a channel. The cross-sectional flow rate is at a maximum at the center of a microchannel, and it drops off parabolically as it gets closer to the edge. Because the reagent and carrier stream are comprised of different fluids, with different refractive indices, a fluid lens is formed at the interface between the two fluids. Light is focused towards the detector as the reagent plug flows through, resulting in a drastic increase in voltage output. Likewise, light

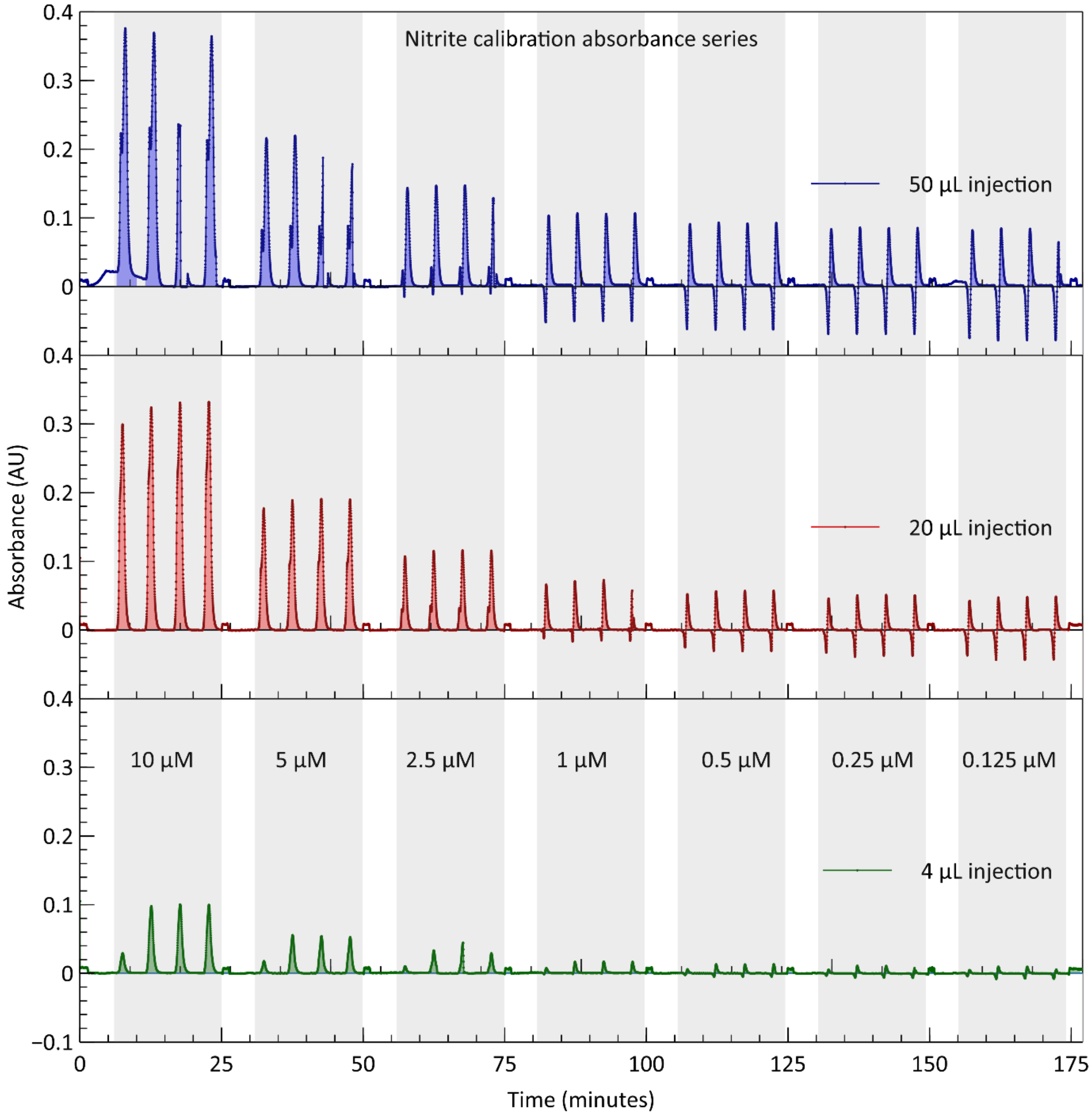

Figure 7.6: Nitrite calibration absorbance series.

is directed away from the detector at the other end of the reagent plug, which results in a decrease in measured light, independent of the carrier stream concentration. However, it is assumed that the effect is repeatable and consistent with every injection and can therefore be calibrated out as long as the absorbance signal is sufficiently large. The Schlieren effect will be discussed in further detail in later sections.

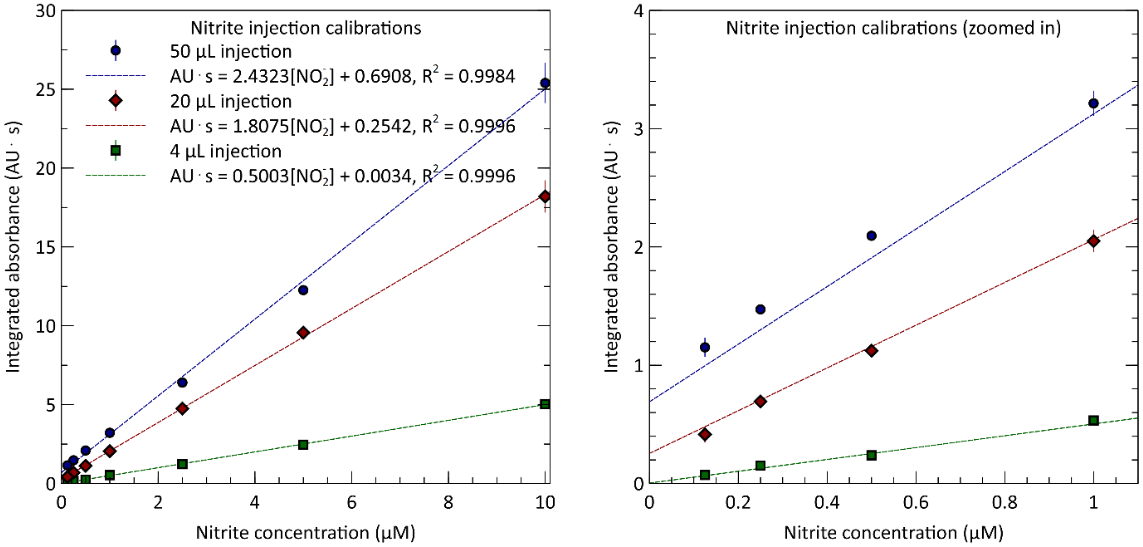

Figure 7.7: Left: Nitrite calibration curve. Right: Calibration curve zoomed in to show lower concentrations. The calibrations show that even using 4 µL, the slope is exceptionally linear, highlighting the potential impact for an in situ unit.

Figure 7.6 shows the absorbance profiles for the three nitrite calibration tests. Of the three injection volumes, the 20 µL injection appears to be the most repeatable and consistent. The 50 µL injection peaks show an absorbance dip in the center, as the plugs have not yet fully mixed. The first of the 4 µL injection peaks in each standard are consistently lower than the following three. Each absorbance peak is integrated to obtain a more sensitive absorbance measurement as the reagent plug flows through the cell. The average value for each set of four integrals is plotted against concentration in Figure 7.7 to form a calibration curve. The slope of each curve indicates the sensitivity of the measurements to nitrite concentration. The right panel of Figure 7.7 is zoomed in to show the calibration curve's lower concentrations more clearly. Although all three data sets display excellent linearity, the curve for the 50 µL injections does show more deviation from the linear fit than the other two. This is likely due to the incomplete reactions and misshapen absorbance peaks. Furthermore, although there is a clear tendency for the sensitivity to increase with injection volume, there is not a discernable relationship between the two values. Further tests would be required to identify any patterns.

7.1.7 Nitrate and Phosphate Calibration Methods

The calibration procedures for the nitrate and phosphate chemistries are nearly identical to the procedures for the nitrite calibration.

For the nitrate chemistry, the analysis and injection process is exactly the same, with only the chemical reagent being modified. Rather than the standard Griess reagent used for nitrite determination, a modified version with the addition of vanadium(III) chloride is used for nitrate determination. The added vanadium(III) chloride reduces nitrate to nitrite so that the standard Griess reaction can form the azo dye. This reduction reaction is described in more detail by [263] and is commonly used by Auto Analyzers for total nitrogen quantification in seawater. However, for the reduction to take place, heat is most often used as a catalyst. Without heating the reagent and analyte to 45 degrees, the reaction can take several hours to occur, which is beyond the capability of this continuous flow system, as there are no integral heaters in either the testing apparatus or the *in situ* device.

The calibration procedure for the phosphate series differs from the nitrite and nitrate series only in that the assay requires a two-part reagent. Referring to Figure 1, the two reagent syringes R1 and R2 are filled with the two parts of the phosphate reagent, which were discussed more thoroughly in CHAPTER 6 The two reagent solutions are mixed together before being mixed with the standard/sample solution at J1. From this point on, the injection procedure is identical to the previous nutrient series.

7.1.8 Nitrate and Phosphate Calibration Results

Figure 7.9, Figure 7.8 and Figure 7.10 show the resultant voltage series, absorbance series and calibration curve for an attempted nitrate calibration test without heating. Although there is evidence that colour is developing by the time the injected reagent plug reaches the absorbance cell, it is also clear that there is very little differentiation between the various concentrations. Figure 7.9 and Figure 7.8 show the voltage and absorbance profiles for 50 µL and 4 µL injection plugs as they move through the cell with decreasing nitrate concentrations. The negative and positive 'absorbance' peaks are similar in size for all the concentrations, ranging from 0.125 µM to 10 µM, showing that there is very little

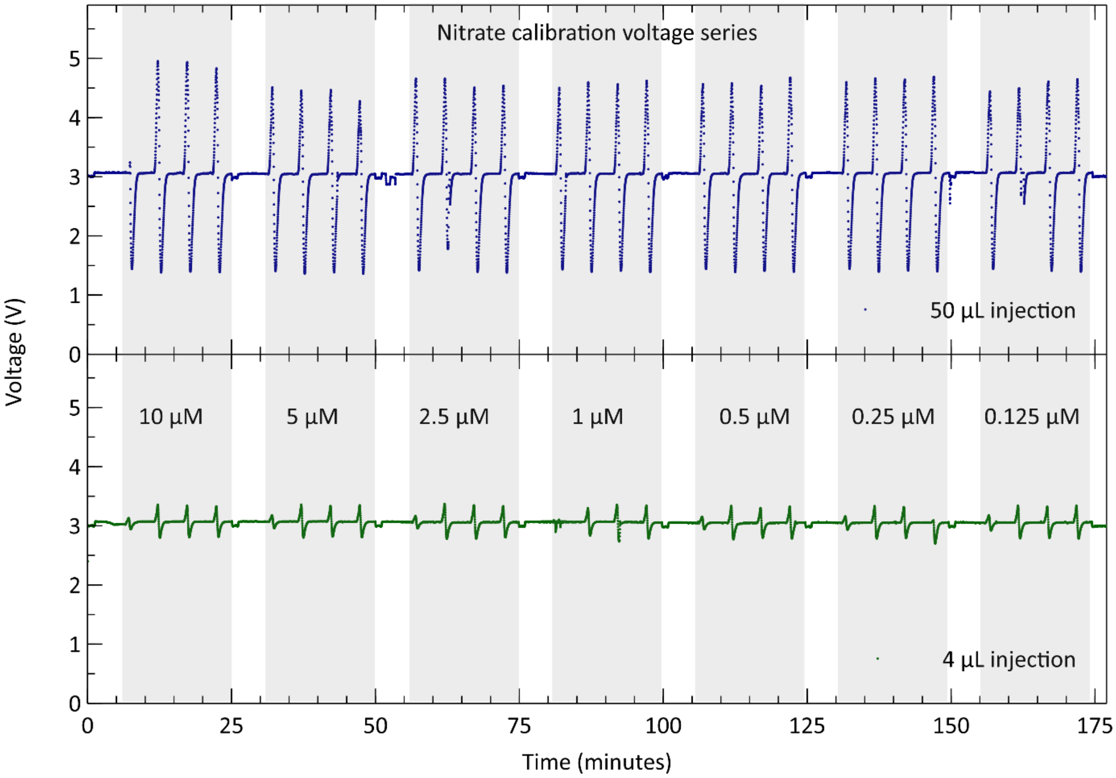

Figure 7.8: Nitrate calibration voltage series for 50 and 4 µL injection volumes.

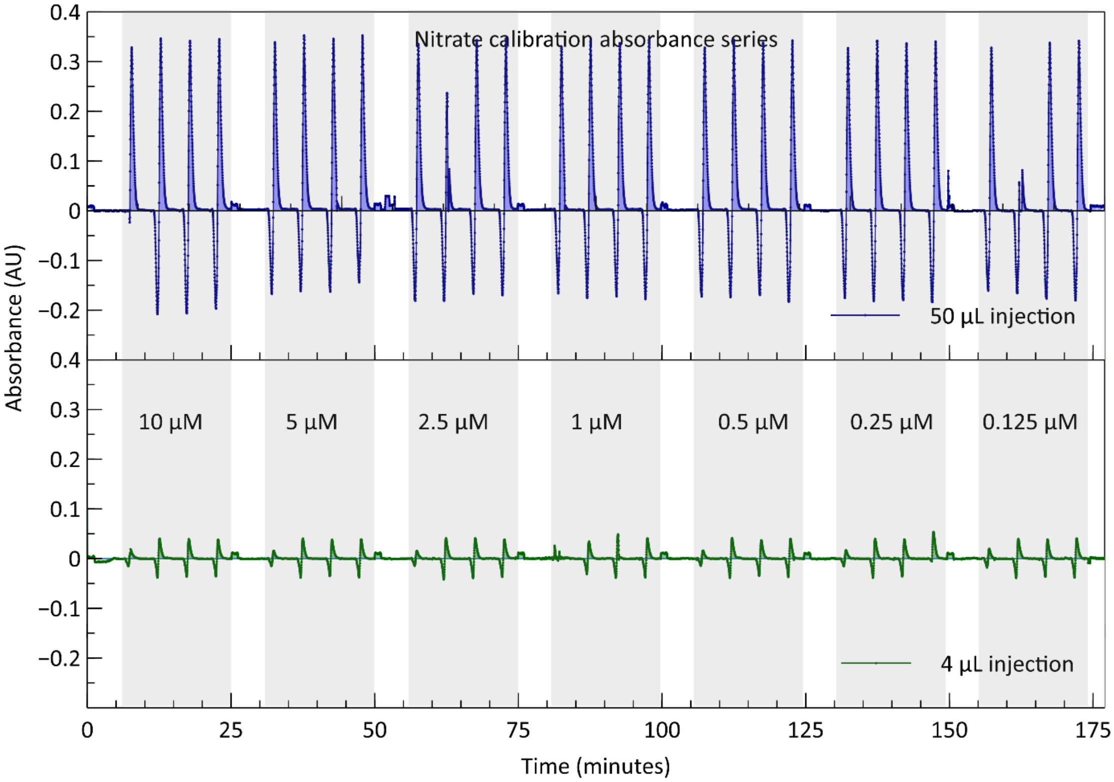

Figure 7.9: Nitrate calibration absorbance series for 50 and 4 µL injection

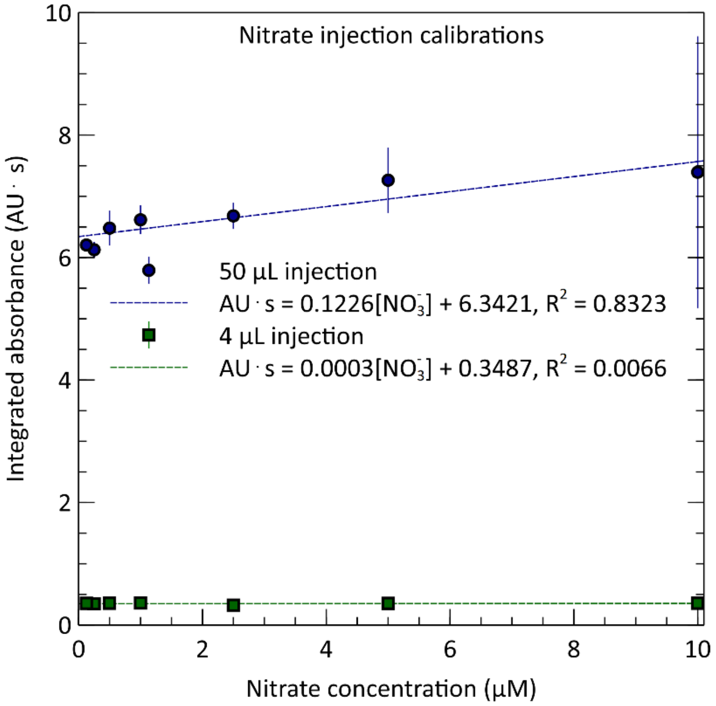

Figure 7.10: Nitrate calibration curves resultant from the 50 and 4 µL injection volumes.

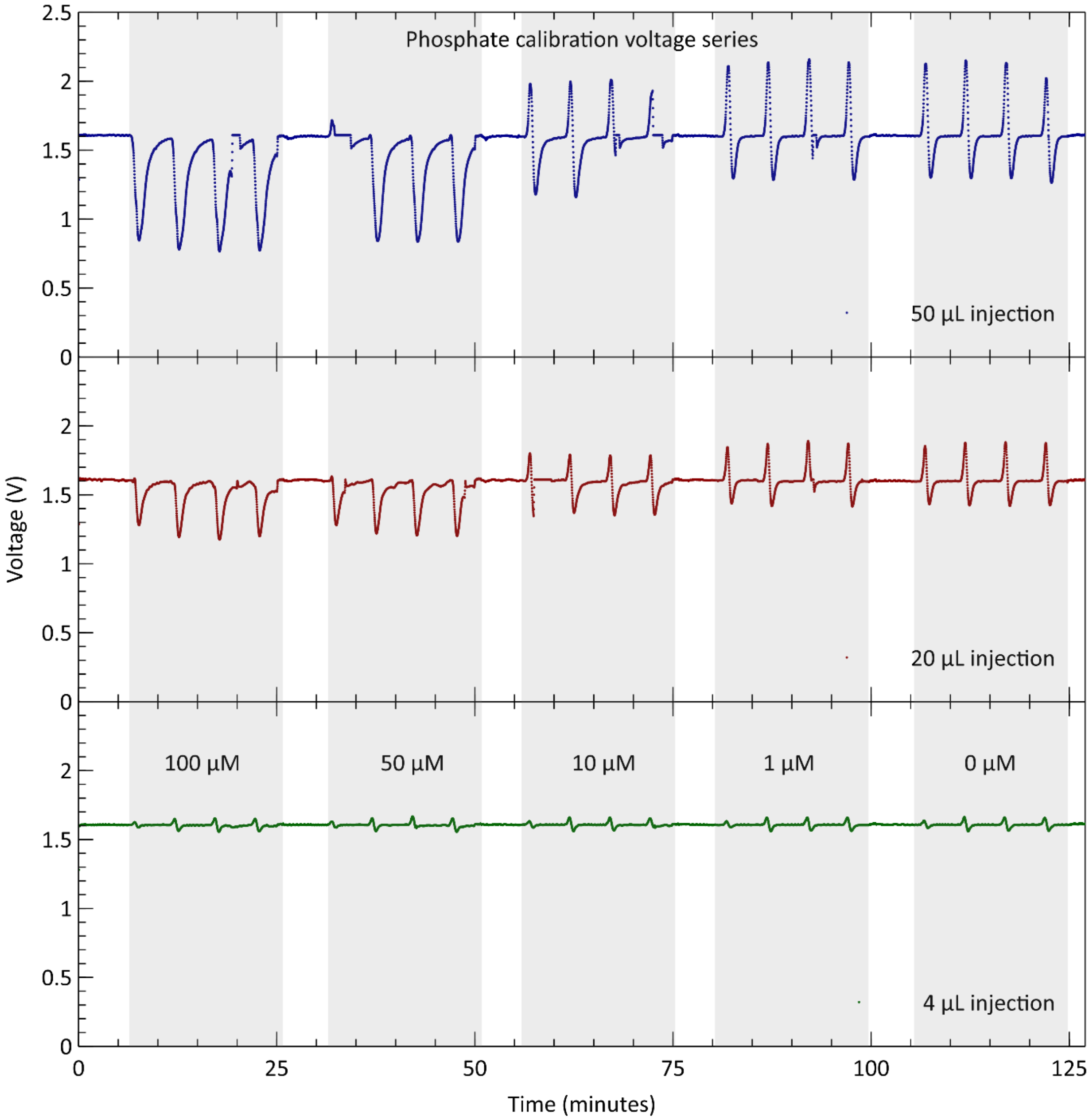

Figure 7.11: High concentration phosphate calibration voltage series for 50, 20 and 4 µL injection volumes.

colour development and that the Schlieren effect is clearly overpowering any development that is there. Figure 7.10 shows the calibration curve for the nitrate absorbance series after being averaged and filtered. The 50 µL injection series shows a very slight positive trend for concentration vs. absorbance, while the 4 µL injection series shows almost no trend at all. However, the calibration curve for the 50 µL injection series had an R^2 value of only

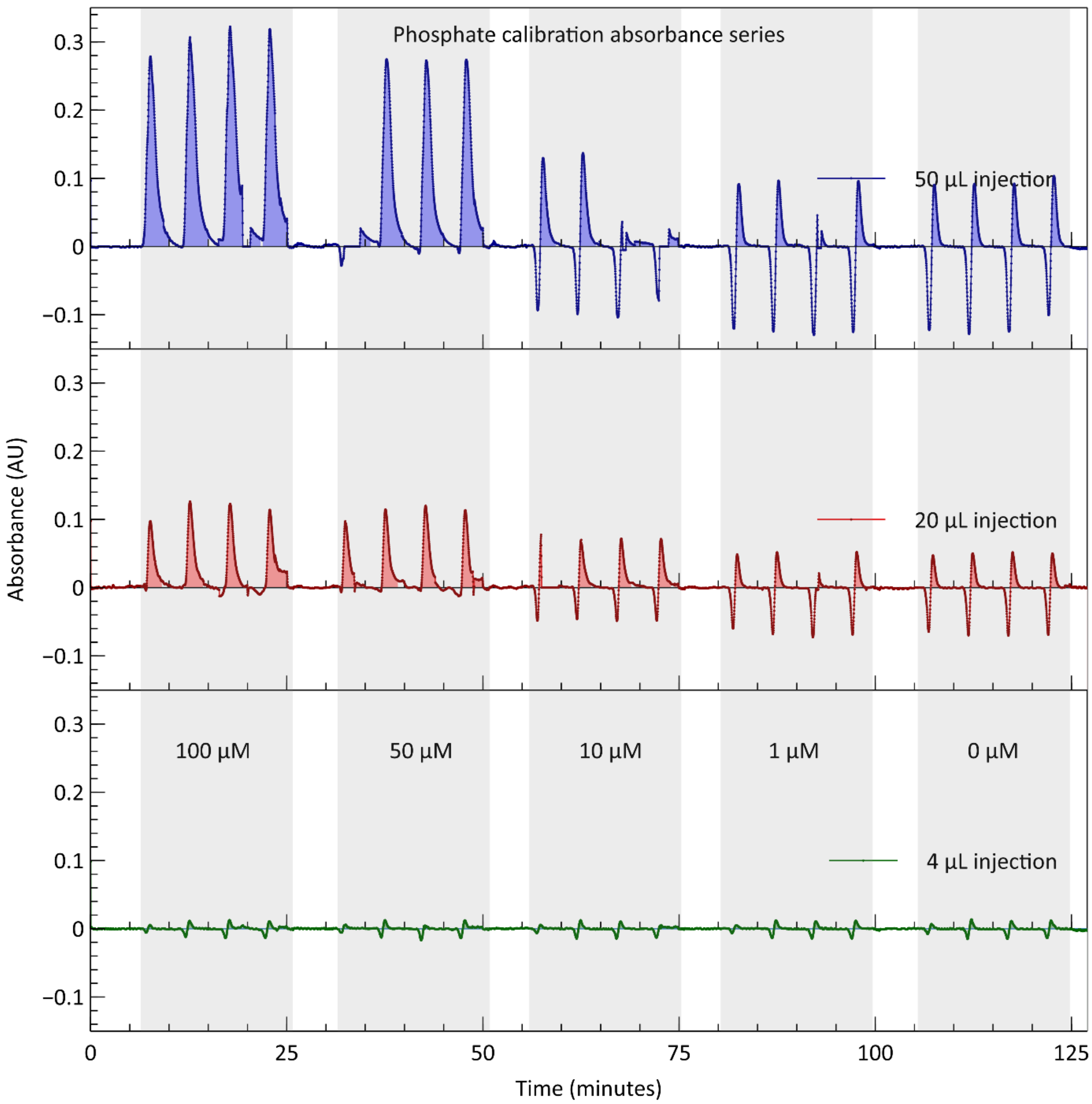

Figure 7.12: High concentration phosphate calibration absorbance series for 50, 20 and 4 µL injection volumes.

0.83, which is much lower and therefore higher variance than displayed by the results for the nitrite calibrations. Furthermore, the slope of the calibration curve for the 50 µL injection series for nitrate was only 0.123, making it roughly 1/20th as sensitive as the curve for 50 µL injection series for nitrite. These results show that CFA is likely not a viable option for nitrate measurement without further modifications. In the absence of an integral

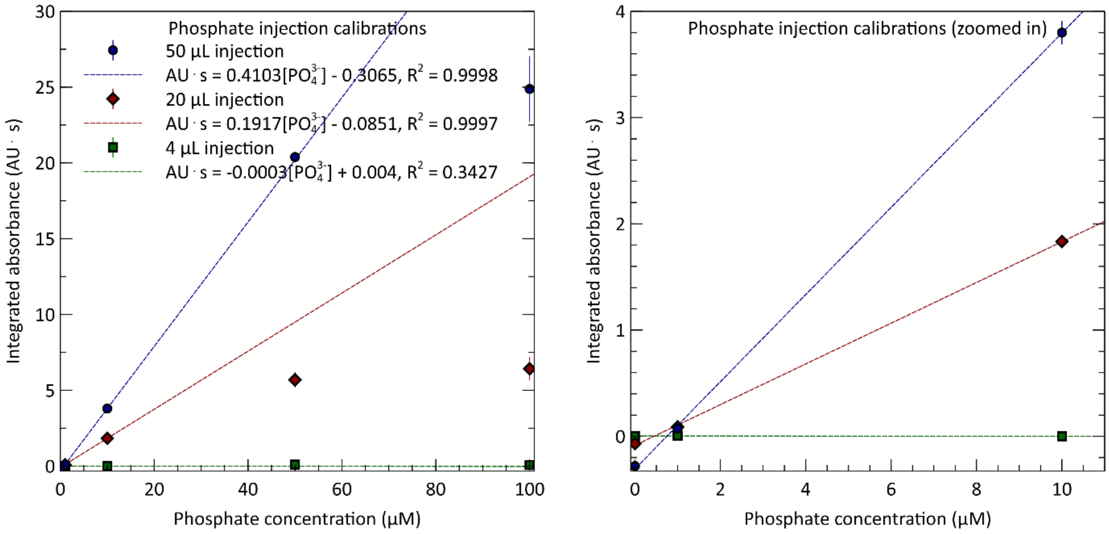

Figure 7.13: Calibration curves for high concentration phosphate series. Fit is accomplished using only the first three data points.

heater to aid with the reduction reaction, CFA does not perform well enough for nitrate determination to justify its use in an *in situ* sensor.

Figure 7.11 and Figure 7.12 show the phosphate voltage and absorbance series for the first set of calibration concentrations ranging from 0 to 100 µM. For these high nutrient concentrations it is immediately visible that there is a positive trend between phosphate concentration and absorbance in the continuous flow setup. It is not until below 50 µM that the ‘positive’ absorbance produced by the Schlieren effect is visible. Figure 7.13 is the calibration curve produced by these high concentration series, and it shows good linearity and low variance with R^2 values over 0.999 for the 20 and 50 µL injection series. However, the R^2 value for the 4 µL injection series is only 0.34 and the slope of the curve is nearly 0, showing that 4 µL reagent injection is insufficient for phosphate determination using this continuous flow setup.

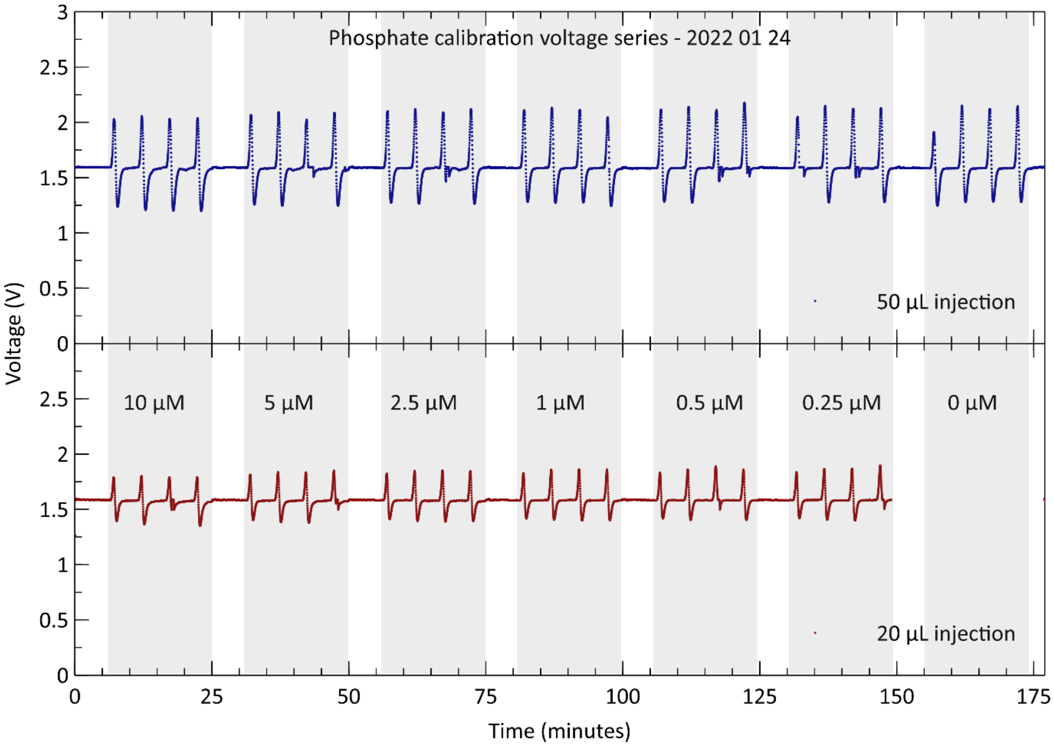

Figure 7.14: Low concentration phosphate calibration voltage series.

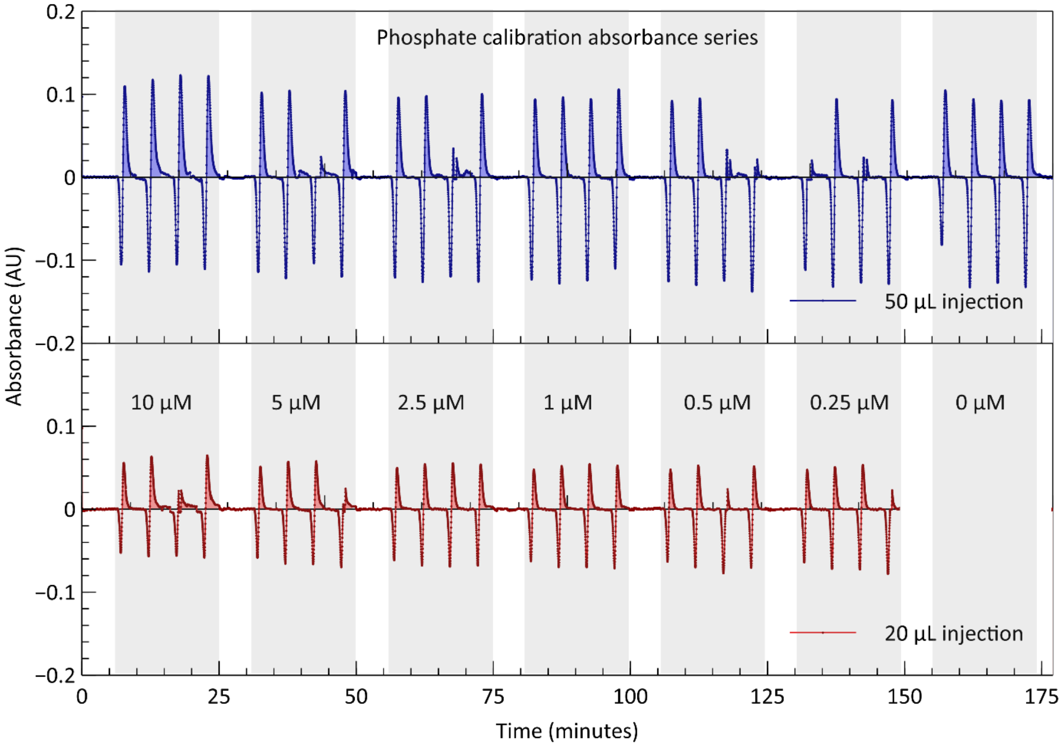

Figure 7.15: Low concentration phosphate calibration absorbance series.

Because the target concentration for phosphate determination *in situ* is typically below 1 µM, a more appropriate calibration range is from 0 to 10 µM. Figure 7.14 and Figure 7.15 show the voltage and absorbance series for phosphate concentrations within the aforementioned range. The variance below 10 µM is still acceptably low, however the spread of measurements below 1 µM as shown in the right panel of Figure 7.16 indicate that the system is not sensitive enough for open ocean applications. A contributor to this sensitivity issue is the overpowering of the signal by the Schlieren effect. At lower concentrations where there is little cover development, the absorbance due to actual colour development is not clearly distinguishable from the positive and negative 'absorbance' peaks caused by the Schlieren effect.

Similar to the nitrate series, the phosphate series requires heating or a significantly longer reaction time to produce discernible results. Although the reaction does occur faster than for nitrate determination, it does not occur fast enough to justify using continuous

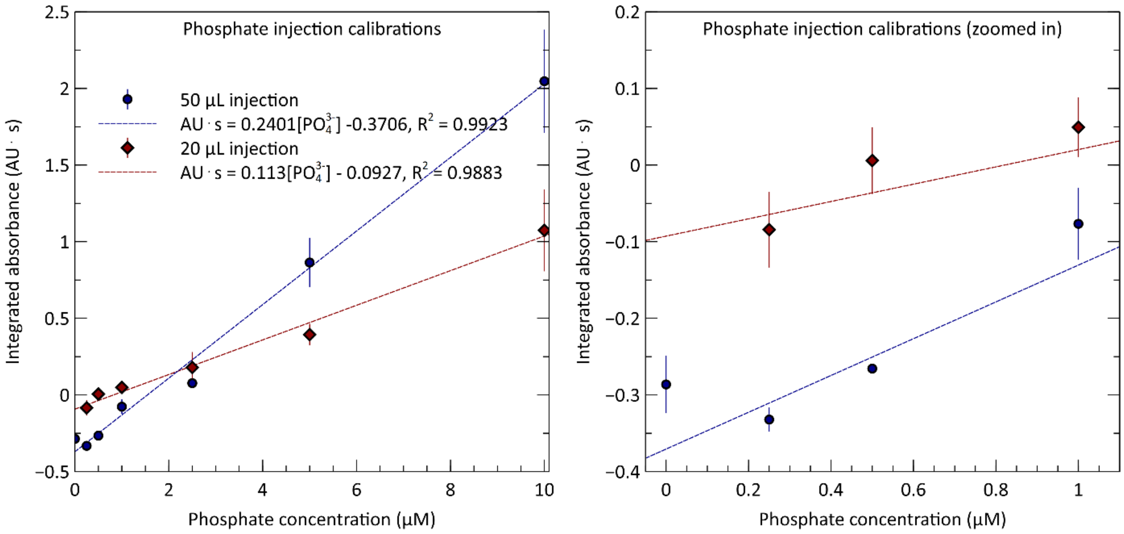

Figure 7.16: Calibration curves for low concentration phosphate series.

flow analysis at this scale. To contextualize these findings, Table 10 contains some documented reaction times for the nitrite reaction [264], nitrate reaction [264] and phosphate reaction [265] respectively, each at room temperature. It is clear that the high throughput of a continuous flow analysis system works well for chemistries with high reaction kinetics and robust environmental resilience. However, for reactions that only produce differentiable results after several minutes, a stop flow system is more appropriate.

Table 10: Reaction Times for Nitrite, Nitrate and Phosphate Reactions

Nutrient	Reaction	Reaction Time
Nitrite	Griess Assay	3- 15 minutes
Nitrate	Reduction	45 – 60 minutes
Phosphate	PMB Assay	15 – 30 minutes

7.1.9 Schlieren Effect Correction Approaches

As displayed in the previously reported data, the Schlieren effect negatively affects the detection limit for assays with slower reaction kinetics. The Schlieren effect is the lensing and scattering of light in the microchannel and is caused by the parabolic flow profile and the difference in composition of the two interfacing fluids. As the reagent plug moves through the absorbance cell, the first fluid interface causes light to be lensed towards the detector, thereby artificially increasing the voltage reported by the photodiode, causing a 'negative' absorbance. As the second interface moves through the cell, the reverse occurs and light is scattered away from the detector, which reads as an increase in absorbance. The artificial increases and decreases in absorbance can easily overpower the real absorbance caused by colour development in the cell, making it worthwhile to explore methods of correcting or circumventing the Schlieren effect.

The most obvious method to minimize the Schlieren effect is to slow down the flow rate of the system. The taper of the parabolic flow profile of the reagent plug is determined only by the channel dimensions and the volumetric flow rate. However, the flowrate used in the test scripts is the slowest that the system is capable of performing. A larger channel cross section would also help to reduce the Schlieren effect because it would cause a shallower and less convex 'lens' at each interface which would reduce any lensing caused by the effect. However, for the purposes of this application, increasing the channel dimensions is impractical. The required injection volume increases with the cube where the cross section increases with the square, which means that one of the main benefits of using continuous flow analysis (reducing reagent consumption) would be undermined if the cross section were to be increased to minimize the Schlieren effect. Increasing the injection plug length would also reduce the impacts of the Schlieren effect because there would be more reacting dye between the two interfaces to provide real absorbance measurements. However, the injection volume still increases with the cube, while the length increases only linearly, meaning that even more reagents would be consumed to pursue this correction method.

Another method that is sometimes used to combat the Schlieren effect is to use what is known as dual wavelength absorption spectroscopy. The premise of the technique is based on the idea that the Schlieren effect will lens/scatter all wavelengths of light in roughly the same amount, but any absorbance caused by colourimetric development will occur primarily in a specific wavelength range. By subtracting the perceived 'absorbance' of a wavelength that is outside of the bandwidth of the absorption peak of the selected

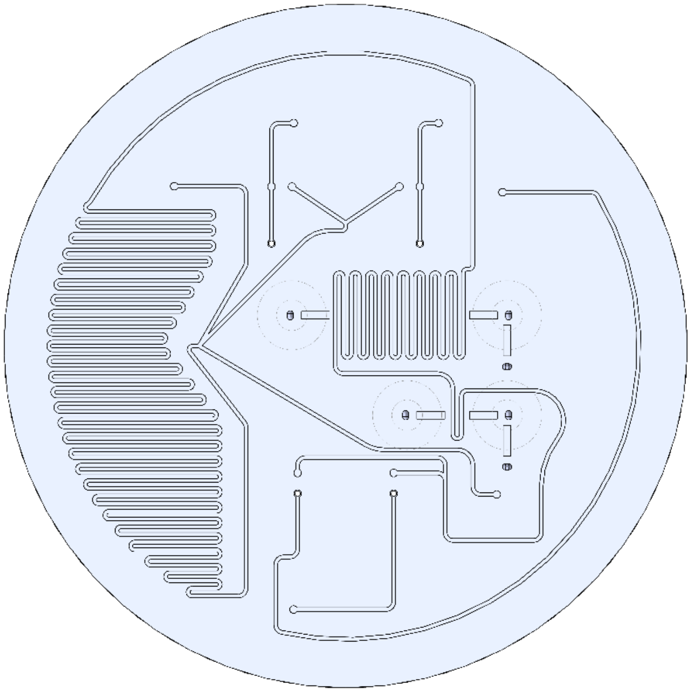

Figure 7.17: Microfluidic chip design with orthogonal flow cell.

analyte from the measured absorbance from a wavelength within the peak, the absorption due to colour development can be isolated from the 'absorbance' from the Schlieren effect.

A third and more novel approach to negate or minimize the Schlieren effect involves taking advantage of the flow geometry in the channel. The traditional Schlieren effect happens when the fluid flow is parallel to the optical path. It is not often observed in applications where the light source and detector are positioned orthogonally to the direction of fluid flow: i.e. they are placed perpendicularly across the flow cell. However, in typical microfluidic applications, the channel cross section is less than 500 µm across which is far too short to reach the lower detection limits required for this application. To increase the effective optical path length while still maintaining orthogonality between the fluid flow and optical path, the microfluidic channel is repeatedly passed perpendicularly across the path between the light source and detector. In this way any lensing from the two fluid interfaces of the reagent plug should not occur. A design with an orthogonal flow cell such as this is shown in Figure 7.17. The fluid channel for the absorbance cell is repeatedly passed through the optical path between the detector and source prisms a total of 17 times for the long path and twice for the short path. Given that the channels are 500 μm wide, the overall length of the absorbing region is 8.5 mm for the long path and 1.0 mm for the short path. Of course the actual distance between the prisms is longer, but any absorption/scattering happening in the PMMA or air regions should be self-consistent and not change with the concentration of the analyte. In that way, it should not affect the calibration curve. The rectangular shape between the cell and fluid channel is an intermediate region filled with air. This was added to create a bridge across the black inlaid portion so that light could pass between the prisms and the optical cell, while still allowing all fluid flow to be perpendicular to the optical path. The figure also shows in faint lines where the circular inlaid portions are, so that the reason for the rectangular bridges can be more easily visualized.

7.1.10 Schlieren Correction Methods

The dual wavelength absorption spectroscopy technique was applied to the phosphate assay in an effort to isolate the colour development of the lower concentrations and lower the detection limit to a point that is comparable with the stop flow system. For this test, the peak wavelength of 880 nm used for phosphate determination is described in previous sections, and the chosen wavelength outside the absorption peak is 500 nm.

An Ocean Optics Flame Spectrometer and a broad band halogen white light were used as the detector and light source respectively. OceanView software was used to capture the intensity at the chosen wavelengths every 1 second, with a moving boxcar average of 20 nm to reduce the noise in the signal. A custom, 3D printed holder was designed and built to interface with the testing apparatus and hold the SMA connector ends of the fiber optic cables in the correct alignment over the source and detector prisms. The cables transmitted the broadband white light from the halogen lamp to the source prism, and from the detector prism to the spectrometer.

Using the same protocols as previously described for the reagent injection, four concentrations of phosphate solutions (0.25 µM, 1 µM, 5 µM and 10 µM) were sequentially run through the system for analysis. The measured absorbance from the 500 nm band was subtracted from the absorbance of the 880 nm band to produce the resultant absorbance profiles for each concentration.

To test the orthogonal flow cell concept, the design previously shown was milled and bonded in clear acrylic, with circular opaque apertures inlaid for optical isolation. The cell was tested using the nitrite assay rather than the nitrate or phosphate assays to reduce the overall uncertainty in the tests. The nitrite assay was previously shown to produce good results in the continuous flow system, so it was chosen for the orthogonal flow cell test. Furthermore, the previous tests provide a baseline against which the results of the orthogonal tests can be compared.

The test itself followed the same protocol as previously described for the nitrite continuous flow calibration tests. Nitrite solutions ranging from 0.125 µM to 10 µM were run through the cell sequentially and total reagent injection volumes of 20 µL and 50 µL were used. The 4 µL injection volume was not considered because it was assumed that the larger volumes would provide the highest likelihood of success.

7.1.11 Schlieren Correction Results and Discussion

Figure 7.18 displays the three absorption profiles for the dual wavelength spectrometer tests with phosphate concentrations ranging between 0.25 and 10 µM. The top panel shows the absorption profile for the 500 nm series, that should show only the Schlieren effect. The middle panel shows the absorption profile for the 880 nm series that should show the combined absorbance from colourimetric development and the Schlieren effect. The bottom panel shows the absorption profile for the difference between the top two panels and should show the absorbance only from the colour development, with the absorbance from the Schlieren effect subtracted off. It is clear from the bottom panel that the Schlieren effect makes up most of the measured absorbance for these concentrations, and that there is almost no visible discernment between the absorbance profiles of the four different concentrations in the chosen range. This implies that either the low signal is being lost in the noise, or more likely, there is not enough time for the reaction to occur to a point where the lower concentrations can be differentiated.

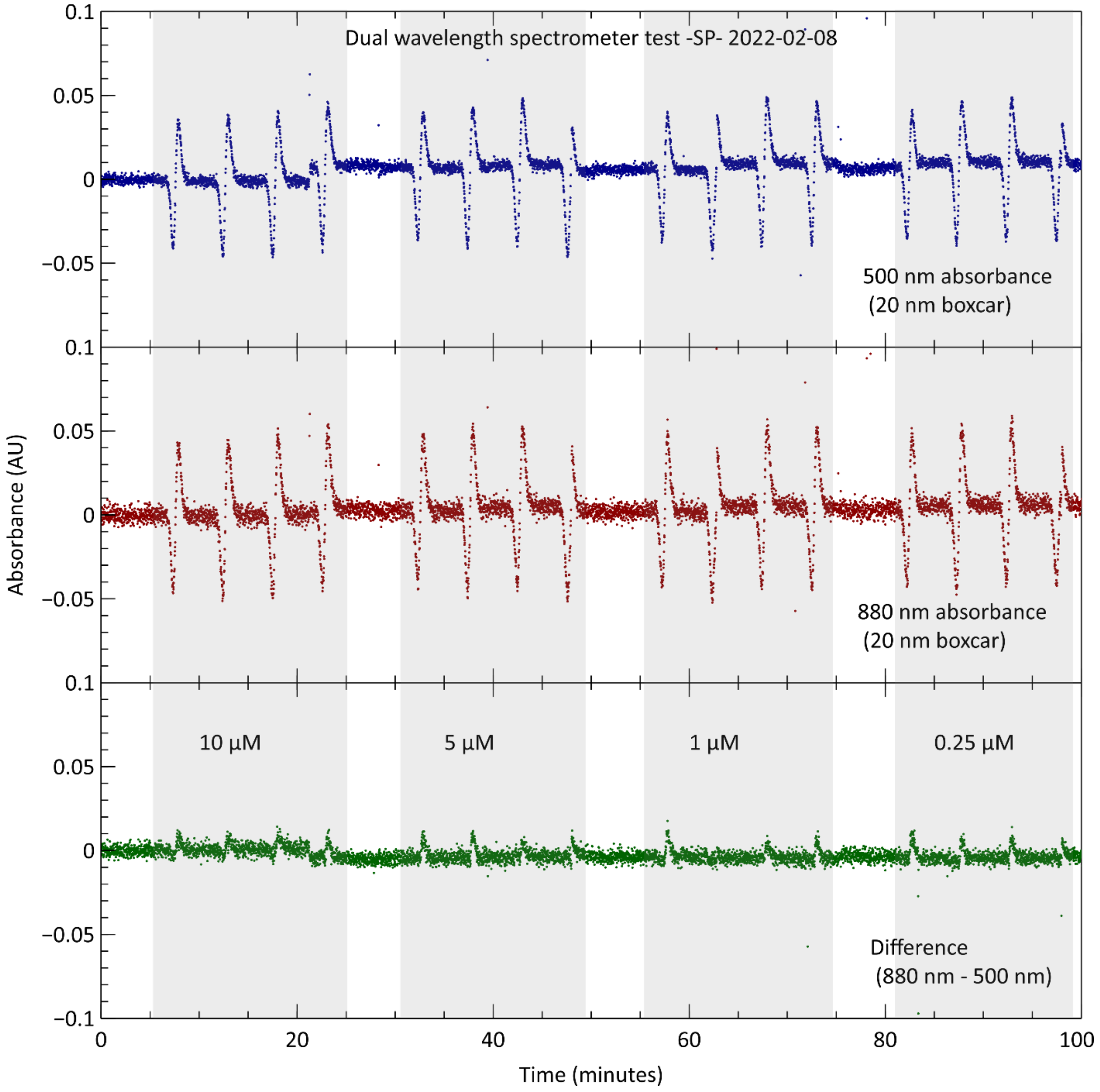

Figure 7.18: Dual wavelength absorbance spectroscopy for the PMB phosphate assay. Top: 500 nm absorbance series. Middle: 880 nm absorbance series. Bottom: Net difference between the Middle and Top panels.

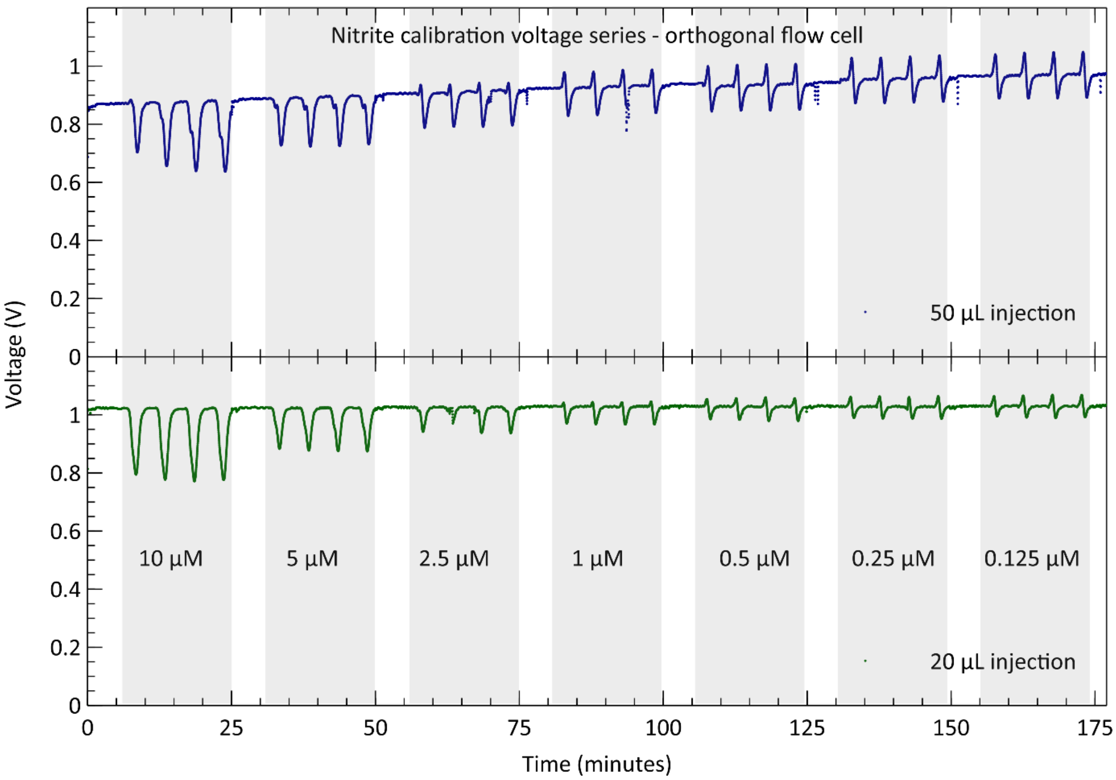

Figure 7.19: Nitrite calibration voltage series with orthogonal flow cell for 50 and 20 µL injection volumes.

Figure 7.19 and Figure 7.20 display the voltage and absorbance data obtained from the nitrite calibration tests performed on the orthogonal flow cell. The overall signal is reduced approximately four-fold when compared to the original flow cell, as was expected because light is lost to scattering at each interface between the PMMA and fluid channel. Furthermore, the magnitude of the absorbance is also reduced by approximately 2.92 times. This is in alignment with the reduction in optical path length, which was reduced from 25.4 mm in the original cell to 8.5 mm, meaning a reduction factor of 2.98. Despite this, it is also immediately evident that the Schlieren effect is still impacting the measurements. The upwards spike in voltage before the decrease caused by colour development is still visible,

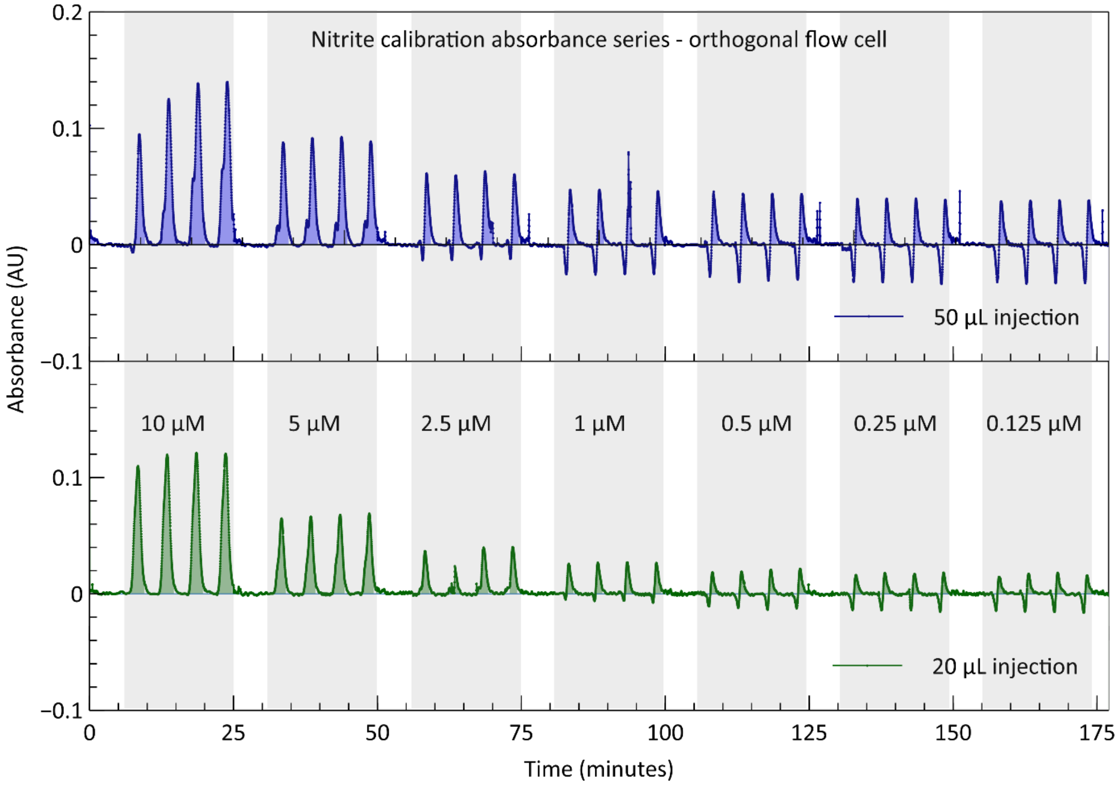

Figure 7.20: Nitrite calibration absorbance series with orthogonal absorbance cell for 50 and 20 µL injection volumes.

especially in the lower concentration ranges. The ‘negative’ ‘absorbance caused by the Schlieren effect is still of similar magnitude to the overall absorbance in the lower concentrations, making it very difficult to extract the correct absorption measurements from the signal.

Figure 7.21 shows the calibration curves formed by the data shown in the previous figure. The sensitivity of the curve is less than the original cell, as is expected with the shorter optical path length. Furthermore, the R^2 values, although still showing excellent linearity, are less than the values for the original cell, indicating that the orthogonal cell did not produce any improvements. We theorize that the Schlieren effect occurred even in the

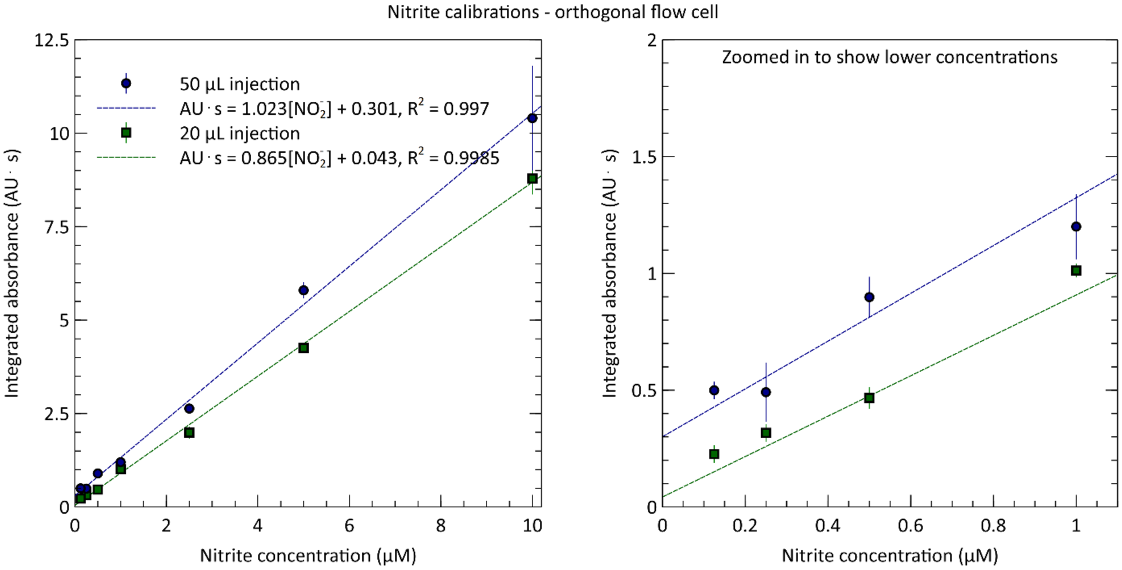

Figure 7.21: Nitrite calibration curves with orthogonal flow cells for 50 and 20 µL injection volumes. Left: Zoomed in below 1 µM.

orthogonal setup due to the concentration gradient of the reagents across the optical path. Because the fluid channel is much longer in the orthogonal set up, there are regions that will have more reagent and regions that will have less. This creates regions of higher or lower refractive index moving through the optical path, which could result in the Schlieren effect. More studies would be required to confirm this and produce methods for correcting it. However, in the current state, it does not appear that the orthogonal flow cell offers any advantages over the standard straight flow cell for continuous flow analysis. The path forward should use these systems to do droplet segmented flow as the dispersion is too problematic to engineer out.

7.2. Cavity Enhanced Absorption Spectroscopy

The basic description and background of cavity enhanced absorption spectroscopy (CEAS) has already been discussed in CHAPTER 5.1 and will only be briefly touched on here. CEAS uses geometry and/or material properties to artificially increase the optical path length of a system without changing the physical form factor of the device. There are several ways in which this may be accomplished, but here we will be discussing mainly CEAS using a multi-bounce system. CEAS using cavity ring down (CRD) is explored using simulation and discussed in APPENDIX E.

7.2.1 CEAS Using a Multi-Bounce System: Concept and Design

The concept of the multi-bounce system is based on the same idea as the embedded microprisms. The difference, however, is that instead of light being directed from outside the chip and then through a channel, light is directed to different points within the chip using in-plane prisms. By milling slots into the acrylic and creating air-filled pockets, TIR can be used to 'bounce' light around the chip before ultimately being directed to the detector. In this way, the optical path can be extended without changing the overall size or shape of the chip itself. Figure 7.22 shows the design for a chip that would employ the multibounce absorbance cell. The initial v-groove prisms are milled so that the source prism will direct light towards the first 45 degree slots, which would then direct the light to the second slot, and then to the detector prism. This design was made to only have two bounces, resulting in an added 26 mm of optical path. However, in theory there could be multiple bounces that could greatly increase the optical path length.

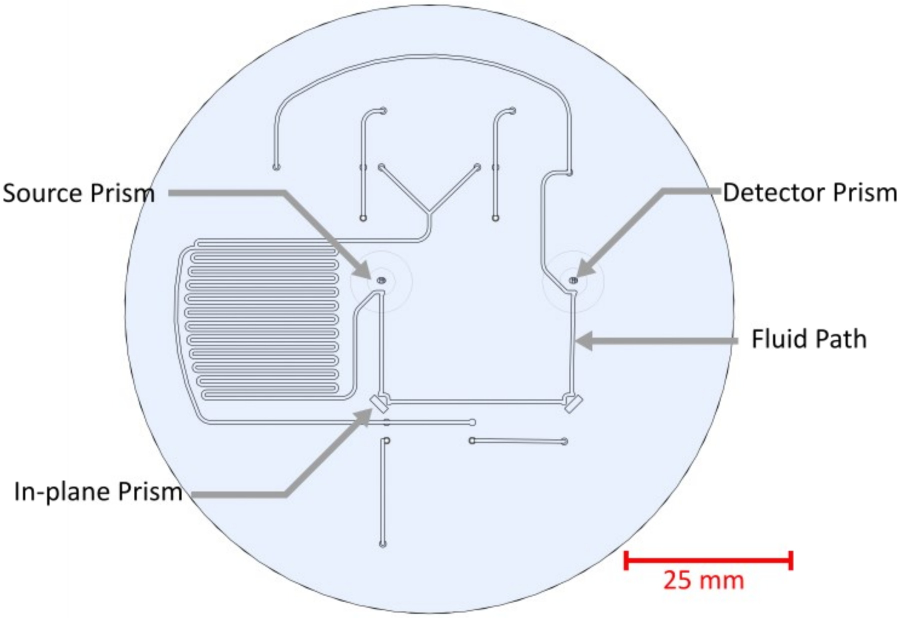

Figure 7.22: Chip design for multi-bounce CEAS. Two slots milled at 45 degrees to the direction of fluid flow act as prisms to redirect light.

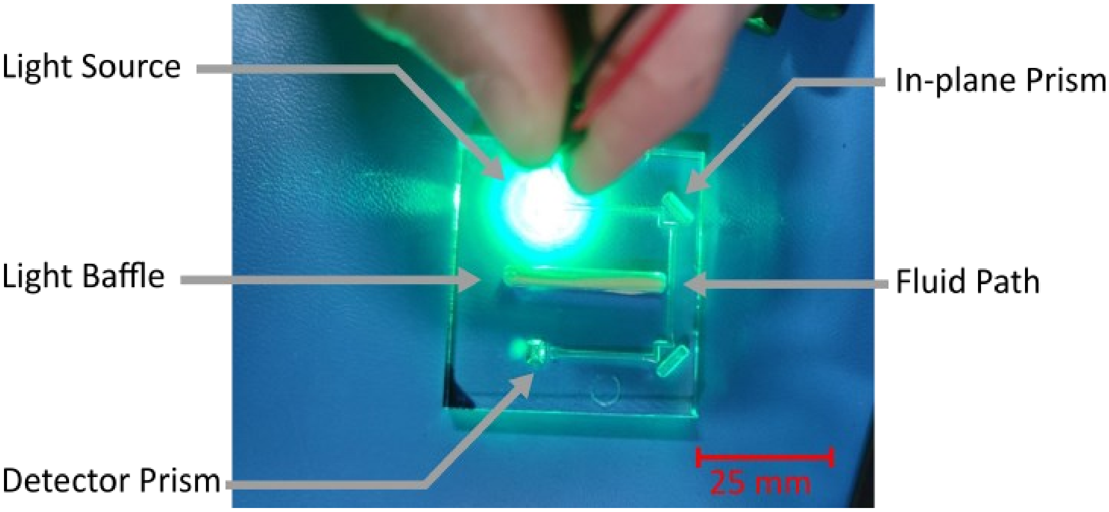

Figure 7.23: Multi-bounce prototype, with no fluid handling or bonding. Light is visible on the detector prism (bottom).

Figure 7.23 is a photograph of a proof of concept chip. The chip shown there was not bonded, and therefore not an enclosed channel. Furthermore, the channels were 1 mm squares and were not fluid filled. The chip showed clearly that light was reaching the detector prism (bottom) when an LED was positioned above the source prism (top). It is also visible that the two 45-degree slots are scattering some light and not reflecting all of it. This is evident by the fact that their edges are glowing a faint green. This is likely caused by surface roughness created by the micro-stepping motion of the mill. This was addressed in further design attempts by subjecting only the 45-degree slots to localized chloroform vapor exposure prior to bonding.

7.2.2 CEAS Using a Multi-Bounce System: Methods

Before attempting to create and test a physical device, the system was modeled and simulated in a ray tracing software called Zemax. The system was set up in multiple configurations. The basic configuration was the same as the setup shown in Figure 7.22, but it was carried further to contain multiple 'bounces' back and forth between the source and detector prisms. These designs were tested in simulation to compare against single pass systems of equal path lengths. The optical power lost at each reflection was determined and plotted. Further designs with other incident angels and 'waveguide' approaches were also considered, and can be found in APPENDIX D.

The first set of simulations were performed on the designs with the 45 degree slots as air prisms. The light source used in the following simulations was modeled off the Cree C503B-GAN LED, with a peak wavelength of 525 nm and a luminous intensity of 50 candela. The angular distribution of the LED was taken from the data sheet and had a 15 degree half power angle. The actual distribution was processed and inputted into the Zemax software to provide an accurate source model.

To determine the optical power loss for each ‘bounce’ in the multibounce system, six different models were created, each with a different number of reflecting points between the source and detector prism. The overall optical path length between the source and detector prism for each model was calculated, and an equivalent single pass system was modeled with the same path length. In this way, the effect of path length could be factored out of the results.

After simulations, the multi-bounce system displayed as a concept in Figure 7.22 was fabricated in PMMA and tested using the same apparatus as all the previous tests. The test consisted of injecting an unknown concentration of red food dye repeatedly into the cell, with Milli-Q rinses in between. The same green LED and photodiode used in the previous nitrite experiments were used as the light source and detector. This preliminary test was to check for basic functionality and repeatability and was used to determine if further tests were warranted.

7.2.3 Multi-Bounce System Results and Discussion

The first set of results that will be discussed are the simulations of the absorbance cells with the 45° in-plane prisms, and the single-pass counterparts for each multi-pass cell. Figure 7.24 displays the power measured at the detector for the single pass and multi-bounce systems. The top panel shows the power of the simple, straight, single pass system as a function of path length. It is predictably linear with length, as the power for such a system is only affected by the solid angle, which changes linearly with distance. The

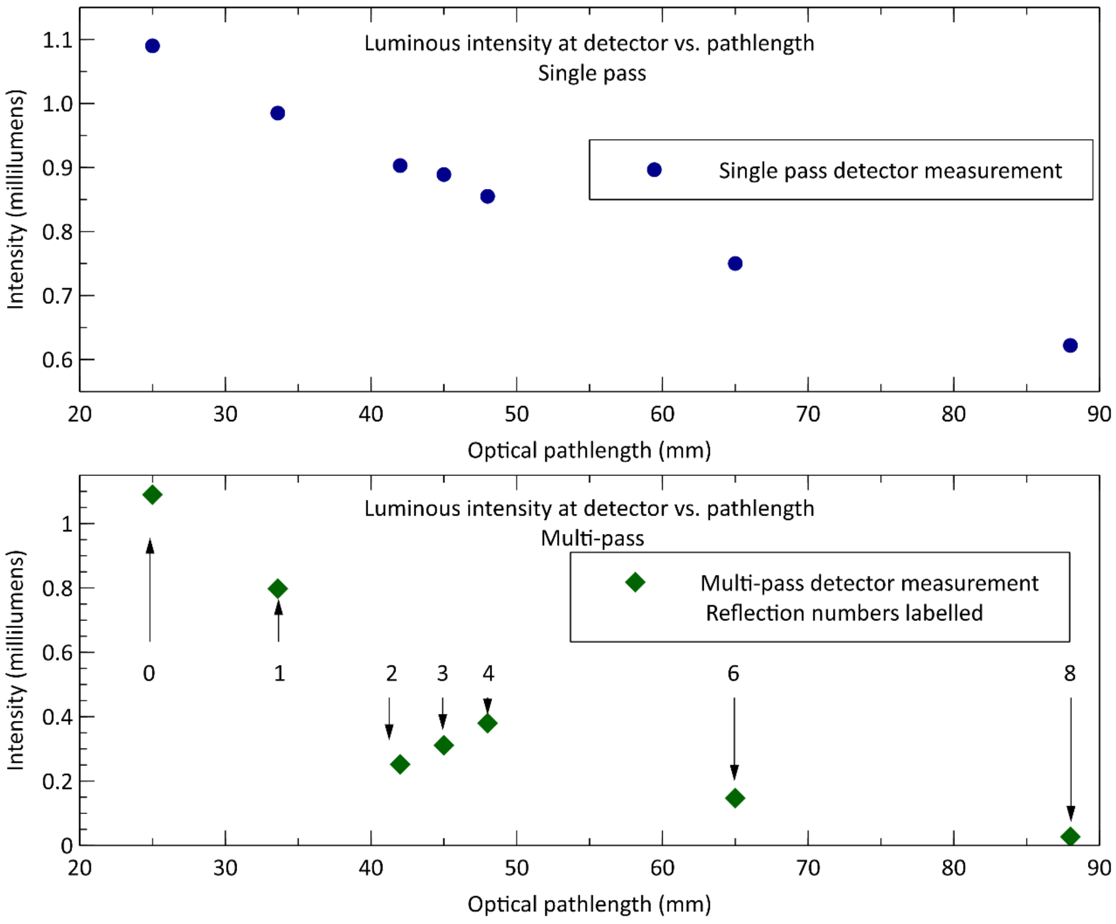

Figure 7.24: Top: Optical power for a single pass system of varying path length. Bottom: Optical power for multi-bounce system, displayed against path length.

bottom panel displays the results for the multi-bounce system. There is not an obvious trend in the data, because each system design has an optical path length that is independent of the number of ‘bounces’. Figure 7.25 shows the ratio between the two plots in Figure 7.24. The power output for each multi-bounce system was divided by the power output of its equivalent single pass system. In that way, the optical path length dependence is negated. The ratio was then subtracted from the single pass results to show the ‘losses’ caused by each additional bounce. It is interesting to note that after 4 bounces the ‘losses’ seem to stop accumulating, meaning that the optical losses from bouncing 8 times is the same as

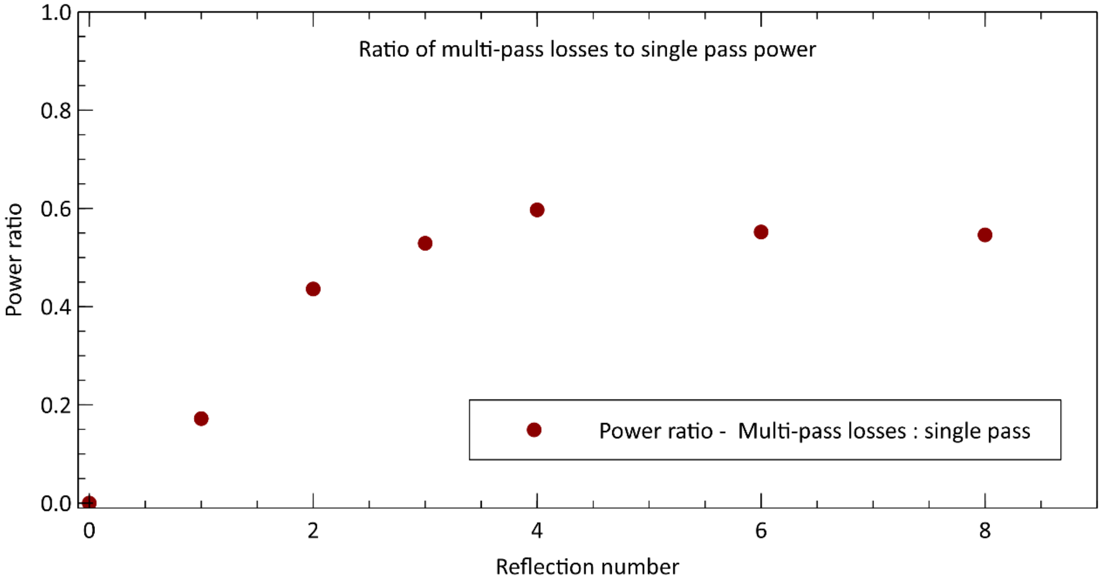

Figure 7.25: Ratio of power at the detector for multi-bounce and single pass systems of equivalent path lengths.

the optical losses from bouncing 4 times. This is likely because after a certain number of bounces, only the perfectly collimated rays will continue to propagate, and if they are perfectly collimated they will propagate indefinitely, resulting in no additional losses. Of course, if the system were real rather than simulated there would be losses caused by scattering and material absorption at each interface.

Despite the simulations showing promising results, there were difficulties in developing the physical system. The results of the preliminary dye test can be seen in Figure 7.26. The primary issue was, predictably, bubbles preventing the optical signal from reaching the detector. After the first dye injection, the signal drops drastically because of the introduction of an air bubble to the system. After that the signal does not recover fully, and the bubble is not expelled. Bubbles have been problematic with other designs as well, but with the multi-bounce designs they were much more impactful and difficult to dislodge.

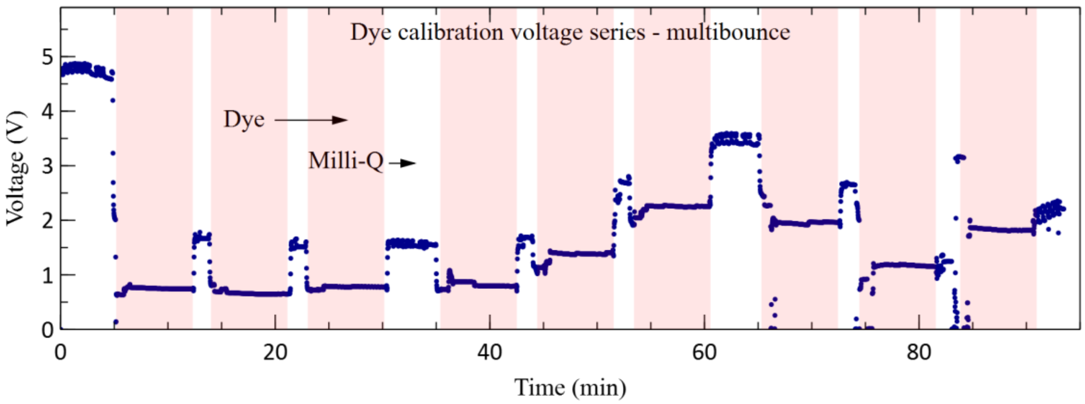

Figure 7.26: Example of voltage data from a dye test on a two-bounce system.

The design of the multi-bounce cell has several corners that tend to trap air bubbles. The corners are unavoidable, as they are required to create a 90 degree interface between the optical path and the PMMA. There are at minimum two corners per bounce, as can be seen in Figure 7.22. The only way in which the bubbles could be dislodged was if the testing apparatus was disassembled and the vias into the chip were blasted with compressed air. Even then, the bubbles were quickly reintroduced and a full calibration was never actually obtained, even when using fluids that had been de-gassed before use. Further work will need to be done to circumvent this issue. Perhaps a bubble trap prior to the absorbance cell could be used, or a design with less sharp angles could be produced.

Although the multi-bounce system was the only cavity enhanced method that was physically fabricated, enhancement using cavity ring down (CRD) was also considered in simulation. The details of the methods and results of these simulations can be found in APPENDIX E. The simulations show that CRD can certainly be used to increase the sensitivity of the absorbance cells, but only if the light source is extremely collimated. To that end, the overarching message interpreted from the results of the simulations is that

CRD cannot be effectively implemented using an LED over the path length required by this form factor.

As a concept CEAS is an excellent option to improve the sensitivity and lower the detection limit of the inlaid optical absorbance cells. However, the physical implementation of CEAS is too complex for the fabrication techniques employed in this work. Furthermore, the issues caused by cavitation and absorbed gasses are only amplified by the geometries required by CEAS. These problems could potentially be addressed by an in-line bubble trap or an integrated de-gassing filter, however further testing is needed.

CHAPTER 8 CONCLUSIONS AND FUTURE WORK

8.1. Summary of Work

Microfluidic technologies are becoming a mainstay for *in situ* ocean variable measurement. Given their comparatively low reagent and power requirements, the traditionally benchtop analysis techniques are being modified and adapted for use in *in situ* applications. Here, we have developed supporting technologies to enable macronutrients to be measured in the environment, without any need to extract samples or perform *ex situ* analysis. The foremost contributions presented in this dissertation are focussed around microfluidic valving, inlaid absorbance cells, the development of a fully functional nutrient sensor, and the preliminary work done to perform flow injection and cavity enhancement techniques on chip.

The magnetically tunable valve design proved to be effective and easily manufactured. The use of embedded permanent magnets allowed the valves to be passively sealed and have a calculable and repeatable cracking pressure. This is crucial for valving on a microfluidic device if fluid ratios are to be conserved. Despite the success of this style of valve, it had limited applicability due to the materials it was constructed with. The ball needed to be made of a ferromagnetic material for the magnet to have any effect, but also needed to be robust to chemical submersion if it were to be used in the reagents. Although the ball was made from what was considered to be corrosion resistant stainless steel, it was still unable to withstand the reagent solutions.

The following valve designs were intended to address the chemical resistance issue by using materials such as nickel alloys, ceramic, Viton, and other FKM elastomers. The two design types that we explored were a ball style valve that was passively sealed by a spring, and an elastomer flap style valve that was passively sealed by its own elasticity. Each design had elements that were successful and elements that were not, although they both showed good chemical resistance. The ball style valve could be set to have a predetermined cracking pressure by adjusting the depth of the cavity in which the spring was set. However, we were unable to find a design that allowed the valve to meet all four criteria for pumping. Furthermore, the fabrication process for the ball style valves was very complicated and difficult to ensure correct alignment of the springs, balls and O-rings. The flap valves were much easier to fabricate, as they did not have multiple stacked parts, and when they did work they were able to meet all four criteria. However, they were unreliable in their performance, and were far too sensitive to the introduction of air bubbles to be used in a fully developed sensor. If a bubble became trapped in the valve, it would not seal properly and could render an entire chip useless.

The most consistently successful piece of technology presented in this dissertation is the inlaid absorbance cell. By using an experimentally determined procedure to embed black PMMA inserts into cavities, a fully optically isolated cell was designed and fabricated. Microprisms milled into clear windows within the black inserts were used to direct light from an LED, then through a fluid channel, and then back up out of the chip and to a photodiode detector. The prisms allowed the optical components to be entirely decoupled from the fluid portion of the sensor, which meant that the sensor itself could be designed to be more modular, with an easily replaceable microfluidic component.

The absorbance cell was further integrated into a fully functional *in situ* phosphate sensor. The sensor was designed and built in cooperation with Dartmouth Ocean

Technologies, and was then characterized, calibrated and deployed. The characterization showed that the sensor had a 15.2 nM limit of detection, and was able to reliably function in environmental temperatures down to 5° C. Furthermore, the sensor design can be modified to measure other nutrients *in situ*, which enables the possibility for an entire suite of *in situ* nutrient sensors.

The other important aspect of the modularity of the sensor is that other microfluidic technologies can be tested and implemented onto the same platform. We looked at performing continuous flow analysis using the same framework and system, but switching out only the chip itself. The tests showed that nitrite could be easily and rapidly measured using continuous flow analysis, and could even be measured using only 4 μL of injected reagent. However, the continuous flow system did not lend itself well to the measurement of phosphate and nitrate, both of which require a longer reaction time to produce discernible results. Another issue that impacted the sensitivity of the system for the other reagents was lensing as a result of the Schlieren effect. Several different approaches for addressing the effect were designed and tested, but none were able to completely negate it.

Lastly, cavity enhancement techniques were explored as a method to improve the sensitivity of the sensor. A multi-bounce sensor was modeled and built but turned out to be too sensitive to air bubbles to be reliably tested. Furthermore, simulations showed that the sensitivity could be improved by an order of magnitude if CRD was used on the absorbance cell. However, they also showed that the light source would need to be nearly perfectly collimated in order for that to work.

8.2. Outlook and Future Directions

Microfluidic devices as platforms for ocean variable monitoring are only gaining traction, and will likely become secure as widely used instruments. Beyond monitoring nutrient cycles, microfluidic devices are being applied to oceanic carbon dioxide removal (CDR) efforts, environmental DNA (eDNA) sampling, and ocean alkalinity enhancement (OAE) efforts. With the increasing number of use cases for microfluidic devices, it is crucial that robust supporting technologies such as valves and absorbance cells be developed. In particular, the development of reliable passive check valves would have far reaching impacts.

The solenoid valves currently integrated into the unit draw 160 mW each when activated using the power saving spike and hold configuration. Typical pumping requires that 3 or 4 valves are open at any given time, creating maximum draw of 640mW during the 15 seconds of pumping per sample. This results in an energy consumption of approximately 10 J, which means that almost 10 % of the total energy consumed during pumping is from the solenoid valves. Without the need for active solenoid valves, microfluidic sensors such as the one presented in this thesis could save a portion of their energy budget, thereby potentially prolonging the deployment time limit by an additional 10 %. Furthermore, without the additional solenoid valves, there need not be any oil-filled compartment adding complexity to the assembly and reducing serviceability. Furthermore, with embedded microvalves, complex fluid configurations and analysis techniques could be employed using the same form factor and no additional power. However, to realize the reliable and robust check valves, the issues identified in this thesis must first be addressed.

The primary two being the inconsistency in the cracking pressures and the sensitivity to air pockets.

The inlaid absorbance cell outlined here has been shown to be effective, simple and robust. It will continue to be used in future microfluidic devices, both in nutrient sensors and others currently under development. However, to make the inlaid cell more marketable, it would need to be more easily mass produced. In the current design, each inlaid piece is individually cut out and then manually inserted into the clear sheet. Only a single sheet can be created at a time, and from beginning to end it takes roughly 8 hours to create a sheet. Only once the sheet has been processed can it be mounted to the mill and the channels and features created. To mass produce these, multiple sheets must be simultaneously created, either with multiple fabrication setups or an alternative fabrication technique such as injection molding, 3D printing, or lithography.

The final sensor developed over the course of this work was the product of several iterations and efforts to address design challenges. In the end, the unit was field tested in the Bedford Basin, and generated results that were in alignment with externally validated measurements. Although the sensor did not meet the ideal requirements for long term deployment on the Argo profiling floats, it did perform within the requirements that were set to make it commercially competitive, as follows:

Metric	Requirement	Performance
Energy consumption (joules/sample)	< 500 J	126 J
Reagent consumption (mL/sample)	< 1 mL	0.5 mL
Sensor size (volume)	< 7000 cm^3	5780 cm^3

Deployment period (time)	> 3 months	2 – 3 months

The stated performance metric above needs context to be fully understood. The energy consumption is only the energy consumed while performing a single measurement. It does not include the energy consumed when flushing or sitting idle. The reagent consumption per sample is strictly how much reagent is used when the sensor is sampling from the environment. It does not represent the total volume of fluid waste that is generated while sampling, as it does not include the sampled fluid or the fluid consumed during flushing or standard measurements. Lastly, the sensor volume is the combined volume of the sensor unit and the reagent housing. The sensor unit on its own has a volume of 2440 cm^3. Furthermore, if the sensor is not connected to an external power source it will require a battery housing which is approximately the same size as the sensor itself. The stated metrics are the performance values required for the sensor to perform at its most basic level.

There is potential for improvement in the above values, particularly in the reagent consumption. The preliminary CFA tests showed that a linear relationship between nitrite concentration and absorbance could be observed using as little as 4 µL of reagent per sample, which is 125 times less reagent than it currently uses. This would also help to reduce the form factor and sensor volume as there would be less need for a large reagent housing. However, as already discussed, it is difficult to apply CFA to nutrients other than nitrite, and it would also likely increase the energy consumption as CFA requires continuous pumping. A way of reducing the energy consumption, if not using CFA, is to use passive check valves, rather than the active solenoid valves currently in the design.

Again, this has been discussed and the difficulties with manufacturing integral passive valves would need to be addressed to realize their potential.

With the emphasis on climate change and anthropogenic impact, there has been an increase of academic focus centered on ocean monitoring in the last few decades; a trend that is clearly observed in the field of microfluidics as well. Microfluidic technologies have been applied to several of the biological Essential Ocean Variables (EOVs) listed by the Global Ocean Observation System (GOOS). Nutrients, trace metals, dissolved organic and inorganic carbon, oxygen and further variables not listed as EOVs have all been applications for microfluidic devices. Advancements such as improved low-power valving and optical interrogation methods will enable sensors to be deployed for longer and more remotely, contributing to a global comprehensive map of ocean variables. Furthermore, other supporting technologies such as integral heaters, reduction columns or advanced reaction chambers will expand the range of variables and techniques available to microfluidic devices. In the coming years, these technologies will also be a foundation for creating *in situ* instruments for studying biodiversity at the genetic level. Microfluidics will be used to further develop *in situ* eDNA samplers, devices with on-chip PCR capabilities and sensors that can carry out assay techniques that are traditionally performed in a lab. Although devices such as those are still under development, they are gaining traction in the microfluidics community. The sensor and technologies presented in this dissertation serve to advance the field, with open ended application. Valves and absorbance cells are a bedrock for microfluidic devices and nutrient analysis provides a foundation for understanding ocean variable dynamics.

BIBLIOGRAPHY

[1] P. Dexter and C. Summerhayes, “Ocean observations: the Global Ocean Observing System,” in *Troubled Waters: Ocean Science and Governance*, Cambridge: Cambridge University Press, 2010, pp. 161–178.

[2] D. Fowler *et al.*, “The global nitrogen cycle in the twenty-first century,” *Philos. Trans. Biol. Sci.*, vol. 368, no. 1621, pp. 1–13, 2013.

[3] T. Tyrrell, “The relative influences of nitrogen and phosphorus on oceanic primary production,” *Nature*, vol. 400, no. 6744, p. 525, Aug. 1999, doi: 10.1038/22941.

[4] R. J. Diaz and R. Rosenberg, “Spreading Dead Zones and Consequences for Marine Ecosystems,” *Science*, vol. 321, no. 5891, pp. 926–929, 2008.

[5] D. Breitburg *et al.*, “Declining oxygen in the global ocean and coastal waters,” *Science*, vol. 359, no. 6371, p. eaam7240, Jan. 2018, doi: 10.1126/science.aam7240.

[6] T. D. Jickells *et al.*, “Global Iron Connections between Desert Dust, Ocean Biogeochemistry, and Climate,” *Science*, vol. 308, no. 5718, pp. 67–71, 2005.

[7] J. J. Cole *et al.*, “Plumbing the Global Carbon Cycle: Integrating Inland Waters into the Terrestrial Carbon Budget,” *Ecosystems*, vol. 10, no. 1, pp. 172–185, Feb. 2007, doi: 10.1007/s10021-006-9013-8.

[8] J. C. Orr *et al.*, “Anthropogenic ocean acidification over the twenty-first century and its impact on calcifying organisms,” *Nature*, vol. 437, no. 7059, pp. 681–686, Sep. 2005, doi: 10.1038/nature04095.

[9] B. Worm *et al.*, “Impacts of Biodiversity Loss on Ocean Ecosystem Services,” *Science*, vol. 314, no. 5800, pp. 787–790, 2006.

[10] E. B. Kujawinski, M. C. Kido Soule, D. L. Valentine, A. K. Boysen, K. Longnecker, and M. C. Redmond, “Fate of Dispersants Associated with the Deepwater Horizon Oil Spill,” *Environ. Sci. Technol.*, vol. 45, no. 4, pp. 1298–1306, Feb. 2011, doi: 10.1021/es103838p.

[11] E. R. Zettler, T. J. Mincer, and L. A. Amaral-Zettler, “Life in the ‘Plastisphere’: Microbial Communities on Plastic Marine Debris,” *Environ. Sci. Technol.*, vol. 47, no. 13, pp. 7137–7146, Jul. 2013, doi: 10.1021/es401288x.

[12] E. Zaikova, A. Hawley, D. A. Walsh, and S. J. Hallam, “Seawater Sampling and Collection,” *J. Vis. Exp. JoVE*, no. 28, Jun. 2009, doi: 10.3791/1159.

[13] A. D. Beaton *et al.*, “Lab-on-Chip Measurement of Nitrate and Nitrite for In Situ Analysis of Natural Waters,” *Environ. Sci. Technol.*, vol. 46, no. 17, pp. 9548–9556, Sep. 2012, doi: 10.1021/es300419u.

[14] F. Choo *et al.*, “Performance evaluation of in situ fluorometers for real-time cyanobacterial monitoring,” *H2Open J.*, vol. 1, no. 1, pp. 26–46, Jul. 2018, doi: 10.2166/h2oj.2018.009.

[15] M. Cuartero, “Electrochemical sensors for in-situ measurement of ions in seawater,” *Sens. Actuators B Chem.*, vol. 334, p. 129635, May 2021, doi: 10.1016/j.snb.2021.129635.

[16] G. M. Whitesides, “The origins and the future of microfluidics,” *Nature*, vol. 442, no. 7101, pp. 368–373, Jul. 2006, doi: 10.1038/nature05058.

[17] A. K. Yetisen, M. S. Akram, and C. R. Lowe, “Paper-based microfluidic point-of-care diagnostic devices,” *Lab. Chip*, vol. 13, no. 12, pp. 2210–2251, May 2013, doi: 10.1039/C3LC50169H.

[18] S. Nagrath *et al.*, “Isolation of rare circulating tumour cells in cancer patients by microchip technology,” *Nature*, vol. 450, no. 7173, pp. 1235–1239, Dec. 2007, doi: 10.1038/nature06385.

[19] D. J. Beebe, G. A. Mensing, and G. M. Walker, “Physics and Applications of Microfluidics in Biology,” *Annu. Rev. Biomed. Eng.*, vol. 4, no. 1, pp. 261–286, Aug. 2002, doi: 10.1146/annurev.bioeng.4.112601.125916.

[20] M. Toner and D. Irimia, “Blood-on-a-Chip,” *Annu. Rev. Biomed. Eng.*, vol. 7, no. 1, pp. 77–103, Aug. 2005, doi: 10.1146/annurev.bioeng.7.011205.135108.

[21] C. Yi, C.-W. Li, S. Ji, and M. Yang, “Microfluidics technology for manipulation and analysis of biological cells,” *Anal. Chim. Acta*, vol. 560, no. 1, pp. 1–23, Feb. 2006, doi: 10.1016/j.aca.2005.12.037.

[22] K. Ohno, K. Tachikawa, and A. Manz, “Microfluidics: Applications for analytical purposes in chemistry and biochemistry,” *ELECTROPHORESIS*, vol. 29, no. 22, pp. 4443–4453, 2008, doi: 10.1002/elps.200800121.

[23] G.-B. Lee, S.-H. Chen, G.-R. Huang, W.-C. Sung, and Y.-H. Lin, “Microfabricated plastic chips by hot embossing methods and their applications for DNA separation and detection,” *Sens. Actuators B Chem.*, vol. 75, no. 1, pp. 142–148, Apr. 2001, doi: 10.1016/S0925-4005(00)00745-0.

[24] N. Shembekar, C. Chaipan, R. Utharala, and C. A. Merten, “Droplet-based microfluidics in drug discovery, transcriptomics and high-throughput molecular genetics,” *Lab. Chip*, vol. 16, no. 8, pp. 1314–1331, 2016, doi: 10.1039/C6LC00249H.

[25] Y. Zhang, H. F. Chan, and K. W. Leong, “Advanced materials and processing for drug delivery: The past and the future,” *Adv. Drug Deliv. Rev.*, vol. 65, no. 1, pp. 104–120, Jan. 2013, doi: 10.1016/j.addr.2012.10.003.

[26] C. Hu, J. E. Morris, and R. L. Hartman, “Microfluidic investigation of the deposition of asphaltenes in porous media,” *Lab. Chip*, vol. 14, no. 12, pp. 2014–2022, May 2014, doi: 10.1039/C4LC00192C.

[27] M. H. Schneider, V. J. Sieben, A. M. Kharrat, and F. Mostowfi, “Measurement of Asphaltenes Using Optical Spectroscopy on a Microfluidic Platform,” *Anal. Chem.*, vol. 85, no. 10, pp. 5153–5160, May 2013, doi: 10.1021/ac400495x.

[28] F. K. Balagaddé, L. You, C. L. Hansen, F. H. Arnold, and S. R. Quake, “Long-term monitoring of bacteria undergoing programmed population control in a microchemostat,” *Science*, vol. 309, no. 5731, pp. 137–140, Jul. 2005, doi: 10.1126/science.1109173.

[29] L. Wang, R. Kodzius, X. Yi, S. Li, Y. S. Hui, and W. Wen, “Prototyping chips in minutes: Direct Laser Plotting (DLP) of functional microfluidic structures,” *Sens. Actuators B Chem.*, vol. 168, pp. 214–222, Jun. 2012, doi: 10.1016/j.snb.2012.04.011.

[30] M. Saqib, O. B. Şahinoğlu, and E. Y. Erdem, “Alternating Droplet Formation by using Tapered Channel Geometry,” *Sci. Rep.*, vol. 8, no. 1, Art. no. 1, Jan. 2018, doi: 10.1038/s41598-018-19966-y.

[31] A. M. Nightingale, A. D. Beaton, and M. C. Mowlem, “Trends in microfluidic systems for in situ chemical analysis of natural waters,” *Sens. Actuators B Chem.*, vol. 221, pp. 1398–1405, Dec. 2015, doi: 10.1016/j.snb.2015.07.091.

[32] J.-H. Ahn, K. H. Jo, and J. H. Hahn, “Standard addition/absorption detection microfluidic system for salt error-free nitrite determination,” *Anal. Chim. Acta*, vol. 886, pp. 114–122, Jul. 2015, doi: 10.1016/j.aca.2015.06.009.

[33] G. Duffy, I. Maguire, B. Heery, C. Nwankire, J. Ducrée, and F. Regan, “PhosphaSense: A fully integrated, portable lab-on-a-disc device for phosphate determination in water,” *Sens. Actuators B Chem.*, vol. 246, pp. 1085–1091, Jul. 2017, doi: 10.1016/j.snb.2016.12.040.

[34] R. Liu, R. Ishimatsu, M. Yahiro, C. Adachi, K. Nakano, and T. Imato, “Photometric flow injection determination of phosphate on a PDMS microchip using an optical detection system assembled with an organic light emitting diode and an organic photodiode,” *Talanta*, vol. 132, pp. 96–105, Jan. 2015, doi: 10.1016/j.talanta.2014.08.057.

[35] A. G. Vincent *et al.*, “Nitrate drawdown during a shelf sea spring bloom revealed using a novel microfluidic in situ chemical sensor deployed within an autonomous underwater glider,” *Mar. Chem.*, vol. 205, pp. 29–36, Sep. 2018, doi: 10.1016/j.marchem.2018.07.005.

[36] X. Cao, S. W. Zhang, D. Z. Chu, N. Wu, H. K. Ma, and Y. Liu, “A design of spectrophotometric microfluidic chip sensor for analyzing silicate in seawater,” *IOP Conf. Ser. Earth Environ. Sci.*, vol. 82, p. 012080, Aug. 2017, doi: 10.1088/1755-1315/82/1/012080.

[37] S. C. Morgan, A. D. Hendricks, M. L. Seto, and V. J. Sieben, “A Magnetically Tunable Check Valve Applied to a Lab-on-Chip Nitrite Sensor,” *Sensors*, vol. 19, no. 21, Art. no. 21, Jan. 2019, doi: 10.3390/s19214619.

[38] S. Morgan, E. Luy, A. Furlong, and V. Sieben, “A submersible phosphate analyzer for marine environments based on inlaid microfluidics,” *Anal. Methods*, vol. 14, no. 1, pp. 22–33, 2022, doi: 10.1039/d1ay01876k.

[39] E. A. Luy, S. C. Morgan, J. J. Creelman, B. J. Murphy, and V. J. Sieben, “Inlaid microfluidic optics: absorbance cells in clear devices applied to nitrite and phosphate detection,” *J. Micromechanics Microengineering*, vol. 30, no. 9, p. 095001, Jun. 2020, doi: 10.1088/1361-6439/ab9202.

[40] C. Sonnichsen *et al.*, “An Automated Microfluidic Analyzer for In Situ Monitoring of Total Alkalinity,” *ACS Sens.*, Jan. 2023, doi: 10.1021/acssensors.2c02343.

[41] S. Morgan, E. Luy, and V. Sieben, “Inlaid microfluidics for nutrient monitoring,” in *The 23rd International Conference on Miniaturized Systems for Chemistry and Life Sciences*, Basel, Switzerland, Oct. 2019.

[42] B. Murphy, S. Morgan, E. Luy, J. Creelman, and V. Sieben, “Lab-on-a-chip Sensor for In Situ Nutrient Monitoring,” in *OCEANS 2019 MTS/IEEE SEATTLE*, Oct. 2019, pp. 1–7. doi: 10.23919/OCEANS40490.2019.8962689.

[43] S. Morgan *et al.*, “An In Situ Phosphate Analyzer for Marine Environments Using Inlaid Microfluidics,” in *OCEANS 2021: San Diego – Porto*, Sep. 2021, pp. 1–9. doi: 10.23919/OCEANS44145.2021.9706097.

[44] S. Morgan, “Inlaid Microfluidics fo In Situ Phosphate Sensing,” in *Emerging Investigators in Microfluidics*, Online, Jul. 2021.

[45] E. Luy *et al.*, “Simultaneous in situ Nitrate and Orthophosphate Measurement Using a Dual Chemistry Microfluidic Sensor,” in *OCEANS 2022, Hampton Roads*, Oct. 2022, pp. 1–8. doi: 10.1109/OCEANS47191.2022.9976956.

[46] S. Morgan, E. Luy, and V. Sieben, “Low-cost Microfluidic Nutrient Sensors,” presented at the Marine Environmental Observation, Prediction and Response Network Annual General Meeting, Victoria, B.C. Canada, 2019.

[47] S. Morgan *et al.*, “In Situ Phosphate Analysis Using Inlaid Microfluidics,” in *The 25th International Conference on Miniaturized Systems for Chemistry and Life Sciences*, Palm Springs, California, 2021.

[48] S. Morgan, A. Hendricks, and V. Sieben, “Improvements to colorimetric absorbance measurement techniques for nutrient analysis on microfluidic devices,” in *Ocean Frontier Institute*, Halifax, Nova Scotia, 2022.

[49] E. A. LUY, S. C. MORGAN, and V. J. Sieben, “Optical cell and methods of manufacturing an optical cell,” US20220082490A1, Mar. 17, 2022 Accessed: Jan. 08, 2023. [Online]. Available: https://patents.google.com/patent/US20220082490A1/en?q=inlaid+optical+cell&oq=inlaid+optical+cell

[50] A. Henriksen, “An automatic method for determining nitrate and nitrite in fresh and saline waters,” *Analyst*, vol. 90, no. 1067, pp. 83–88, Jan. 1965, doi: 10.1039/AN9659000083.

[51] Adrian M. Nightingale, S.-U. HASSAN, G. W.H. Evans, S. M Coleman, and X. Niu, “Nitrate measurement in droplet flow: Gas-mediated crosstalk and correction,” *Lab. Chip*, vol. 18, Jun. 2018, doi: 10.1039/C8LC00092A.

[52] G. S. Clinton-Bailey *et al.*, “A Lab-on-Chip Analyzer for in Situ Measurement of Soluble Reactive Phosphate: Improved Phosphate Blue Assay and Application to Fluvial Monitoring,” *Environ. Sci. Technol.*, vol. 51, no. 17, pp. 9989–9995, Sep. 2017, doi: 10.1021/acs.est.7b01581.

[53] J. Murphy and J. P. Riley, “A modified single solution method for the determination of phosphate in natural waters,” *Anal. Chim. Acta*, vol. 27, pp. 31–36, Jan. 1962, doi: 10.1016/S0003-2670(00)88444-5.

[54] J. B. Mullin and J. P. Riley, “The spectrophotometric determination of nitrate in natural waters, with particular reference to sea-water,” *Anal. Chim. Acta*, vol. 12, pp. 464–480, Jan. 1955, doi: 10.1016/S0003-2670(00)87865-4.

[55] W. B. Fortune and M. G. Mellon, “Determination of Iron with o-Phenanthroline: A Spectrophotometric Study,” *Ind. Eng. Chem. Anal. Ed.*, vol. 10, no. 2, pp. 60–64, Feb. 1938, doi: 10.1021/ac50118a004.

[56] L. L. Stookey, “Ferrozine---a new spectrophotometric reagent for iron,” *Anal. Chem.*, vol. 42, no. 7, pp. 779–781, Jun. 1970, doi: 10.1021/ac60289a016.

[57] T. Korenaga, S. Motomizu, and K. Tôei, “Spectrophotometric determination of boron in natural waters by solvent extraction with chromotropic acid and removal of the excess of reagent,” *The Analyst*, vol. 103, no. 1228, pp. 745–753, 1978, doi: 10.1039/AN9780300745.

[58] M. Kajiwara and K. Goto, “Successive spectrophotometric determinations of manganese and iron in water with formaldoxime,” *Bunseki Kagaku*, vol. 13, no. 6, pp. 529–532, 1964, doi: 10.2116/bunsekikagaku.13.529.

[59] A. S. Madison, B. M. Tebo, and G. W. Luther III, “Simultaneous determination of soluble manganese(III), manganese(II) and total manganese in natural (pore)waters,” *Talanta*, vol. 84, no. 2, pp. 374–381, 2011, doi: 10.1016/j.talanta.2011.01.025.

[60] C. M. Rushworth, J. Davies, J. T. Cabral, P. R. Dolan, J. M. Smith, and C. Vallance, “Cavity-enhanced optical methods for online microfluidic analysis,” *Chem. Phys. Lett.*, vol. 554, pp. 1–14, Dec. 2012, doi: 10.1016/j.cplett.2012.10.009.

[61] M. T. Meyer, V. Roy, W. E. Bentley, and R. Ghodssi, “A microfluidic platform for optical absorbance monitoring of bacterial biofilms,” in *2010 IEEE SENSORS*, Nov. 2010, pp. 2291–2294. doi: 10.1109/ICSENS.2010.5690803.

[62] A. Chandrasekaran and M. Packirisamy, “Absorption detection of enzymatic reaction using optical microfluidics based intermittent flow microreactor system,” *IEE Proc. - Nanobiotechnology*, vol. 153, no. 6, pp. 137–143, Dec. 2006, doi: 10.1049/ip-nbt:20060012.

[63] Y. Li and X.-L. Su, “Microfluidics-Based Optical Biosensing Method for Rapid Detection of Escherichia Coli O157:h7,” *J. Rapid Methods Autom. Microbiol.*, vol. 14, no. 1, pp. 96–109, Mar. 2006, doi: 10.1111/j.1745-4581.2006.00034.x.

[64] Y.-C. Tung *et al.*, “Optofluidic detection for cellular phenotyping,” *Lab. Chip*, vol. 12, no. 19, pp. 3552–3565, Aug. 2012, doi: 10.1039/C2LC40509A.

[65] E. Banoth, V. K. Jagannadh, and S. S. Gorthi, “Single-Cell Optical Absorbance Characterization With High-Throughput Microfluidic Microscopy,” *IEEE J. Sel. Top. Quantum Electron.*, vol. 22, no. 3, pp. 111–116, May 2016, doi: 10.1109/JSTQE.2015.2414912.

[66] N. Yanagisawa, “Development of microfluidic devices for biological analyses and energy applications,” Ph.D., University of Wyoming, United States -- Wyoming, 2013. Accessed: Oct. 11, 2018. [Online]. Available: https://search.proquest.com/docview/1492137807/abstract/1C956C34A586417APQ/1

[67] A. Zamyadi, R. K. Henderson, R. Stuetz, G. Newcombe, K. Newtown, and B. Gladman, “Cyanobacterial management in full-scale water treatment and recycling processes: Reactive dosing following intensive monitoring,” *Environ. Sci. Water Res. Technol.*, vol. 2, no. 2, pp. 362–375, 2016, doi: 10.1039/c5ew00269a.

[68] M. Soja-Woźniak, S. E. Craig, S. Kratzer, B. Wojtasiewicz, M. Darecki, and C. T. Jones, “A Novel Statistical Approach for Ocean Colour Estimation of Inherent Optical Properties and Cyanobacteria Abundance in Optically Complex Waters,” *Remote Sens.*, vol. 9, no. 4, Art. no. 4, Apr. 2017, doi: 10.3390/rs9040343.

[69] J. J. Creelman, E. A. Luy, G. C. H. Beland, C. Sonnichsen, and V. J. Sieben, “Simultaneous absorbance and fluorescence measurements using an inlaid microfluidic approach,” *Sensors*, vol. 21, no. 18, 2021, doi: 10.3390/s21186250.

[70] H. C. Bittig *et al.*, “Oxygen Optode Sensors: Principle, Characterization, Calibration, and Application in the Ocean,” *Front. Mar. Sci.*, vol. 4, 2018, doi: 10.3389/fmars.2017.00429.

[71] E. Fritzsche *et al.*, “A validation and comparison study of new, compact, versatile optodes for oxygen, pH and carbon dioxide in marine environments,” *Mar. Chem.*, vol. 207, pp. 63–76, Nov. 2018, doi: 10.1016/j.marchem.2018.10.009.

[72] A. Tengberg *et al.*, “Evaluation of a lifetime-based optode to measure oxygen in aquatic systems: Lifetime-based optode to measure oxygen,” *Limnol. Oceanogr. Methods*, vol. 4, no. 2, pp. 7–17, Feb. 2006, doi: 10.4319/lom.2006.4.7.

[73] M. M. F. Choi and D. Xiao, “Oxygen-sensitive reverse-phase optode membrane using silica gel-adsorbed ruthenium(II) complex embedded in gelatin film1This work was submitted to Chinese Patent office for patent application (Application no. 98 1 12477.1) on 12 May 1998.1,” *Anal. Chim. Acta*, vol. 387, no. 2, pp. 197–205, Apr. 1999, doi: 10.1016/S0003-2670(99)00040-9.

[74] X. Xiong, D. Xiao, and Martin. M. F. Choi, “Dissolved oxygen sensor based on fluorescence quenching of oxygen-sensitive ruthenium complex immobilized on silica–Ni–P composite coating,” *Sens. Actuators B Chem.*, vol. 117, no. 1, pp. 172–176, Sep. 2006, doi: 10.1016/j.snb.2005.11.044.

[75] P. Hartmann, M. J. P. Leiner, and P. Kohlbacher, “Photobleaching of a ruthenium complex in polymers used for oxygen optodes and its inhibition by singlet oxygen quenchers,” *Sens. Actuators B Chem.*, vol. 51, no. 1, pp. 196–202, Aug. 1998, doi: 10.1016/S0925-4005(98)00188-9.

[76] S. M. Borisov, G. Zenkl, and I. Klimant, “Phosphorescent Platinum(II) and Palladium(II) Complexes with Azatetrabenzoporphyrins—New Red Laser Diode-Compatible Indicators for Optical Oxygen Sensing,” *ACS Appl. Mater. Interfaces*, vol. 2, no. 2, pp. 366–374, Feb. 2010, doi: 10.1021/am900932z.

[77] D. A. Zubenko, M. A. Noginov, V. A. Smirnov, and I. A. Shcherbakov, “Different mechanisms of nonlinear quenching of luminescence,” *Phys. Rev. B*, vol. 55, no. 14, pp. 8881–8886, Apr. 1997, doi: 10.1103/PhysRevB.55.8881.

[78] A. Penzkofer and Y. Lu, “Fluorescence quenching of rhodamine 6G in methanol at high concentration,” *Chem. Phys.*, vol. 103, no. 2, pp. 399–405, Apr. 1986, doi: 10.1016/0301-0104(86)80041-6.

[79] H. Boaz and G. Rollefson, “The Quenching of Fluorescence - Deviations from the Stern Volmer Law,” *J. Am. Chem. Soc.*, vol. 72, no. 8, pp. 3435–3443, 1950, doi: 10.1021/ja01164a032.

[80] C. von Bültzingslöwen, A. K. McEvoy, C. McDonagh, and B. D. MacCraith, “Lifetime-based optical sensor for high-level pCO2 detection employing fluorescence resonance energy transfer,” *Anal. Chim. Acta*, vol. 480, no. 2, pp. 275–283, Mar. 2003, doi: 10.1016/S0003-2670(02)01653-7.

[81] J. S. Clarke, E. P. Achterberg, D. P. Connelly, U. Schuster, and M. Mowlem, “Developments in marine pCO2 measurement technology; towards sustained in situ observations,” *TrAC Trends Anal. Chem.*, vol. 88, pp. 53–61, Mar. 2017, doi: 10.1016/j.trac.2016.12.008.

[82] C. Staudinger *et al.*, “A versatile optode system for oxygen, carbon dioxide, and pH measurements in seawater with integrated battery and logger,” *Limnol. Oceanogr. Methods*, vol. 16, no. 7, pp. 459–473, 2018, doi: https://doi.org/10.1002/lom3.10260.

[83] J. W. Grate, B. Liu, R. T. Kelly, N. C. Anheier, and T. M. Schmidt, “Microfluidic Sensors with Impregnated Fluorophores for Simultaneous Imaging of Spatial Structure and Chemical Oxygen Gradients,” *ACS Sens.*, vol. 4, no. 2, pp. 317–325, Feb. 2019, doi: 10.1021/acssensors.8b00924.

[84] J. W. Grate *et al.*, “Chemical sensing and imaging in microfluidic pore network structures relevant to natural carbon cycling and industrial carbon sequestration,” in *Micro- and Nanotechnology Sensors, Systems, and Applications V*, SPIE, Jun. 2013, pp. 397–404. doi: 10.1117/12.2018520.

[85] M. A. Ashagre and T. Masadome, “A New Microfluidic Polymer Chip with an Embedded Cationic Surfactant Ion-selective Optode as a Detector for the Determination of Cationic Surfactants,” *Anal. Sci.*, vol. 34, no. 2, pp. 195–199, 2018, doi: 10.2116/analsci.34.195.

[86] R. Millard, J. Toole, and M. Swartz, “A fast responding temperature measurement system for CTD applications,” *Ocean Eng.*, vol. 7, no. 3, pp. 413–427, Jan. 1980, doi: 10.1016/0029-8018(80)90007-4.

[87] E. P. Achterberg and C. Braungardt, “Stripping voltammetry for the determination of trace metal speciation and in-situ measurements of trace metal distributions in marine waters,” *Anal. Chim. Acta*, vol. 400, no. 1, pp. 381–397, Nov. 1999, doi: 10.1016/S0003-2670(99)00619-4.

[88] C. Collado-Sánchez, J. Pérez-Peña, M. D. Gelado-Caballero, J. A. Herrera-Melian, and J. J. Hernández-Brito, “Rapid determination of copper, lead and cadmium in unpurged seawater by adsorptive stripping voltammetry,” *Anal. Chim. Acta*, vol. 320, no. 1, pp. 19–30, Feb. 1996, doi: 10.1016/0003-2670(95)00513-7.

[89] R. W. Jakuba, J. W. Moffett, and M. A. Saito, “Use of a modified, high-sensitivity, anodic stripping voltammetry method for determination of zinc speciation in the North Atlantic Ocean,” *Anal. Chim. Acta*, vol. 614, no. 2, pp. 143–152, May 2008, doi: 10.1016/j.aca.2008.03.006.

[90] E. Bakker and E. Pretsch, “Modern Potentiometry,” *Angew. Chem. Int. Ed.*, vol. 46, no. 30, pp. 5660–5668, 2007, doi: 10.1002/anie.200605068.

[91] V. Rérolle *et al.*, “Development of a novel hybrid pH sensor for deployment on autonomous profiling platforms,” in *OCEANS 2019 - Marseille*, Jun. 2019, pp. 1–8. doi: 10.1109/OCEANSE.2019.8867572.

[92] C. M. Yentsch, “Flow cytometry and sorting,” *Eos Trans. Am. Geophys. Union*, vol. 64, no. 23, pp. 403–403, 1983, doi: 10.1029/EO064i023p00403-03.

[93] P. Rodriguez-Mateos, N. F. Azevedo, C. Almeida, and N. Pamme, “FISH and chips: a review of microfluidic platforms for FISH analysis,” *Med. Microbiol. Immunol. (Berl.)*, vol. 209, no. 3, pp. 373–391, 2020, doi: 10.1007/s00430-019-00654-1.

[94] G. Gerdts and G. Luedke, “FISH and chips: Marine bacterial communities analyzed by flow cytometry based on microfluidics,” *J. Microbiol. Methods*, vol. 64, no. 2, pp. 232–240, 2006, doi: 10.1016/j.mimet.2005.05.001.

[95] J. R. Hands and G. A. Cooksey, “Integrated optical waveguides for in situ microflow measurement,” presented at the 21st International Conference on Miniaturized Systems for Chemistry and Life Sciences, MicroTAS 2017, 2020, pp. 1513–1514.

[96] E. E. Clerc, J.-B. Raina, B. S. Lambert, J. Seymour, and R. Stocker, “In situ chemotaxis assay to examine microbial behavior in aquatic ecosystems,” *J. Vis. Exp.*, vol. 2020, no. 159, 2020, doi: 10.3791/61062.

[97] D. S. de Bruijn, P. M. ter Braak, D. B. van de Waal, W. Olthuis, and A. van den Berg, “Ocean carbon cycle studied by single-cell impedance cytometry on calcifying algae,” presented at the MicroTAS 2020 - 24th International Conference on Miniaturized Systems for Chemistry and Life Sciences, 2020, pp. 803–804.

[98] M. Héder, “From NASA to EU: the evolution of the TRL scale in Public Sector Innovation,” *Innov. J.*, vol. 22, no. 2, Art. no. 2, 2017.

[99] G. Moschonas *et al.*, “Nitrogen dynamics and phytoplankton community structure: the role of organic nutrients,” *Biogeochemistry*, vol. 134, no. 1, pp. 125–145, Jul. 2017, doi: 10.1007/s10533-017-0351-8.

[100] D. G. Capone, J. P. Zehr, H. W. Paerl, B. Bergman, and E. J. Carpenter, “Trichodesmium, a globally significant marine cyanobacterium,” *Science*, vol. 276, no. 5316, pp. 1221–1229, 1997, doi: 10.1126/science.276.5316.1221.

[101] J. J. Elser *et al.*, “Global analysis of nitrogen and phosphorus limitation of primary producers in freshwater, marine and terrestrial ecosystems,” *Ecol. Lett.*, vol. 10, no. 12, pp. 1135–1142, 2007, doi: 10.1111/j.1461-0248.2007.01113.x.

[102] S. Malviya *et al.*, “Insights into global diatom distribution and diversity in the world’s ocean,” *Proc. Natl. Acad. Sci.*, vol. 113, no. 11, pp. E1516–E1525, Mar. 2016, doi: 10.1073/pnas.1509523113.

[103] E. V. Dafner, “Segmented continuous-flow analyses of nutrient in seawater: intralaboratory comparison of Technicon AutoAnalyzer II and Bran+Luebbe Continuous Flow AutoAnalyzer III,” *Limnol. Oceanogr. Methods*, vol. 13, no. 10, pp. 511–520, 2015, doi: https://doi.org/10.1002/lom3.10035.

[104] V. J. Sieben, C. F. A. Floquet, I. R. G. Ogilvie, M. C. Mowlem, and H. Morgan, “Microfluidic colourimetric chemical analysis system: Application to nitrite detection,” *Anal. Methods*, vol. 2, no. 5, pp. 484–491, 2010, doi: 10.1039/C002672G.

[105] I. R. G. Ogilvie, V. Sieben, C. F. A. Floquet, R. Zmijan, M. Mowlem, and H. Morgan, *Solvent processing of PMMA and COC chips for bonding devices with optical quality surfaces*, vol. 2. 2010.

[106] A. D. Beaton *et al.*, “Lab-on-Chip for In Situ Analysis of Nutrients in the Deep Sea,” *ACS Sens.*, vol. 7, no. 1, pp. 89–98, Jan. 2022, doi: 10.1021/acssensors.1c01685.

[107] A. D. Beaton *et al.*, “High-Resolution in Situ Measurement of Nitrate in Runoff from the Greenland Ice Sheet,” *Environ. Sci. Technol.*, vol. 51, no. 21, pp. 12518–12527, Nov. 2017, doi: 10.1021/acs.est.7b03121.

[108] A. M. Nightingale *et al.*, “A Droplet Microfluidic-Based Sensor for Simultaneous in Situ Monitoring of Nitrate and Nitrite in Natural Waters,” *Environ. Sci. Technol.*, vol. 53, no. 16, pp. 9677–9685, Aug. 2019, doi: 10.1021/acs.est.9b01032.

[109] M. M. Grand *et al.*, “A Lab-On-Chip Phosphate Analyzer for Long-term In Situ Monitoring at Fixed Observatories: Optimization and Performance Evaluation in Estuarine and Oligotrophic Coastal Waters,” *Front. Mar. Sci.*, vol. 4, 2017, doi: 10.3389/fmars.2017.00255.

[110] A. Donohoe, G. Lacour, P. McCluskey, D. Diamond, and M. McCaul, “Development of a Cost-Effective Sensing Platform for Monitoring Phosphate in Natural Waters,” *Chemosensors*, vol. 6, no. 4, p. 57, Dec. 2018, doi: 10.3390/chemosensors6040057.

[111] T. Hull, N. Greenwood, A. Birchill, A. Beaton, M. Palmer, and J. Kaiser, “Simultaneous assessment of oxygen- and nitrate-based net community production in a temperate shelf sea from a single ocean glider,” *Biogeosciences*, vol. 18, no. 23, pp. 6167–6180, Dec. 2021, doi: 10.5194/bg-18-6167-2021.

[112] S. A. Lahari, K. Amreen, S. K. Dubey, R. N. Ponnalagu, and S. Goel, “Modified Ultra Micro-Carbon Electrode for Efficient Ammonia Sensing for Water Quality Assessment,” *IEEE Trans. NanoBioscience*, pp. 1–1, 2022, doi: 10.1109/TNB.2022.3188605.

[113] P. Rajasulochana *et al.*, “Paper-based microfluidic colorimetric sensor on a 3D printed support for quantitative detection of nitrite in aquatic environments,” *Environ. Res.*, vol. 208, 2022, doi: 10.1016/j.envres.2022.112745.

[114] J. O’Grady, N. Kent, and F. Regan, “Design, build and demonstration of a fast, reliable portable phosphate field analyser,” *Case Stud. Chem. Environ. Eng.*, vol. 4, 2021, doi: 10.1016/j.cscee.2021.100168.

[115] Y. Chen *et al.*, “Toward an in situ phosphate sensor in natural waters using a microfluidic flow loop analyzer,” *J. Electrochem. Soc.*, vol. 165, no. 14, pp. B737–B745, 2018, doi: 10.1149/2.0891814jes.

[116] W. Khongpet, S. Pencharee, C. Puangpila, S. K. Hartwell, S. Lapanantnoppakhun, and J. Jakmunee, “A compact hydrodynamic sequential injection system for consecutive on-line determination of phosphate and ammonium,” *Microchem. J.*, vol. 147, pp. 403–410, 2019, doi: 10.1016/j.microc.2019.03.040.

[117] C. Barus *et al.*, “First Deployment and Validation of in Situ Silicate Electrochemical Sensor in Seawater,” *Front. Mar. Sci.*, vol. 5, 2018, Accessed: Aug. 01, 2022. [Online]. Available: https://www.frontiersin.org/articles/10.3389/fmars.2018.00060

[118] M. Yücel, A. D. Beaton, M. Dengler, M. C. Mowlem, F. Sohl, and S. Sommer, “Nitrate and Nitrite Variability at the Seafloor of an Oxygen Minimum Zone Revealed by a Novel Microfluidic In-Situ Chemical Sensor,” *PLoS ONE*, vol. 10, no. 7, Jul. 2015, doi: 10.1371/journal.pone.0132785.

[119] “Griess Reagent for nitrite extrapure |SRL Chemicals India.” http://srlchemicals.com/products/compound/Griess-Reagent-for-Nitrite/35657 (accessed Apr. 26, 2023).

[120] S. Tsang, F. Phu, M. M. Baum, and G. A. Poskrebyshev, “Determination of phosphate/arsenate by a modified molybdenum blue method and reduction of arsenate by S2O42−,” *Talanta*, vol. 71, no. 4, pp. 1560–1568, Mar. 2007, doi: 10.1016/j.talanta.2006.07.043.

[121] H. Heidari-Bafroui, A. Charbaji, C. Anagnostopoulos, and M. Faghri, “A Colorimetric Dip Strip Assay for Detection of Low Concentrations of Phosphate in Seawater,” *Sensors*, vol. 21, no. 9, Art. no. 9, Jan. 2021, doi: 10.3390/s21093125.

[122] D. Copetti, L. Valsecchi, A. G. Capodaglio, and G. Tartari, “Direct measurement of nutrient concentrations in freshwaters with a miniaturized analytical probe: evaluation and validation,” *Environ. Monit. Assess.*, vol. 189, no. 4, p. 144, Apr. 2017, doi: 10.1007/s10661-017-5847-0.

[123] A. Tagliabue, A. R. Bowie, P. W. Boyd, K. N. Buck, K. S. Johnson, and M. A. Saito, “The integral role of iron in ocean biogeochemistry,” *Nature*, vol. 543, no. 7643, Art. no. 7643, Mar. 2017, doi: 10.1038/nature21058.

[124] C. M. Rushworth, Y. Yogarajah, Y. Zhao, H. Morgan, and C. Vallance, “Sensitive analysis of trace water analytes using colourimetric cavity ringdown spectroscopy,” *Anal. Methods*, vol. 5, no. 1, pp. 239–247, Dec. 2012, doi: 10.1039/C2AY25889G.

[125] C. M. Longhini, F. Sá, and R. R. Neto, “Review and synthesis: iron input, biogeochemistry, and ecological approaches in seawater,” *Environ. Rev.*, vol. 27, no. 2, pp. 125–137, Jun. 2019, doi: 10.1139/er-2018-0020.

[126] J. Woods and M. Mellon, “Thiocyanate Method for Iron: A Spectrophotometric Study,” *Ind. Eng. Chem. Anal. Ed.*, vol. 13, no. 8, pp. 551–554, Aug. 1941, doi: 10.1021/i560096a013.

[127] K. H. Coale, C. S. Chin, G. J. Massoth, K. S. Johnson, and E. T. Baker, “In situ chemical mapping of dissolved iron and manganese in hydrothermal plumes,” *Nature*, vol. 352, no. 6333, Art. no. 6333, Jul. 1991, doi: 10.1038/352325a0.

[128] S. Blain and P. Tréguer, “Iron (II) and iron(III) determination in sea water at the nanomolar level with selective on-line preconcentration and spectrophotometric determination,” *Anal. Chim. Acta*, vol. 308, no. 1, pp. 425–432, Jun. 1995, doi: 10.1016/0003-2670(94)00456-V.

[129] M. I. Pascual-Reguera, I. Ortega-Carmona, and A. Molina-Díaz, “Spectrophotometric determination of iron with ferrozine by flow-injection analysis,” *Talanta*, vol. 44, no. 10, pp. 1793–1801, Oct. 1997, doi: 10.1016/S0039-9140(97)00050-7.

[130] P.-M. Sarradin, N. Le Bris, C. Le Gall, and P. Rodier, “Fe analysis by the ferrozine method: Adaptation to FIA towards in situ analysis in hydrothermal environment,” *Talanta*, vol. 66, no. 5, pp. 1131–1138, Jun. 2005, doi: 10.1016/j.talanta.2005.01.012.

[131] J.-Z. Zhang, C. Kelble, and F. J. Millero, “Gas-segmented continuous flow analysis of iron in water with a long liquid waveguide capillary flow cell,” *Anal. Chim. Acta*, vol. 438, no. 1, pp. 49–57, Jul. 2001, doi: 10.1016/S0003-2670(01)01031-5.

[132] A. Milani, P. J. Statham, M. C. Mowlem, and D. P. Connelly, “Development and application of a microfluidic in-situ analyzer for dissolved Fe and Mn in natural waters,” *Talanta*, vol. 136, pp. 15–22, May 2015, doi: 10.1016/j.talanta.2014.12.045.

[133] F. Geißler *et al.*, “Evaluation of a Ferrozine Based Autonomous in Situ Lab-on-Chip Analyzer for Dissolved Iron Species in Coastal Waters,” *Front. Mar. Sci.*, vol. 4, 2017, Accessed: Apr. 12, 2022. [Online]. Available: https://www.frontiersin.org/article/10.3389/fmars.2017.00322

[134] M. Grand, H. M. Oliveira, J. Ruzicka, and C. Measures, “Determination of dissolved zinc in seawater using micro-Sequential Injection lab-on-valve with fluorescence detection,” *Analyst*, vol. 136, no. 13, pp. 2747–2755, Jun. 2011, doi: 10.1039/C1AN15033B.

[135] M. M. Grand, P. Chocholouš, J. Růžička, P. Solich, and C. I. Measures, “Determination of trace zinc in seawater by coupling solid phase extraction and fluorescence detection in the Lab-On-Valve format,” *Anal. Chim. Acta*, vol. 923, pp. 45–54, Jun. 2016, doi: 10.1016/j.aca.2016.03.056.

[136] Q. Zhang *et al.*, “A feedback-controlling digital microfluidic fluorimetric sensor device for simple and rapid detection of mercury (II) in costal seawater,” *Mar. Pollut. Bull.*, vol. 144, pp. 20–27, Jul. 2019, doi: 10.1016/j.marpolbul.2019.04.063.

[137] M. Deng *et al.*, “A paper-based colorimetric microfluidic sensor fabricated by a novel spray painting prototyping process for iron analysis,” *Can. J. Chem.*, vol. 97, no. 5, pp. 373–377, May 2019, doi: 10.1139/cjc-2018-0346.

[138] R. Ghosh, V. Vaishampayan, A. Mahapatra, R. Malhotra, S. Balasubramanian, and A. Kapoor, “Enhancement of limit of detection by inducing coffee-ring effect in water quality monitoring microfluidic paper-based devices,” *DESALINATION WATER Treat.*, vol. 156, pp. 316–322, 2019, doi: 10.5004/dwt.2019.23715.

[139] WWF, “Living Planet Report 2020,” WWF, WWF, Gland, Switzerland, 2020. Accessed: Sep. 08, 2022. [Online]. Available: https://f.hubspotusercontent20.net/hubfs/4783129/LPR/PDFs/ENGLISH-FULL.pdf

[140] A. Valentini *et al.*, “Next-generation monitoring of aquatic biodiversity using environmental DNA metabarcoding,” *Mol. Ecol.*, vol. 25, no. 4, pp. 929–942, 2016, doi: 10.1111/mec.13428.

[141] J. A. Darling and A. R. Mahon, “From molecules to management: adopting DNA-based methods for monitoring biological invasions in aquatic environments,” *Environ. Res.*, vol. 111, no. 7, pp. 978–988, Oct. 2011, doi: 10.1016/j.envres.2011.02.001.

[142] K. M. Ruppert, R. J. Kline, and M. S. Rahman, “Past, present, and future perspectives of environmental DNA (eDNA) metabarcoding: A systematic review in methods, monitoring, and applications of global eDNA,” *Glob. Ecol. Conserv.*, vol. 17, p. e00547, Jan. 2019, doi: 10.1016/j.gecco.2019.e00547.

[143] C. M. Preston *et al.*, “Underwater Application of Quantitative PCR on an Ocean Mooring,” *PLOS ONE*, vol. 6, no. 8, p. e22522, Aug. 2011, doi: 10.1371/journal.pone.0022522.

[144] D. M. Pargett, J. M. Birch, C. M. Preston, J. P. Ryan, Y. Zhang, and C. A. Scholin, “Development of a mobile ecogenomic sensor,” in *OCEANS 2015 - MTS/IEEE Washington*, Oct. 2015, pp. 1–6. doi: 10.23919/OCEANS.2015.7404361.

[145] K. M. Yamahara *et al.*, “In situ Autonomous Acquisition and Preservation of Marine Environmental DNA Using an Autonomous Underwater Vehicle,” *Front. Mar. Sci.*, vol. 6, 2019, Accessed: Apr. 15, 2022. [Online]. Available: https://www.frontiersin.org/article/10.3389/fmars.2019.00373

[146] H. Ribeiro *et al.*, “Development of an autonomous biosampler to capture in situ aquatic microbiomes,” *PLOS ONE*, vol. 14, no. 5, p. e0216882, May 2019, doi: 10.1371/journal.pone.0216882.

[147] N. Formel, I. C. Enochs, C. Sinigalliano, S. R. Anderson, and L. R. Thompson, “Subsurface automated samplers for eDNA (SASe) for biological monitoring and research,” *HardwareX*, vol. 10, p. e00239, Oct. 2021, doi: 10.1016/j.ohx.2021.e00239.

[148] R. J. Diaz and D. L. Breitburg, “Chapter 1 The Hypoxic Environment,” in *Fish Physiology*, J. G. Richards, A. P. Farrell, and C. J. Brauner, Eds., in Hypoxia, vol. 27. Academic Press, 2009, pp. 1–23. doi: 10.1016/S1546-5098(08)00001-0.

[149] “Dissolved Oxygen,” *Environmental Measurement Systems*. https://www.fondriest.com/environmental-measurements/parameters/water-quality/dissolved-oxygen/ (accessed Dec. 07, 2020).

[150] A. H. Altieri and K. B. Gedan, “Climate change and dead zones,” *Glob. Change Biol.*, vol. 21, no. 4, pp. 1395–1406, 2015, doi: https://doi.org/10.1111/gcb.12754.

[151] S. A. Rounds, F. D. Wilde, and G. F. Ritz, "Chapter A6. Section 6.2. Dissolved oxygen," U.S. Geological Survey, Reston, VA, USGS Numbered Series 09-A6.2, 2006. doi: 10.3133/twri09A6.2.

[152] J. Erez, M. D. Krom, and T. Neuwirth, "Daily oxygen variations in marine fish ponds, Elat, Israel," *Aquaculture*, vol. 84, no. 3, pp. 289–305, Feb. 1990, doi: 10.1016/0044-8486(90)90094-4.

[153] "NMSU: Important Water Quality Parameters in Aquaponics Systems." https://aces.nmsu.edu/pubs/_circulars/CR680/welcome.html (accessed Nov. 26, 2020).

[154] T. Mikouchi and G. Saxton, "Construction and Use of a Modified Clark-Type of Oxygen Electrode for Liquid or Gas Analysis," *Fed. Proc.*, vol. 17, no. 1, pp. 111–111, 1958.

[155] L. C. Clark, R. Wolf, D. Granger, and Z. Taylor, "Continuous Recording of Blood Oxygen Tensions by Polarography," *J. Appl. Physiol.*, vol. 6, no. 3, pp. 189–193, Sep. 1953, doi: 10.1152/jappl.1953.6.3.189.

[156] S. Wang, J. San, J. Yu, R. Lee, and N. Liu, "A downhole CO2 sensor to monitor CO2 movement in situ for geologic carbon storage," *Int. J. Greenh. Gas Control*, vol. 55, pp. 202–208, Dec. 2016, doi: 10.1016/j.ijggc.2016.10.007.

[157] R. Fuenzalida, W. Schneider, J. Garcés-Vargas, L. Bravo, and C. Lange, "Vertical and horizontal extension of the oxygen minimum zone in the eastern South Pacific Ocean," *Deep Sea Res. Part II Top. Stud. Oceanogr.*, vol. 56, Jul. 2009, doi: 10.1016/j.dsr2.2008.11.001.

[158] Y. Wei, Y. Jiao, D. An, D. Li, W. Li, and Q. Wei, "Review of Dissolved Oxygen Detection Technology: From Laboratory Analysis to Online Intelligent Detection," *Sensors*, vol. 19, no. 18, Sep. 2019, doi: 10.3390/s19183995.

[159] J. M. Hall-Spencer and B. P. Harvey, "Ocean acidification impacts on coastal ecosystem services due to habitat degradation," *Emerg. Top. Life Sci.*, vol. 3, no. 2, pp. 197–206, May 2019, doi: 10.1042/ETLS20180117.

[160] S. C. Doney, V. J. Fabry, R. A. Feely, and J. A. Kleypas, "Ocean Acidification: The Other CO2 Problem," *Annu. Rev. Mar. Sci.*, vol. 1, no. 1, pp. 169–192, 2009, doi: 10.1146/annurev.marine.010908.163834.

[161] V. J. Fabry, B. A. Seibel, R. A. Feely, and J. C. Orr, "Impacts of ocean acidification on marine fauna and ecosystem processes," *ICES J. Mar. Sci.*, vol. 65, no. 3, pp. 414–432, Apr. 2008, doi: 10.1093/icesjms/fsn048.

[162] K. J. Kroeker *et al.*, "Impacts of ocean acidification on marine organisms: quantifying sensitivities and interaction with warming," *Glob. Change Biol.*, vol. 19, no. 6, pp. 1884–1896, 2013, doi: https://doi.org/10.1111/gcb.12179.

[163] N. Bates and J. Mathis, "The Arctic Ocean marine carbon cycle: evaluation of air-sea CO2 exchanges, ocean acidification impacts and potential feedbacks," *Biogeosciences Discuss.*, vol. 6, Jul. 2009, doi: 10.5194/bgd-6-6695-2009.

[164] "Carbon Dioxide Capture and Storage — IPCC." https://www.ipcc.ch/report/carbon-dioxide-capture-and-storage/ (accessed Nov. 23, 2020).

[165] P. Fietzek, B. Fiedler, T. Steinhoff, and A. Körtzinger, "In situ Quality Assessment of a Novel Underwater pCO2 Sensor Based on Membrane Equilibration and NDIR Spectrometry," *J. Atmospheric Ocean. Technol.*, vol. 31, no. 1, pp. 181–196, Jan. 2014, doi: 10.1175/JTECH-D-13-00083.1.

[166] Z. Liu *et al.*, "Midinfrared Sensor System Based on Tunable Laser Absorption Spectroscopy for Dissolved Carbon Dioxide Analysis in the South China Sea: System-Level Integration and Deployment," *Anal. Chem.*, vol. 92, no. 12, pp. 8178–8185, Jun. 2020, doi: 10.1021/acs.analchem.0c00327.

[167] Y. Nakano, H. Kimoto, S. Watanabe, K. Harada, and Y. W. Watanabe, "Simultaneous vertical measurements of in situ pH and CO2 in the sea using spectrophotometric profilers," *J. Oceanogr.*, vol. 62, no. 1, pp. 71–81, Feb. 2006, doi: 10.1007/s10872-006-0033-y.

[168] D. Atamanchuk *et al.*, "Performance of a lifetime-based optode for measuring partial pressure of carbon dioxide in natural waters," *Limnol. Oceanogr. Methods*, vol. 12, no. 2, pp. 63–73, 2014, doi: https://doi.org/10.4319/lom.2014.12.63.

[169] P. J. Thomas, D. Atamanchuk, J. Hovdenes, and A. Tengberg, "The use of novel optode sensor technologies for monitoring dissolved carbon dioxide and ammonia concentrations under live haul conditions," *Aquac. Eng.*, vol. 77, pp. 89–96, May 2017, doi: 10.1016/j.aquaeng.2017.02.004.

[170] J. S. Clarke *et al.*, "Characterization of a Time-Domain Dual Lifetime Referencing pCO(2) Optode and Deployment as a High-Resolution Underway Sensor across the High Latitude North Atlantic Ocean," *Front. Mar. Sci.*, vol. 4, p. 396, 2017, doi: 10.3389/fmars.2017.00396.

[171] S. E. Cullison Gray, M. D. DeGrandpre, T. S. Moore, T. R. Martz, G. E. Friederich, and K. S. Johnson, "Applications of in situ pH measurements for inorganic carbon calculations," *Mar. Chem.*, vol. 125, no. 1–4, pp. 82–90, 2011, doi: 10.1016/j.marchem.2011.02.005.

[172] L. Raimondi, J. B. R. Matthews, D. Atamanchuk, K. Azetsu-Scott, and D. W. R. Wallace, "The internal consistency of the marine carbon dioxide system for high latitude shipboard and in situ monitoring," *Mar. Chem.*, vol. 213, pp. 49–70, Jul. 2019, doi: 10.1016/j.marchem.2019.03.001.

[173] P. J. Bresnahan *et al.*, "Autonomous in situ calibration of ion-sensitive field effect transistor pH sensors," *Limnol. Oceanogr. Methods*, vol. 19, no. 2, pp. 132–144, 2021, doi: 10.1002/lom3.10410.

[174] S. Yamamoto *et al.*, "Development of an automated transportable continuous system to measure the total alkalinity of seawater," *Talanta*, vol. 221, p. 121666, Jan. 2021, doi: 10.1016/j.talanta.2020.121666.

[175] Q. Shangguan, C.-Z. Lai, C. M. Beatty, F. L. Young, R. S. Spaulding, and M. D. DeGrandpre, "Autonomous in situ measurements of freshwater alkalinity," *Limnol. Oceanogr. Methods*, vol. 19, no. 2, pp. 51–66, 2021, doi: 10.1002/lom3.10404.

[176] E. M. Briggs, E. H. De Carlo, C. L. Sabine, N. M. Howins, and T. R. Martz, "Autonomous Ion-Sensitive Field Effect Transistor-Based Total Alkalinity and pH Measurements on a Barrier Reef of Kāne'ohe Bay," *ACS Earth Space Chem.*, vol. 4, no. 3, pp. 355–362, Mar. 2020, doi: 10.1021/acsearthspacechem.9b00274.

[177] J. Newton, R. Feely, E. Jewett, P. Williamson, and J. Mathis, “Global Ocean Acidification Observing Network: Requirements and Governance Plan.” GOA-ON, 2015. [Online]. Available: http://www.goa-on.org/docs/GOA-ON_plan_print.pdf.

[178] A. J. Fassbender, S. R. Alin, R. A. Feely, A. J. Sutton, J. A. Newton, and R. H. Byrne, “Estimating Total Alkalinity in the Washington State Coastal Zone: Complexities and Surprising Utility for Ocean Acidification Research,” *Estuaries Coasts*, vol. 40, no. 2, pp. 404–418, 2017, doi: 10.1007/s12237-016-0168-z.

[179] G. K. Saba *et al.*, “The Development and Validation of a Profiling Glider Deep ISFET-Based pH Sensor for High Resolution Observations of Coastal and Ocean Acidification,” *Front. Mar. Sci.*, vol. 6, 2019, Accessed: May 24, 2022. [Online]. Available: https://www.frontiersin.org/article/10.3389/fmars.2019.00664

[180] P. E. Land *et al.*, “Optimum satellite remote sensing of the marine carbonate system using empirical algorithms in the global ocean, the Greater Caribbean, the Amazon Plume and the Bay of Bengal,” *Remote Sens. Environ.*, vol. 235, p. 111469, Dec. 2019, doi: 10.1016/j.rse.2019.111469.

[181] “SAMI-Alk in Clark Fork River.” http://www.sunburstsensors.com/resarch/sami-alk-in-clark-fork-river.html (accessed Sep. 09, 2022).

[182] Q. Shangguan, A. Prody, T. S. Wirth, E. M. Briggs, T. R. Martz, and M. D. DeGrandpre, “An inter-comparison of autonomous in situ instruments for ocean CO2 measurements under laboratory-controlled conditions,” *Mar. Chem.*, vol. 240, 2022, doi: 10.1016/j.marchem.2022.104085.

[183] A. K. Au, W. Lee, and A. Folch, “Mail-order microfluidics: Evaluation of stereolithography for the production of microfluidic devices,” *Lab. Chip*, vol. 14, no. 7, pp. 1294–1301, 2014, doi: 10.1039/c3lc51360b.

[184] D. J. Guckenberger Jr., T. E. De Groot, A. M. D. Wan, D. J. Beebe, and E. W. K. Young, “Micromilling: A method for ultra-rapid prototyping of plastic microfluidic devices,” *Lab. Chip*, vol. 15, no. 11, pp. 2364–2378, 2015, doi: 10.1039/c5lc00234f.

[185] N. Bhattacharjee, A. Urrios, S. Kang, and A. Folch, “The upcoming 3D-printing revolution in microfluidics,” *Lab. Chip*, vol. 16, no. 10, pp. 1720–1742, 2016, doi: 10.1039/c6lc00163g.

[186] S. Queste, R. Salut, S. Clatot, J.-Y. Rauch, and C. G. Khan Malek, “Manufacture of microfluidic glass chips by deep plasma etching, femtosecond laser ablation, and anodic bonding,” *Microsyst. Technol.*, vol. 16, no. 8–9, pp. 1485–1493, 2010, doi: 10.1007/s00542-010-1020-1.

[187] D. C. Duffy, J. C. McDonald, O. J. A. Schueller, and G. M. Whitesides, “Rapid prototyping of microfluidic systems in poly(dimethylsiloxane),” *Anal. Chem.*, vol. 70, no. 23, pp. 4974–4984, 1998, doi: 10.1021/ac980656z.

[188] A. B. Azouz, S. Murphy, S. Karazi, M. Vázquez, and D. Brabazon, “Fast fabrication process of microfluidic devices based on cyclic olefin copolymer,” *Mater. Manuf. Process.*, vol. 29, no. 2, pp. 93–99, 2014, doi: 10.1080/10426914.2013.811739.

[189] S. Su *et al.*, “One-step bonding and hydrophobic surface modification method for rapid fabrication of polycarbonate-based droplet microfluidic chips,” *Sens. Actuators B Chem.*, vol. 282, pp. 60–68, 2019, doi: 10.1016/j.snb.2018.11.035.

[190] T. Yin *et al.*, "A Novel Lab-on-Chip Spectrophotometric pH Sensor for AutonomousIn SituSeawater Measurements to 6000 m Depth on Stationary and Moving Observing Platforms," *Environ. Sci. Technol.*, vol. 55, no. 21, pp. 14968–14978, 2021, doi: 10.1021/acs.est.1c03517.

[191] S. Prakash and S. Kumar, "Determining the suitable CO2 laser based technique for microchannel fabrication on PMMA," *Opt. Laser Technol.*, vol. 139, 2021, doi: 10.1016/j.optlastec.2021.107017.

[192] I.-H. Song and T. Park, "PMMA solution assisted room temperature bonding for PMMA-PC hybrid devices," *Micromachines*, vol. 8, no. 9, 2017, doi: 10.3390/mi8090284.

[193] D. Mark, S. Haeberle, G. Roth, F. Von Stetten, and R. Zengerle, "Microfluidic Lab-on-a-Chip Platforms: Requirements, Characteristics and Applications," in *Microfluidics Based Microsystems*, S. Kakaç, B. Kosoy, D. Li, and A. Pramuanjaroenkij, Eds., in NATO Science for Peace and Security Series A: Chemistry and Biology. Springer Netherlands, 2010, pp. 305–376.

[194] M. Yew, Y. Ren, K. S. Koh, C. Sun, and C. Snape, "A Review of State-of-the-Art Microfluidic Technologies for Environmental Applications: Detection and Remediation," *Glob. Chall.*, vol. 3, no. 1, p. 1800060, Jan. 2019, doi: 10.1002/gch2.201800060.

[195] V. J. Sieben, C. F. A. Floquet, I. R. G. Ogilvie, M. C. Mowlem, and H. Morgan, "Microfluidic colourimetric chemical analysis system: Application to nitrite detection," *Anal. Methods*, vol. 2, no. 5, pp. 484–491, 2010, doi: 10.1039/C002672G.

[196] E. F. Hasselbrink, T. J. Shepodd, and J. E. Rehm, "High-Pressure Microfluidic Control in Lab-on-a-Chip Devices Using Mobile Polymer Monoliths," *Anal. Chem.*, vol. 74, no. 19, pp. 4913–4918, Oct. 2002, doi: 10.1021/ac025761u.

[197] M. Tweedie, D. Sun, B. Ward, and P. D. Maguire, "Long-term hydrolytically stable bond formation for future membrane-based deep ocean microfluidic chemical sensors," *Lab. Chip*, vol. 19, no. 7, pp. 1287–1295, Mar. 2019, doi: 10.1039/C9LC00123A.

[198] A. K. Au, H. Lai, B. R. Utela, and A. Folch, "Microvalves and Micropumps for BioMEMS," *Micromachines*, vol. 2, no. 2, pp. 179–220, Jun. 2011, doi: 10.3390/mi2020179.

[199] L. Clime, J. Daoud, D. Brassard, L. Malic, M. Geissler, and T. Veres, "Active pumping and control of flows in centrifugal microfluidics," *Microfluid. Nanofluidics*, vol. 23, no. 3, p. 29, Feb. 2019, doi: 10.1007/s10404-019-2198-x.

[200] S. A. Mousavi Shaegh *et al.*, "Plug-and-play microvalve and micropump for rapid integration with microfluidic chips," *Microfluid. Nanofluidics*, vol. 19, Apr. 2014, doi: 10.1007/s10404-015-1582-4.

[201] I. R. G. Ogilvie, V. J. Sieben, M. C. Mowlem, and H. Morgan, "Temporal Optimization of Microfluidic Colorimetric Sensors by Use of Multiplexed Stop-Flow Architecture," *Anal. Chem.*, vol. 83, no. 12, pp. 4814–4821, Jun. 2011, doi: 10.1021/ac200463y.

[202] A. Pourmand *et al.*, "Fabrication of whole-thermoplastic normally closed microvalve, micro check valve, and micropump," *Sens. Actuators B Chem.*, vol. 262, pp. 625–636, Jun. 2018, doi: 10.1016/j.snb.2017.12.132.

[203] P. R. Porwal, S. M. Thompson, D. K. Walters, and T. Jamal, “Heat transfer and fluid flow characteristics in multistaged Tesla valves,” *Numer. Heat Transf. Part Appl.*, vol. 73, no. 6, pp. 347–365, Mar. 2018, doi: 10.1080/10407782.2018.1447199.

[204] D. Kim, Y. W. Hwang, and S.-J. Park, “Passive microfluidic gas valves using capillary pressure,” *Microsyst. Technol.*, vol. 15, no. 6, pp. 919–923, Jun. 2009, doi: 10.1007/s00542-009-0826-1.

[205] T. H. Kang, S. W. Park, J. H. Lee, H. C. Yoon, and S. S. Yang, “Portable multi-immunosensing lab-on-a-chip (LOC) triggered by air bladder,” *Biomems Nanotechnol. Iii*, vol. 6799, p. UNSP 67991C, 2008.

[206] J. Hyeon and H. So, “Microfabricaton of microfluidic check valves using comb-shaped moving plug for suppression of backflow in microchannel,” *Biomed. Microdevices*, vol. 21, no. 1, p. 19, Feb. 2019, doi: 10.1007/s10544-019-0365-1.

[207] M. M. Aeinehvand *et al.*, “Elastic reversible valves on centrifugal microfluidic platforms,” *Lab. Chip*, vol. 19, no. 6, pp. 1090–1100, Mar. 2019, doi: 10.1039/C8LC00849C.

[208] M. Rahbar, L. Shannon, and B. L. Gray, “Design, fabrication and characterization of an arrayable all-polymer microfluidic valve employing highly magnetic rare-earth composite polymer,” *J. Micromechanics Microengineering*, vol. 26, no. 5, p. 055012, May 2016, doi: 10.1088/0960-1317/26/5/055012.

[209] C. Yamahata, F. Lacharme, Y. Burri, and M. A.M. Gijs, “A ball valve micropump in glass fabricated by powder blasting,” *Sens. Actuators B Chem.*, vol. 110, pp. 1–7, Sep. 2005, doi: 10.1016/j.snb.2005.01.005.

[210] A. M. Matthews, “The development of the Starr-Edwards heart valve.,” *Tex. Heart Inst. J.*, vol. 25, no. 4, pp. 282–293, 1998.

[211] M. Shen, C. Yamahata, and M. A. M. Gijs, “A high-performance compact electromagnetic actuator for a PMMA ball-valve micropump,” *J. Micromechanics Microengineering*, vol. 18, no. 2, p. 025031, Feb. 2008, doi: 10.1088/0960-1317/18/2/025031.

[212] A. Gaspar, M. E. Piyasena, L. Daroczi, and F. A. Gomez, “Magnetically controlled valve for flow manipulation in polymer microfluidic devices,” *Microfluid. Nanofluidics*, vol. 4, no. 6, pp. 525–531, Jun. 2008, doi: 10.1007/s10404-007-0204-1.

[213] D. Sun, M. Tweedie, D. R. Gajula, B. Ward, and P. D. Maguire, “High-strength thermoplastic bonding for multi-channel, multi-layer lab-on-chip devices for ocean and environmental applications,” *Microfluid. Nanofluidics*, vol. 19, no. 4, pp. 913–922, Oct. 2015, doi: 10.1007/s10404-015-1620-2.

[214] “Magnetic attraction forces on ferromagnetic particles,” *Maurer Magnetic*, 2015. https://maurermagnetic.ch/PDF/White-Paper-E-magnetic-attraction-particles.pdf (accessed May 02, 2019).

[215] J. D. Jackson, *Classical Electrodynamics*, 3rd ed. New York: John Wiley and Sons, 1999.

[216] I. R. G. Ogilvie, “Novel Fabrication Techniques For Microfluidic Based In-Situ Oceanographic Nutrient Sensors,” PhD Thesis, University of Southampton, Southampton, 2012.

[217] Y. Oda, H. Oshima, M. Nakatani, and M. Hashimoto, “Vacuum-driven fluid manipulation by a piezoelectric diaphragm micropump for microfluidic droplet generation with a rapid system response time,” *ELECTROPHORESIS*, vol. 40, no. 3, pp. 414–418, 2019, doi: 10.1002/elps.201800357.

[218] R. F. Ismagilov *et al.*, “Pressure-Driven Laminar Flow in Tangential Microchannels: an Elastomeric Microfluidic Switch,” *Anal. Chem.*, vol. 73, no. 19, pp. 4682–4687, Oct. 2001, doi: 10.1021/ac010374q.

[219] E. Luy, “Inlaid Microfluidics: A Novel Approach to Optical Measurements on Lab-on-Chip Devices,” Thesis, 2020. Accessed: Jan. 03, 2023. [Online]. Available: https://DalSpace.library.dal.ca//handle/10222/80126

[220] D. Onoshima *et al.*, “A deep microfluidic absorbance detection cell replicated from a thickly stacked SU-8 dry film resist mold,” *Anal. Methods*, vol. 4, no. 12, pp. 4368–4372, Nov. 2012, doi: 10.1039/C2AY26099A.

[221] F. Starecki *et al.*, “IR emitting Dy3+ doped chalcogenide fibers for in situ CO2 monitoring in high pressure microsystems,” *Int. J. Greenh. Gas Control*, vol. 55, pp. 36–41, Dec. 2016, doi: 10.1016/j.ijggc.2016.10.015.

[222] M. H. Huesemann, A. D. Skillman, and E. A. Crecelius, “The inhibition of marine nitrification by ocean disposal of carbon dioxide,” *Mar. Pollut. Bull.*, vol. 44, no. 2, pp. 142–148, Feb. 2002, doi: 10.1016/S0025-326X(01)00194-1.

[223] R. Gupta and N. J. Goddard, “Broadband absorption spectroscopy for rapid pH measurement in small volumes using an integrated porous waveguide,” *Analyst*, vol. 142, no. 1, pp. 169–176, Dec. 2016, doi: 10.1039/C6AN01896C.

[224] R. Gupta, B. Bastani, N. J. Goddard, and B. Grieve, “Absorption spectroscopy in microfluidic flow cells using a metal clad leaky waveguide device with a porous gel waveguide layer,” *Analyst*, vol. 138, no. 1, pp. 307–314, Nov. 2012, doi: 10.1039/C2AN35898K.

[225] R. Liu, R. Ishimatsu, M. Yahiro, C. Adachi, K. Nakano, and T. Imato, “Photometric flow injection determination of phosphate on a PDMS microchip using an optical detection system assembled with an organic light emitting diode and an organic photodiode,” *Talanta*, vol. 132, pp. 96–105, Jan. 2015, doi: 10.1016/j.talanta.2014.08.057.

[226] M. Grumann *et al.*, “Optical beam guidance in monolithic polymer chips for miniaturized colorimetric assays,” in *18th IEEE International Conference on Micro Electro Mechanical Systems, 2005. MEMS 2005.*, Jan. 2005, pp. 108–111. doi: 10.1109/MEMSYS.2005.1453879.

[227] G. Duffy, I. Maguire, B. Heery, P. Gers, J. Ducrée, and F. Regan, “ChromiSense: A colourimetric lab-on-a-disc sensor for chromium speciation in water,” *Talanta*, vol. 178, pp. 392–399, Feb. 2018, doi: 10.1016/j.talanta.2017.09.066.

[228] C. M. Rushworth, G. Jones, M. Fischlechner, E. Walton, and H. Morgan, “On-chip cavity-enhanced absorption spectroscopy using a white light-emitting diode and polymer mirrors,” *Lab. Chip*, vol. 15, no. 3, pp. 711–717, Jan. 2015, doi: 10.1039/C4LC01264J.

[229] Tiansong. Wang, J. H. Aiken, C. W. Huie, and R. A. Hartwick, “Nanoliter-scale multireflection cell for absorption detection in capillary electrophoresis,” *Anal. Chem.*, vol. 63, no. 14, pp. 1372–1376, Jul. 1991, doi: 10.1021/ac00014a007.

[230] H. Salimi-Moosavi, Y. Jiang, L. Lester, G. McKinnon, and D. J. Harrison, "A multireflection cell for enhanced absorbance detection in microchip-based capillary electrophoresis devices," *ELECTROPHORESIS*, vol. 21, no. 7, pp. 1291–1299, Apr. 2000, doi: 10.1002/(SICI)1522-2683(20000401)21:7<1291::AID-ELPS1291>3.0.CO;2-5.

[231] A. Llobera, S. Demming, R. Wilke, and S. Büttgenbach, "Multiple internal reflection poly(dimethylsiloxane) systems for optical sensing," *Lab. Chip*, vol. 7, no. 11, pp. 1560–1566, Oct. 2007, doi: 10.1039/B704454B.

[232] C. M. Rushworth, G. Jones, M. Fischlechner, E. Walton, and H. Morgan, "On-chip cavity-enhanced absorption spectroscopy using a white light-emitting diode and polymer mirrors," *Lab. Chip*, vol. 15, no. 3, pp. 711–717, Jan. 2015, doi: 10.1039/C4LC01264J.

[233] "Starna Scientific Ltd - Cells and Reference Materials for all your scientific applications." https://www.starna.com/ (accessed Dec. 21, 2018).

[234] "Fluidics Intelligently Automated - FIAlab." https://www.flowinjection.com/ (accessed Apr. 28, 2022).

[235] J. R. Casey *et al.*, "Phytoplankton taxon-specific orthophosphate (Pi) and ATP utilization in the western subtropical North Atlantic," *Aquat. Microb. Ecol.*, vol. 58, no. 1, pp. 31–44, 2009, doi: 10.3354/ame01348.

[236] A. C. Martiny, Y. Huang, and W. Li, "Occurrence of phosphate acquisition genes in Prochlorococcus cells from different ocean regions," *Environ. Microbiol.*, vol. 11, no. 6, pp. 1340–1347, Jun. 2009, doi: 10.1111/j.1462-2920.2009.01860.x.

[237] E. J. Lessard, A. Merico, and T. Tyrrell, "Nitrate: Phosphate Ratios and Emiliania huxleyi Blooms," *Limnol. Oceanogr.*, vol. 50, no. 3, pp. 1020–1024, 2005.

[238] M. Garrett, J. Wolny, E. Truby, C. Heil, and C. Kovach, "Harmful algal bloom species and phosphate-processing effluent: Field and laboratory studies," *Mar. Pollut. Bull.*, vol. 62, no. 3, pp. 596–601, Mar. 2011, doi: 10.1016/j.marpolbul.2010.11.017.

[239] "Chapter NR 217: Effluent Standards and Limitations for Phosphorus," Department of Natural Resources, United States -- Wisconsin, Administrative Code, 2011.

[240] "Canada's Challenges and Opportunities to Address Contaminants in Wastewater," Canadian Water Network, Mar. 2018. [Online]. Available: https://cwn-rce.ca/wp-content/uploads/projects/other-files/Canadas-Challenges-and-Opportunities-to-Address-Contaminants-in-Wastewater/CWN-Report-on-Contaminants-in-WW-Supporting-Doc-2.pdf

[241] U. Sivasankaran *et al.*, "Ultrasensitive electrochemical sensing of phosphate in water mediated by a dipicolylamine-zinc(II) complex," *Sens. Actuators B Chem.*, vol. 321, p. 128474, Oct. 2020, doi: 10.1016/j.snb.2020.128474.

[242] C. Warwick *et al.*, "Conductance based sensing and analysis of soluble phosphates in wastewater," *Biosens. Bioelectron.*, vol. 52, pp. 173–179, Feb. 2014, doi: 10.1016/j.bios.2013.08.048.

[243] X. Song *et al.*, "Europium-based infinite coordination polymer nanospheres as an effective fluorescence probe for phosphate sensing," *Rsc Adv.*, vol. 7, no. 14, pp. 8661–8669, 2017, doi: 10.1039/c6ra27819a.

[244] M. D. Patey, M. J. A. Rijkenberg, P. J. Statham, M. C. Stinchcombe, E. P. Achterberg, and M. Mowlem, "Determination of nitrate and phosphate in seawater at nanomolar concentrations," *TrAC Trends Anal. Chem.*, vol. 27, no. 2, pp. 169–182, Feb. 2008, doi: 10.1016/j.trac.2007.12.006.

[245] C. Warwick, A. Guerreiro, and A. Soares, "Sensing and analysis of soluble phosphates in environmental samples: A review," *Biosens. Bioelectron.*, vol. 41, pp. 1–11, Mar. 2013, doi: 10.1016/j.bios.2012.07.012.

[246] M. Bowden and D. Diamond, "The determination of phosphorus in a microfluidic manifold demonstrating long-term reagent lifetime and chemical stability utilising a colorimetric method," *Sens. Actuators B Chem.*, vol. 90, no. 1, pp. 170–174, Apr. 2003, doi: 10.1016/S0925-4005(03)00024-8.

[247] J. Murphy and J. P. Riley, "A modified single solution method for the determination of phosphate in natural waters," *Anal. Chim. Acta*, vol. 27, pp. 31–36, Jan. 1962, doi: 10.1016/S0003-2670(00)88444-5.

[248] "Method 365.3: Phosphorous, All Forms (Colorimetric, Ascorbic Acid, Two Reagent)," p. 5.

[249] E. A. Nagul, I. D. McKelvie, P. Worsfold, and S. D. Kolev, "The molybdenum blue reaction for the determination of orthophosphate revisited: Opening the black box," *Anal. Chim. Acta*, vol. 890, pp. 60–82, Aug. 2015, doi: 10.1016/j.aca.2015.07.030.

[250] "HydroCycle PO_4 | Sea-Bird Scientific - Downloads | Sea-Bird." https://www.seabird.com/hydrocycle-po/product-downloads?id=54721314201 (accessed Apr. 06, 2021).

[251] J. M. Zhu *et al.*, "Optofluidic marine phosphate detection with enhanced absorption using a Fabry–Pérot resonator," *Lab. Chip*, vol. 17, no. 23, pp. 4025–4030, Nov. 2017, doi: 10.1039/C7LC01016H.

[252] F.-E. Legiret *et al.*, "A high performance microfluidic analyser for phosphate measurements in marine waters using the vanadomolybdate method," *Talanta*, vol. 116, pp. 382–387, Nov. 2013, doi: 10.1016/j.talanta.2013.05.004.

[253] A. D. Beaton *et al.*, "Lab-on-Chip Measurement of Nitrate and Nitrite for In Situ Analysis of Natural Waters," *Environ. Sci. Technol.*, vol. 46, no. 17, pp. 9548–9556, Sep. 2012, doi: 10.1021/es300419u.

[254] A. J. Birchill *et al.*, "Exploring Ocean Biogeochemistry Using a Lab-on-Chip Phosphate Analyser on an Underwater Glider," *Front. Mar. Sci.*, vol. 0, 2021, doi: 10.3389/fmars.2021.698102.

[255] I. R. G. Ogilvie, V. J. Sieben, M. C. Mowlem, and H. Morgan, "Temporal Optimization of Microfluidic Colorimetric Sensors by Use of Multiplexed Stop-Flow Architecture," *Anal. Chem.*, vol. 83, no. 12, pp. 4814–4821, Jun. 2011, doi: 10.1021/ac200463y.

[256] P. C. Bartels and A. F. Roijers, "A kinetic study on the influence of the parameters in the determination of inorganic phosphate by the molybdenum blue reaction," *Clin. Chim. Acta Int. J. Clin. Chem.*, vol. 61, no. 2, pp. 135–144, Jun. 1975, doi: 10.1016/0009-8981(75)90307-1.

[257] A. Shrivastava and V. Gupta, "Methods for the determination of limit of detection and limit of quantitation of the analytical methods," *Chron. Young Sci.*, vol. 2, no. 1, p. 21, 2011, doi: 10.4103/2229-5186.79345.

[258] S. Shan and J. Sheng, "Examination of circulation, flushing time and dispersion in Halifax Harbour of Nova Scotia," *Water Qual. Res. J.*, vol. 47, no. 3–4, pp. 353–374, Aug. 2012, doi: 10.2166/wqrjc.2012.041.

[259] W. J. Burt, H. Thomas, K. Fennel, and E. Horne, "Sediment-water column fluxes of carbon, oxygen and nutrients in Bedford Basin, Nova Scotia, inferred from ^{224}Ra measurements," *Biogeosciences*, vol. 10, no. 1, pp. 53–66, Jan. 2013, doi: 10.5194/bg-10-53-2013.

[260] W. K. W. Li, Bedford Institute of Oceanography, Canada, Department of Fisheries and Oceans, and Ocean and Ecosystem Sciences Division, *The state of phytoplankton and bacterioplankton at the Compass Buoy Station: Bedford Basin Monitoring Program 1992-2013*. Dartmouth: Fisheries and Oceans Canada, Maritimes Region, Ocean and Ecosystem Sciences Division, Bedford Institute of Oceanography, 2014.

[261] R. Aris and G. I. Taylor, "On the dispersion of a solute in a fluid flowing through a tube," *Proc. R. Soc. Lond. Ser. Math. Phys. Sci.*, vol. 235, no. 1200, pp. 67–77, Apr. 1956, doi: 10.1098/rspa.1956.0065.

[262] D. Dutta and D. T. Leighton, "Dispersion in large aspect ratio microchannels for open-channel liquid chromatography," *Anal. Chem.*, vol. 75, no. 1, pp. 57–70, Jan. 2003, doi: 10.1021/ac020179r.

[263] B. Schnetger and C. Lehners, "Determination of nitrate plus nitrite in small volume marine water samples using vanadium(III)chloride as a reduction agent," *Mar. Chem.*, vol. 160, pp. 91–98, Mar. 2014, doi: 10.1016/j.marchem.2014.01.010.

[264] S.-C. Pai, Y.-T. Su, M.-C. Lu, Y. Chou, and T.-Y. Ho, "Determination of Nitrate in Natural Waters by Vanadium Reduction and the Griess Assay: Reassessment and Optimization," *ACS EST Water*, vol. 1, no. 6, pp. 1524–1532, Jun. 2021, doi: 10.1021/acsestwater.1c00065.

[265] M. Pokhrel, S. Adhikari, K. Subedi, S. Dhungana, and B. Poudel, "Spectrophotometric determination of phosphate in presence of arsenate," *Sci. World*, vol. 15, pp. 10–17, Jun. 2022, doi: 10.3126/sw.v15i15.45636.

[266] A. E. Bowden and J. Bergström, "39 - Computer Modeling and Simulation of UHMWPE," in *UHMWPE Biomaterials Handbook (Third Edition)*, S. M. Kurtz, Ed., Oxford: William Andrew Publishing, 2016, pp. 753–771. doi: 10.1016/B978-0-323-35401-1.00039-9.

[267] T. K. Kim, J. K. Kim, and O. C. Jeong, "Measurement of nonlinear mechanical properties of PDMS elastomer," *Microelectron. Eng.*, vol. 88, no. 8, pp. 1982–1985, Aug. 2011, doi: 10.1016/j.mee.2010.12.108.

[268] D. Z. Tansel, J. Brenneman, G. K. Fedder, and R. Panat, "Mechanical characterization of polydimethylsiloxane (PDMS) exposed to thermal histories up to 300 °C in a vacuum environment," *J. Micromechanics Microengineering*, vol. 30, no. 6, p. 067001, Apr. 2020, doi: 10.1088/1361-6439/ab82f4.

[269] K. Thanakhun and T. Puttapitukporn, "PDMS Material Models for Anti-fouling Surfaces Using Finite Element Method," *Eng. J.*, vol. 23, no. 6, pp. 381–398, Nov. 2019, doi: 10.4186/ej.2019.23.6.381.

APPENDIX A. FLAP VALVE COMSOL SIMULATIONS

A.1 COMSOL Simulations

Simulations using COMSOL software were done to further parametrize and optimize the elastomer flap valve designs. Rather than simulating the entire valve during its opening and closing phases, which is too computationally expensive with the fluid dynamics, only the elastomer flap part of the valve was considered, with a constant contact force used in place of the resultant force from fluid flow.

Working with the co-op student Luke LaFond, a suite of COMSOL simulations were carried out with the oval flap design. The parameters explored by the simulations were: elastomer material, computational model, elastomer thickness, and hydrostatic pressure. All the simulation conditions and parameters can be found in APPENDIX B. For every simulation, the flap model had a boundary condition that fixed the position around the perimeter. The measured deflection was taken as the difference between the original height of the top face of the flap and the height of the deformation peak above the inlet after the force has been applied. Preliminary studies using the solid-fluid interface of COMSOL were done to find an empirical relationship between flow rate and applied force on the membrane. From these, a maximum applied force of 0.05 N spread over the circular input region of 0.7 mm diameter was chosen for all the simulations. This corresponds to a maximum outlet pressure of approximately 130 kPa, which was experimentally determined to be the upper bound in the physical system.

A.2 COMSOL Simulation Testing Methods

The first study looked at the deformation of flaps made from different materials: PDMS, Teflon, silicone, and soft and hard Viton. For PDMS, Teflon, and silicone, the built-in COMSOL material parameters were used. The Shore scale durometer values for the soft and hard Viton (40 and 75 Shore-A respectively) were used to approximate the Youngs Modulus for the two materials, as it is not contained in the COMSOL material library. A thickness of 0.4 mm was chosen for all materials, as it was the measured thickness of the flap materials used in the physical design.

The first set of simulations were done using the linear elastic model for the materials, which assumes that stress varies linearly with strain. An elastic material will return to its original shape after deformation. This model uses density, Young's modulus and Poissons ratio to determine the linear relationship, and is much less computationally expensive than others. However it is meant for applications where the strain is small (<1 % [266]) compared to the material thickness, which is not the case in this situation. A more accurate, but still computationally efficient model is the hyperelastic material model, which is meant to be used when the stress-strain curve of the material moves into the non-linear region, which is more common in rubber-like materials. All hyper-elastic material models are based on data sets that are determined by laboratory measurements, which means that they differ between applications. For conditions with high strain, such as this one, second order Ogden models are appropriate because they preserve flexibility where other models are still too stiff [267]. Three different hyperelastic Ogden models were tested for comparison, with the deformation distance as the metric.

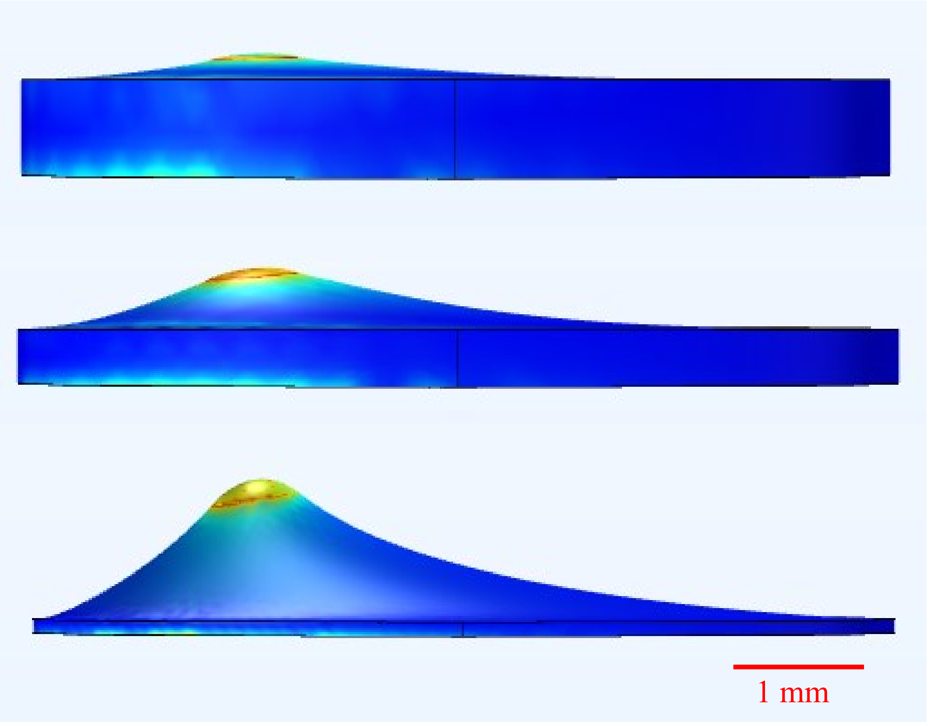

Figure A-1: Visualization of membrane deflection under 0.05 N inlet force. Top: 0.7 mm membrane thickness. Middle: 0.4 mm membrane thickness. Bottom: 0.1 mm membrane thickness.

The next simulation study was done on the thickness of the membranes. Although the measured thickness of the physical material was 0.4 mm, other thicknesses were considered. The minimum membrane thickness chosen for the material study was 0.1 mm, and the thickest membrane in the study is 0.7 mm. Again, the deflection at the inlet was used as the metric for the study.

The last study was to determine the effect of hydrostatic pressure on the deformation of the valve flaps. The end use application of the valves requires them to be used at deep ocean pressures, which means their change in deformation must be minimal with increased hydrostatic pressure. Two different valve flaps with hyperelastic models for PDMS were subjected to increasing simulated hydrostatic pressure by applying a constant pressure as a boundary condition to the surfaces of the flap. Again, 0.05 N were applied to the inlet at each simulated pressure and the deflection distance was used as a metric.

A.3 Elastomer Valve Simulation Results

The results reported here are products of the simulations performed in COMSOL. Figure A-1 is a COMSOL visualization of how different thicknesses of the membrane deform under 0.05 N of force at the inlet location, still using the linear elastic model. Figure A-2 shows the preliminary deflection curves for the five different materials based only on the linear elastic models. Although the linear elastic model is not entirely appropriate for this

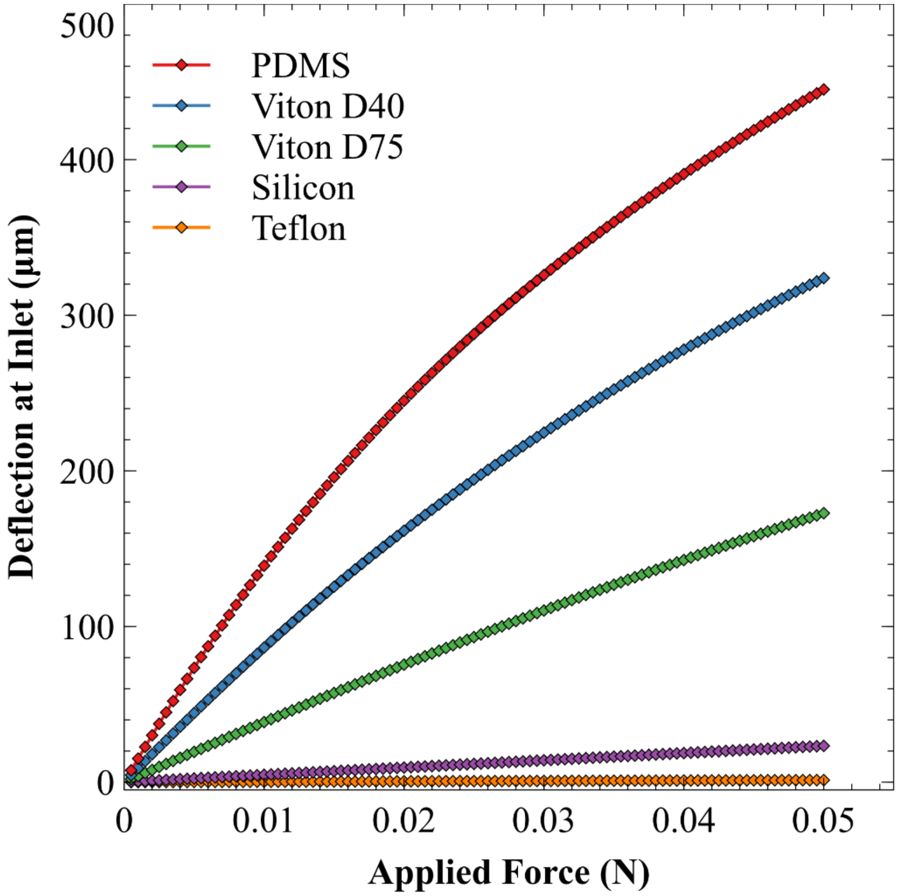

Figure A-2: Material deflection curves with a linear elastic model for PDMS, Teflon, silicon, hard and soft Viton, all using a thickness of 0.4 mm.

application, it is still very clear that Teflon and pure silicon are much too stiff, as the deflection magnitude does not come close to the minimum pedestal height of 0.1 mm.

The material with the largest deformation in the linear model was PDMS, which was expected. The low durometer Viton also deformed well, but PDMS was chosen as the simulation material going forward because there were more built-in pre-sets in COMSOL for PDMS and it is a much more widely used and studied material in microfluidics than Viton, despite the fact that Viton is more robust. Viton will be revisited as a simulation material pending the results of the work shown here.

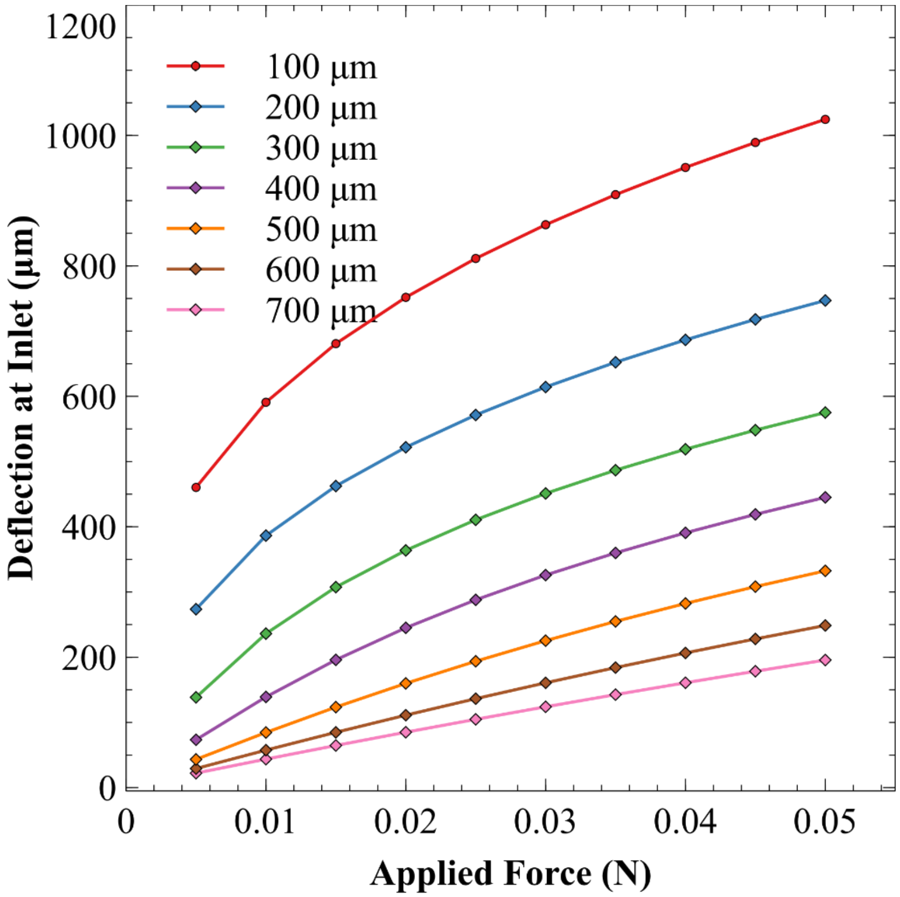

Figure A-3: PDMS deflection curves for membrane thickness study.

Figure A-3 shows the results of thickness on the deflection for a PDMS membrane using the linear elastic model. The 0.7 mm membrane shows a very linear increase in deflection with force at the scale chosen here. As the membranes get thinner, the relationship starts to become nonlinear, particularly at lower forces. This could be a result of the linear elastic model not being appropriate for the application, where the deflection exceeds the material thickness.

As previously mentioned, the linear elastic model is likely not the best choice for this application, and a hyperelastic model is probably more suitable. To that end, several

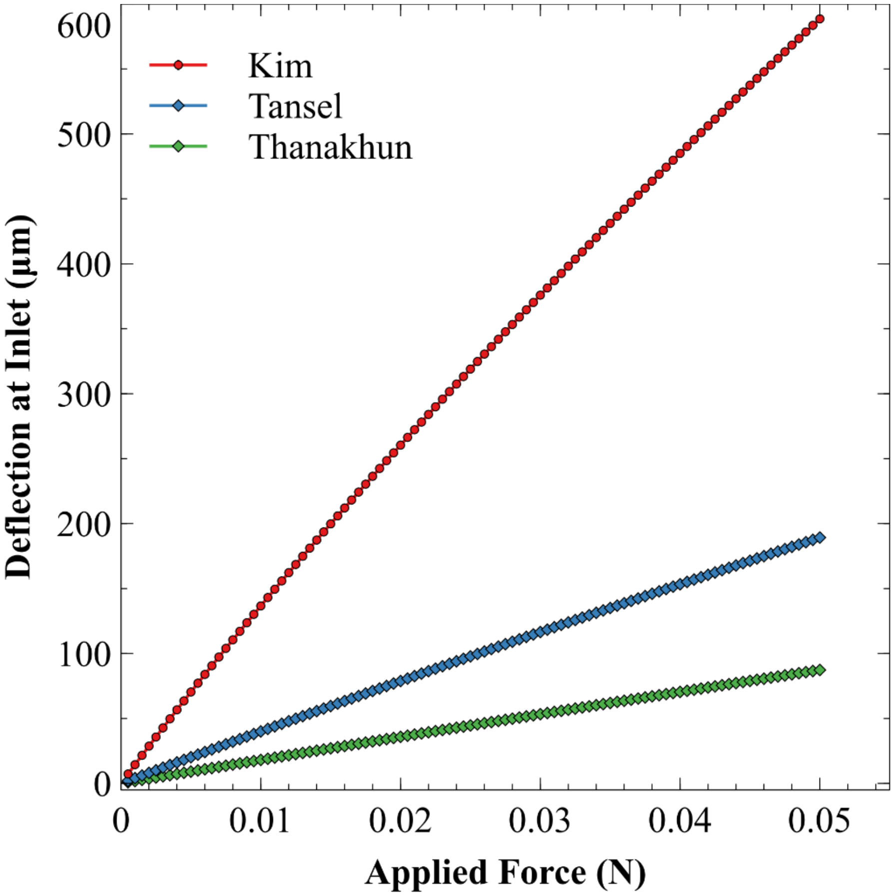

Figure A-4: PDMS deflection over the inlet using second order Ogden parameters for hyperelastic models.

groups have performed stress-strain studies on PDMS to develop second order hyperelastic Ogden models that can be used for more accurate simulations. The three models considered for this purpose were developed by Kim et al. [267], Tansel et al. [268], and Thanakhun et al. [269].

Figure A-4 shows the membrane deflection above the inlet for the three different hyperelastic models, all using a 0.4 mm thick PDMS membrane. The model presented by Thanakhun et al. used parameters that were determined by their study on PDMS

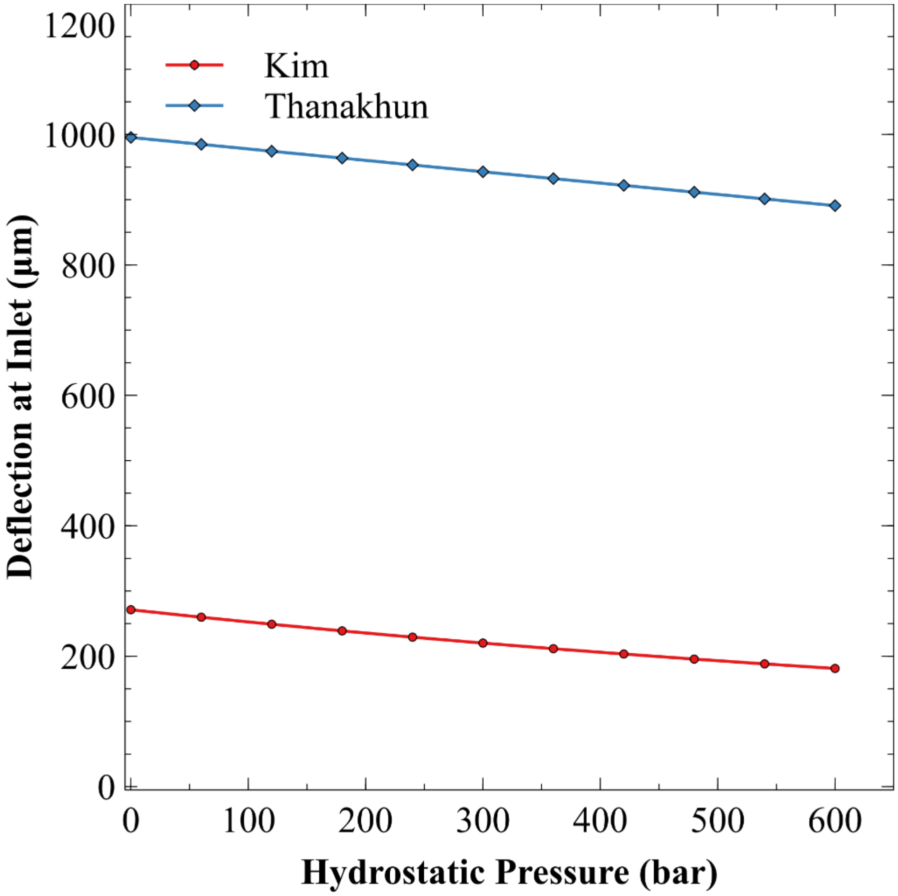

Figure A-5: Effect of hydrostatic pressure on membrane deflection. Red set: Ogden model based on Kim. Blue set: Ogden model based on Thanakhun. The scale corresponds to approximate 0 to 6000 m ocean depth.

micropillars, which is not a geometry relevant to this application. Tansel et al. and Kim et al. both studied thin PDMS sheets, which is much more relevant to the flap valves. However, the study done by Tansel et al. was performed on a PDMS sheet at 300 °C, which is too hot for these valves. For that reason, the study by Kim et al was chosen as the most relevant and closely related to the application. Of the three hyperelastic models, the Kim model also has the steepest deflection curve, theoretically meaning less force is required to open or close the valves. Only 7 mN of force is required to deflect the 0.4 mm membrane by 0.1 mm.

The last simulation study was done to determine the effect of hydrostatic pressure on the overall membrane deflection. Figure A-5 shows the results of the study, with simulated hydrostatic pressures ranging from 0 to 600 bar to imitate ocean depths from 0 to 6000 m. The Ogden parameters presented by Kim et al and Thanakhun et al were used to have two points of comparison. Both models showed that the maximum deflection decreased linearly at the same rate with increased hydrostatic pressure. In both models, at the maximum pressure of 600 bar, the deflection peak only decreased by roughly 0.1 mm. Although a 0.1 mm reduction in deformation could cause the valves to fail, the valves can likely be designed to accommodate that amount of variance.

A.4 Conclusions

Although the simulations show that there is clear potential for the elastomer flap valves to work, the practical aspect of fabricating them to be repeatable and consistent turned out to be too challenging to move forward with. To further develop these valves, work must be done to increase their repeatability and sealing ability. The simulations show that there are materials that can deform well enough and withstand the effects of hydrostatic pressure to function in these valves. However, in the physical designs the performance of the valves was unreliable.

APPENDIX B. COMSOL VALVE PARAMETERS AND DIMENSIONS

Table B-1: COMSOL Model Settings

Multiphysics Model:	Solid Mechanics, Nonlinear Structural Materials
Solver Configuration:	Stationary, Adaptive Mesh Refinement
Maximum Mesh Element Size:	1×10^{-3} m
Minimum Mesh Element Size:	1.8×10^{-4} m

Table B-2: COMSOL Material Parameters

	PDMS	Teflon	Silicone	Viton D40	Viton D75
Youngs Modulus (MPA)	0.750	500	25	1.3	3
Density (kg/m^3)	970	2200	1700	1800	1800
Poisson’s Ratio	0.49	0.42	0.48	0.48	0.48

Ogden Parameters (PDMS)	Kim	Tansel	Thanakhun
Order	2nd	2nd	1st
μ_1 (MPa)	63.5	0.065	0.263
μ_2 (MPa)	0.041	-0.172	n/a
α_1	6.371×10^{-10}	4.140	4.753
α_2	3.812	-1.259	n/a

Table B-3: COMSOL Circular Valve Dimension Parameters

Parameter	Value	Description
Blength	15[mm]	Length of all three layers
Bwidth	40[mm]	Width of all three layers
Bheight	6[mm]	Height of all three layers
Flapl	10[mm]	Length of the flap oval
Flapw	7[mm]	Width of the flap oval
Flapt	0.79375[mm]	Thickness of the Viton flap
Ellipsed	0.7[mm]	Depth of the ellipse extrude
MlellipseCenterx	12.5[mm]	Used for making the various holes in the middle layer
MellipseCentery	7.5[mm]	Used for making the various holes in the middle layer
MrellipseCenterx	27.5[mm]	Used for making the various holes in the middle layer
Mbcirclerad	1.4[mm]	Outer radius of the pedestal
Mscirclerad	0.65[mm]	Inner radius for the pedestal
Mcircleoffset	1.6[mm]	Offset of the circle from the middle of each ellipse
Throughholedia	0.7[mm]	Diameter of the through holes
FlapCavityx	7[mm]	Flap cavity dimensions for the top
FlapCavityy	4[mm]	Flap cavity dimensions for the top
ped_h	0.5[mm]	Height of the pedestals
u_in	0.1[ml/min]	Inlet volumetric flow

Table B-4: COMSOL Oval Valve Dimension Parameters

Parameter	Value	Description
Center	30[mm]	X coordinate center of the system
CenterY	15[mm]	Y coordinate center of the system
CenterOffset	8[mm]	From the middle of the outlet tubes to the absolute center
Holediameter	0.7[mm]	Diameter of inlet and outlet tubes
MiddleHoleL	Center-CenterOffset	X coordinate of the left middle flap tube
MiddleHoleR	Center+CenterOffset	X coordinate of the right middle flap tube
InOutSpace	1.25[mm]	Distance between the inlet and outlet tube centers for each flap segment
FlapInletL	MiddleHoleL-InOutSpace	X coordinate of the left flap inlet
FlapInletR	MiddleHoleR-InOutSpace	X coordinate of the right flap inlet
SectionHeight	6[mm]	Hight of each section in the three-part assembly
CavityCircleDia	6[mm]	Diameter of the cavity insert tube
CavityHeight	1[mm]	Height of the cavity insert
CavityDepth	0.5[mm]	Depth of water space within the cavity insert
CavityWallThick	0.75[mm]	Wall thickness of the cavity insert
CavitySmallCircleDia	0.6[mm]	Diameter of the four bumpers on the cavity inlet
CavitySmallCircleOffset	0.53[mm]	Distance of the bumpers from the center
CavitySmallCirclesDepth	0.25[mm]	Depth of the bumpers
CavityInnerDiameter	4.5[mm]	Diameter of the inner cavity water region
FlapCavityDia	5[mm]	Diameter of the flap
FlapCavityThic	0.4[mm]	Flap thickness
PedSinkOuterDia	3.5[mm]	Outer diameter of the sink region surrounding the pedestals
PedSinkInnerDia	1.3[mm]	Pedestal diameter
PedSink	0.5[mm]	Depth of the bottom pedestal
CenterTubeH	5.3[mm]	Length of the middle outlet tubes
InletTubeLength	4.8[mm]	Length of the inlet tubes
SweepAddition	0.35[mm]	Regulates the angle of the 45-degree pipe connecting the two flap systems
FluidLayerT	0.002[mm]	Thickness of the very small fluid layer between the flap in pedestal (helps with convergence)
u_in	3[ml/min]	Inlet fluid volume flow
ramp	1	Ramping coefficient to help convergence

APPENDIX C. SPECTRA FOR ABSORBANCE SPECTROPHOTOMETRY

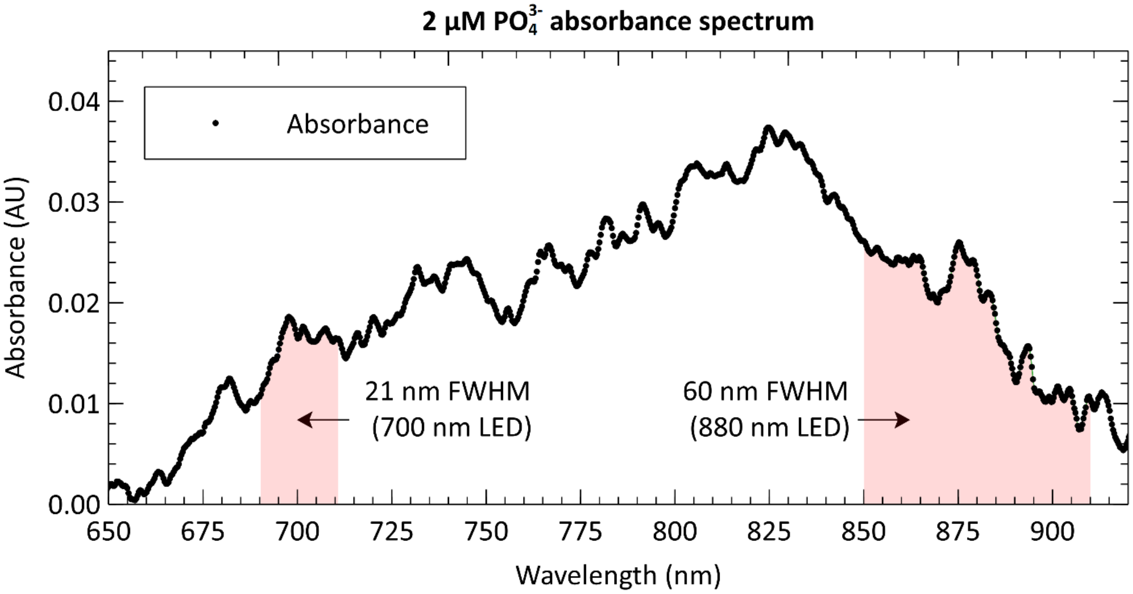

Figure C-1: Absorbance spectrum as measured by a spectrometer (Ocean Optics USB 2000+) for a 2 µM sample after having reacted with the PMB assay for a total of 10 minutes. The absorbance peak at 880 nm is 33 % higher than at the peak at 700 nm. The respective full width half maximum (FWHM) values for a 700 nm LED (LED700-02AU, Roithner LaserTechnik, Vienna, Austria) and an 880 nm LED (MTE8800NK2, Marktech Optoelectronics, New York, United States) are indicated as red shaded areas.

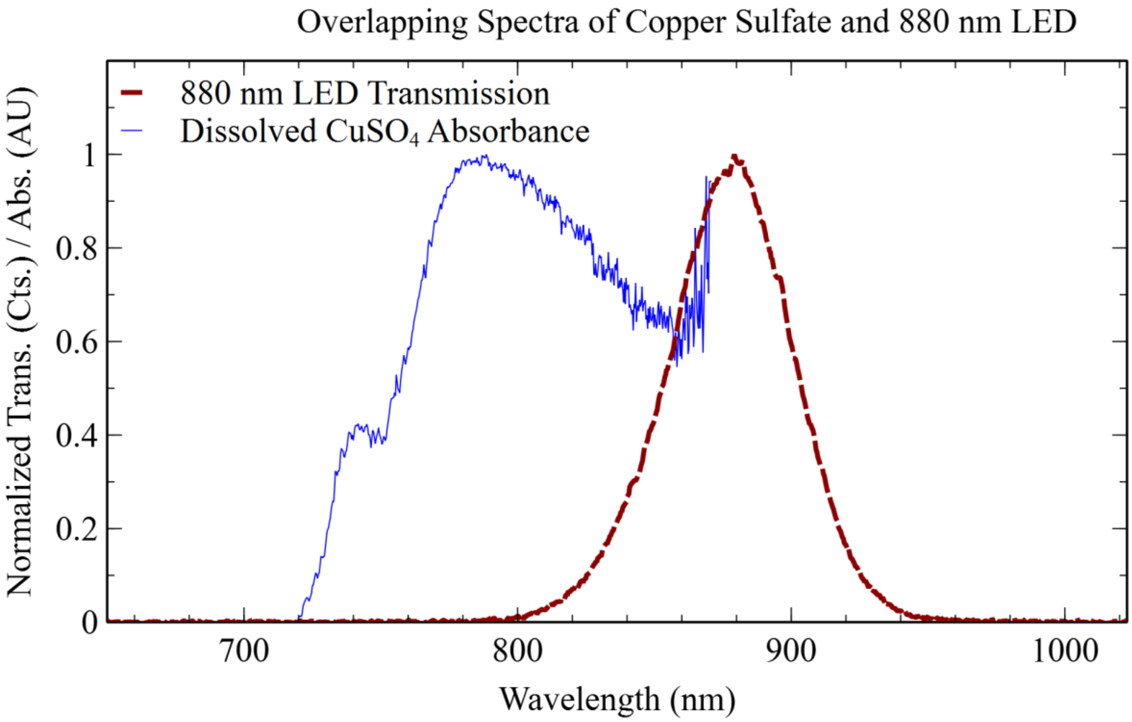

Figure C-2: Absorbance and transmission spectra for copper sulfate and the LED

Absorbance and transmission spectra as measured by a spectrometer (Ocean Optics USB 2000+) for a dissolve copper sulfate sample and the 880 nm LED (MTE8800NK2, Marktech Optoelectronics, New York, United States) respectively.

APPENDIX D. CEAS MUTLI-BOUNCE SIMULATIONS

Here I have included some alternative designs and preliminary Zemax simulation data for multi-bounce absorbance cells. In an effort to fully take advantage of TIR and maximise the amount of redirected light, the incident angle was reduced from 45 degrees to 22.5 degrees in some of the designs. Figure D-1 shows the design progression for one some of the 22.5 degree configurations. The first panel is the most basic setup in which two dead ended channels are positioned at 22.5 degrees to the air prism. Because the end of the channel is normal to the layout ray, there is no refraction and the light is redirected at the same angle. However, when the channels are joined together, as shown in the second panel,

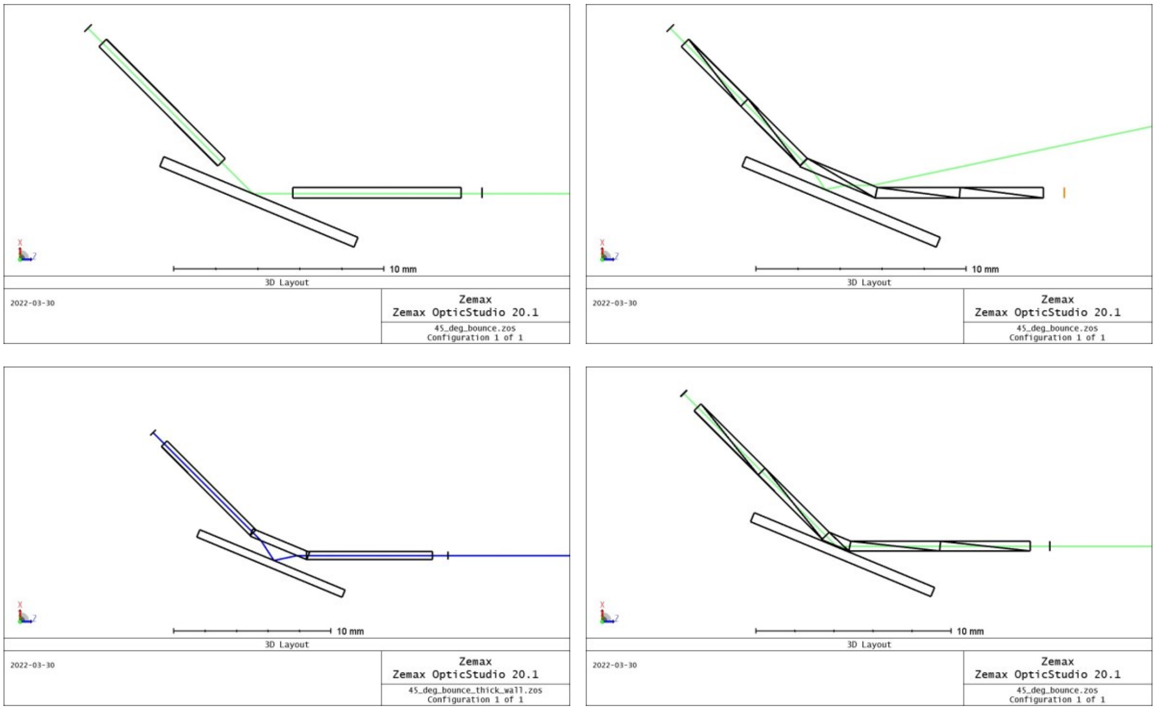

Figure D-1: Top Left: Two disjointed fluid channels, positioned at 22.5 degrees to the air prism. Top Right: Same fluid channels, now joined with a parallel channel 1 mm from the air prism. Bottom Left: Joined channels positioned to account for refractive index changes, still 1 mm from the air prism. Bottom Right: Joined channels, positioned 0.1 mm from the air prism.

the light is no longer normal to the interface between the water filled channel and the PMMA, causing it to refract and then reflect at an angle away from the detector. Using the relative refractive indices of PMMA and water, the refraction angle can be easily calculated and the channels can be designed with a geometry that takes it into account, as shown in the third panel. However, that setup is not very robust to non-collimated light or slight differences in the refractive index. An alternative solution is to minimize the distance that the light needs to travel through the PMMA, thereby minimizing the angular deviation that the refraction causes. This is displayed in the fourth panel. This concept can be taken even further, and used to create a continuous 2-dimensional waveguide, as displayed in Figure D-2.

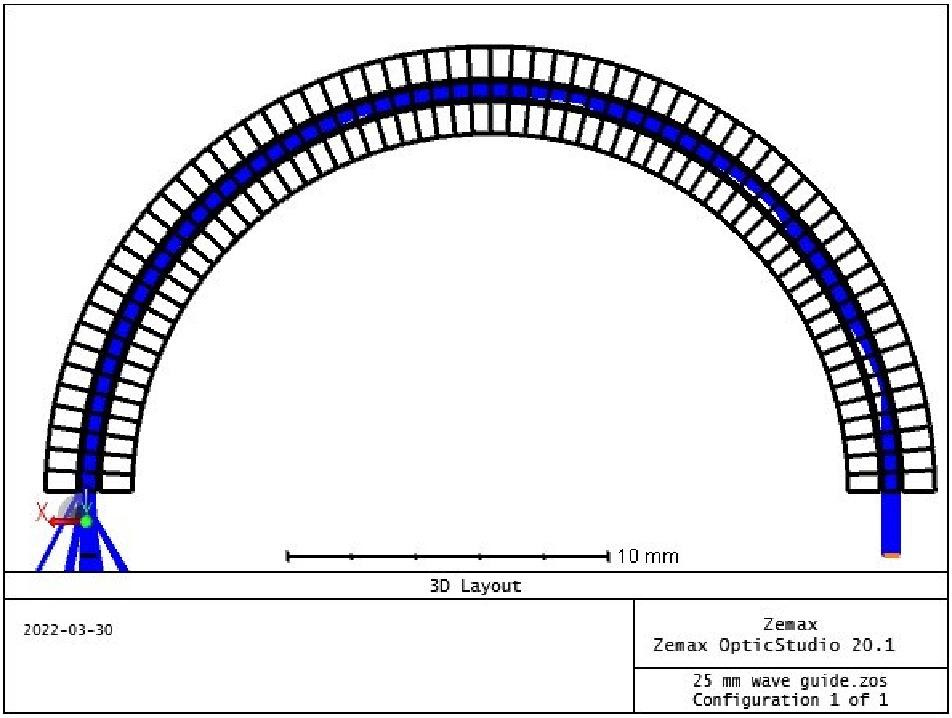

Figure D-2: Simulated model of an in-plane waveguide using air pockets to direct light.

APPENDIX E. CEAS USING CAVITY RING DOWN

E.1 CEAS Using Cavity Ring Down

The concepts of cavity ring down have already been discussed, so here we will present a design intended for application on our *in situ* nutrient sensors. The setup explored here is designed to match the form factor of the existing sensor, with the intention that the microfluidic chip can simply be swapped out with the current device. However, there are two potential issues that would likely prevent a simple swap. The LED is likely not collimated enough to perform cavity ring down, and the LED might not be powerful enough to perform cavity ring down over such a large absorbance cell. CRD on a microfluidic chip has been accomplished in the literature [232], but it was done over an optical path of only 50 µm, rather than the 25 mm or 10 mm paths on the chips here. Before attempting to build a physical system, the setup was again modeled in Zemax so that simulations could be used to give insight into if it is feasible.

The absorbance cell was modeled in the same manner as the mutli-bounce cell, only with a single, straight cell and no additional bounces. An object with a partially reflective surface was placed above both the detector and source prisms. The objects were modeled such that light could freely pass through from one direction, but would reflect with a specified rate from the other direction. The attenuation coefficient of reacted Griess assay and nitrite was used to create several “concentrations” of nitrite ranging between 0 and 10 µM that could be used to create a simulated calibration curve. For each test, the absorbance cell was set to be filled with a pre-determined concentration of the simulated solution. The same LED model was initially used, but after a preliminary test it was clear that the LED model was not nearly collimated enough to be effective. The two parameters set up for study in the simulations were the reflectivity of the mirrors and the angular spread of the light source. Calibration curves were produced for each study, and the slope of the curves (sensitivity) was used as the metric for comparison. For all of the simulations, a 2.67 Watt light source with 10 million rays was used to create each data point.

E.2 Cavity Ring Down Results and Discussion

The preliminary set of tests were performed using the original, uncollimated model of the LED. Four calibration curves were created, with dye solutions ranging between 0 and 10 µM. This was done using four different reflectivity percentages on the mirrors: 0%, 50%, 75% and 90%. Figure E-1 shows the results of these tests. The absorbance for each simulated concentration was determined by comparing the measured luminous intensity at the detector to the measured luminous intensity of the zero concentration blank, and taking

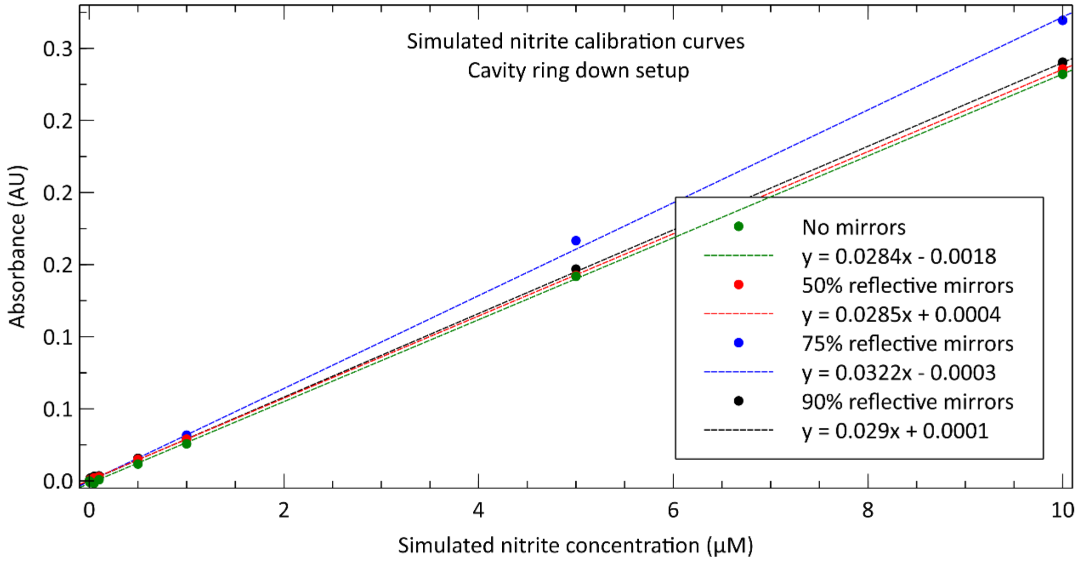

Figure E-1: CRD reflectivity sweep with uncollimated LED source.

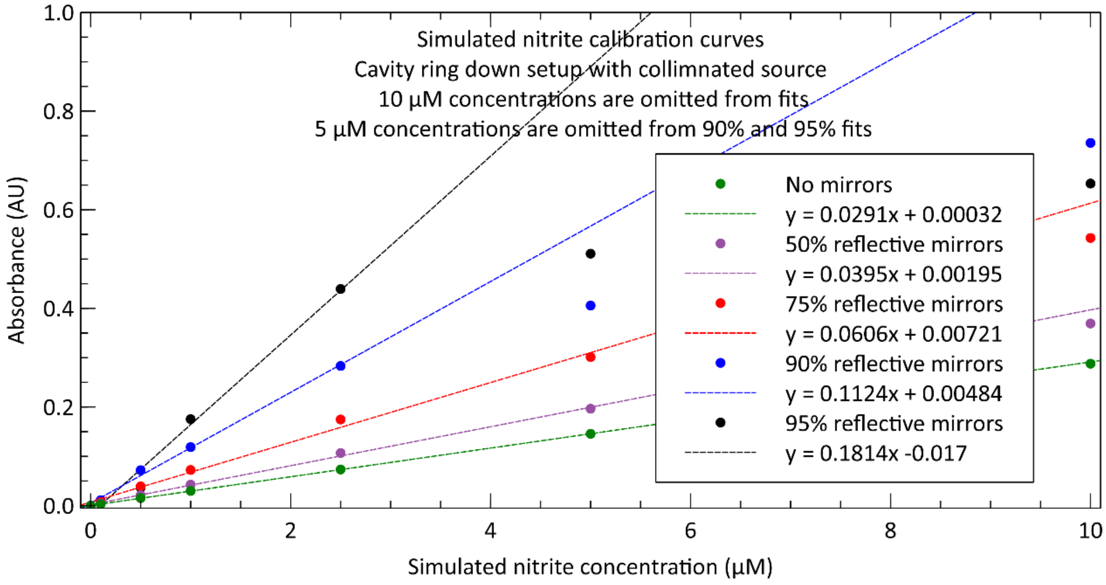

Figure E-2: CRD reflectivity sweep with collimated light source.

the negative logarithm of their ratio. It is obvious in Figure E-1 that there is very little differentiation between the four calibration curves. This was because the LED was not collimated, and any light that hit the detector side mirror was just reflected away from the cavity and not back into it. In this way, there was only ever one pass per light ray, no matter how reflective or transmissive the mirrors were. It was at this point that it was decided to use a collimated light source for further simulations.

The previous test was repeated, but with a perfectly collimated source rather than an LED model, and the results, shown in Figure E-2, were much more diverse than in the first set of simulations. As expected, the slope of the calibration curves increased as the reflectivity of the mirror was increased, highlighting the benefits of using a CRD system if it is feasible. It needs to be noted that certain data points were omitted from the fits, particularly in the 90 % and 95 % reflectivity curves. This was due to the limits of the simulation and available computing power. At these higher reflective values, not enough

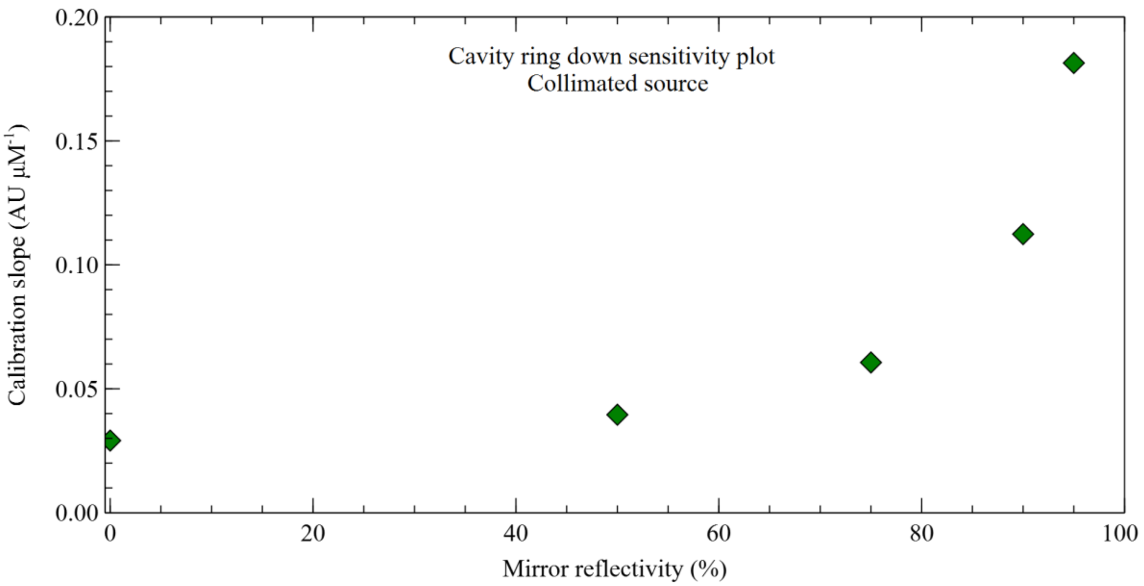

Figure E-3: CRD calibration sensitivity plotted against mirror reflectivity.

rays are able to actually reach the detector to be representative of reality. The slopes from each curve were then plotted against the mirror reflectivity to visualize the relationship more easily. This is shown in Figure E-3. There is asymptotic behavior as the reflectivity approaches 100 % and it is very clear that the closer to 100 % reflectivity, the more sensitive the cell will be. This is in alignment with literature claims that the mirrors should be at least 98 % reflective in a traditional CRD setup. However, it was not possible to simulate a system with 98 % reflectivity or higher, because there were not enough transmitted rays to produce a signal. The simulations each had 10 million rays, but to go any higher was beyond the capabilities of the computer on which the simulations were being run. Furthermore, the number of segments per ray was maxed out in the software to a value of 4000. This means that after a single ray has interacted with 4000 surfaces, it is considered to have too little power to continue propagation and is terminated.

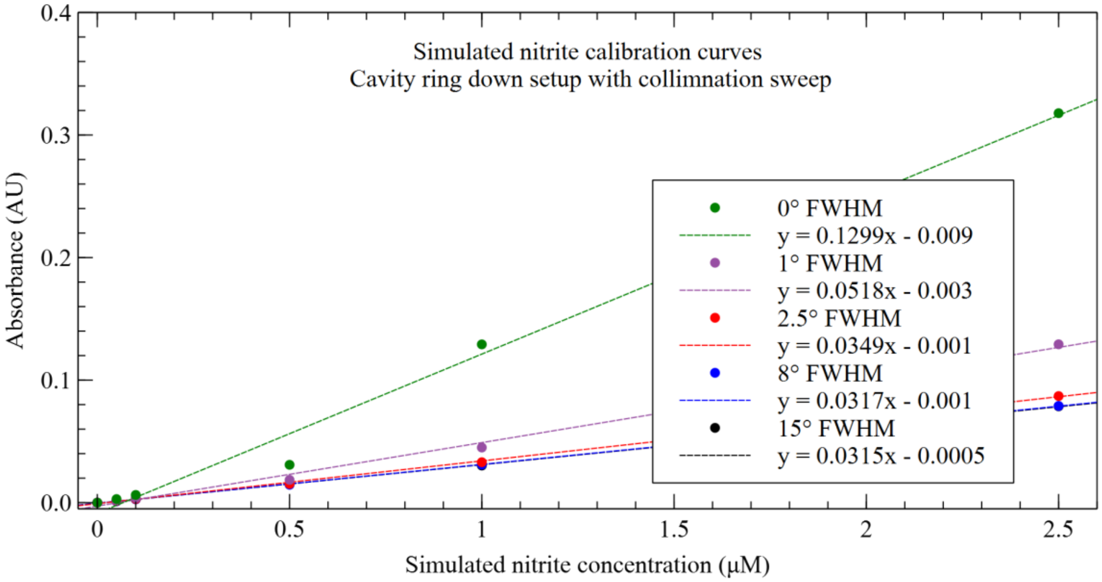

Figure E-4: CRD collimation sweep with 95 % reflective mirrors.

The next set of simulations were to study the impact of collimation on the results. It was obvious from the preliminary test that the original 15° FWHM value for the LED was too divergent to be effective. Therefore, 15° was chosen as the maximum bound for the simulation sweep. The light source was modeled to have a half maximum value at each of the set divergence angles: 0°, 1°, 2.5°, 8°, and 15°. Again, a calibration curve was generated at each angle, with all other variables kept constant, and a mirror reflectivity of 95 %.

Figure E-4 displays the five calibration curves that were generated using the five LED half max angles. It is clear from the figure that the slopes of the curves quickly become shallower when the beam divergence is increased. It is also worth noting that the calibration slope of the 0° FWHM data set is less than the calibration slope of the perfectly collimated data set for the 95 % reflective mirrors displayed in Figure E-2. This is most likely due to the difference in source models in Zemax. In the perfectly collimated data set, the source

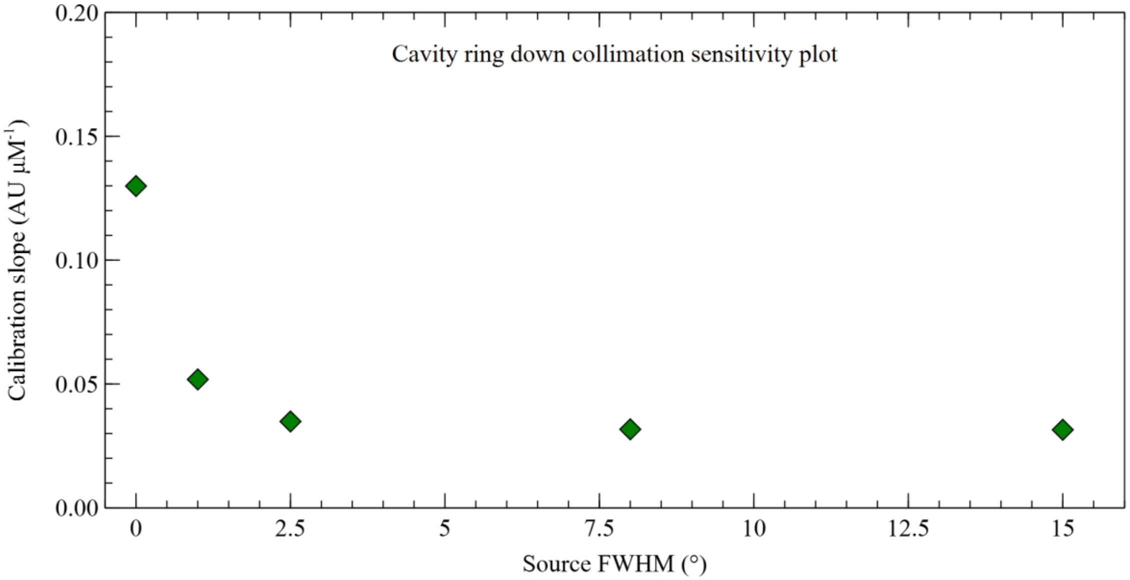

Figure E-5: CRD calibration sensitivity plotted against source divergence angle.

was simply a circle area that outputted a certain number of perfectly collimated rays in the chosen direction. In the collimation sweep data set, the source was a circular area where each ray was directed in an angle determined by a Gaussian distribution that had the FWHM value chosen by the sweep. Creating a Gaussian distribution with a 0° FWHM is not possible, so the 0° data point is actually 0.01°, which was the smallest FWHM value allowed by the software, but is still likely large enough to account for the discrepancy between the two simulations. Figure E-5 shows the slopes of the calibration curves plotted against the FWHM value. All of the data points after 2.5° are roughly the same, showing exactly how important collimation is to the overall function of a CRD system. Most benchtop CRD setups use lasers rather than LEDs, as they are much more collimated. For context, a typical FWHM value for a green laser is 0.6 mrad, which is 0.034°. It is not possible to collimate a standard LED such as the CREE C503B-GAN to that degree. Indeed it would be much more feasible to replace the light source in the physical setup with either a laser or a specialized highly collimated LED.